University of Zagreb
Faculty of Science
Physics Department

Tomislav Ševa

Experimental Study of Hypernuclei Electroproduction by
High Precision Spectroscopy

Doctoral Thesis
submitted to the Department of Physics
Faculty of Science, University of Zagreb
for the academic degree of
Doctor of Natural Sciences (Physics)

Zagreb, 2009

BASIC DOCUMENTATION CARD

University of Zagreb   Dissertation
Faculty of Science
Physics Department

Experimental Study of Hypernuclei Electroproduction by High Precision Spectroscopy

Tomislav Ševa

University of Zagreb

Faculty of Science, Physics Department

Bijenička 32, 10000 Zagreb, Croatia

Abstract

Λ hypernuclear spectroscopy by the $(e, e'K^+)$ reaction is a powerful tool to investigate ΛN interaction because this reaction excites various states up to deep inside of hypernucleus and sub-MeV resolution can be achieved thanks to the high quality primary electron beam from CEBAF at JLab. The second generation hypernuclear spectroscopy at JLab Hall C, E01-011 experiment, was successfully performed in the summer of 2005 introducing High resolution Kaon Spectrometer (HKS) and a new configuration for scattered electron spectrometer. These unique techniques significantly improved both energy resolution and hypernuclear tagging efficiency, and we succeeded to study various hypernuclei including $^{12}_{\Lambda}$B and $^{28}_{\Lambda}$Al with high resolution and sufficient statistics for the first time by this reaction.

ABSTRACT

Jlab experiment E01-011, carried out in 2005 in JLab Hall C, is the second generation of the hypernuclear spectroscopy experiments by the (e,e′K$^+$) reaction.

The (e,e'K$^+$) reaction is complimentary to the associated production reactions (K$^-$,π^-), (π^+,K$^+$) since, due to a larger momentum transfer to a hyperon, excitations of both spin-non-flip and spin-flip states are possible.

The experiment uses high quality and continuous primary electron beam to produce neutron rich hypernuclei on various targets by the electroproduction. The experimental setup consists of splitter magnet, high resolution kaon spectrometer (HKS) and electron spectrometer (Enge) implemented in new configuration, the so called "Tilt Method".

Production data was taken on multiple targets: CH$_2$, ^{6}Li, ^{7}Li, ^{9}Be, ^{10}B, ^{12}C and ^{28}Si. In present study the analysis of CH$_2$, ^{12}C and ^{28}Si is presented. The elementary processes of p(e,e'K$^+$)Λ/Σ from CH$_2$ data were used for calibration of the spectrometer optics and kinematics. The hypernuclear spectra of $^{12}_{\Lambda}$B was obtained with ground state resolution of 0.47±0.07 MeV (FWHM), the best ever achieved. Feasibility of the electroproduction reaction to study medium to heavy targets has been proven with the first high resolution beyond p-shell hypernuclear spectra from $^{28}_{\Lambda}$Al hypernuclei.

The obtained results of the E01-011 experiment confirmed that hypernuclear spectroscopy by the (e,e'K$^+$) reaction is a very useful technique.

Contents

Chapter 1

INTRODUCTION

1.1 Hypernucleus

A hypernucleus is a particle-stable nuclear system formed when one or more nucleons in a normal nucleus are replaced by strange baryons - hyperons.

Hyperons , such as Λ, Σ and Ξ, in $SU(3)_f$ quark model classification are baryons with spin $J = 1/2$ with at least one of the quarks in qqq structure being a strange quark. Baryon octet with strangeness $S = -1$ hyperons is shown in Fig.1.1. Conservation laws allow heavier hyperons to decay strongly in the nuclear matter to Λ hyperons which then can decay weakly. With a typical lifetime of 263 ps Λ hyperon can bound to nuclear medium and form stable system, Λ hypernucleus with lifetime of 200 ps [7] [34].

With this new degree of freedom, strangeness, hyperon is distinguishable from nucleons and therefore does not experience Pauli blocking from nucleons in the nucleus. With this property hyperon can populate deeply bound states and allow us to investigate the interior structure of nuclei which is not possible by excitation of normal nuclei. Without Pauli blocking Λ hypernuclear level structure becomes narrower when compared to the the ordinary nuclei. This effect is discussed in Ref.[5] showing that while nucleon deep hole states have widths of few 10 MeV, widths of Λ bound states are on the order few 100 keV because ΛN interaction is weaker than the NN interaction.
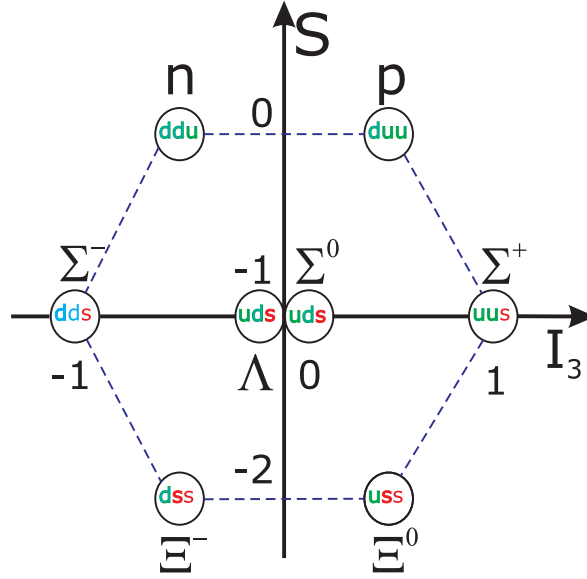
FIGURE 1.1: THE OCTET OF LIGHT $J^\pi = 1/2^+$ BARYONS DISPLAYED ON ISOSPIN I3 AND STRANGENESS S PLANE.

1.2   Hyperon-nucleon Interaction

There is still an ongoing effort in physics community to understand baryon-baryon interaction. A part of this is also the study of hyperon-nucleon interaction which will provide us with information on hyperon-nucleon interaction and the relation of hyperon-nucleon (YN) and nucleon-nucleon (NN) forces and ultimately leading to a unified understanding of SU(3) structure of baryon-baryon interaction [13] [90] [18] [19].

In large measure the Λ maintains its identity in the nuclear medium. Thus, the structure of the hypernuclei can be described using a simple single-particle model basis [75]. The binding energies B_Λ up to the g-shell have been extracted from analysis if the structure observed in the (π, K) reaction as shown in Fig.1.2. Also, the extracted depth of a local Woods-Saxon (Λ-nucleus) potential well was $\approx$30 MeV. Binding energy data can be described [89] with a phenomenological Λ-nucleus potential based on a spherical Skyrme Hartree-Fock approach as shown in solid curves in Fig. 1.2.

With Λ being a isoscalar particle, since it does not posses isospin (T=0), the long range one-pion-exchange (OPE) force as seen in NN interaction is not present in the $\Lambda - N$ interaction because nucleons carry isospin T=1/2 and so Λ and nucleon can not exchange a single pion (T=1). Without OPE force present in the $\Lambda - N$ interaction the short range properties of the baryon-baryon interaction become important. The long-range component is due to two-pion-exchange, in the three body ΛNN interaction, which is overshadowed by OPE in the NN force in the ordinary nuclear physics. The OPE is still present but only in second order through $\Lambda N - \Sigma N$ coupling. With the Λ-Σ mass difference is only 80 MeV, the Λ (T=0) and the Σ (T=1) couples more strongly than the N and D in the non-strange sector. This strong coupling leads to a non negligible tensor force in the ΛN channel and could be responsible for the glue-like role of Λ in the nuclear medium which shrinks the nuclear size.

Through the Λ hypernuclear production experiments it has been found that the weak coupling model which assumes that the Λ couples weakly to the ground and excited states of the core nucleus well reproduced observed hypernuclear ground and excited level structures [26]. The Hamiltonian for the particle-hole shell model configuration can be expressed as [13] [90]:

$$H = H_{\mathrm{N}} + H_{\Lambda} + V_{\Lambda \mathrm{N}}, \qquad (1.1)$$

where H_N is the nuclear core Hamiltonian, H_{Λ} is Λ single-particle term and $V_{\Lambda N}$ is the $\Lambda - N$ interaction. The $V_{\Lambda N}$ is often expressed in phenomenological effective YN interaction by G-matrix method starting from the two-body interaction in free space [63]. The phenomenological effective interactions used: $V_{\Lambda N} = \sum_{\alpha} V_{\alpha}(r)$, where α represents the central (V_c), tensor (V_T), spin-orbit (V_{LS}) and antisymmetric spin-orbit (V_{ALS}) components. The spin-orbit splitting predicted by different models vary widely [60].

For the case of p-shell hypernuclei with a Λ in an s orbit, the $p_N s_{\Lambda}$ interaction can be described in terms of five radial integrals V, Δ, S_{Λ}, S_N and T. The mentioned integrals are associated with the average central, spin-spin, Λ spin-orbit, induced nucleon spin-orbit and tensor terms in the potential and assumed to be constant across the p-shell [18]. In terms of the five integrals

the interaction can be expressed as [18] [90]:

$$V_{\Lambda N}(r) = V_0(r) + V_\sigma(r)\vec{s}_N \cdot \vec{s}_\Lambda + V_\Lambda(r)\vec{l}_{N\Lambda} \cdot \vec{s}_\Lambda + V_N(r)\vec{l}_{N\Lambda} \cdot \vec{s}_N + V_T(r)S_{12} \quad (1.2)$$

where $l_{\Lambda N}$ is the relative $\Lambda - N$ orbital angular momentum and S_{12} is the usual spin-tensor operator defined as:

$$S_{12} = 3(\sigma_N \cdot \hat{r})(\sigma_\Lambda \cdot \hat{r}) - \sigma_N \cdot \sigma_\Lambda \quad (1.3)$$

with $\hat{r} = (r_\Lambda \times r_N)|r_\Lambda \times r_N|$. The $V_\alpha(r)$ coefficients are parametrized in a three-range Gaussian form [111] as

$$V_\alpha(r) = \sum_i (a_i + b_i k_F + c_i k_F^2) \; exp \left[-(r/\beta_i)^2 \right] \quad (1.4)$$

where k_F is the Fermi momentum and parameters a_i, b_i and c_i exist for each α.

1.3   Hypernuclear production mechanisms

A Λ hypernucleus can be produced by two mechanisms: strangeness exchange (K^-, π^-) and associated production (π^+, K^+) or (γ, K^+), $(e, e'K^+)$ reactions, as shown in Fig. 1.3. In (K^-, π^-) and (π^+, K^+) reactions, a neutron in the target nucleus $^A Z$ is converted into a Λ which then couples to nuclear core and forms a Λ hypernucleus $^A_\Lambda Z$. In contrast photoproduction (γ, K^+) and electroproduction $((e, e'K^+))$ reactions convert a proton in a $^A Z$ nucleus to Λ which then couples to nuclear core and forms a neutron rich Λ hypernucleus $^A_\Lambda (Z-1)$.

Strangeness exchange reaction (K^-, π^-) using secondary meson beams and associated production (π^+, K^+) reaction are described by elementary processes:

$$K^- + n \rightarrow \pi^- + \Lambda \quad (1.5)$$

$$\pi^+ + n \rightarrow K^+ + \Lambda \quad (1.6)$$
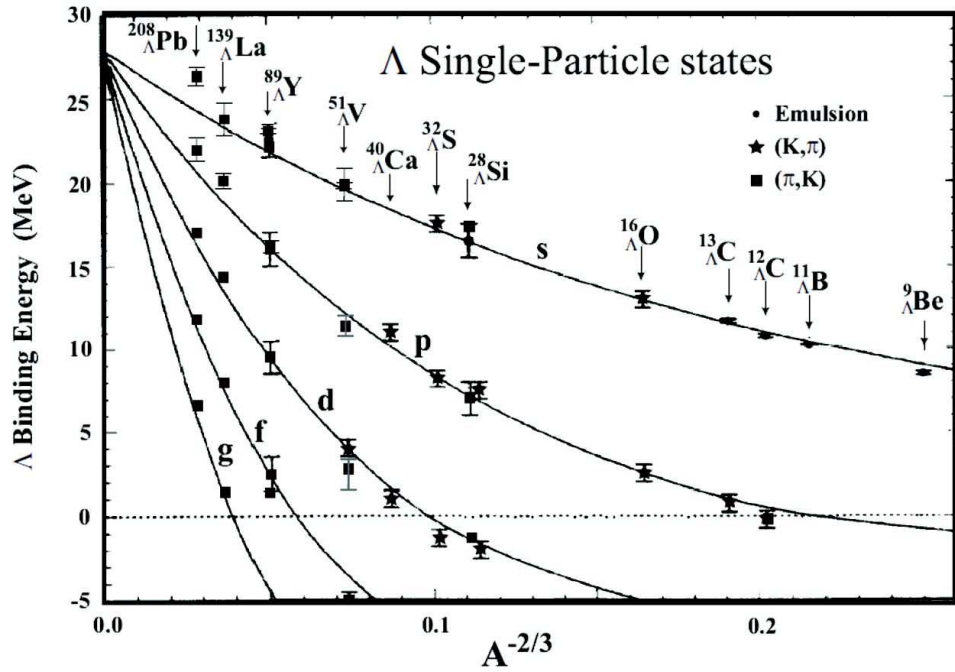
FIGURE 1.2: THE BINDING ENERGY OF Λ SINGLE PARTICLE STATES AS A FUNC-
TION OF CORE NUCLEUS MASS NUMBER (A) [89]. THE SOLID LINE CURVES ARE
FITTINGS TO THE DATA ACCORDING TO A PHENOMENOLOGICAL Λ POTENTIAL
BASED ON SPHERICAL SKYRME-HATREE-FOCK APPROACH [18] [105].

(a) Hadronic production   (b) Electroproduction
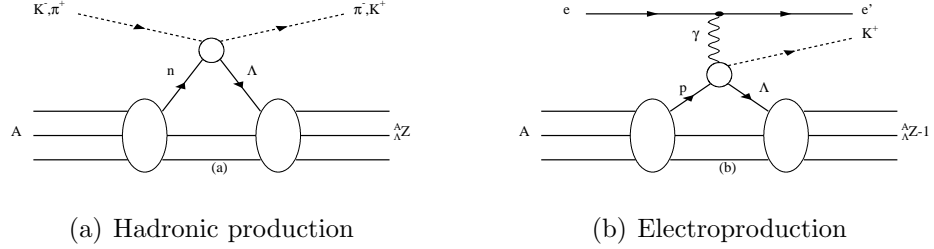
FIGURE 1.3: HYPERNUCLEAR PRODUCTION MECHANISMS

while photoproduction can be expressed as:

$$\gamma + p \rightarrow \Lambda + K^+ \tag{1.7}$$

Hypernucleus can be produced with all interactions that produce hyperons in the nucleus[16] but experimentally useful [76] are only those with significant cross section and detectable reaction products. Hypernuclear production cross section depends mainly on reaction processes elementary cross section (elementary amplitude), target and hypernuclear wave functions, momentum transfer to the Λ hyperon and absorption of incoming and outgoing particles [5]. Characteristics of various hypernucleus production reactions [5] are listed in Table 1.1.

Reaction	$p_{threshold}$ [GeV/c]	$p_{projectile}$ [GeV/c]	q_Y [GeV/c]	σ [νb/sr]	Comments
$(K^-, \pi^{\pm})$	0	0.4-0.8	<0.1	10^3	Substitutional Λ, Σ ($\Delta L = 0$)
K^- stopped		0	0.3 (Λ)	10^2	Substitutional+non-subst. Λ, Σ
(π, K^+)	0.6-0.8	1.0-1.5	>0.3	10	High J,deep Y orbits,polarization
(γ, K^+)	0.65-0.9 (Λ) 0.73-1.05 (Σ)	1.0-1.4	>0.2	0.1	unnatural parity strong spinflip
$(e,e'K^+)$				10^{-3}	high resolution, mag. momentum
(K^-,K^+)	0.73-1.05	1.1-2.0	$\approx$0.5	10	ΔS=-2
(p,K^+)	1.6	2.0-5.0	>1.0	$<<10^{-3}$	

TABLE 1.1: CHARACTERISTICS OF VARIOUS HYPERNUCLEUS PRODUCTION REACTIONS [5]. MOMENTA: $p_{threshold}$-THRESHOLD, $p_{projectile}$-INCIDENT , q_Y-RECOIL

Cross section

In Fig.1.4 (Top), typical cross sections are shown schematically versus momentum transfer for some of the reactions used in hypernuclear spectroscopy.

The biggest cross section, of the elementary process reactions mentioned, has the strangeness exchange reaction (K^-, π^-) with cross section up to 10 mb/sr and on the order of 5 mb/sr near $p_K = 800$ MeV/c at forward angle after Fermi-averaging over the nucleons [18] [21].

Strangeness production (π^+, K^+) reaction cross section peaks strongly at $p_\pi = 1.05$ GeV/c with cross section approximately one order of magnitude smaller than the strangeness exchange cross section [29] [78]. With available pion beams with intensities much higher than that of kaon beams the smaller cross section can be compensated .

The photoproduction process, (γ, K^+) reaction, with cross section of about 2 μb/sr, two order of magnitude less than (π^+, K^+) [59]. This small cross section can be partially compensated by the high intensity electron beam, as provided by the CEBAF at JLab.

Momentum transfer

For hypernucleus to be produced, the hyperon created with the reaction on nucleons has to stay in the nucleus. This is described by so called "Sticking probability" which is largely depended on the momentum transferred to the created hyperon. Momentum transfer (q) to the Λ hyperon for mentioned reactions as a function of the incident particle momentum is shown in Fig.1.4 (Bottom). Sticking probability of the hyperon in the nucleus will be small if momentum transfered is too large, when compared to the nuclear Fermi momentum ($p_F \approx 270$ MeV/c). In the situation when momentum transfered is very small the sticking probability should be high with hyperon obtaining orbital numbers of the original nucleon [5].

As shown in Fig. 1.4, the typical momentum transfer at zero degree scattering angle for (K^-, π^-) process is 50-150 MeV/c, while it is about 300-400 MeV/c for (π^+, K^+) reaction and similarly for (γ, K^+) reaction. The
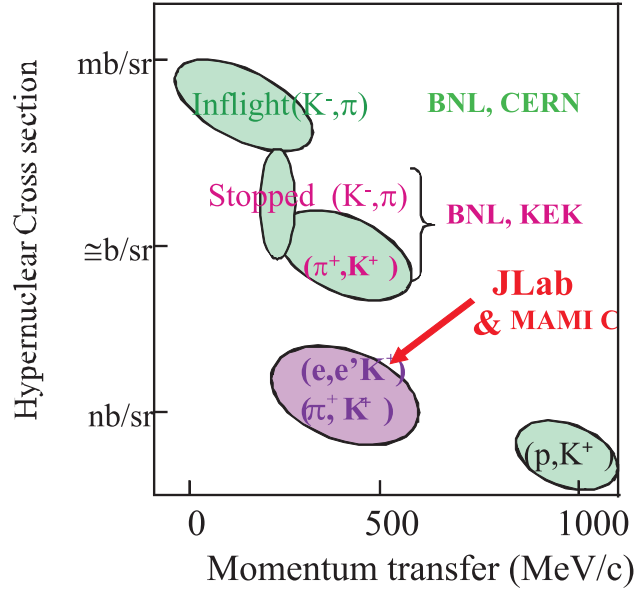
(a) Hypernuclear production cross section for typical reactions versus momentum transfer
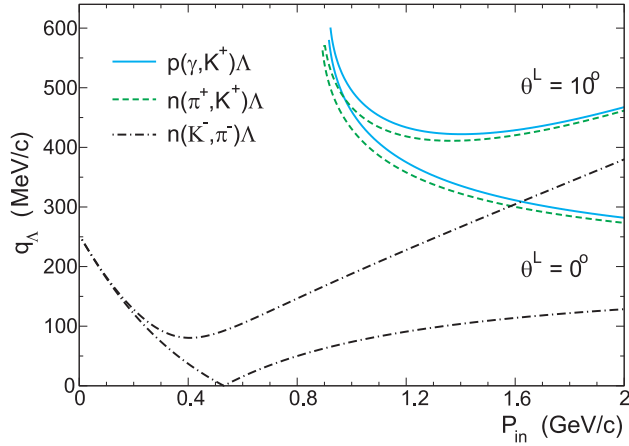
(b) Momentum transfer to the Λ hyperon is plotted as a function of projectile laboratory momentum P$_{in}$

FIGURE 1.4: CROSS SECTIONS AND Λ RECOIL MOMENTUM FOR DIFFERENT ELEMENTARY REACTIONS. (A) HYPERNUCLEAR PRODUCTION CROSS SECTION [44] [78] (B) MOMENTUM TRANSFER TO THE Λ HYPERON IS PLOTTED AS A FUNCTION OF PROJECTILE LABORATORY MOMENTUM P$_{in}$. THE TWO CURVES FOR EACH REACTION CORRESPOND TO THE TWO VALUES OF THE KAON (PION) ANGLE $\theta^L = 0°$ (LOWER CURVES) AND $\theta^L = 10°$ (UPPER CURVES) [99] [5].

(K^-, π^-) process is exothermic, while the (π^+, K^+) and (γ, K^+) reactions are both endothermic. Common properties for both endothermic reactions is that the momentum transfer is maximal at the reaction threshold with slow decrease with increasing incident particle momentum going into the saturation region. The threshold value of the π^+ lab momentum for the (π^+, K^+) process to take place is 0.89 GeV/c.

In the (K^-, π^-) reaction, as shown in Fig.1.4, a recoilless Λ hyperon can be produced at the so called "magic momentum" of the incident kaon at approximately $p_{K^-} \approx 0.55$ GeV [21]. Characteristic of the (K^-, π^-) reaction, because momentum transfered to the created Λ hyperon is small and at the magic momentum of the incident kaon even zero, the orbital angular momentum $\delta L = 0$ and spin $\delta J = 0$ transfer to the Λ are favored. As a result created Λ will populate the same angular momentum states as the neutron it was created from. In the case of the hypernuclear ground state this means that Λ will have the same angular momentum as the neutron in the outermost shell. This are so called "substitutional states".

Contrary to the strangeness exchange mechanism, the associated production reactions (π^+, K^+), (γ, K^+) and $(e, e'K^+)$ transfer a large momentum, larger than the nuclear Fermi-momentum, to the recoil hypernucleus, as shown in Fig. 1.4. The effect of large momentum transfer is reflected in production of hypernuclei with high-spin hypernuclear states [5]. This high-spin stretched configurations have maximum angular momentum, $J_{max} = l_n + l_\Lambda$ for the (π^+, K^+) reaction and $J_{max} = l_n + l_\Lambda + 1$ for the photo-production and electroproduction since photons carry spin. With such a momentum configuration the parity of a state defined as $(-1)^J$ is influenced. The reaction (π^+, K^+) populates natural parity states ($J_{max} = l_n + l_\Lambda$) while electroproduction $(e, e'K^+)$ can populate un-natural parity states ($J_{max} = l_n + l_\Lambda + 1$). This also is a consequence of the dominance of the spin-dependent terms over the spin-independent terms in the elementary transition matrix of electroproduction [60].

Hypernuclear excitations functions obtained on a ^{12}C target by the reaction channels, (K^-, π^-), (π^+, K^+) and $(e, e'K^+)$, of hypernuclear production mechanism are shown in Fig.1.5 [78].
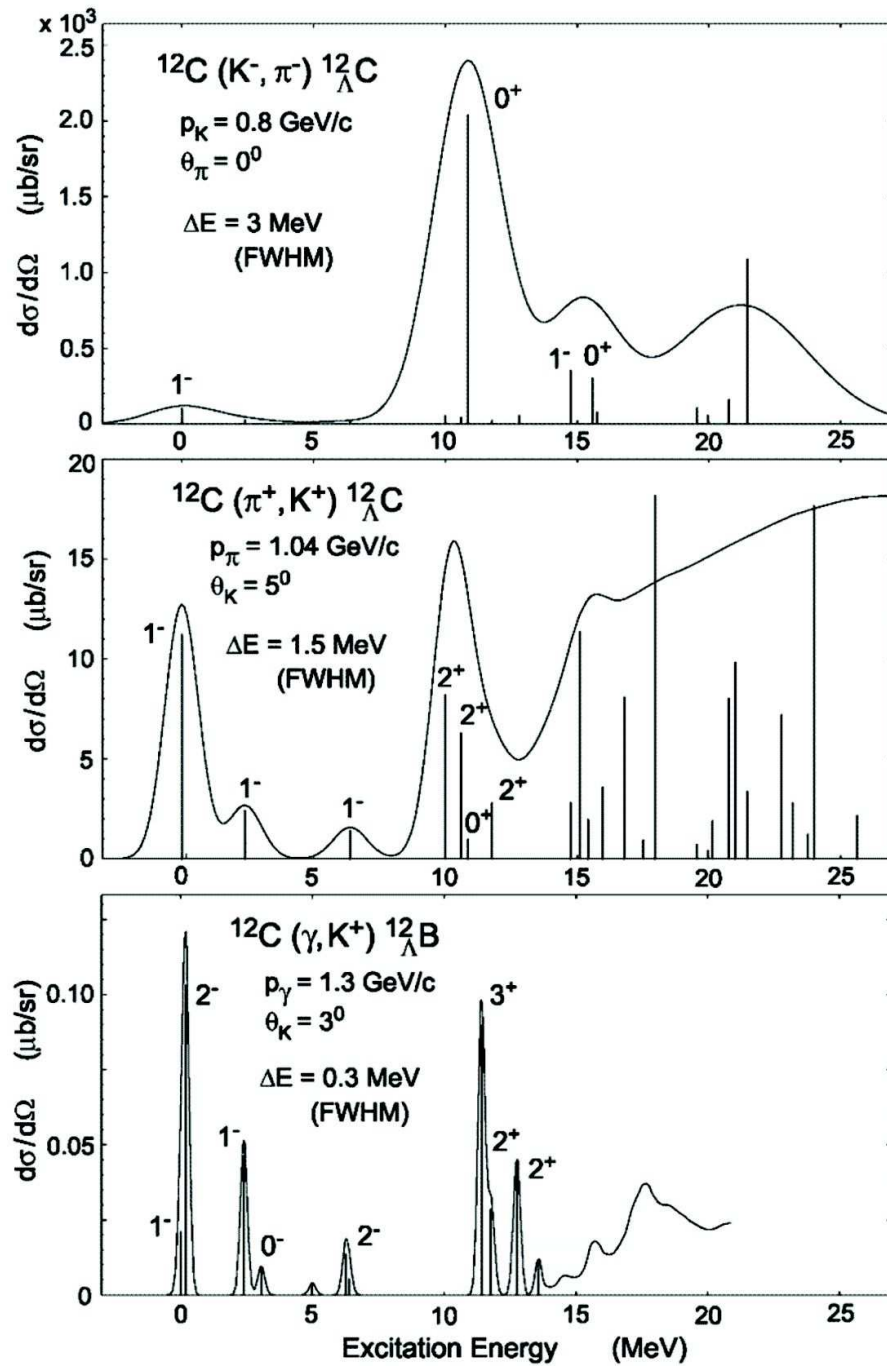
FIGURE 1.5: COMPARISON OF THE EXCITATION FUNCTIONS TO BE OBSERVED IN THE (K^-, π^-), (π^+, K^+) AND $(e, e'K^+)$ REACTIONS ON A ^{12}C TARGET [78].

1.4 Hypernuclear Experiments

1.4.1 Overview

The first observation of a hypernucleus, as shown in Fig.1.6, was made by M. Danysz and J. Pniewski [14] in a balloon-flown, 600 μm thick, glass-blacked Ilford G5 emulsion plate. The Λ hypernucleus was formed by cosmic ray and identified by its decay product [15]. This marked the beginning of hypernuclear physics.

The most of the observed hypernuclei are Λ hypernuclei, when a single Λ is bounded to the nuclear core represents, and as such have been extensively studied [76]. Events have also been found which attribute to the formation of $S = -2$ $\Lambda\Lambda$ hypernuclei [108]. Because heavier hyperons, such as Σ and Ξ, decay via strong decay the $\Sigma + N \to \Lambda + N$ and $\Xi + N \to \Lambda + \Lambda$ processes the formed Σ and Ξ hypernuclei are unstable a width less than 5 MeV for such configuration would be remarkable. Σ hypernuclei were also studied and measured peak structures show a width of 7-8 MeV [32] [61].

Following O. Hashimoto and H. Tamura [78], the experimental development of hypernuclear spectroscopy may be divided in four stages: studies by the emulsions, counter experiments with (K^-, π^-) reaction, use of the associated (π^+, K^+) reaction and γ-ray spectroscopy and $(e, e'K^+)$ reaction.

Summary of the Λ hypernuclei, which have been identified experimentally so far, are summarized in Fig. 1.7.

First stage: emulsion technique

In this stage first observation of hypernucles was achieved, as shown in Fig. 1.6. Shown are the tracks of particles in a photographic emulsion. A cosmic ray, marked "p" in the figure, has collided with a nucleus in the emulsion. One of the fragments from the collision decayed to lower down the cross point marked as B to produce three new tracks. The faintest of these, traveling towards the lower left (and marked 3 on the original), is probably due to a pion. Reconstructed energy in the disintegration process is consistent with
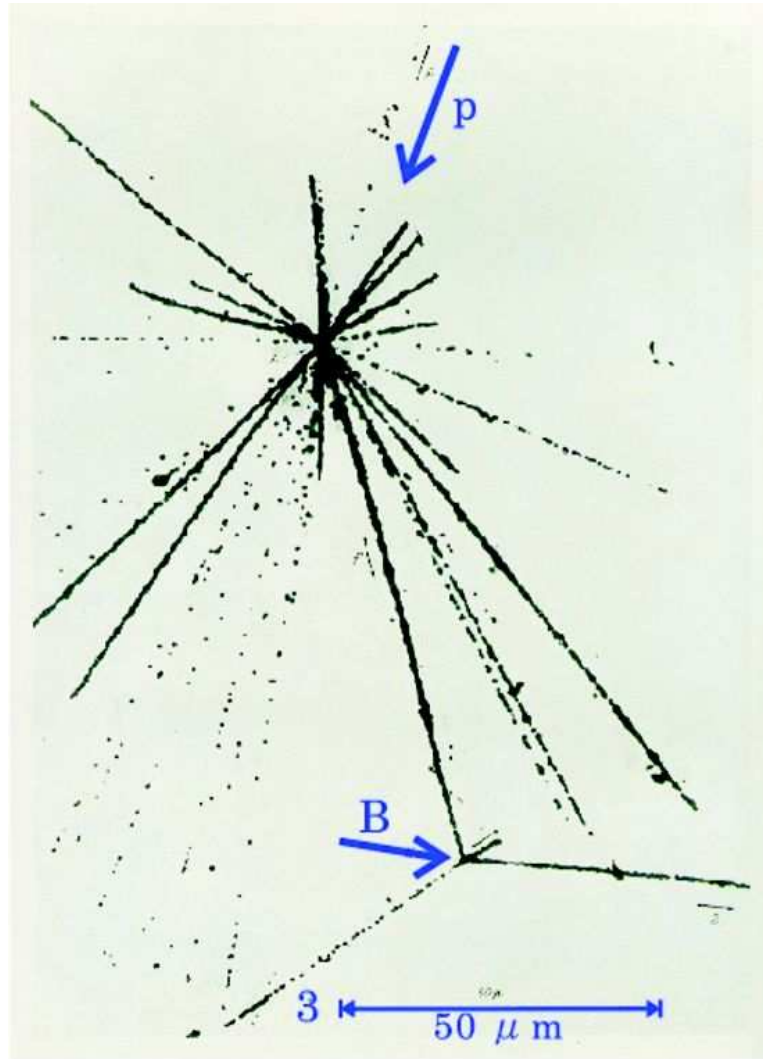
FIGURE 1.6: THE FIRST OBSERVED HYPERNUCLEAR DECAY IN A PHOTOGRAPHIC EMULSION BY M.DANYSZ *et al.* [14].
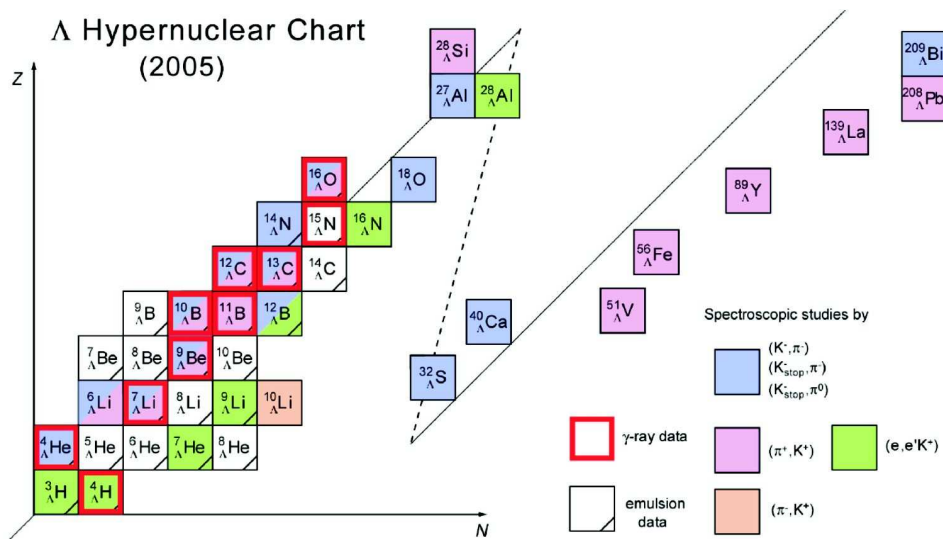
FIGURE 1.7: Λ HYPERNUCLEAR CHART. THE EXPERIMENTALLY IDENTIFIED Λ HYPERNUCLEI AND THE EXPERIMENTAL METHODS USED TO STUDY THEM ARE SHOWN. UPDATE FROM REF. [78].

the decay of a lambda particle in the original nuclear fragment.

In this stage hypernuclei were produced by incident cosmic rays and secondary meson beams on emulsions or bubble chambers. This stage provided measurements of binding energies of only light hypernuclei ($3 < A < 16$) ground states (and a few excited states) from weak decay of Λ hypernuclei [30]. The Λ potential well depth was found to be approximately 2/3 of the nucleon potential.

The results of this experiments [15] showed that biding energy of Λ increased with higher mass number (A) of the nuclear core on the order of 1 MeV per nucleon in the core. Possibility of charge symmetry breaking was suggested due to a small difference in the Λ binding energy of the mirror hypernuclei $^4_\Lambda$He and $^4_\Lambda$H.

Second stage: counter experiments with K^- beams

The second stage in the hypernuclear spectroscopy, started in the 1970s with the counter detector experiments through the use of low momentum, high intensity K^- beams, first at CERN (Centre Européen pour la Recherche Nucleaire) [23] and later at Brookhaven National Laboratory (BNL). Spectroscopic studies including excited states of hypernuclei became possible by the (K^-, π^-) reaction. After the first experiment by the (K^-_{stop}, π^-) reaction [40] the study of the hypernuclei continued with the in-flight (K^-, π^-) reaction near the magic momentum producing an almost recoilless hypernuclei [64] [65] [66] [8] [48] [49] [50].

The major impact of the in-flight (K^-, π^-) reaction was on the possibility to study light p-shell hypernuclei. From measured data it was concluded that the spin-orbit splittings of Λ orbits are very small [66]. Problems encountered were due to low statistics and low beam intensities oof K^- beams.

Third stage: use of the associated (π^+, K^+) reaction

In the mid 1980s, a new program using the associated production reaction (π^+, K^+) began at the alternating gradient synchrotron (AGS) of Brookhaven

National Laboratory (BNL) on a carbon target [91] . This usage of this reaction in the hypernuclear investigations was studied previously, but due smaller cross section when compared to the (K^-, π^-) reaction [74] [42] [51] it was not considered suitable for spectroscopy. High intensity pion beams compensated for the small cross section.

Since then Λ hypernuclear spectroscopic studies were done on the higher atomic mass targets, up to the A=89, at BNL [100] but also at the 12 GeV proton synchrotron (PS) of the High Energy Accelerator Organization (KEK, Japan) [41].

Hypernuclear mass spectra with an energy resolution of 1.45-2.0 MeV (FWHM) up to a mass number of A=208 were measured with finished Superconducting Kaon Spectrometer (SKS) at the KEK [53] [45] [77]. High-quality Λ spectra were measured and deeply bound states, such as s_Λ and p_Λ, were identified for various Λ hypernuclei. Fine peak structures related to core-excited states were observed for light hypernuclei of $^{10}_{\Lambda}B$ and $^{12}_{\Lambda}C$ helping to understand the ΛN interaction by precise comparisons with configuration mixing shell model calculations [12] [84] [83]. This effort established hypernuclear spectroscopy as a broadly applicable, quantitative tool.

Fourth stage: γ-ray spectroscopy and $(e, e'K^+)$ reaction

New era in hypernuclear investigations began in the last decade with development of two new experimental techniques based on electromagnetic probes: the γ-ray spectroscopy [33] on the hadronic hypernuclei production reaction and hypernuclear spectroscopy with the (e, e'K$^+$) reaction [56].

The use of γ-ray spectroscopy in the hypernuclear spectroscopy was introduced in 1970s [23] but only recently the full capabilities of its usefulness has been exploited. The gamma rays are produced by selected transitions of excited hypernuclear states produced by the reaction (K^-, π^-) or (π^+, K^+). The first observation of γ-ray transition on the p-shell Λ hypernuclei was done at the BNL-AGS [88] [87]. With the use of a germanium detector array called Hyperball at KEK, precision spectroscopy has been carried out with unprecedented resolution of a few keV [33]. Further γ-ray spectroscopic

studies with the Hyperball have been done at KEK [38] [37] [69] and at BNL [31] [43].

With such a resolution the investigation of Λ hypernuclei structure by γ spectroscopy allows us to study in detail the ΛN interaction, especially the spin-dependent interactions (spin–spin, spin–orbit, and tensor interactions), the ΛN–ΣN coupling interaction and charge symmetry breaking.

The second important development in the hypernuclear spectroscopy is the use of the $(e, e'K^+)$ reaction. The high quality, high-intensity CW electron beams available at the Thomas Jefferson National Accelerator Facility (JLab), USA, permitted the first successful $(e, e'K^+)$ spectroscopy measurements [56] [39]. More on the obtained results in the following section.

A better understanding of the interior structure of the Λ hypernuclei is expected by combining absolute mass levels obtained by the $(e, e'K^+)$ spectroscopy and spin doublet splittings values obtained by the γ-ray spectroscopy.

1.4.2   E89-009 experiment

The first successful hypernuclear spectroscopy measurements by the electroproduction $(e, e'K^+)$ reaction was carried out at the Thomas Jefferson National Accelerator Facility (JLab) in the year 2000 by the E89-009 experiment : ”Investigation of the Spin Dependence of the AN Effective Interaction in the P Shell” (HNSS for Hyper-Nuclear Spectroscopic System) [80].

The HNSS experiment showed that high resolution hypernuclear spectroscopy with the $(e, e'K^+)$ reaction is possible [56] [39]. The zero degree electron tagging method was used to maximize the hypernuclear yield. The hypernuclear mass resolution was affected by the hadron spectrometer momentum resolution and acceptance and high background rates of the bremsstrahlung electrons in the electron spectrometer system (Enge). To minimize the high background rate in the electron arm the used beam intensity had to be low ($< 1\mu A$ for ^{12}C target) resulting in a small hypernuclear production rate.

The obtained hypernuclear mass spectra in the HNSS experiment from CH_2 and ^{12}C target are shown in Fig.1.8. Characteristic Λ single particle states corresponding to s_Λ and p_Λ orbits, as well as a few core excited states are clearly seen in the $^{12}_\Lambda B$ hypernuclear mass spectra. The resolution of the $^{12}_\Lambda B$ ground state was 750 keV (FWHM), the best resolution at the time.

1.5 Electroproduction of Hypernuclei

The basic characteristics of photoproduction interactions (γ, K^+), with real $(\gamma + p \rightarrow K^+ + \Lambda)$ and virtual photons $(e + p \rightarrow e' + K^+ + \Lambda/\Sigma^0)$, are large momentum transfer (q>400MeV) to the created hyperon and the strong spin-flip $(\triangle S = 1)$ terms. The spin-flip, due to the virtual photon γ^* spin, means that photoproduction reactions will excite states with natural and unnatural parity. The spin-flip unnatural parity states with $J = J_{max} = l_n + l_\Lambda + 1$ are suppressed in (K^-, π^-) and (π^+, K^+) reactions. Thus photoproduction reactions are complementary to hadronic reactions.

The disadvantage of the photoproductions is that, due to large momentum transfer, the cross sections are strongly suppressed by the nucleus-hypernucleus transition form factor. On the other hand, in contrast to the purely hadronic processes, target nuclei are essentially transparent to the incident photons and the distortion of K^+ is rather small. Due to transparency of the nuclei to the incident photons deeply bound particle-hole states can be formed with Λ deep inside nuclei for heavy nuclei. Additionally, since $(e, e'K^+)$ reaction uses low emittance and high energy stability $(< 10^{-4})$ primary electron beam the beam energy uncertainty is very small. With well defined beam energy, high beam intensity and high resolution spectrometers hypernuclear states can be observed with sub-MeV resolution which may allow us to observe the spin-orbit splittings for high orbital states.

In contrast to the hadronic processes, which produce hyperons in interaction with neutrons, in the electroproduction $(e, e'K^+)$ interaction hyperons are created on protons and so, for zero isospin $T = 0$ nuclei, it will excite neutron rich $T > 0$ mirror hypernucleus to (K^-, π^-) and (π^+, K^+) reactions.
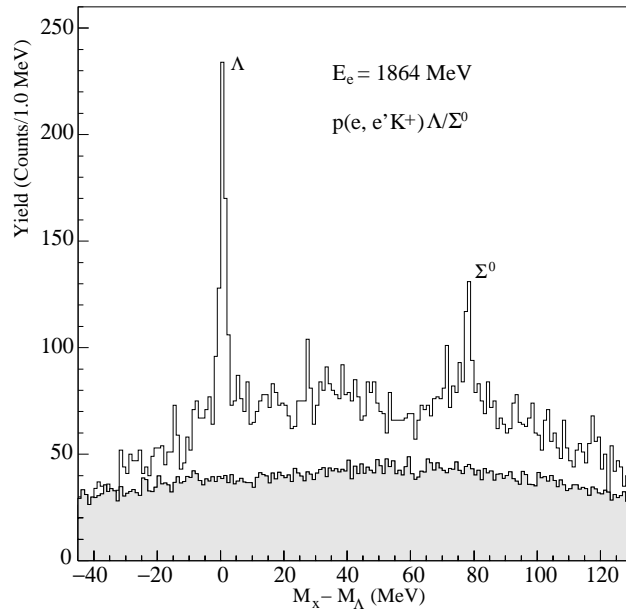
(a) Missing mass spectra from CH_2 target
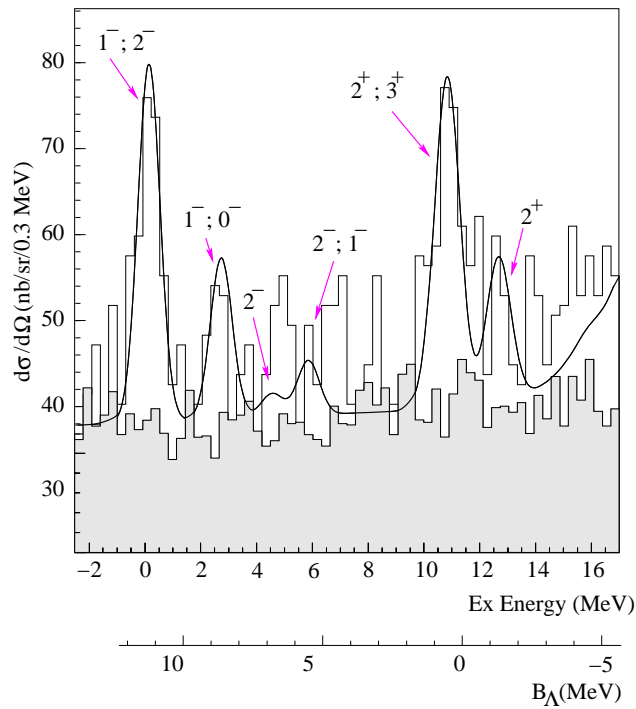
(b) Spectrum of the $^{12}_{\Lambda}B$ hypernuclei

FIGURE 1.8: MISSING MASS SPECTRA OBTAINED IN THE E89-009 EXPERIMENT. CH_2 AND ^{12}C TARGET WERE USED [56] [39] [110].
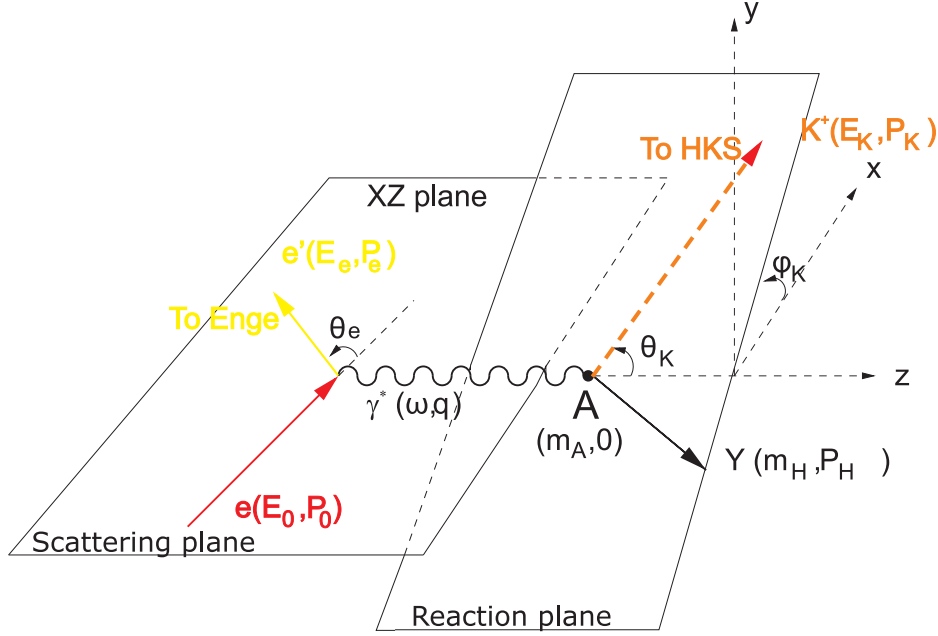
FIGURE 1.9: KINEMATICS OF THE ELECTROPRODUCTION. THE INITIAL (p_e) AND FINAL $(p_{e'})$ ELECTRON MOMENTA DEFINE THE SCATTERING PLANE xz. THE TRANSFERRED MOMENTUM $q = p_e - p_{e'}$ DIRECTED ALONG THE Z-AXIS, AND THE MOMENTUM OF THE KAON $p_{K}+$ DEFINES THE REACTION PLANE.

By studying the mirror hypernuclei, created by $(e, e'K^+)$ and (K^-, π^-) or (π^+, K^+) reactions, Charge Symmetry Breaking effect (CSB), expected to be significant for heavy hypernuclei with large neutron excess, can be studied.

Elementary amplitude and kinematics

The kinematics of the electroproduction reaction, the elementary process of electron scattering from proton, as sketched in Fig.1.9, can be written:

$$e(p_e) + \text{p}(p_\text{p}) \rightarrow e(p_{e'}) + \Lambda(p_\Lambda) + \text{K}^+(p_{K+}), \qquad (1.8)$$

where variables in the parentheses represents the four-momentum of the corresponding particle.

The four momentum of the virtual photon $q = (\omega, \vec{q})$ transferred to the

nucleon is defined by $\vec{q} = \vec{p_e} - \vec{p_e}$ and $\omega = E_e - E_{e'}$. An azimuthal angle $\Phi_{\mathrm{K}+}$ defines the angle between the scattering and reaction planes. The differential cross section of the process, Eqn. 1.8, may be written as [96]:

$$d\sigma = \frac{E_e}{p_e}\frac{m_e}{E_e}\frac{m_p}{E_p}\frac{m_e}{E_{e'}}\frac{d\vec{p_{e'}}}{(2\pi)^3}\frac{1}{2E_K}\frac{d\vec{p_K}}{(2\pi)^3}\frac{m_\Lambda}{E_\Lambda}\frac{d\vec{p_\Lambda}}{(2\pi)^3}(2\pi)^4\delta^4(p_p+q-p_K-p_\Lambda)\sum_{spins}|M_{fi}|^2$$

(1.9)

The transition amplitude M_{fi} can be written as the invariant product of leptonic (j_μ) and hadronic (J^μ) currents:

$$M_{fi} = j_\mu(p_{e'}, p_e)\frac{1}{q^2}J^\mu(q, p_p, p_K, p_\Lambda)$$

(1.10)

The triple-differential cross section can be written as the product of lepton $L_{\mu\nu}$ and hadron tensors $W^{\mu\nu}$:

$$\frac{d^3\sigma}{dE_{e'}d\Omega_e, d\Omega_{\mathrm{K}+}} = \beta L_{\mu\nu}W^{\mu\nu}$$

(1.11)

The lepton tensor $L_{\mu\nu}$ can be written as:

$$\begin{aligned} L_{\mu\nu} &= \frac{(2m_e)^2}{2}\sum_{spins} j_\mu(p_{e'}, p_e)j_\nu^+(p_{e'}, p_e) && (1.12) \\ &= L_{\mu\nu}^s + L_{\mu\nu}^a && (1.13) \\ &= 2(p_{e'\mu}p_{e\nu} + p_{e\mu}p_{e'\nu}) - g_{\mu\nu}Q^2 + 2im_e\epsilon_{\mu\nu\alpha\beta}q^\alpha q^\beta && (1.14) \end{aligned}$$

The hadron tensor $W^{\mu\nu}$ can be written as:

$$\begin{aligned} W^{\mu\nu} &= \frac{1}{(2\pi)^3}\frac{m_{\mathrm{p}}m_\Lambda}{E_{\mathrm{p}}E_\Lambda}\int d|\vec{p_{\mathrm{K}+}}|\frac{|\vec{p_{\mathrm{K}+}}|^2}{2E_{\mathrm{K}}}d\vec{p_\Lambda}\delta^4(p_\Lambda + p_{\mathrm{K}} - p_{\mathrm{p}} - q) \\ &\quad\times \frac{1}{2}\sum_{spin} J^\mu(p_{\mathrm{K}}p_\Lambda, p_{\mathrm{p}}q)J^{\nu^+}(p_{\mathrm{K}}p_\Lambda, p_{\mathrm{p}}q) \end{aligned}$$

(1.15)

The hadron current for electroproduction of pseudoscalar mesons can be

written as a sum of six independent gauge invariant terms:

$$J^\mu(p_K + p_\Lambda, p_p q) = \sum_i A_i \bar{u}(p_\Lambda) M_i^\mu u(p_p) \tag{1.16}$$

$$M_1^\mu = \frac{1}{2}\gamma_5\{(\gamma \cdot q)\gamma^\mu - \gamma^\mu(\gamma \cdot q)\} \tag{1.17}$$

$$M_2^\mu = \gamma_5\{q^2 p_p^\mu - (q \cdot p_p)q^\mu\} \tag{1.18}$$

$$M_3^\mu = \gamma_5\{q^2 p_\Lambda^\mu - (q \cdot p_\Lambda)q^\mu\} \tag{1.19}$$

$$M_4^\mu = \gamma_5\{\gamma^\mu(q \cdot p_p) - (\gamma \cdot q)p_p^\mu\} \tag{1.20}$$

$$M_5^\mu = \gamma_5\{\gamma^\mu(q \cdot p_\Lambda) - (\gamma \cdot q)p_\Lambda^\mu\} \tag{1.21}$$

$$M_6^\mu = \frac{1}{2}\gamma_5\{(\gamma \cdot q)q^\mu - \gamma^\mu q^2\} \tag{1.22}$$

The detail description of the scalar form factors A_i is given in [35].

Performing the integration in Eqn.1.15

$$W^{\mu\nu} = \frac{1}{(2\pi)^3}\frac{m_p m_\Lambda}{E_p E_\Lambda}\frac{|\vec{p_{K^+}}|^2}{4E_K R}\sum_{spin} J^\mu(p_K p_\Lambda, p_p q)J^{\nu^+}(p_K p_\Lambda, p_p q)$$

$$= \frac{1}{(2\pi)^3}\frac{m_p m_\Lambda}{E_p E_\Lambda}\frac{|\vec{p_{K^+}}|^2}{4E_K R}\tilde{W}^{\mu\nu} \tag{1.23}$$

$$R = \frac{|\vec{p_K}|}{E_K} - \frac{\vec{p_K} \cdot \vec{p_\Lambda}}{p_K E_\Lambda}$$

where p_Λ and $|P_K+|$ are fixed by the energy and momenta conservation.

In the reference frame where $\vec{q}\|\hat{z}$ and the xz-plane is defined by electron momenta, the triple-differential cross section can be written as [35] [96]:

$$\frac{d^3\sigma}{dE_{e'}d\Omega_e, d\Omega_{K+}} = \frac{1}{|v_e - v_p|}\frac{\alpha^2}{Q^2}\frac{E_{e'}}{E_e}\frac{1}{1-\epsilon}\{(W^{xx} + W^{yy}) \tag{1.24}$$

$$+ \epsilon(W^{xx} - W^{yy}) + 2\epsilon\frac{Q^2}{\omega^2}W^{zz} - \sqrt{2\epsilon(1+\epsilon)\frac{Q^2}{\omega^2}}(W^{zx} + W^{xz})\}$$

where $(y = e^2/4\pi = 1/137$, $Q^2 = -q^2 > 0$ and

$$\epsilon = (1 + \frac{2|\vec{q}|^2}{Q^2}\,tan^2\frac{\theta_e}{2})^{-1} \tag{1.25}$$

with the electron scattering angle of θ_e.

Finally, putting $|v_e - v_p| = (p_e \cdot p_p)/(E_e E_p)$ (for $m_e = 0$), the cross section is:

$$\frac{d^3\sigma}{dE_{e'}d\Omega_e, d\Omega_{\mathrm{K}+}} = \frac{1}{(2\pi)^3}\frac{\alpha^2}{Q^2(1-\epsilon)}\frac{E_{e'}m_{\mathrm{p}}}{(p_e \cdot p_{\mathrm{p}})}\frac{m_\Lambda |p_{\mathrm{K}+}|^2}{4E_\Lambda E_{\mathrm{K}} + R}\{(\tilde{W}^{xx} + \tilde{W}^{yy}) \quad (1.26)$$
$$+ \quad \epsilon(\tilde{W}^{xx} - \tilde{W}^{yy}) + 2\epsilon\frac{Q^2}{\omega^2}\tilde{W}^{zz} - \sqrt{2\epsilon(1+\epsilon)\frac{Q^2}{\omega^2}}(\tilde{W}^{zx} + \tilde{W}^{xz})\}$$

To express the cross section Eqn.1.26 in the form that allows an easy connection to the photo-production (by real photons), the effective photon energy E_γ and the virtual photon flux Γ (commonly evaluated using the lab frame) are defined:

$$E_\gamma = \omega - \frac{q^2}{2m_{\mathrm{p}}} \qquad (1.27)$$

$$\Gamma = \frac{\alpha}{2\pi^2 Q^2}\frac{1}{1-\epsilon}\frac{E_{e'}m_{\mathrm{p}}}{(p_e \cdot p_{\mathrm{p}})}E_\gamma \overset{Lab}{=} \frac{\alpha}{2\pi^2 Q^2}\frac{E_\gamma}{1-\epsilon}\frac{E_{e'}}{E_e} \qquad (1.28)$$

The effective photon energy E_γ represents the energy of the real photon that would yield (in the lab frame) the same $s = (p_p + p_\gamma)^2$ as the actual virtual photon in the electroproduction.

Then separating the $\Phi_{\mathrm{K}+}$ dependent part and Γ^1, the triple-differential cross section is written as [6] [52]:

$$\frac{d^3\sigma}{dE_e, d\Omega_e, d\Omega_{\mathrm{K}+}} = \Gamma \left\{\frac{d\sigma_{\mathrm{T}}}{d\Omega_{\mathrm{K}+}} + \epsilon\frac{d\sigma_{\mathrm{L}}}{d\Omega_{\mathrm{K}+}} + \epsilon\frac{\sigma_{\mathrm{p}}}{d\Omega_{\mathrm{K}+}} + \sqrt{2\epsilon(1+\epsilon)}\frac{d\sigma_{\mathrm{I}}}{d\Omega_{\mathrm{K}+}}\cos 2\Phi_{\mathrm{K}} + \right\} (1.29)$$

where σ_{T}, σ_{L}, σ_{P} and σ_{I} are called transverse, longitudinal, polarization and interference cross section, respectively. They are given in terms of the baryon currents:

$$\frac{\sigma_{\mathrm{T}}}{d\Omega_{\mathrm{K}}} = \frac{\alpha}{4\pi}\frac{m_{\Lambda}}{E_{\Lambda}}\frac{|p_{\mathrm{K}}|^2}{4E_{\mathrm{K}}R}\frac{1}{E_{\gamma}}(\tilde{W}^{xx}+\tilde{W}^{yy})_{\Phi_{\mathrm{K}}=0} \tag{1.30}$$

$$\frac{\sigma_{\mathrm{L}}}{d\Omega_{\mathrm{K}}} = \frac{\alpha}{4\pi}\frac{m_{\Lambda}}{E_{\Lambda}}\frac{|p_{\mathrm{K}}|^2}{4E_{\mathrm{K}}R}\frac{1}{E_{\gamma}}\frac{2Q^2}{\omega^2}(\tilde{W}^{zz})_{\Phi_{\mathrm{K}}=0} \tag{1.31}$$

$$\frac{\sigma_{\mathrm{P}}}{d\Omega_{\mathrm{K}}} = \frac{\alpha}{4\pi}\frac{m_{\Lambda}}{E_{\Lambda}}\frac{|p_{\mathrm{K}}|^2}{4E_{\mathrm{K}}R}\frac{1}{E_{\gamma}}(\tilde{W}^{xx}-\tilde{W}^{yy})_{\Phi_{\mathrm{K}}=0} \tag{1.32}$$

$$\frac{\sigma_{\mathrm{I}}}{d\Omega_{\mathrm{K}}} = \frac{\alpha}{4\pi}\frac{m_{\Lambda}}{E_{\Lambda}}\frac{|p_{\mathrm{K}}|^2}{4E_{\mathrm{K}}R}\frac{1}{E_{\gamma}}\sqrt{\frac{Q^2}{\omega^2}}(\tilde{W}^{zx}+\tilde{W}^{xz})_{\Phi_{\mathrm{K}}=0} \tag{1.33}$$

Although it is possible to calculate the hadronic tensor $\tilde{W}^{ij}$ directly from Eqn. 1.24, it is more convenient to go over to a two-component formalism. In the CMS frame ($\vec{p_{\mathrm{p}}} = -\vec{q}, \vec{p_{\Lambda}} = -\vec{p_{\mathrm{K}+}}$) :

$$\begin{aligned}\vec{\epsilon}\cdot\vec{J}(p_{\mathrm{K}}p_{\Lambda},p_{\mathrm{p}}q) &= f_1(\vec{\sigma}\cdot\vec{\epsilon})+if_2(\vec{\sigma}\cdot\hat{p}_{\mathrm{K}})\{\vec{\sigma}\cdot(\hat{q}\times\vec{\epsilon})\}+f_3(\vec{\sigma}\cdot\hat{q})(\hat{p}_{\mathrm{K}}\cdot\vec{\epsilon})\\ &+ f_4(\vec{\sigma}\cdot\hat{p}_{\mathrm{K}})(\hat{p}_{\mathrm{K}}\cdot\vec{\epsilon})+f_5(\vec{\sigma}\cdot\hat{q})(\hat{q}\cdot\vec{\epsilon})+f_6(\vec{\sigma}\cdot\hat{p}_{\mathrm{K}})(\hat{q}\cdot\vec{\epsilon})\end{aligned}$$
$$\tag{1.34}$$

where $\hat{q}=\vec{q}/|\vec{q}|, \hat{p}_{\mathrm{K}}=\vec{p_{\mathrm{K}}}/|\vec{p_{\mathrm{K}}}|, \sigma$ are the Pauli matrices, ϵ is the polarization vector of the virtual photon. The functions f_i are expressed in terms of the form factors A_i (Appendix B, Ref. [35]). Additional information can also be found in references [96],[78],[1],[20] and [6].

Electroproduction of hypernuclei

The cross section of the electroproduction of hypernuclei:

$$e + \mathrm{A} \rightarrow e' + \mathrm{K}^+ + \mathrm{H}$$

is again given by Eqn. 1.26, with the proton (hyperon) 4-momenta, masses and so on replaced by those of the nucleus A (hypernucleus H).

The hadron current t in Eqn. 1.22 is substituted by the corresponding many-particle matrix element between the non-relativistic nuclear and hypernuclear wave functions:

$$T_{if}^{\mu} = \langle\Psi_{\mathrm{H}}|\sum_{n=1}^{\mathrm{Z}}\chi_{\gamma}\chi_{\mathrm{K}}^{*}J^{\mu}(n)|\Psi_{\mathrm{A}}\rangle,$$

where the sum runs over the Z target protons and $\Psi_H(\Psi_K)$ is the many-particle translationally invariant (shell model) wave functions of target nucleus (hypernucleus). χ_γ is the virtual photon wave function, or more precisely the product of the wave functions of incoming and outgoing electrons in the plane wave approximation (the Coulomb distortion is neglected). χ_K is kaon distorted wave function. χ_K is calculated with the first order optical potential determined by [25]

1) the target nucleus density,

2) the appropriately averaged kaon-proton and kaon-neutron forward scattering amplitudes.

All calculations are treated in the nucleus laboratory frame. The Fermi motion of the target protons is neglected (frozen nucleon approximation), therefore the one-particle hadron current J^μ must be expressed in the proton laboratory frame.

In the many-body system, the transition matrix of the electroproduction in Eqn. 1.34 is written as the following form [35]

$$M = \epsilon_\mu J^\mu = F_1(\sigma \cdot \epsilon) + iF_2(\hat{q} \times \hat{p}_{K^+}) \cdot \epsilon + F_3(\sigma \cdot \hat{q})(\hat{p}_K + \cdot \epsilon)$$

$$+ F_4(\sigma \cdot \hat{p}_{K^+})(\hat{p}_K + \cdot \epsilon) + F_5(\sigma \cdot \hat{q})(\hat{q} \cdot \epsilon) + F_6(\sigma \cdot \hat{p}_{K^+})(\hat{q} \cdot \epsilon),$$

The $(\hat{q} \times \hat{p}_{K^+}) \cdot \epsilon$ term is used instead of the term quadratic in the Pauli matrices $(\sigma \cdot \hat{p}_{K^+})\{\sigma. \ (\hat{q} \times \epsilon)\} + f_3(\sigma \cdot \hat{q})(\hat{p}_K + \cdot \epsilon)$, which is used in the amplitude Eqn. 1.34 in the CMS frame. Six amplitudes F_i are expressed as linear combinations of covariant form factors A_i [35].

Chapter 2

EXPERIMENTAL APPARATUS AND DATA ACQUISITION

2.1 Overview

The hypernuclear spectroscopic experiment E01-011 "Spectroscopic study of Λ hypernuclei up to medium-heavy mass region through the $(e, e'K^+)$ reaction" was carried out in 2005 (from June to October) in the experimental Hall C of the Thomas Jefferson National Accelerator Facility (JLab). Experiment was proposed with a goal to measure (determine) energy levels of Λ binding states in the s and p shell region for variety of targets and the first study of the hypernuclear spectrum beyond the p-shell by the electromagnetic reaction achieved in the reaction $^{28}Si\left(e, e'K^+\right)^{28}_{\Lambda}Al$. Depending on final resolution with this experimental setup we can study energy levels of the core excited states and expected p shell splittings in heavier nuclei since LS splitting is expected to increase with increasing Z.

Focus in the second generation hypernuclear electroproduction at JLAB was set on the reaction $^{28}Si\left(e, e'K^+\right)^{28}_{\Lambda}Al$ since this is the first hypernuclear spectrum beyond p-shell by electroproduction. Data were taken also on the

following targets CH_2,^6Li,^7Li,^9Be,^{10}B,^{12}C and ^{28}Si. CH_2 target was used for calibration purpose, since in scattering of proton from hydrogen in CH_2 Λ and Σ are produced whose masses are very well established and therefore can be used for calibration. The reaction $^{12}C\left(e, e'K^+\right)^{12}_\Lambda B$, first achieved in HNSS experiment, was carried out in order to improve statistics and resolution of HNSS spectra. It is also used in calibration procedure. In addition to the above list other reaction were studied. For the design of future Hall C hypernuclear experiments data was taken for heavier targets ^{51}V, ^{89}Y, ^{208}Pb to study rates, quasi free production...

The E01-011 experiment is coincidence type of experiment where incident electron beam interacts with target and Λ hypernuclei and K^+ are created. After interaction kaon was detected in coincidence with inelastically scattered electron using the two Hall C spectrometers, High Resolution Kaon Spectrometer (HKS) and Enge spectrometer (Enge).

Since electromagnetic interaction has small cross section high luminosity and high quality electron beam ,available to us thanks to the Continuous Electron Beam Accelerator Facility (CEBAF) at JLab, is crucial factor in electromagnetic study of hypernuclear systems. Detailed overview of kinematic conditions, Jefferson lab accelerator facility and experimental setup is to follow.

2.2 Kinematic conditions

The reaction $\left(e, e'K^+\right)$, represented in figure 2.1: incident electron with energy of 1.854 GeV, through the emission of virtual photon, interacts with the proton embedded in nucleus. Scattered electron reaches ENGE scattering plane with central momentum of 0.319Gev/c which means that virtual photon carries momentum of 1.5GeV. Virtual photon interacts with proton and creates strange quark-antiquark pair and as a result proton is converted in one hadron, Λ with quark content uds, and one strange meson, kaon K^+ with quark content $u\bar{s}$. Λ remains in nucleus forming a bound state with binding energy E_b, and kaon K^+ is emitted with central momentum of

1.2GeV/c.
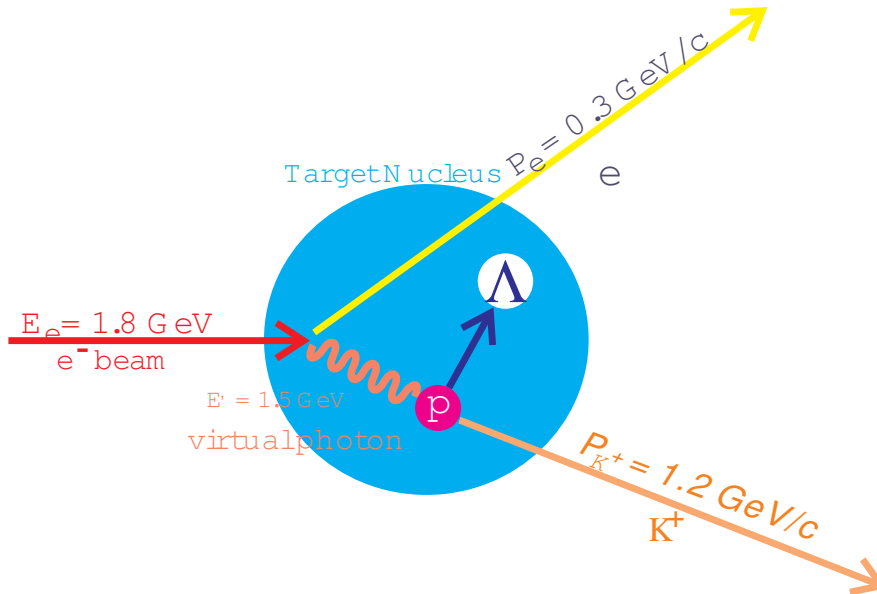
FIGURE 2.1: ELECTROPRODUCTION OF HYPERNUCLEI BY $(e, e'K^+)$ REACTION.

Kinematic conditions were chosen having in mind that in order to have best possible statistics we need to investigate kinematic region with highest cross section with limitation that electron spectrometer (ENGE) has limited kinematic region of scattered electron since it was designed with central momentum of 0.3 GeV. The total cross section of Λ photoproduction as a function of photon energy, measured by SAPHIR group [10], is shown in Fig. 2.2.

As seen in Fig.2.2 the total cross section for kaon photoproduction channel $p(\gamma, K^+)\Lambda$ has maximum values in the region $1.1 - 1.5$ GeV. This information together with ENGE limitations set the final value of incident electron beam to $E_e = 1.8 GeV$. This sets central momentum of outgoing kaon $p_{K^+} = 1.2 GeV$ and for this value of central momentum high resolution kaon spectrometer (HKS) was designed and built.

Due to four momentum conservation there is momentum correlation of scattered kaon and electron, shown in Figure 2.3.

After reviewing momentum dependence in order to optimize (maximize)
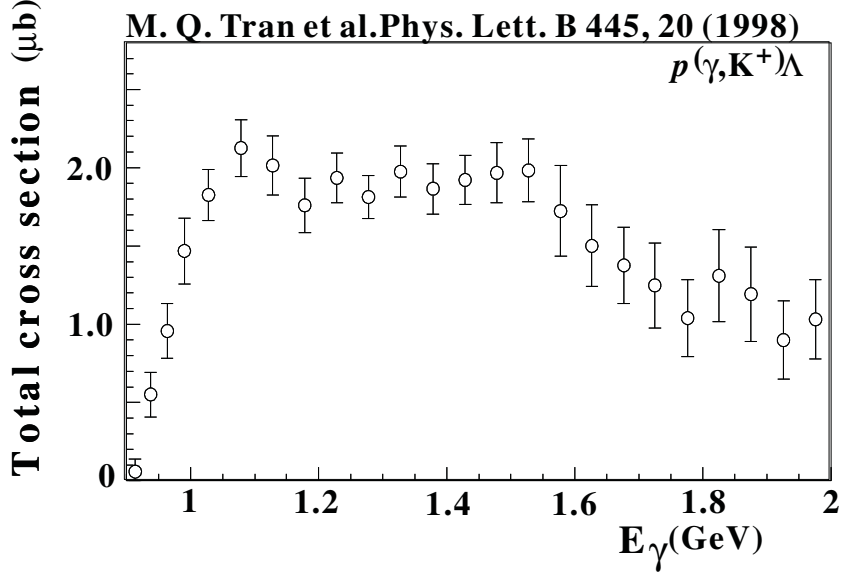
FIGURE 2.2: TOTAL CROSS SECTION OF THE $p(\gamma, K^+)\Lambda$ REACTION [10].

event rate (statistics) the same review has to be done for angular dependence. Angular dependence has to be optimized having in mind two factors, maximizing electroproduction of Λ particle and at the same time background events (bremsstrahlung, Moller scattering) need to be minimized in order to achieve best possible signal to noise ratio (an important feature in optical calibration). Detailed account of background events will be given in Section 2.4.2.

As shown in section 1.5 differential cross section can be written as a product of virtual photon flux and kaon angular dependence factor. Since virtual photon flux is

$$
\begin{aligned}
\Gamma(E_e, \omega, \theta_e) &= \frac{\alpha}{4\pi^2\omega}[\frac{E_e^2 + E_{e'}^2}{2E_e^2}(\frac{m_e^2\omega^2}{4E_e^2E_{e'}^2} + \sin^2\frac{\theta_{e'}}{2})^{-1} - \frac{E_{e'}}{E_e}\frac{m_e^2\omega^2}{4E_e^2E_{e'}^2}(\frac{m_e^2\omega^2}{4E_e^2E_{e'}^2} \\
&+ \sin^2\frac{\theta_{e'}}{2})^{-2} - \frac{(E_e + E_{e'})^2}{4E_e^2}(\frac{\omega^2}{4E_eE_{e'}} + \sin^2\frac{\theta_{e'}}{2})^{-1}]
\end{aligned} \tag{2.1}
$$

Virtual photon flux has maximum in electron scattering angle θ_e for following value:

$$
\theta_e = \sin^{-1}(\frac{m_e\omega}{4E_eE_e}) \tag{2.2}
$$
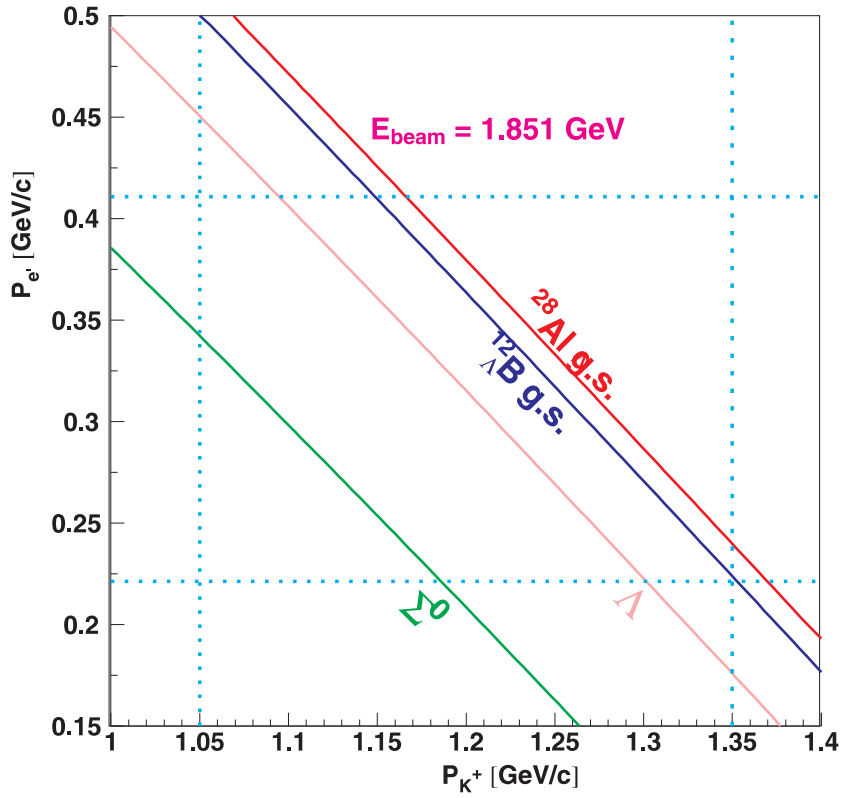
FIGURE 2.3: MOMENTUM ACCEPTANCE OF KAON AND SCATTERED ELECTRON SPECTROMETERS. (IT IS CALCULATED WITH: BEAM ENERGY 1.851 GEV, ASSUMED BINDING ENERGY OF $^{12}_{\Lambda}B$ GROUND STATES -11.37 MEV [82] AND $^{28}_{\Lambda}Al$ GROUND STATE -16.92 MEV [58].)
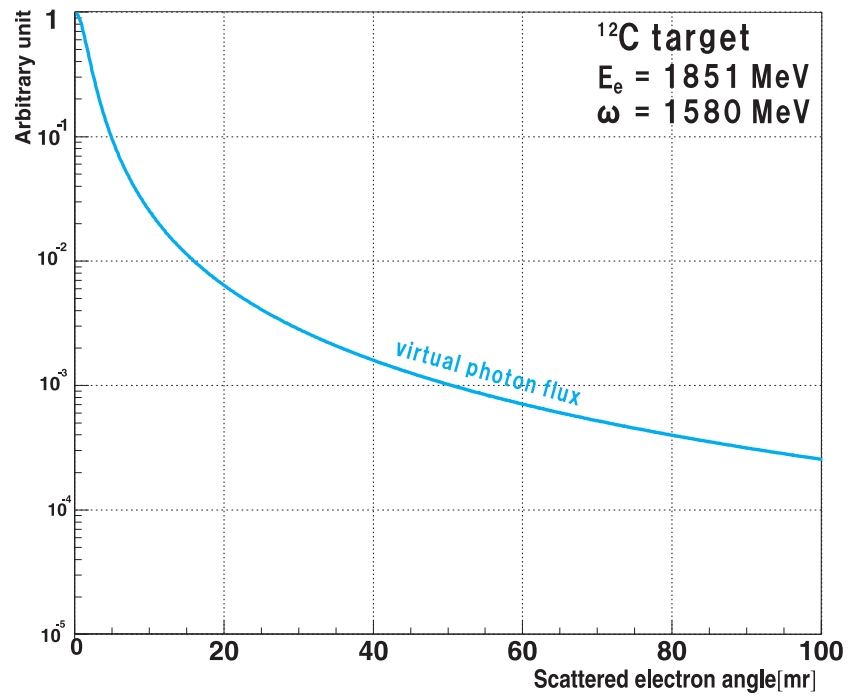
FIGURE 2.4: VIRTUAL PHOTON FLUX DEPENDENCE ON SCATTERED ELECTRON ANGLE FOR ^{12}C TARGET. PLOT IS OBTAINED WITH FOLLOWING KINEMATICS $E_e = 1.851 GeV$ AND $\omega = 1.580 GeV$.
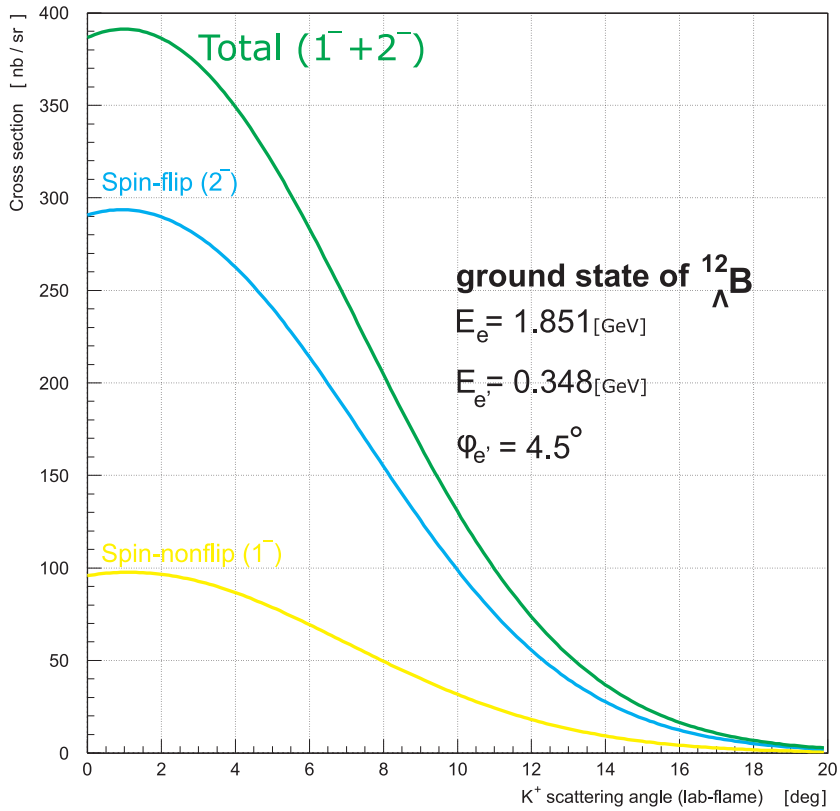
FIGURE 2.5: SCATTERED KAON ANGULAR DISTRIBUTION OF THE PHOTO PRO-
DUCTION OF $^{12}_{\Lambda}$B GROUND STATE DOUBLET WITH A DWIA CALCULATION [95].

It is immediately obvious that this value is close to zero due to very small
electron mass meaning that we expect maximum in differential cross section
for very forward scattered electrons, as seen in Fig. 2.4, and that detector
package for electron arm should be in the scattering plane.

From Fig. 2.4 and Fig. 2.5 conclusion was that, in order to achieve high-
est possible yield of Λ hypernuclei production, scattered electron and kaon
need to be detected at forward angle. Further discussion on angular depen-
dence of electrons associated with virtual photon flux, Moller scattered and
bremsstrahlung electrons is left for the section 2.4.2, where new configuration
of the Enge spectrometer and it's implications are discussed.
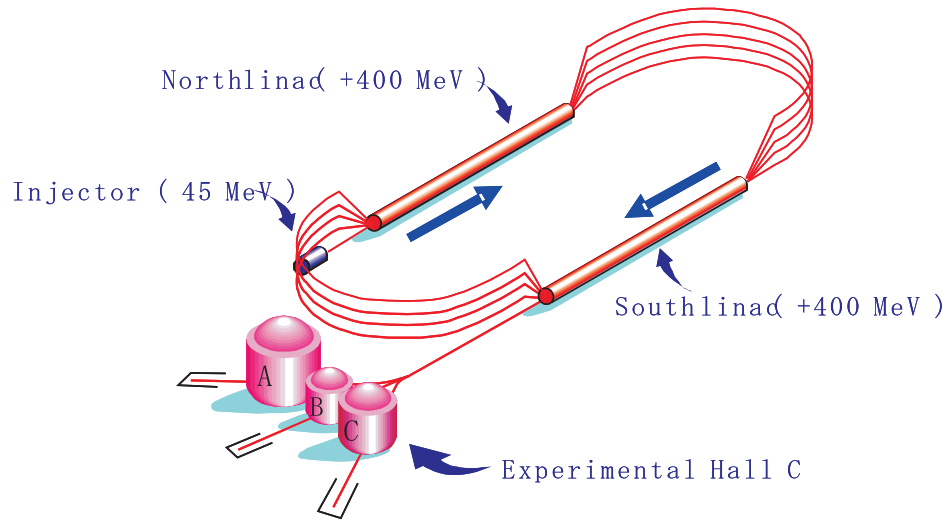
FIGURE 2.6: SCHEMATIC OVERVIEW OF CEBAF AND EXPERIMENTAL HALLS A,B AND C AT JLAB.

2.3   Jlab overview

Jlab is an electron accelerator facility offering high quality electron beam produced by Continuous Electron Beam Accelerator Facility (CEBAF), Fig. 2.6. CEBAF is an electron linear accelerator producing continuous wave (CW) beam with currents up to 200 μA. That beam can be delivered to experimental halls as un-polarized or 75 % polarized in energy range between 0.6 GeV to 6 GeV. Relative momentum spread of the beam is of the order of 10^{-5} with geometric emittance of 10^{-9} mrad and excellent reproducibility of the beam conditions with almost 100% duty factor [11]. It is capable of delivering high current and high polarization beams to Hall A and Hall C and at the same time delivering to Hall B beam with high polarization and low current.

2.3.1   CEBAF Accelerator

Injector The electron beam is produced by state-of-the-art Gallium Arsenide photocathode gun system 2.7 in the accelerator using three separate
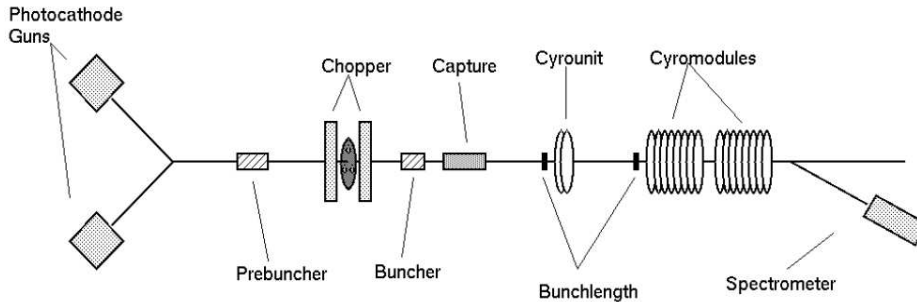
FIGURE 2.7: THE INJECTOR SYSTEM LAYOUT.

radio frequency (RF) gain switched lasers operating at 499 MHz, with 120 degree phase separation, which provide a 1497 MHz bunch train at 100 KeV [104]. The laser micro pulses are about 55ps long (FWHM), the beam has the same time structure of the lasers. In the bunching section the beam is then adiabatically compressed to 2 picoseconds and accelerated by superconducting cavities. The beam quality such as polarization, optics and energy are confirmed prior to injection into the main machine in the injector matching region.

Linacs The 67MeV, 2ps electron bunch from the injector enters accelerator through north linac, see Fig. 2.6. Once in accelerator electrons are accelerated through a unique recirculating beamline. Beamline itself consists of two linear accelerators, the north 2.8(a) and south linac, connected with two 180° arcs, the east 2.8(b) and west arc, with a radius of 80 meters. North and south linac, each accelerates electrons by 600 MeV with an array of superconducting radio frequency (SRF) cavities. Linacs altogether consist of twenty cryomodules, each having eight superconducting niobium cavities. The beam after one pass; acceleration at North linac, steering by the east arc to the south linac gains 1.2 GeV and can be delivered to experimental halls or be recirculated into the linacs by the west arc.

Recirculated electrons are accelerated in the same beam line in the linacs but due to differences in energy after each pass in order to bend the beam back to the linac different magnetic fields are needed for each pass. For this reason the arcs are separated and stacked, see Fig. 2.8(b) and 2.6, and

(a) North Linac   (b) East Arc

FIGURE 2.8: CEBAF ACCELERATOR COMPONENTS

with different magnetic field configurations. They are recombined before sent into the linac. The beam can be recirculated up to five times to get to the maximum energy of 6 GeV.

Beam switchyard At the end of each pass the beam can be delivered simultaneously to all three halls by a Beam SwitchYard (BSY) set at the end of the South linac. At the BSY the beam is steered into a hall's transport channel by a RF module operating at 499 MHz frequency. At this frequency RF module is capable of directing every third bunch of the 1497 MHz beam to each Hall. Finally, the CW beam reaching each hall comes in bunches of 2 ps in length every 2ns.

This microstructure provides a good time reference for the experiments. One of the important features of the CEBAF accelerator is its flexibility. The energy of the beam is quite flexible since the energy gain in the linacs may be changed. Also the range of currents can vary from 100 pA to 200 μA; although the maximum current used by experiments is 50 pA for Hall B and 140 μA for Halls A and C. These features plus the high quality of the beam (emittance, energy stability, and high polarization) are important characteristics of this unique machine.The accelerator can deliver the first four passes to one hall only. The fifth pass can be sent to all three halls.
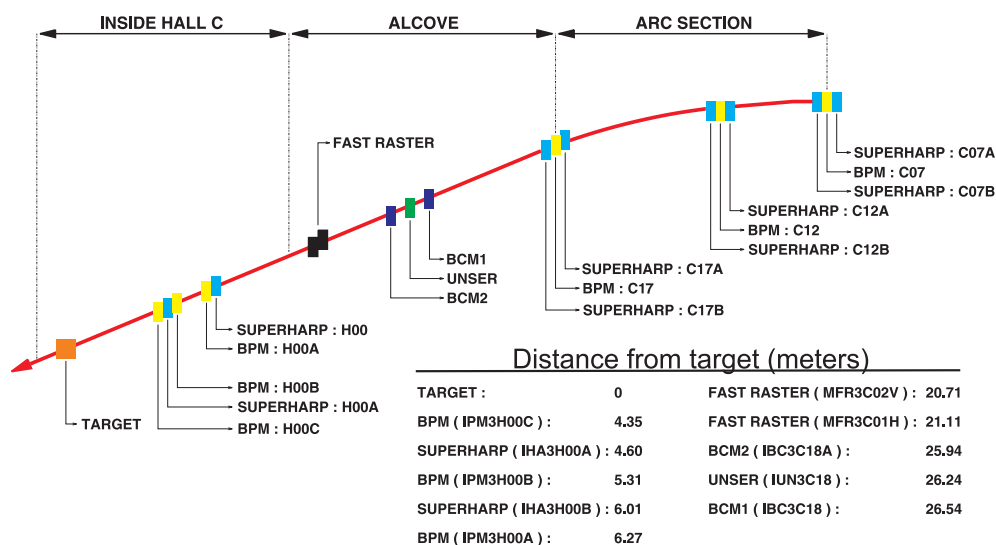
FIGURE 2.9: HALL C ARC AND BEAMLINE LAYOUT. THE POSITIONS OF USED BEAM DIAGNOSTIC DEVICES : HARPS, BPMs AND BCMs IS SHOWN.

2.3.2   Hall C

The beam, after being is steered into a hall's transport channel by a BSY RF module, is transported to the target through Hall C Arc and beamline. Hall C Arc consists of a system of dipole and quadruple magnets, in order to steer and focus the beam on the target. In order to monitor conditions of the beam during the experiment there are several beam diagnostic elements, see Fig. 2.9.

Beam diagnostic, in the duration of E01-011 experiment, consisted of 2 Beam Current Monitors (BCMs), Fig 2.9, 6 Beam Position Monitors (BPMs), 8 Beam Profile Monitors (Super-harp) and a unser monitor for BCM calibration. Detailed accounts of beam diagnostic monitors can be found in [2], [27], [79], [101].

Superharps located in different portions of the Hall C Arc and beamline, are beam wire scanners that allow for precision measurement of a two-dimensional beam profile and absolute beam position. Superharps are also used for measurement of beam energy in Hall C and calibration of the ab-

solute positions of other beam position monitors (BPM). Superharp is made of wooden fork with three tungsten wires, one horizontal and two vertical PROVJERI. As superharp is inserted into beam line tungsten wires interact with electron beam. Charges induced in the wire give a signal for each wire of the superharp. From signal induced in the horizontal wire vertical position of the beam is determined and from signal of two vertical wires horizontal. In order to extract beam profile and beam position superharp wire need to interact with the beam and for this reason superharp scan can not be done while experiment is in data taking mode.

Beam Position Monitors unlike superharps are used to determine beam position while experiment is in data taking mode. The BPM is cylindrical cavity with four antennae rotated by $45°$ in the plane (y axis is in direction opposite to gravity, x is horizontal) perpendicular to beam direction (z-axis). When beam goes through cavity induced signals in antennae are measured. Amplitudes are proportional to the distance between the beam and antennae. From this information only beam positions relative to cavity center can be obtained. To obtain absolute positions calibration with superharps is necessary. With superharps measurement offsets of the cavity center to the ideal beam trajectory are established. With constant beam current the accuracy for relative beam position is ~ 0.1 mm. Accuracy of absolute position of the beam obtained with BPMs is ± 1.02 mm [98].

Measurements from BPMs during the experiment are used to determine the beam position and direction at the target and can, as superharps, be used in beam energy measurements. The beam delivered to hall's has undesirable positional and energy fluctuations caused by electromagnetic fields generated by accelerator electronic equipment. Beam energy fluctuations are obtained from BPM measurement. It is possible to minimize them by applying real time corrections to electromagnets and RF verniers along the beam line with the energy feedback system [103]. PROVJERI. This is important since one of the goals of E01-011 is significant sub-MeV resolution of hypernuclear bound states which means that the energy of the beam must be known to $\delta E/E \leq 1.0 \times 10^{-4}$(FWHM). For this to be fulfilled beam energy spread and stability have to be less than 10^{-4}.

Beam Current Monitors Hall C current was continuously measured during the data taking by Beam Current Monitors(BCM) [2],[79],[101]. The BCM are cylindrical RF resonance cavities where transverse electromagnetic (TEM) modes are excited by the beam. Wire loop antennae pick up excited EM waves and convert it's power to frequencies. Current is being calculated from these frequencies. To calibrate gains and offsets of BCM1 and BCM2, we have another kind of BCM, a parametric current transformer (Unser monitor), which has very good gain stability and can measure absolute current. It can be used to calibrate the other two BPMs.

Fast Raster The beam used in the E01-011 experiment was a high intensity CW beam and had small transverse size and on interaction with the target deposits high energy amounts which could damage the target and/or produce local boiling effects generating density variation. To prevent this the Fast Raster [28] system, located 25 m upstream of the target, was used. The fast raster system consists of two dipole magnets that, with sinusoidally changing current powering them, spread the beam in both horizontal and vertical directions. Periodicity of powering current is such that there is an unstable Lissajous pattern (frequencies are not multiplier of each other) on the target producing more uniform illumination within the beam spot. During the E01-011 experiment Fast Raster with the size of 5x5 mm2 was used but not for all targets, see Table 2.2.

Hall C layout, as represented in Fig. 2.10, shows hall's both standard equipment, HMS and SOS spectrometers [3], [110] and the non-standard equipment, in this case the HKS and ENGE spectrometers installed in order to carry out the E01-011 measurements. Special feature of the E01-011 experiment is that one of the magnets, the splitter magnet used to separate scattered electron and kaon after the target, is part of Hall C beamline and deflects non-scattered electron so additional two correction magnets, as seen in Fig. 2.10, are needed so that the non-scattered electron as well as bremsstrahlung photons end up at the Hall C beam dump.

High resolution
Kaon Spectrometer
(HKS)

HMS

Beam dump

Beam line

G0

SOS

Enge
spectrometer

10 feet
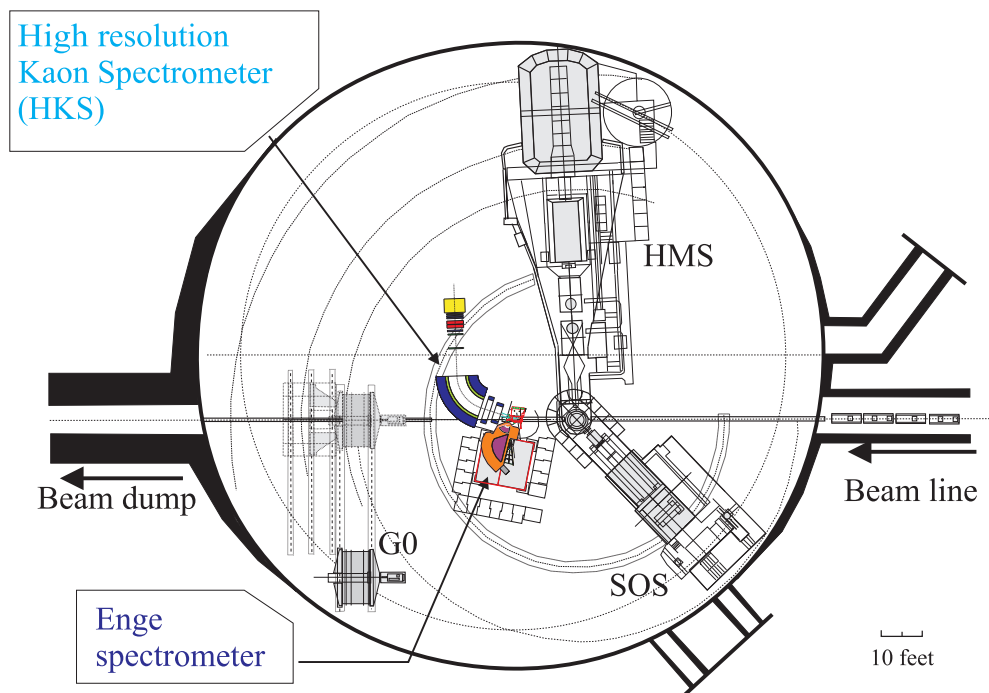
FIGURE 2.10: HALL C LAYOUT WITH POSITIONS OF EXPERIMENTAL EQUIPMENT
DURING E01-011 RUNNING PERIOD.

2.4 E01-011 spectrometer system

In the E01-011 experiment the spectrometer system consisted of One Splitter magnet and two spectrometer arms, Enge spectrometer and High Resolution Kaon Spectrometer, to detect the scattered e′ and electroproduced K^+ in coincidence. Top view of the experimental setup is shown in figure 2.11. Geometrical configuration of the spectrometer system is shown in figures 2.11 and 2.12.

For Enge spectrometer a new technique was introduced, the so called Tilt method. To be able to detect particles at as forward angles as possible and to bend e′ to Enge and K^+ to HKS the splitter magnet was used. With this setup we were able to detect kaons in horizontal plane with angles from 0° to 14° and avoid zero degree bremsstrahlung and Moller electrons in the Enge spectrometer.

To minimize the multiple scatterings the whole system, the beam line and region of e^- and K^+ trajectories, was under vacuum all the way to the exit windows of the spectrometers of both arms. Enge spectrometer (as well as Splitter magnet) was already used in HNSS so in E01-011 it is reused but a new technique was introduced, the so called Tilt method. High Resolution Kaon Spectrometer (HKS) was designed and built from scratch.

2.4.1 Splitter Magnet and Target Chamber

Splitter was a normal conducting C-type dipole magnet, as shown in Fig. 2.13(a), already used in the HNSS experiment [44] modified by the enlargement of the gap (15.24 cm width) because of the new kaon arm spectrometer. SOS was replaced by the newly built HKS, which had bigger geometrical acceptance. The splitter was used having in mind kinematic settings of Λ hypernuclei electroproduction so there are two basic requirements that demanded the usage of Splitter magnet:

- as shown, see Fig.2.5 and 2.4, cross section for Λ hypernuclei electroproduction has maximum value at very forward angles of both scattered
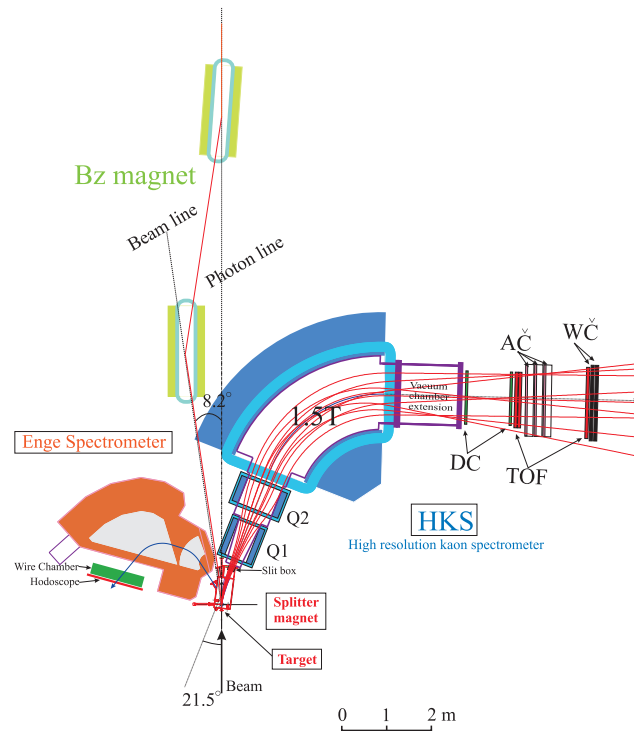
FIGURE 2.11: SCHEMATIC OVERVIEW OF THE E01-011 SPECTROMETER SYSTEM:
SPLITTER MAGNET, ENGE AND HKS SPECTROMETERS.

(a) CAD drawing   (b) Picture taken in Hall C
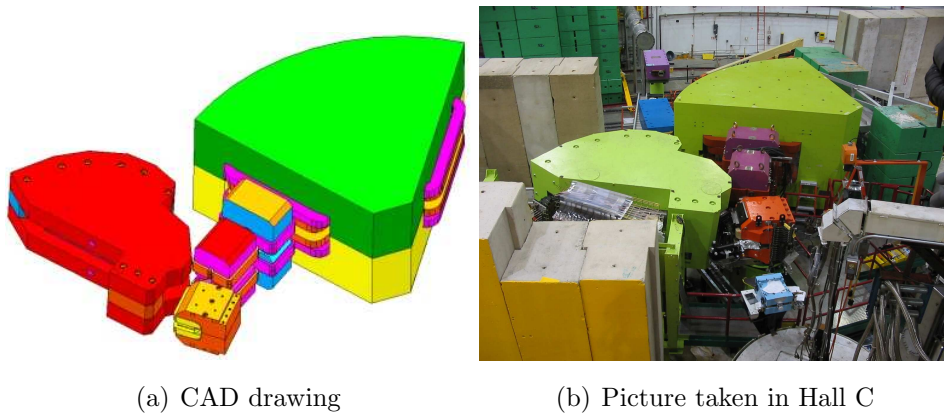
FIGURE 2.12: 3D OVERVIEW OF THE E01-011 SPECTROMETER SYSTEM: SPLIT-
TER MAGNET, ENGE AND HKS SPECTROMETERS.

TABLE 2.1: MAIN CHARACTERISTICS OF THE SPLITTER MAGNET.

Parameter	Value
Pole gap width	15.24 cm
Weight	6.35 ton
Max field	1.8 T
Designed setting	780A (1.546 T)
Used setting	942.5A (1.70586 T ?)

e^- and K^+. This region can be observed with the splitter magnet.

- Separates particles with different charges; negatively charged particles are bent toward ENGE Split Pole Spectrometer (ESPS) and positive toward High Resolution Kaon Spectrometer (HKS).

Magnetic field on the mid-plane of the splitter magnet was measured with the hall probe in the Test Lab in 2005. Magnetic field was tested for powering current in the range from 0A to 780A, see Fig.2.4.1. Designed value for the Splitter magnetic field of 1.546 T was achieved with the current setting of 780A.

In the commissioning period of the E01-011 experiment it was found that the experiment can not run with this field setting. The problem arose with beam alignment which could not be done with Splitter field at 1.546 T. For successful beam alignment an increase of 8.5% of the magnetic field of the Splitter magnet was needed. The experiment was run with the Splitter current set at $I = 942.5A$ and since the new setting was outside the measured range the field was calculated by TOSCA. Measured field and field calculated by Tosca of the Splitter magnet are plotted in Fig.2.4.1 and the basic characteristics are in Table 2.1.

The target chamber, located in the pole gap of the Splitter magnet, was built for sole purpose of holding the target in vacuum and to be the vacuum connection of beam line and Enge spectrometer, exit beam line and HKS spectrometer, as shown in Fig.2.12(b). To help align and tune the beam there is a viewer window with a CCD camera to visually see the beam spot

TABLE 2.2: TARGETS USED IN THE E01-011 EXPERIMENT AND THEIR POSITIONS ON THE TARGET LADDER.

Target	Thickness [mg/cm²]	Ladder			
		1	2	3	4
BeO		1	1	1	1
CH_2	465	4	2,3,4,5	2	
^6Li					2
^7Li	189				3
^9Be	188	5		5	
^{10}B	114			4	
^{12}C	100	3	6		
^{28}Si	65	6		6	
^{51}V	59.6				4
^{89}Y	56				5
^{208}Pb					6

on the BeO target. The target ladder,located inside the target chamber, was made of aluminum and could hold maximum of six targets in the form of squares 1.5cmx1.5cm in dimension. The target ladder was moved into the beam at the specific position by remote control. At each position there was a different target, with maximum of six targets as described in Table 2.2, which allowed target change during the experiment.

2.4.2   Enge Split-Pole Spectrometer

Enge Split-Pole Spectrometer is a spectrometer system for electron arm and was already used in the first (e,e'K) experiment, E89-009. Major improvement was done in geometrical configuration of the system, the so-called Tilt method. Enge is a normal conducting split pole dipole magnet. It is called Split-pole spectrometer because it is constructed from two separate pole pieces enveloped by a single coil [22] [81], as seen in Fig. 2.15. The main characteristics of Enge are listed in Table 2.3.

(a) Splitter: 3D schematic view

(b) Design of splitter with target chamber
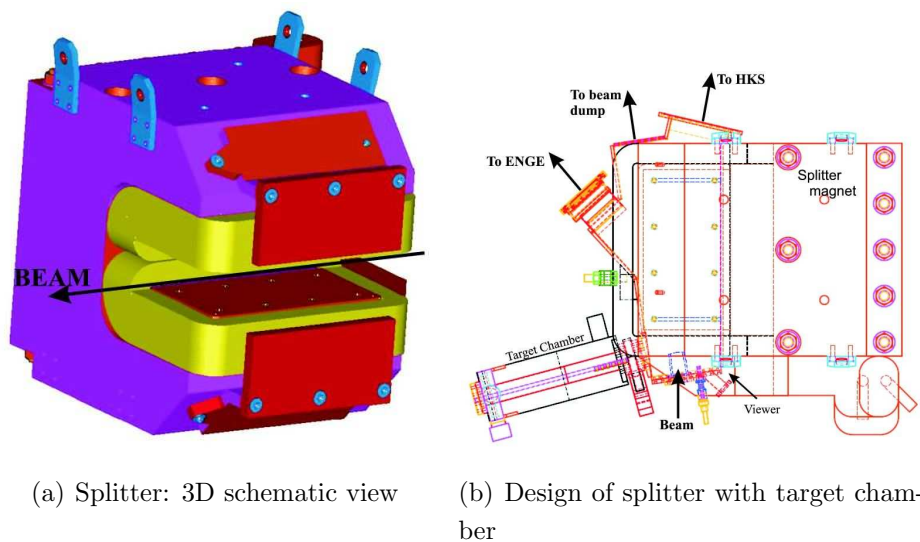
FIGURE 2.13: SPLITTER MAGNET AND TARGET CHAMBER

TABLE 2.3: MAIN CHARACTERISTICS OF ESPS.

Parameter	Value
Pole gap	46.6 mm
Mean radius	Max. 1100 mm
Momentum	228 - 338 MeV/c (nominal)
Design Central Momentum	276 MeV
Total Length	∼5m
Solid Angle Acceptance	1.6 msr
Horizontal	25 mr
Vertical	20mr
Momentum Bite	±20%
Focal Plane Geometry:	
Length	74 cm
Tilt	48.8°
Dispersion	1.5 cm/%
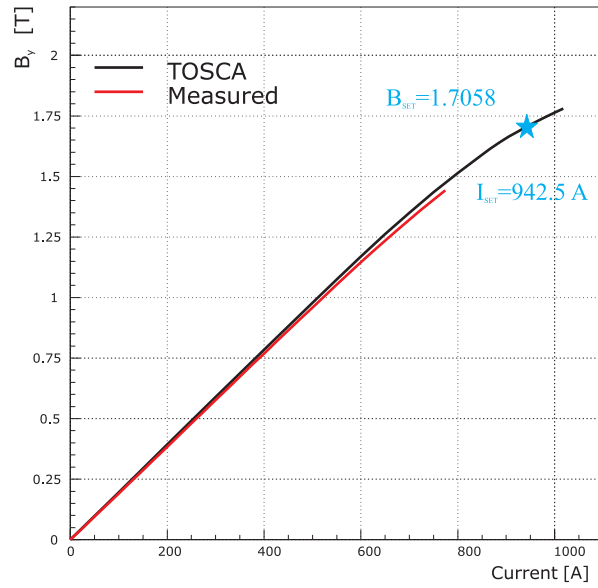
FIGURE 2.14: EXCITATION CURVE OF THE SPLITTER MAGNET CALCULATED BY TOSCA AND MEASURED. THE STAR REPRESENTS THE USED SETTING.
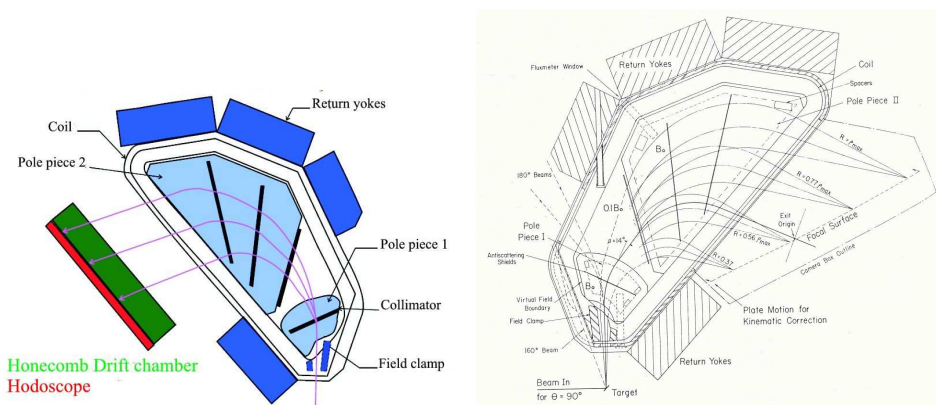
FIGURE 2.15: SCHEMATIC VIEW OF THE ENGE SPLIT POLE SPECTROMETER.
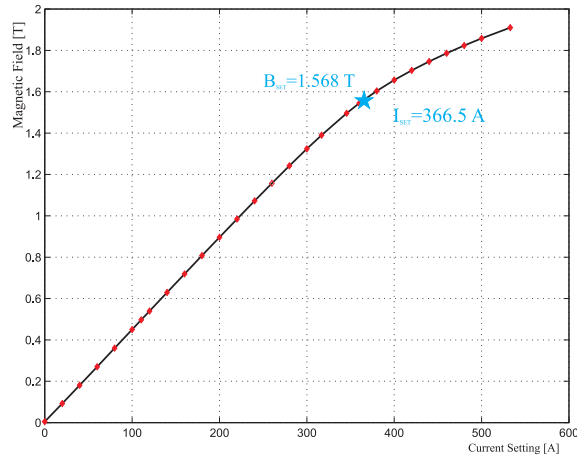
FIGURE 2.16: ENGE MAGNET EXCITATION CURVE MEASURED AT TEST LAB [110].
THE STAR REPRESENTS THE USED SETTING.

Magnetic field vs current excitation curve of Enge spectrometer magnet
was measured before the experiment obtained results are shown in Fig. 2.16.
As mentioned in section 2.4.1, the Splitter magnet settings needed to be
changed for the beam to be properly aligned. To compensate for the effect
that this change had to hypernuclear yield, the Enge magnetic field settings
were also changed and E01-011 was run with Enge current set at 366.5 A
producing the field of 1.5685 T. This current setting was 8.5% bigger than
the design value, and caused a mismatch between the ENGE and the Splitter
fields. The design values were matched to get an optimal physics yield by
maximizing the virtual photon integral. The change of the optics of the
system changed the ENGE acceptance, reducing the physics yield.

Tilt method

Tilt method stands for the simultaneous usage of vertical offsets and tilt an-
gle to the Enge spectrometer with respect to the Splitter dispersion plane.
The reason to use Tilt method came from the experience gained in the pilot
hypernuclear experiment. Since in E89-009 the background was dominated
with bremsstrahlung electrons the idea was to use the difference in angu-
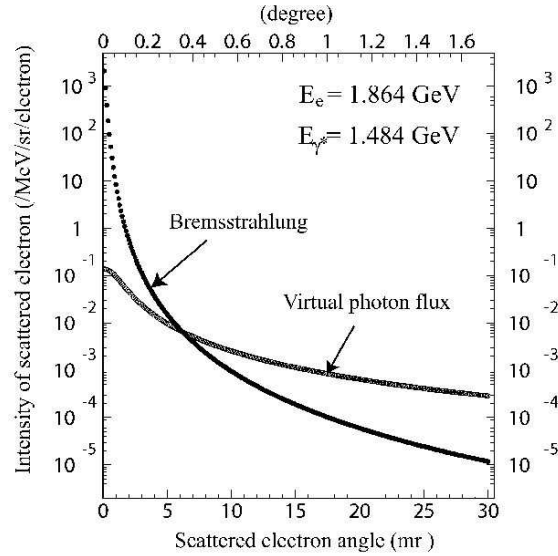
FIGURE 2.17: ANGULAR DISTRIBUTION OF THE VIRTUAL PHOTON FLUX AND BREMSSTRAHLUNG ELECTRONS CALCULATED WITH $E_e = 1.864 GeV$, $E_\gamma = 1.484 GeV$ [44].

lar distribution between the electrons associated with virtual photons and bremsstrahlung electrons to minimize background, see Fig. 2.17. In E89-009 Enge was placed in the Splitter plane, see Fig.2.18(a), and the effect of the $0°$ background effects can be seen in the measured $^{12}_{\Lambda}B$ spectrum which had poor signal to accidental (S/A) ratio limiting the achieved resolution and yield, see Fig. 1.8(b).

By tilting the Enge spectrometer with respect to the Splitter magnet, see Fig. 2.18(b), bending plane extremely high rates of Möller scattered and bremsstrahlung electrons are avoided, see Fig.2.19. The disadvantage of this is that at the same time the number of virtual photons that are accepted is also decreasing. Using the Raytrace Monte Carlo simulation to simulate events associated with these three processes tilt angle was optimized balancing two main issues: the number of accepted virtual photons should be as big as possible; contribution from bremsstrahlung and Moller scattered electrons should be as small as possible. As can be seen from Fig.2.19 the Figure of Merritt (FoM) calculation shows best the behavior in the region
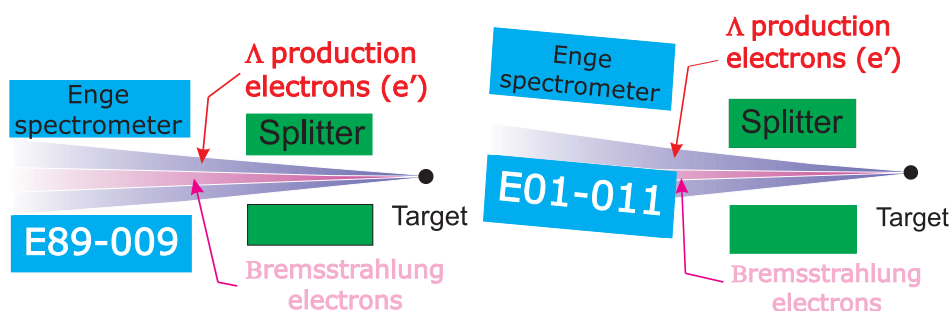
(a) Enge configuration used in E89-009. (b) Enge configuration used in E01-001.

FIGURE 2.18: ENGE CONFIGURATION AS USED IN E89-009: ENGE SET IN THE SPLITTER PLANE, AND FOR E01-001: ENGE HAD VERTICAL OFFSET AND TILT WITH RESPECT TO THE SPLITTER PLANE.

with scattering angle bigger than 7°. Since hypernuclear yield has to be optimized as well, the acceptable region for electron scattering angle (Enge tilt) is between 7°-8°.

Enge tilt angle and vertical shift length were optimized using RAY-TRACE with results shown in Fig.2.20

The effect of the Tilt method on reducing background events is already seen when single arm electron rates measured in E89-009 are compared with the ones measured in E01-011. For E89-009 the measured values were 2×10^5 kHz while for E01-011 they were 1×10^3, 200 times less allowing beam intensities up to 30μA (E89-009 ran with currents less than 1 μA).

2.4.3 High resolution kaon spectrometer

High resolution kaon spectrometer (HKS) is a new spectrometer system designed to detect kaons produced in $(e, e'K^+)$ reaction for the E01-011 experiment. The spectrometer consists of two quadrupoles, one vertically (Q2) and one horizontally (Q1) focusing, followed by a horizontally bending dipole. The basic characteristics of HKS magnets are listed in Table 2.4. The design and properties of QQD system were studied using TOSCA and before using them in the experiment field mapping was done. The Q1 and Q2 were
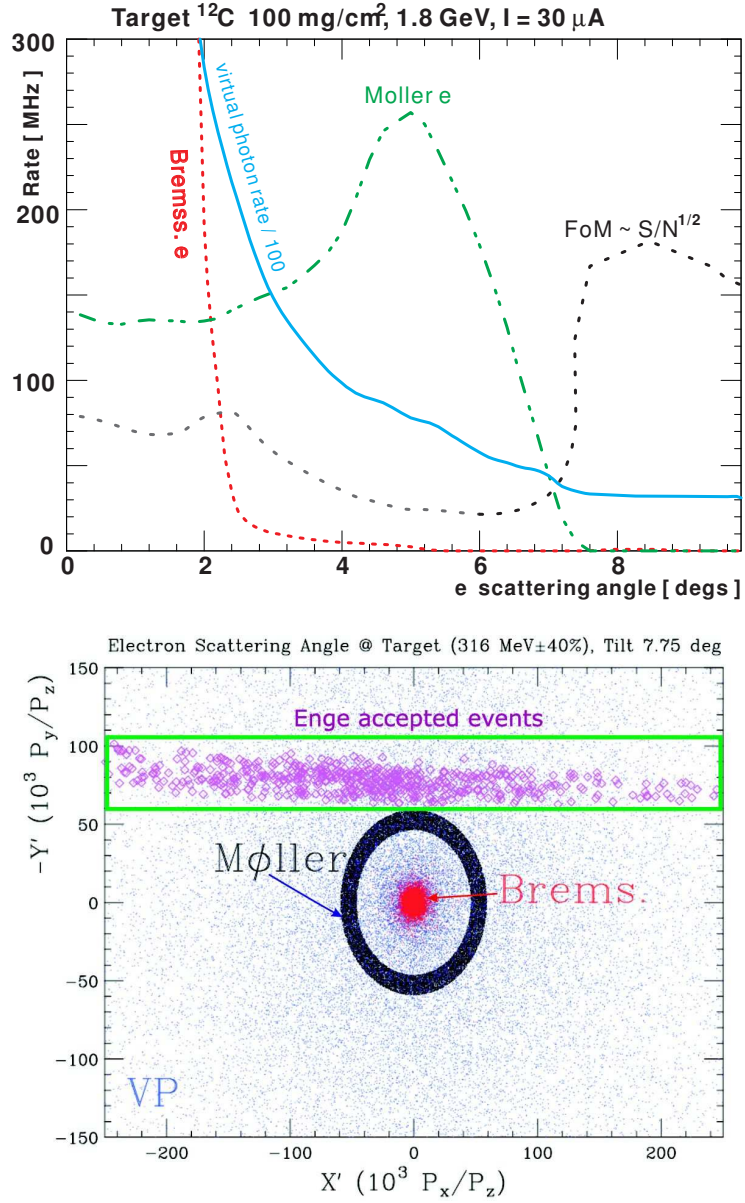
FIGURE 2.19: ANGULAR DEPENDENCE OF THE CALCULATED RATES FOR: BREMS-
STRAHLUNG AND MOLLER SCATTERED ELECTRONS AND VIRTUAL PHOTO FLUX.
RATES ARE CALCULATED FOR ^{12}C TARGET WITH DENSITY 100 MG/CM^2 AT BEAM
CURRENT I=$30\mu A$. FIGURE OF MERIT (FOM) DEFINED AS FOM= $S/N^{\frac{1}{2}}$, S-
VIRTUAL PHOTON FLUX; N - SUM OF BREMSSTRAHLUNG AND MOLLER SCAT-
TERED ELECTRONS, FOM IS SCALED WITH ARBITRARY FACTOR [44].
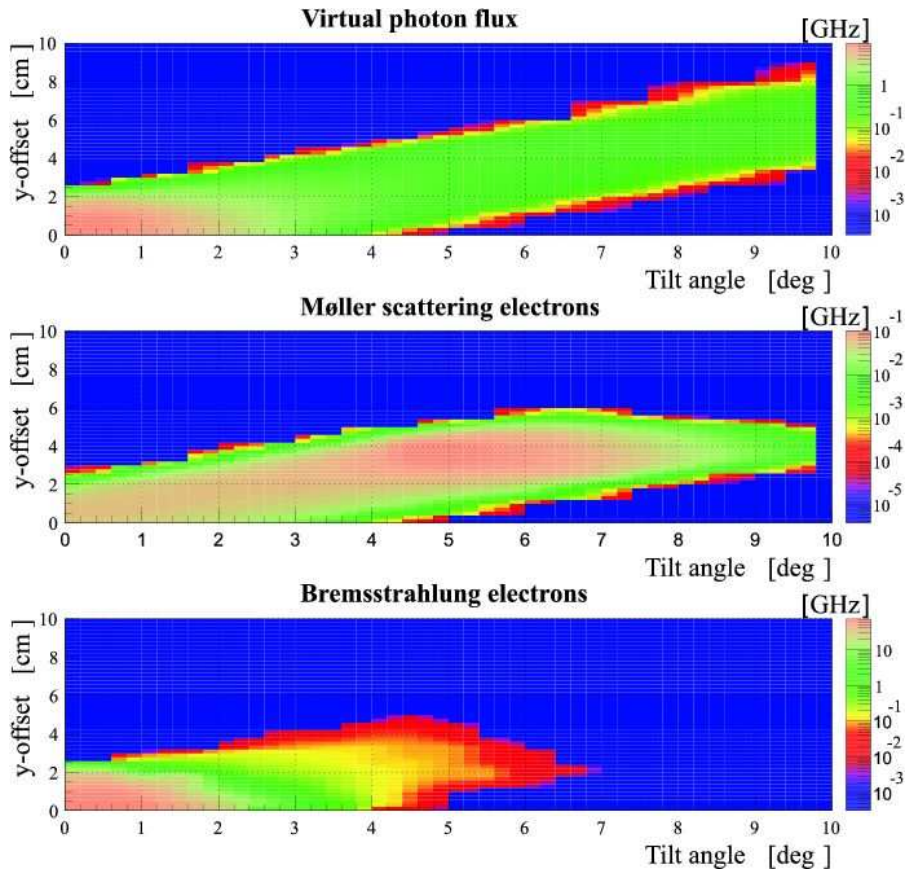
FIGURE 2.20: ELECTRON RATES DEPENDENCE ON THE ENGE TILT ANGLE AND VERTICAL OFFSET FOR: ELECTRONS ASSOCIATED WITH VIRTUAL PHOTON FLUX (HYPERNUCLEAR PRODUCTION), MOLLER SCATTERED AND BREMSSTRAHLUNG ELECTRONS [44]. RATES ARE CALCULATED FOR ^{12}C TARGET WITH DENSITY 100 MG/CM^2 AT BEAM CURRENT I$=30\mu A$.

TABLE 2.4: HKS QQD MAGNETS PARAMETERS.

Parameter	Q1	Q2	D	
Bore radius [mm]	120	145		
Pole length [mm]	840	600	3254	
Pole gap height [mm]			200	
Number of turns	256	320	256	
Conductor size				
Maximum current [A]	875	450	1140	
Maximum field [T]			1.53	
Maximum field gradient [T/m]	6.6	4.19		
Maximum voltage [V]	159	53.8	165	
			Gap	Yoke
Cooling water flow rate [l/min]	49.6	17.3	66.3	68.8
No. of coolant circuits	16	8	8	8
Pressure drop [MPa]	0.36	0.38	0.32	0.35
Total Weight [ton]	8.2	10.5	210	

mapped with a Hall probe attached to a field mapper which can scan the space in three dimensions. Hall probe itself can also be rotated by 90° to measure Bx and By. For pictures and excitation curves of the magnets of the HKS QQD magnet system see Fig.2.21.

Whole HKS spectrometer system is rotated in horizontal plane by 7° accepting kaons emitted with angle in 1°-13° range. With this angular acceptance 0° positrons are being avoided.

2.5 Detector package

The E01-011 experiment is a coincidence type of experiment, meaning simultaneous detection of kaons in HKS detector package and scattered electron in Enge detector package. The design of experimental apparatus involved three basic types of detectors: time of flight hodoscopes, tracking chambers and particle identification detectors. All these detectors are housed in a concrete shielding house against background particles.
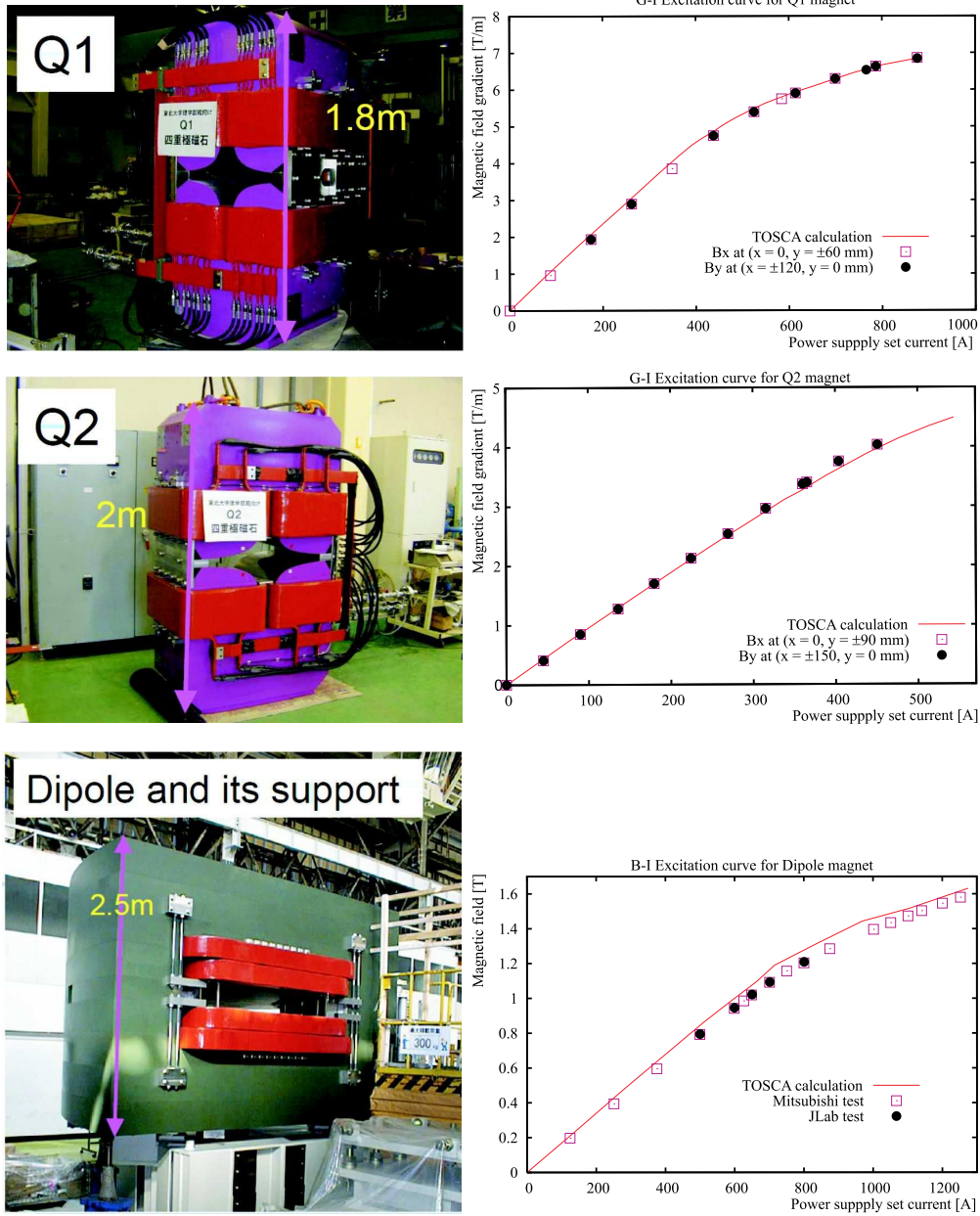
FIGURE 2.21: PICTURES OF THE HKS MAGNETS:QUADRUPOLES Q1 AND Q2 AND A DIPOLE. PLOTS OF THE EXCITATION CURVES: MAGNETIC FIELD FOR DIPOLE AND GRADIENT OF THE FIELD FOR QUADRUPOLES.

TABLE 2.5: HKS SPECTROMETER PARAMETERS

Parameter	Value
Configuration	Q-Q-D
Maximum field	1.53 T (normal conducting)
Central momentum at B_{nom}	1.2 GeV/c
Momentum Acceptance	$\pm 12.5\%$
Momentum Dispersion	4.7 cm/%
Momentum resolution	2×10^{-4}
Solid angle	16 msr (with Splitter)
Solid angle	30 msr (without Splitter)
Bending radius	2.5m
Bending angle	70 %
Maximum Horizontal Angular Acceptance	± 100 mr
Maximum Vertical Angular Acceptance	± 75 mr
Vertical Opening Angle	80 mr
Focal Plane size	40×120 cm
Focal Plane Tilt Angle	$69°$
Focal plane distance from target	8.35 m
Flight length to last TOF	10.0 m
Kaon detection angle	$7°$ horizontal (1-13°)
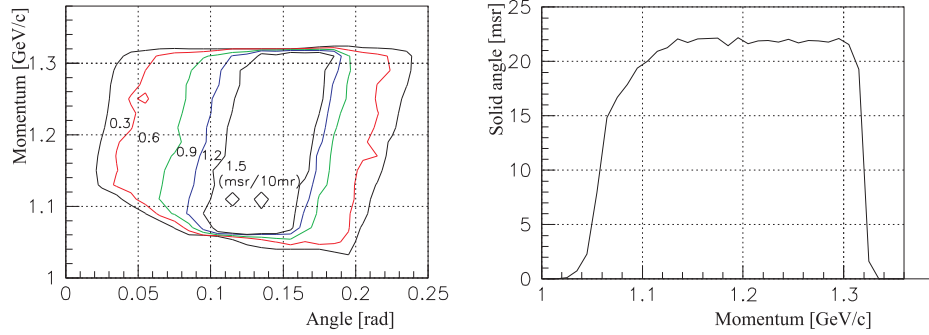
FIGURE 2.22: ANGULAR AND MOMENTUM DEPENDENCE OF SOLID ANGLE OF THE HKS SPECTROMETER SYSTEM [44]. LEFT FIGURE SHOWS ANGULAR AND MOMENTUM DEPENDENCE OF SOLID ANGLE. LEFT FIGURE SHOWS MOMENTUM DEPENDENCE OF TOTAL SOLID ANGLE.

2.5.1 Enge detector package

Enge detector package consists of a honeycomb drift chamber (EDC) used for tracking and two hodoscopes planes (EHODO1 and EHODO2) of scintillation counters used for timing. For timing calibration of EHODO1 and EHODO2 another scintillator (EHODO3) was used. The detector package was mounted to the exit of the Enge magnet.

The upgrade from HNSS comes from the introduction of Honeycomb drift chamber while in HNSS silicon strip detectors were used. Silicon strip detectors were capable of measuring only position of the scattered electron on the focal plane while EDC measures position and angle. The need for this upgrade arose because of the change in configuration of the Enge spectrometer (Tilt method) which destroyed the optics on the dispersion plane so angular components need to be involved into calculation of the focal plane optics.

Honeycomb drift chamber

Enge drift chamber (EDC) was positioned right after the Enge magnet, mounted directly on the Enge magnet exit. The position and angles at the focal plane of the scattered electron were obtained from EDC data. Geometrical center plane of EDC actually coincided with the focal plane definition. EDC is made of ten planes of sense wires and their field wires surrounding them in hexagon structure. Hence the name honeycomb drift chamber, see Fig.2.23.

This design was chosen because of the requirement for large incident angle and a momentum resolution of 4×10^{-4} (FWHM). Sense (anode) wires were made of gold plated tungsten with a diameter of $20\mu m$ and field wires were made of gold plated aluminum with a diameter of $80\mu m$. Sense wires formed ten layers (planes) in the configuration xx'uu'xx'vv'xx'. Wires in prime planes are parallel to the ones in unprimed planes, x'(u',v') wires are parallel to x(u,v) wires, but with a shift of half cell (cell size is 0.5 cm). This shift in unprimed planes resolves left-right position ambiguity in x-position obtained by x-plane. The u and v wires are rotated with respect to x wires, the u wires have an angle of $30°$ degrees and v wires $-30°$. The
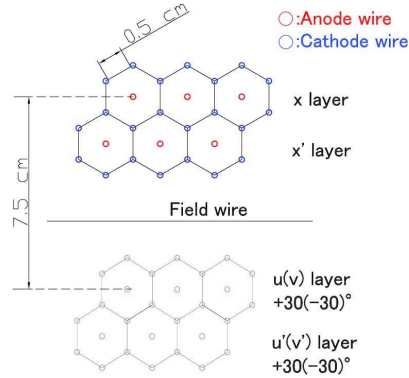
FIGURE 2.23: HONEYCOMB CELL STRUCTURE OF THE ENGE DRIFT CHAMBER.

TABLE 2.6: ENGE DRIFT CHAMBER PARAMETERS

Parameter	
Wire plane configuration	X, X', U, U', X, X', V, V' X, X'
Effective region	$12^H cm \times 100^W cm \times 30^T cm$
Gas content	Argon-Ethane 50/50 mixture
Gas pressure	16 psi
Operation HV	2200 V
Threshold	2.0 V

distance between the planes is 7.5cm. The parameters of EDC are listed in Table2.6. Design of EDC chamber is shown in Fig.2.24. EDC was filled with Argon-Ethane (50-50) gas mixture. The signal from the anode wire went to nanometric N277L cards which preamplified and discriminated the signal. For EDC there were 70 amplifier-discriminator cards on each side,top and bottom, 35 cards. The same type of cards was also used in the HKS drift chamber.

Enge hodoscopes

Enge hodoscope system is made of two layers of plastic scintillators, EHODO1 and EHODO2, placed after EDC and used for trigger and timing measurement. Each plane consists of 25 scintillator detectors, see Fig.2.25, with the planes having an offset to each other of half a width of the scintillator. At
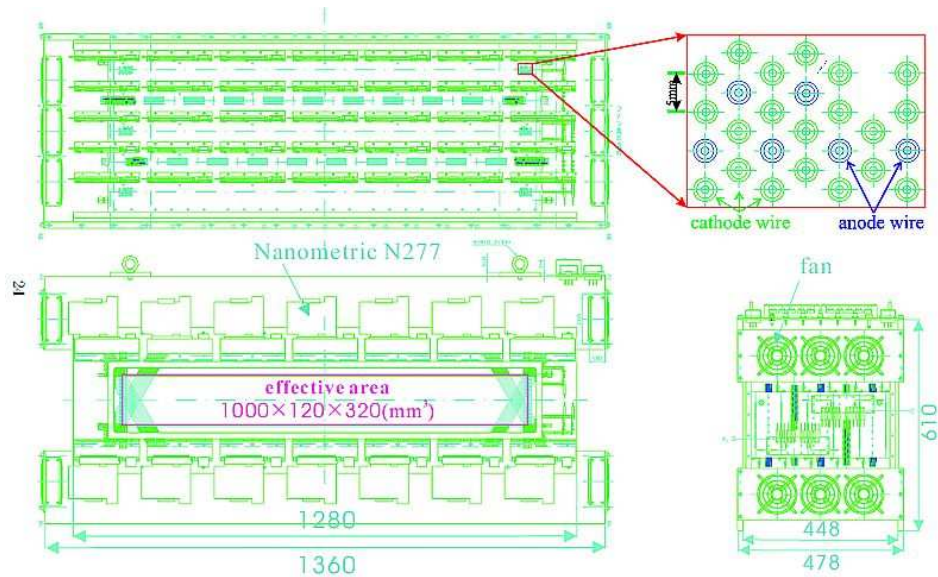
FIGURE 2.24: SCHEMATIC VIEW OF THE ENGE HONEYCOMB DRIFT CHAMBER.

both ends of the scintillator slab there was a PMT connected to the scintillator with acrylic light guides.PMTs were made by Hamamatsu and two types were used: H6612 and R3478. Third scintillator layer, EHODO3, was actually a single scintillator detector that covered the entire focal plane and was used for the calibration of EHODO1 and EHODO2.

The operating settings of the hodoscopes, high voltage on the dynods and threshold voltage on the discriminator, for both Enge and HKS hodoscopes were chosen based on the efficiency plateau curve test. The efficiency is the ratio of the hits in the detector under study and the triggers of the system. By doing a PMT high voltage and discriminator voltage threshold scan for each PMT efficiency plateau curve was obtained, see Fig.2.26.

2.5.2 HKS detector package

The HKS detector package consisted of detectors for tracking of particle , particle identification, time determination and trigger. Details of the package are shown in Fig.2.27; for tracking two layers of drift chambers (HDC1 and
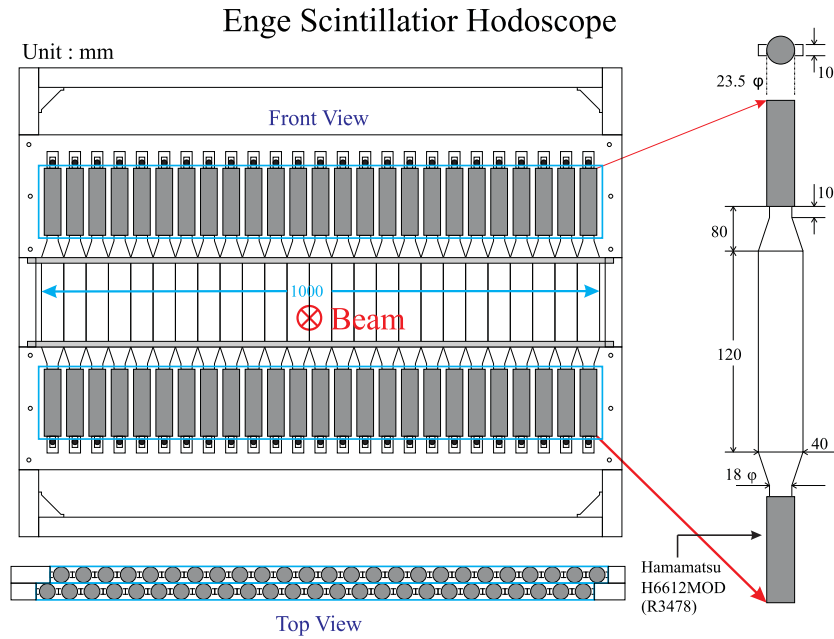
FIGURE 2.25: SCHEMATIC VIEW OF THE ENGE HODOSCOPE.

HDC2), for particle identification three layers of Aerogel Čerenkov (AC1,AC2 and AC3) and two layers of Water Čerenkov (WC1 and WC2), for timing scintillation hodoscopes. Because of the small kaon production cross section (compared to positrons, pions and protons) important part of the HKS detector package are particle identification detectors enabling good kaon identification. Three layers of aerogel Čerenkov discriminated pions from kaons while two layers of Water Čerenkov discriminated protons from kaons which together with timing obtained from hodoscopes enabled good kaon particle identification. All these detectors were shielded from background particles by concrete shielding house and from dipole fringe field by the so called "German fortress", an iron box completely surrounding the HKS detectors.

HKS drift chambers

The two HKS drift chambers (HDCs) determined the particle trajectories. HDCs were positioned after the HKS dipole magnet and mounted to the vacuum extension from the exit of the dipole to the window of the first
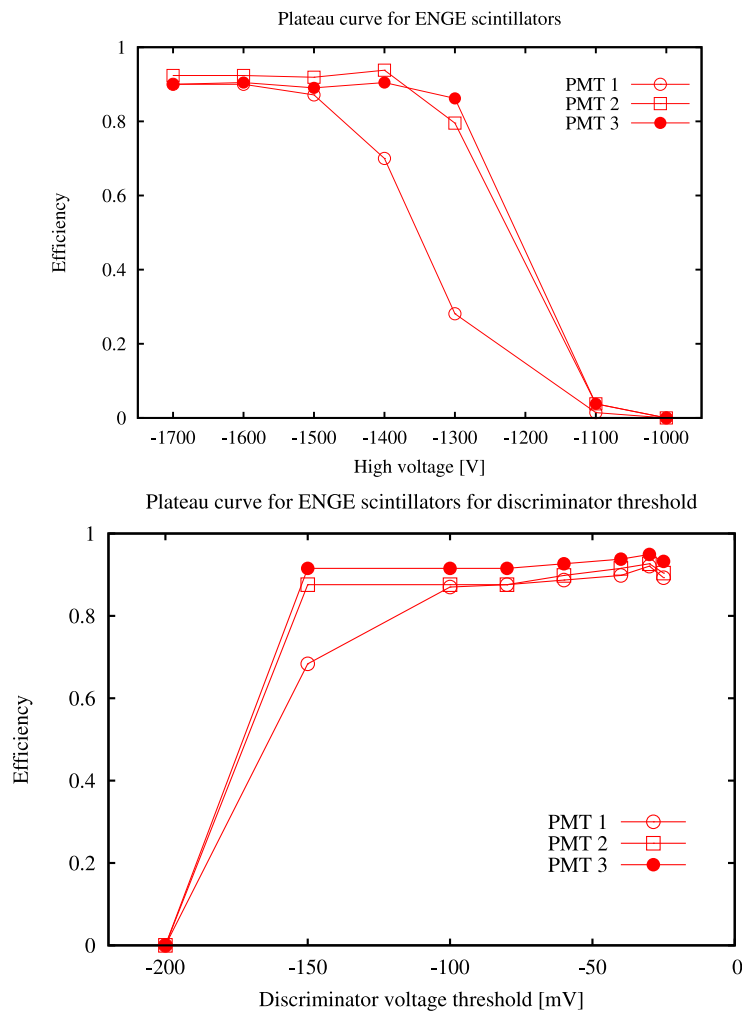
FIGURE 2.26: *Top* HIGH VOLTAGE PLATEAU FOR THE ENGE HODOSCOPE PMTS. *Bottom* DISCRIMINATOR THRESHOLD PLATEAU FOR THE ENGE HODOSCOPE PMTS.
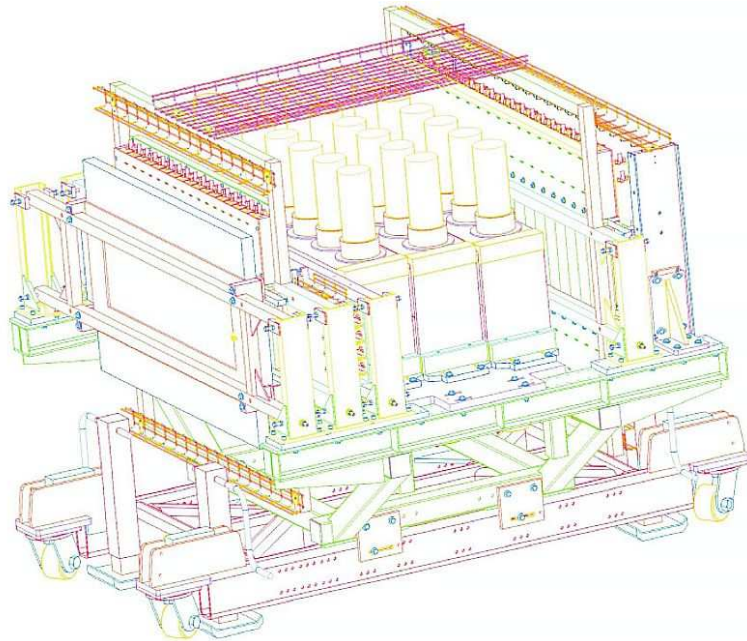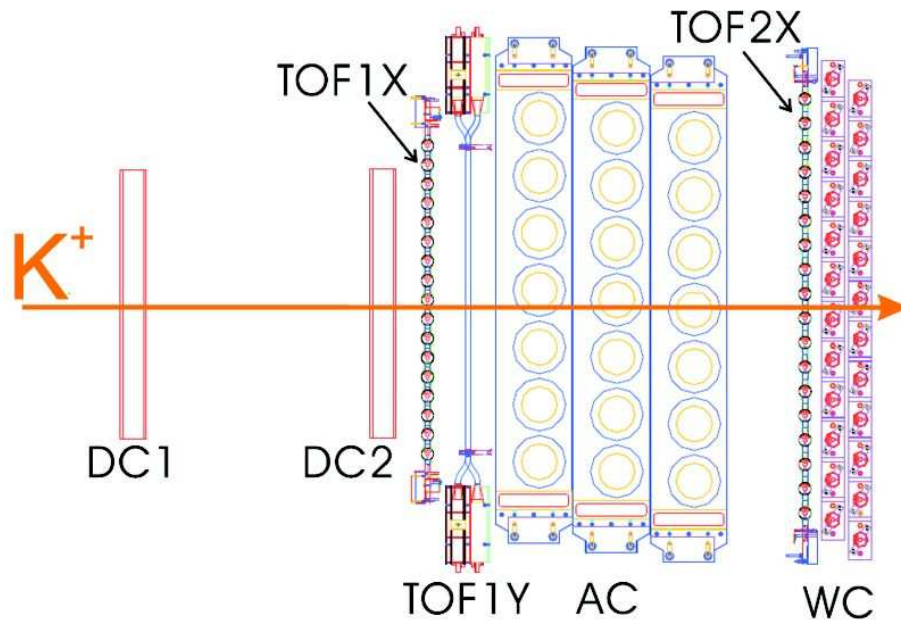
FIGURE 2.27: DETECTOR PACKAGE OF THE HKS, CONSISTING OF DRIFT CHAMBERS, TIME OF FLIGHT HODOSCOPES, AEROGEL AND WATER ČERENKOV DETECTORS.

HKS DC Coordinate Systems and Wire Orientations
(beam's eye view)
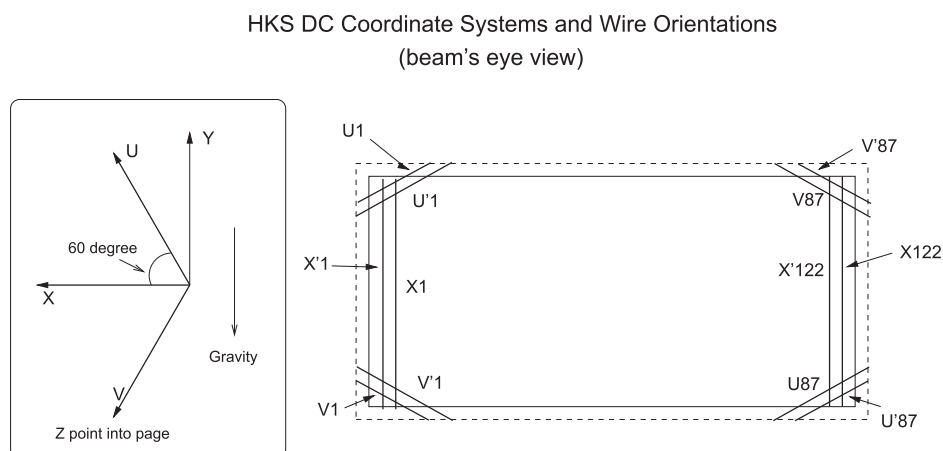
FIGURE 2.28: SCHEMATIC VIEW OF THE HKS DRIFT CHAMBER WIRE DIRECTIONS.

HDC. The separation between chambers was 1m and in between there was a Helium bag to minimize multiple scattering of the particles. This is also the reason why drift chambers are the closest to the HKS dipole. HDCs were constructed by Hampton University group by design similar to the ones used in HNSS experiment [110] [3]. Each of the HDCs had six wire planes, transverse to central trajectory. Layout of the wires in x (u and v) plane is transverse to x (u and v) axes. With respect to X axis U axis is tilted 60° and V axis by −60° with positive direction being clockwise, see Fig.2.28. Wire layer configuration in HDCs were UU'XX'VV', see Fig.2.29 and 2.30. Primed layers had the same direction as unprimed ones but with an offset of half a cell size (1cm) to resolve left-right ambiguity of the position measured by unprimed plane. The plane had an effective area of $122cm \times 30cm$ each.

The sense (anode) wires were made of gold plated Tungsten, 25 μm in diameter, connected to the ground. Potential wires were made of a Beryllium Copper alloy, 90 μm in diameter, connected to negative high voltage. The cathode foils are made of 1/2 mil of Mylar coated on both sides with 1,200 Å of Cu. The distance between two cathode foils was 0.635 cm. The separation between two sense wires, as well as for two potential wires, was 1 cm which gave maximum drift distance of 0.5 cm. The number of sense wires on planes X,X' was 122 while U,U',V,V' had 87 wires.
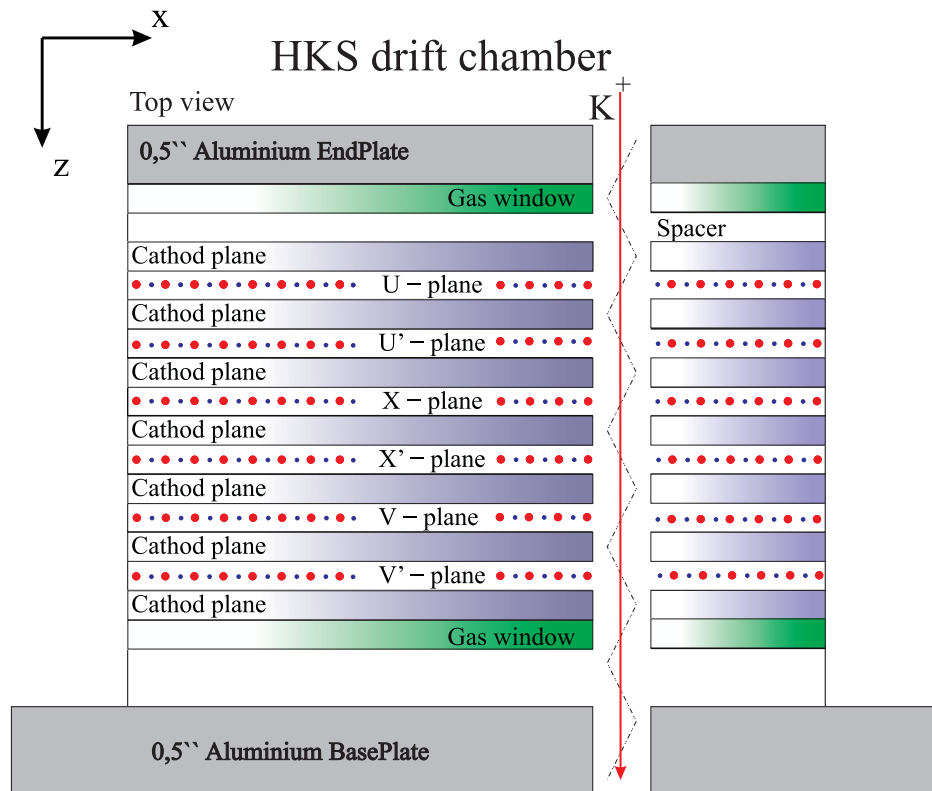
FIGURE 2.29: SCHEMATIC VIEW OF THE HKS DRIFT CHAMBER.
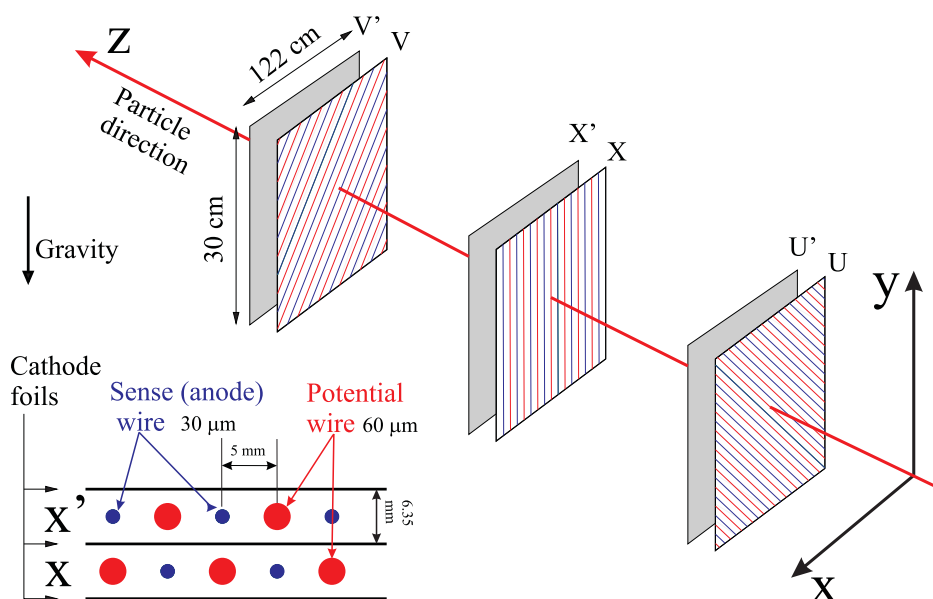
FIGURE 2.30: SCHEMATIC VIEW OF THE HKS DRIFT CHAMBER.

The signal in the drift chamber is produced when a particle, traveling through the chamber, ionizes gas producing an avalanche when electrons drift towards the anode. The gas mixture that was used was a 50:50 mixture, by weight, of argon and ethane(C_2H_6) gas. This mixture is used because argon has good ionization and ethane good quenching properties.

Signals from sense wires went to Nanometrics N277-L, see Fig.2.33, which amplified and discriminated the signal. There were 20 cards per chamber, mounted on both sides of the chamber, using power input of both $\pm 5V$. Discriminated ECL signals from cards were processed by (Lecroy 1877) Fast-Bus multihit TDC which can store 16 hits with the resolution of 500ps. TDC information for each HDC wire was readout when trigger signal has been sent to stop the Fast-Bus multihit TDC in the window of μs before the trigger. This TDC values were used to obtain drift time, time needed for drifting electron to arrive to sense wire from the point of ionization. Position of the track is calculated from wire position and measured drift time. With the cell size being 0.5 cm and Ar-Ethane gas mixture the maximum drift time was about 150 ns.
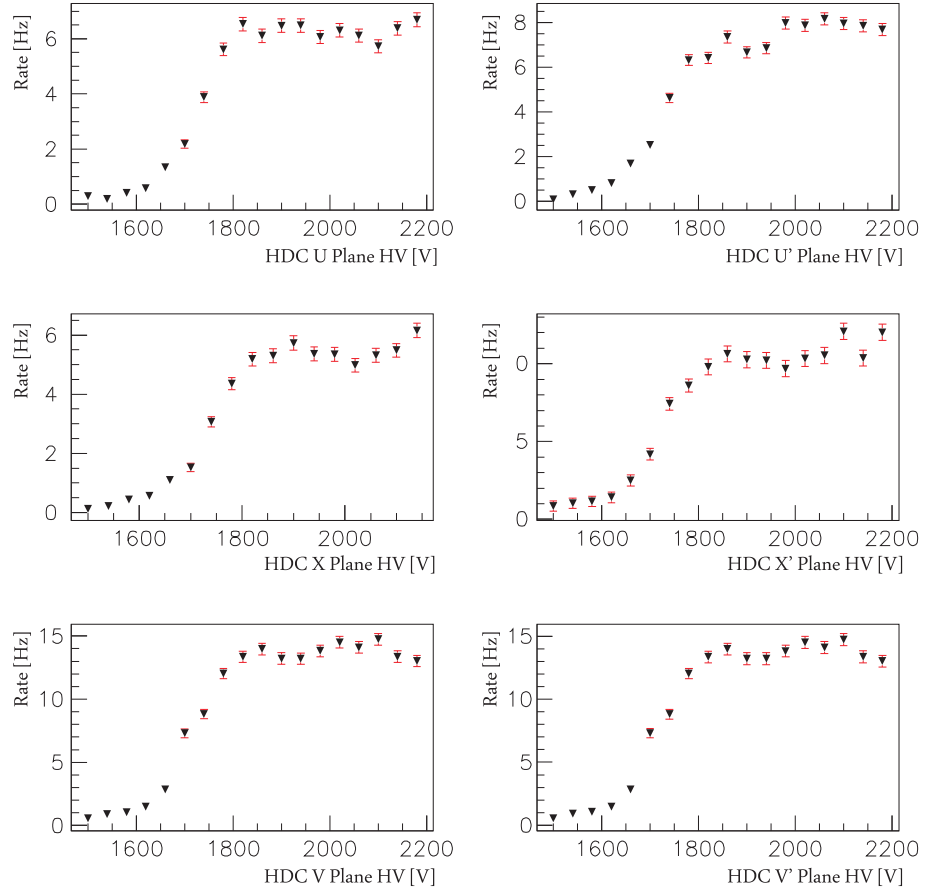
FIGURE 2.31: PARTICLE RATE DEPENDENCE OF HDC PLANES ON HIGH VOLTAGE SET ON CATHODE FOILS AND POTENTIAL WIRES.

Drift chambers were tested before the experiment with cosmic data so that operational high voltages of the cathode foils and potential wires could be optimized. High voltage plateau region is shown in Fig.2.31 and 2.32.

HKS hodoscopes

In HKS three layers of plastic scintillation hodoscopes HTOF1X, HTOF1Y and HTOF2X were part of the trigger setup and were also used for measuring the time of flight (TOF) between the hodoscope planes of the charged particles. Hodoscopes HTOF1X and HTOF2X were segmented in X direction (see
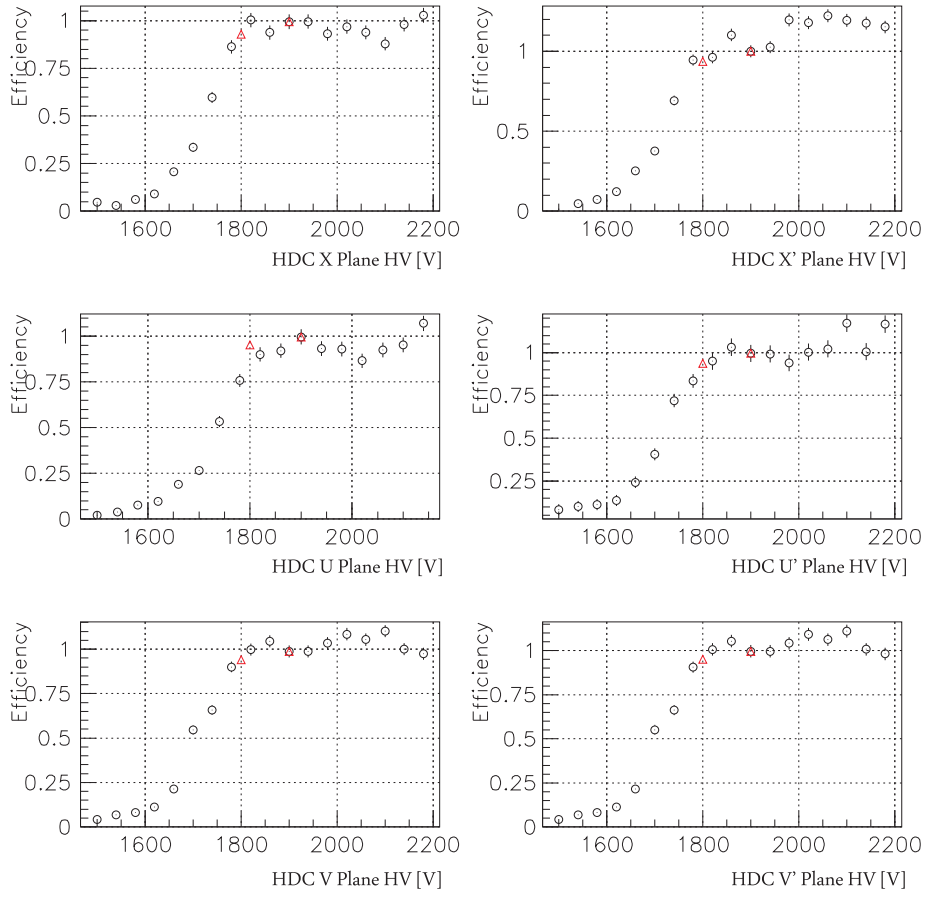
FIGURE 2.32: HDC TRAJECTORY EFFICIENCY DEPENDENCE ON HIGH VOLTAGE
SET ON CATHODE FOILS AND POTENTIAL WIRES.

TABLE 2.7: GEOMETRICAL AND OPERATIONAL PARAMETERS OF THE HKS DRIFT
CHAMBER. POSITION IS MEASURED FROM FOCAL PLANE DEFINITION.

Parameter	
Wire plane configuration	U, U', X, X', V, V'
Dimensions	$57.8^H\,cm \times 150.5^W\,cm \times 7.6^T\,cm$
Effective region	$30.5^H\,cm \times 122.4^W\,cm$
Z Position of the HDC1 center [cm]	-48.095
Z Position of the HDC2 center [cm]	51.905
Gas content	Argon-Ethane 50/50 mixture
Gas pressure	16 psi
Operation HV	1970 V
Threshold	3.0 V
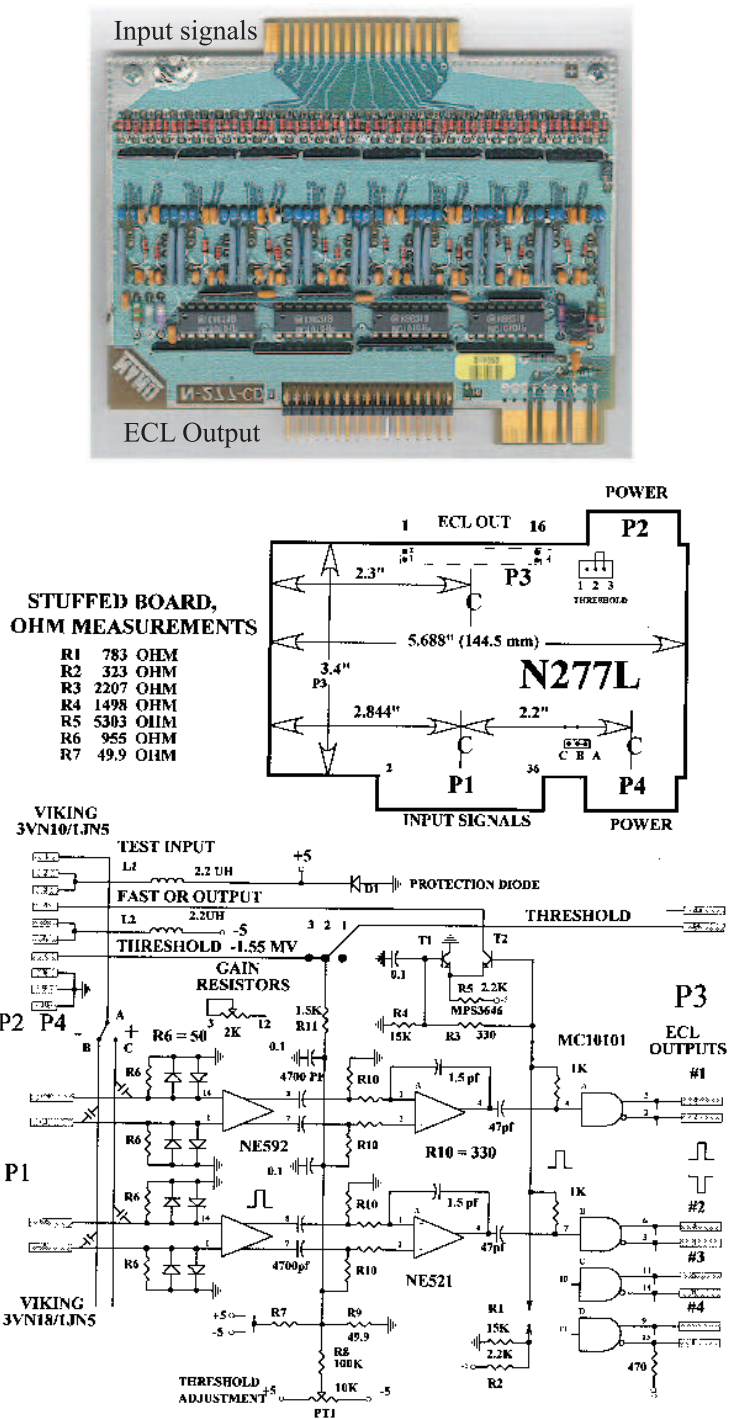
FIGURE 2.33: PICTURE AND SCHEME OF THE NANOMETRICS N277-L CARD.

TABLE 2.8: PARAMETERS OF THE HKS HODOSCOPES. POSITION IS MEASURED FROM FOCAL PLANE DEFINITION.

Parameter	HTOF1X	HTOF1Y	HTOF2X
Height [cm]	30	30	30
Width [cm]	125	125	170
Thickness [cm]	2	2	2
Segments	17×7.5 cm	9×3.5 cm	18×7.5 cm
Z Position [cm]	69.2	85.1	218.7
PMTs	Hamamatsu H1949-50		
High Voltage [V]	-1800		

Fig.2.34), the PMTs pointed in Y direction, while HTOF1Y was segmented in Y direction (see Fig.2.35), the PMTs pointed in X direction. TOF was calculated using 1X and 2X hodoscopes and, in the absence of signal from one of them, time information obtained by HTOF1Y was used for TOF calculation. Positions of HKS hodoscopes can been seen in Fig.2.27. HTOF1X and HTOF1Y were placed after HDCs with 1Y after 1X while HTOF2X was after Aerogel Čerenkov and before Water Černkov. The distance between HTOF1X and HTOF2X was 149.5 cm chosen to separate kaons from pions and protons in the designed HKS momentum region.

HKS hodoscopes were constructed from Bicron BC408 scintillators and on both sides Hamamatsu H1949-50 phototubes were used. The parameters of HKS hodoscopes are listed in Table2.8.

When charged particle passes through the scintillator it loses energy, due to interaction with material, and light is produced. It is transmitted to PMTs on both sides and converted to electric pulse. This signal was sent by coaxial cable to counting house and divided into two signals in 1/3 ratio and 2/3 ratio by a splitter. The larger signal was delayed and used for pulse size analysis done in fastbus ADC [LRS1881M]. The smaller one was processed by leading edge discriminator [PS7105] and the output was after delay used for timing and analyzed by a fastbus TDC [LRS1872A] and for forming trigger.
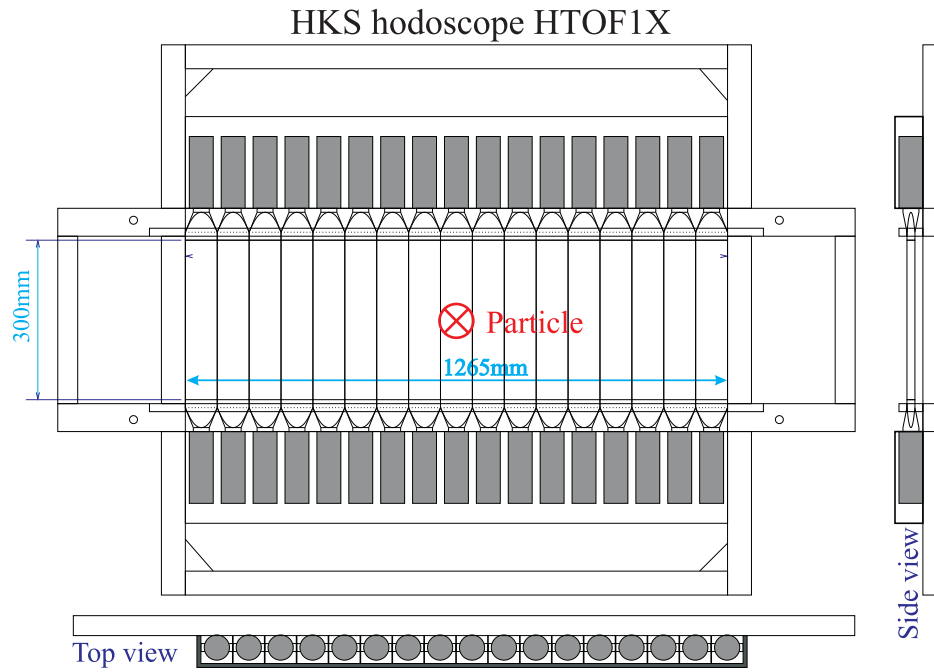
FIGURE 2.34: SCHEMATIC VIEW OF THE HKS HODOSCOPE, LAYER 1X.
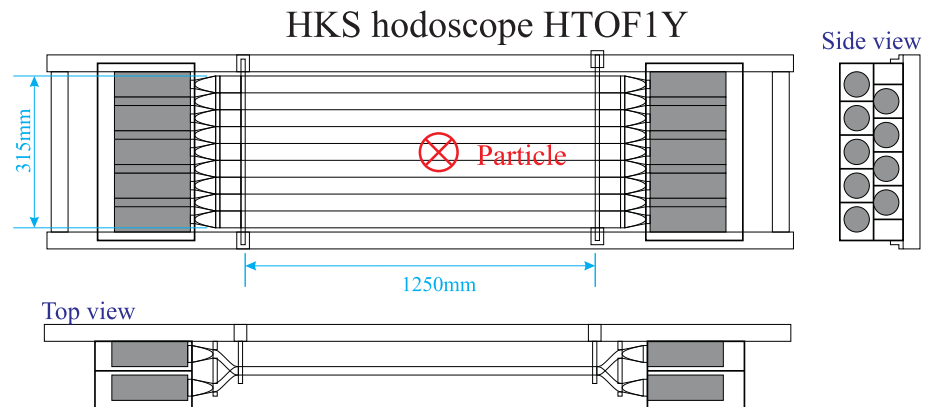
FIGURE 2.35: SCHEMATIC VIEW OF THE HKS HODOSCOPE, LAYER 1Y.

Aerogel Čerenkov

The HKS Aerogel Čerenkov detectors (AC) were an important part of the HKS package. Because of the small difference between Kaon (m_{K+}=439.7 Mev) and Pion (m_{Π}=139.5 MeV) masses they can not be completely separated with TOF information obtained with HKS hodoscopes. The ACs were used to discriminate, reject pions from kaons in kaon trigger because in this momentum range protons and kaons should not produce a signal in AC detector. There were three layers each consisting of 7 segments of AC detectors and all were light tight. AC was segmented in X direction, the PMTs pointed in Y direction. The radiator material used in AC was hydrophobic silica aerogel ($n(SiO_2) + 2n(H_2O)$) SP50 from Matsushita Electric Works with a refraction index 1.055 which enables the separation of kaons from pions in momentum region of $1.2 GeV \pm 12.5\%$. By using AC in kaon trigger in veto mode pion suppression by a factor of 10^{-4} was achieved.

Each AC layer ($46^H cm \times 169^W cm \times 31^T cm$) was inside of diffusion box optically separated into seven segments by tedlar film sandwiched between two layers of Millipore paper. The inside walls were covered with white milipore filter paper which acts as diffusion reflector. Each segment was filled with 5 layers of aerogel bricks ($11.3 cm \times 11.3 cm \times 0.5 cm$) covering an area of $46 cm \times 23 cm$ with radiation length of 5cm. On one side the aerogel tiles rested on one of the side walls and from the other side they were kept in place by nylon wires. When particle with $\beta > 0.948$ passes through the silica aerogel, it emits Čerenkov light in a $\pm 18.6°$ wide forward pointing cone. The light produced in aerogel tiles was collected by 2 PMTs, see Fig 2.36. Two types of PMTs were used, 28 Hamamatsu R1250 PMTs for first and second AC layer and 14 Photonis XP4572B/D1 PMTs for third layer. The two discriminated logical signals are then ANDed to form the HKS aerogel pretrigger signal, AERO. This signal was a part of the HKS pretrigger logics as a veto signal to reject pions at trigger level. The HVs on the PMTs were set so that the one-photo-electron (OPE) peaks were at about the same position in their ADC spectra.

In the commissioning period of the experiment the HKS dipole fringe
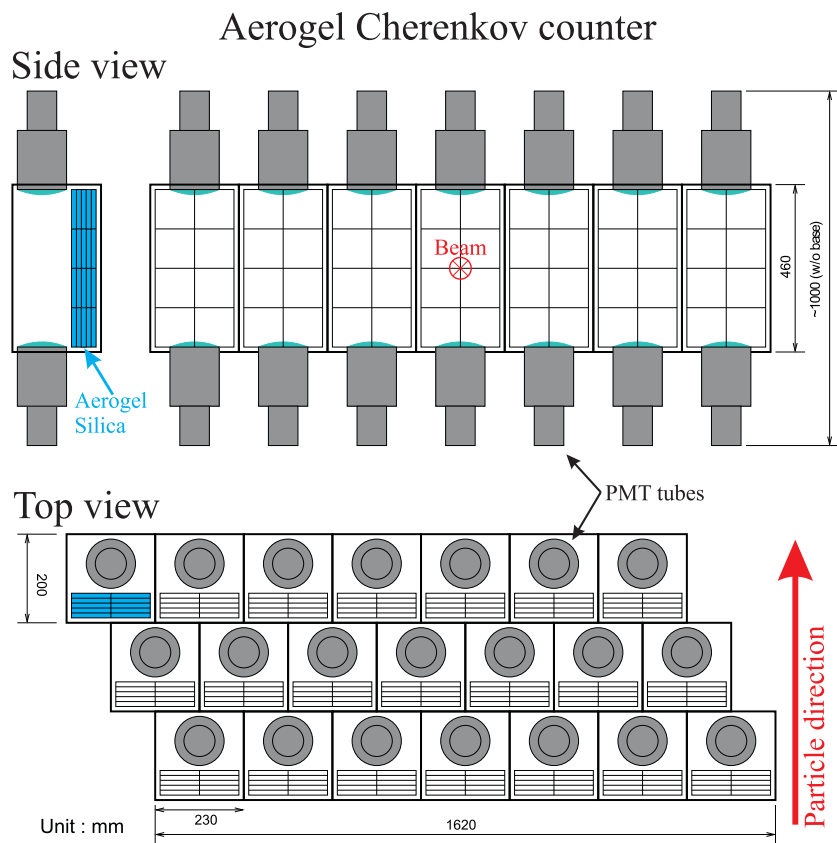
FIGURE 2.36: SCHEMATIC SIDE AND TOP VIEW OF THE HKS AEROGEL ČERENKOV DETECTOR.
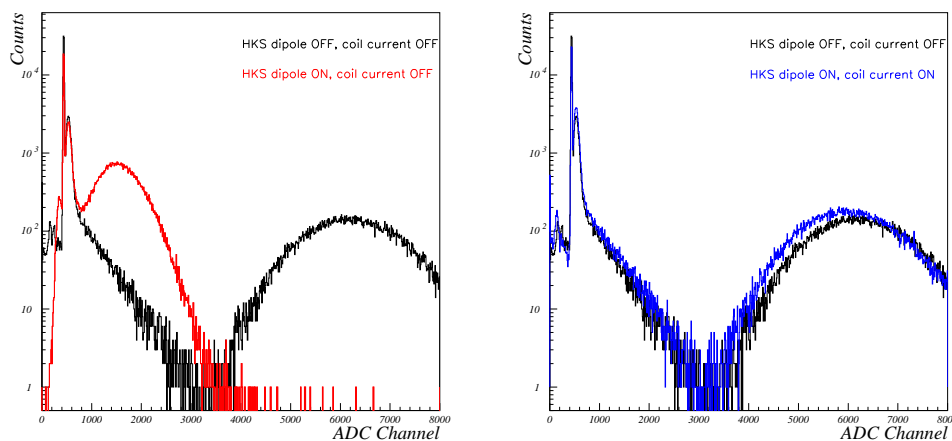
FIGURE 2.37: *Left*, EFFECT OF THE FRINGE FIELD ON THE PERFORMANCE OF THE AC PMTS. *Right* RECOVERED PERFORMANCE OF THE AC PMT WITH COILED WIRE INDUCED FIELD THAT CANCELED HKS DIPOLE FRINGE FIELD.

field of five Gauss influenced the performance of the aerogel PMTs, as seen in Fig. 2.37. In order to solve this unexpected effect detectors were enclosed in an iron plate structure, the so called "German fortress". This reduced the fringe field from 5 Gauss to 2.5 Gauss but was not good enough and the AC PMTs did not perform to the satisfactory level. The problem was solved with local magnetic field around aerogel PMTs created by coiling an AWG 12 wire around them, see Fig. 2.38. The DC current of 3A in the wires created magnetic field and canceled the fringe field restoring the PMTs performance. The performance of AC is in detail discussed in Section 3.4.4.

Water Čerenkov

The HKS Water Čerenkov detectors (WC) were used: online as a part of the kaon trigger and offline for the separation of protons from kaons which can not be completely done with TOF information. On the online level WCs were a part of the kaon trigger in AND mode rejecting protons with efficiency of 5×10^{-4}. For this suppression effect to be achieved two layers of water Čerenkov (WC1 and WC2), each consisting of 12 segments of WC detectors,
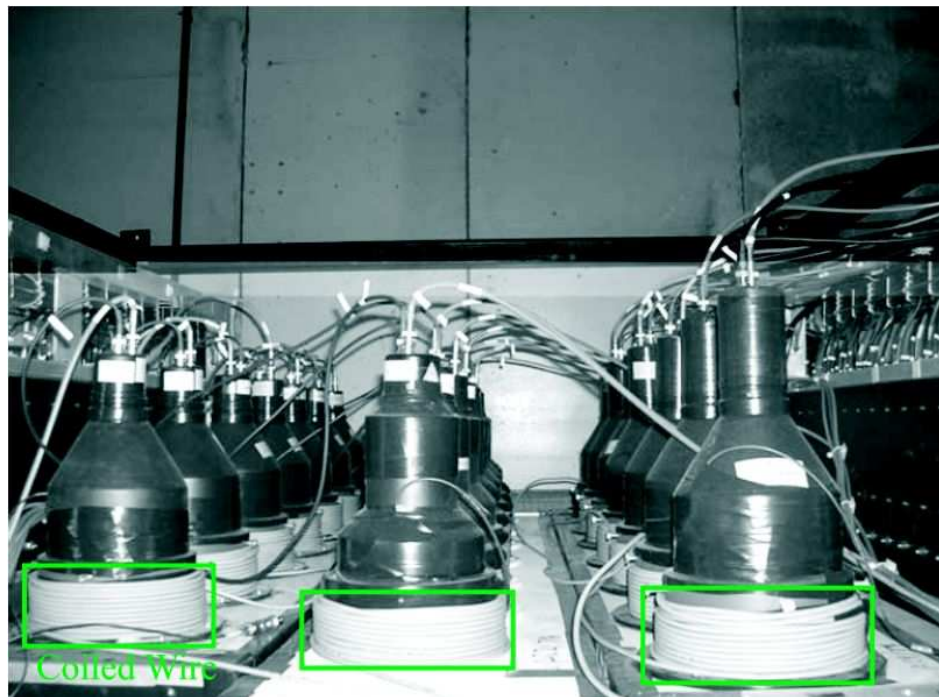
FIGURE 2.38: PICTURE OF AEROGEL ČERENKOV WITH COILED WIRE NEEDED TO CANCEL HKS DIPOLE FRINGE FIELD.
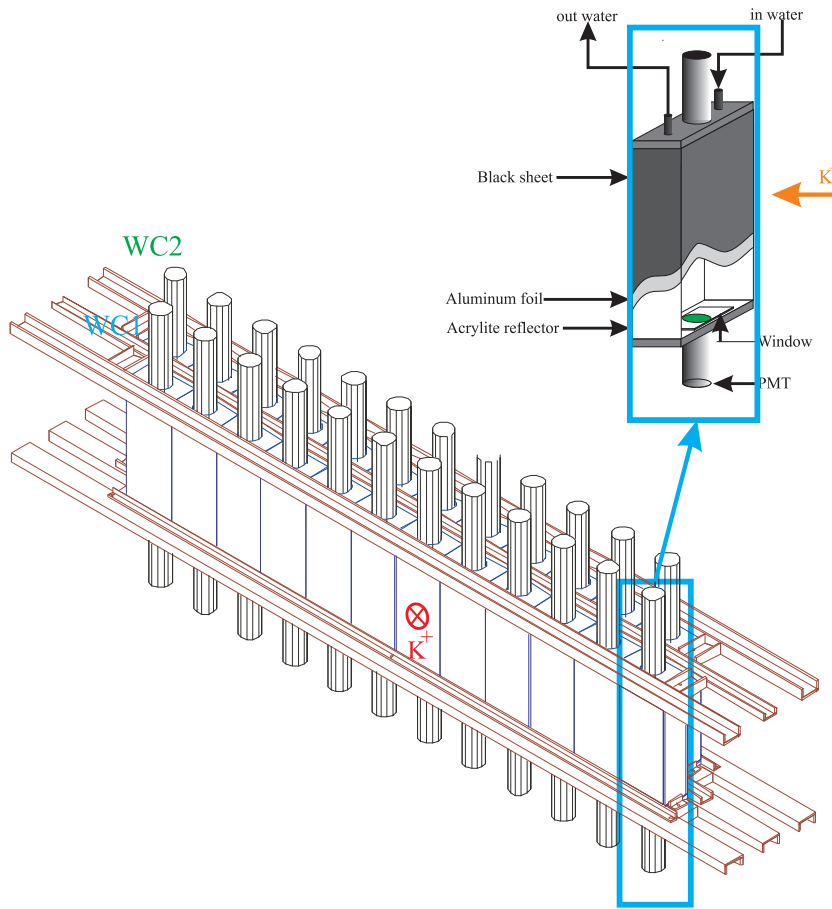
FIGURE 2.39:   SCHEMATIC DRAWING OF WATER ČERENKOV PLANES AND COUNTER.

were used. WC was segmented in X direction, the PMTs were pointed in Y direction. The schematic view of the WC layer and detector design is shown in Fig.2.39.

The radiator material used was pure (de-ionized) water with added (50 mg per liter) wavelength shifter (amino-G-salt: 2-amino-6, 8-naphthalene-disulfonic acid). The wavelength shifter was added to make the light response isotropic and to increase the number of observed Čerenkov photons by re-radiating the produced light at a longer wavelengths which are more suitable for the response of photomultiplier tubes.

The water mixture was contained in a white acrylic (Mitsubishi: Acrylite 402 with diffuse reflectance of 94.8%) box with dimensions $35^H cm \times 15^W cm \times 7.5^T cm$. Water containers were light shielded by wrapping them in aluminum foil and black plastic sheet. The Čerenkov light produced was collected by two PMTs (Hamamatsu H7135) attached to two UVT transparent acrylic windows (Mitsubishi: Acrylite 000 with effective wavelength region transmittance og 90%) on both ends of water, see Fig.2.39.

The dependence of the number of photons on particle momentum for two radiators, pure water with added wavelength shifter(n=1.33) and acryl (n=1.49) is shown in Fig.2.40.

2.5.3   Trigger

To kinematically reconstruct Λ hypernuclear states incident electron, kaon and scattered electron momenta must be known on event to event basis so the coincidence of the scattered electron and kaon was needed. The experiment E01-011 was a coincidence type of experiment with the trigger formed as coincidence of pretriggers from HKS and Enge detector packages. Enge pretrigger was the coincidence signal of the Enge hodoscope layers (on the Enge side there was no need for particle identification detectors) with coincidence window of 12.5 ns.

$$EHODOpretrig = EHODO1 \otimes EHODO2 \qquad (2.3)$$

The HKS pretrigger is formed from hodoscope, Aerogel Čerenkov and Water Čerenkov signals. Depending on what we want to study, the HKS pretrigger can be set to one of the possibilities listed in Table 2.9. An unbiased trigger required only coincidence between HKS hodoscopes so the spectrum is dominated by pions and protons. Pion trigger will be formed if signal is produced in both Čerenkov detectors, as explained in 2.5.2. Hence, a pion trigger was $1X \otimes 2X \otimes AC \otimes WC$. Since kaon and proton do not produce a signal in AC, their triggers had AC signal in veto mode. Both proton and kaon produce light in WC. With threshold set on WC signal protons can be separated from kaons since they produce less light, see Fig.2.40. Proton
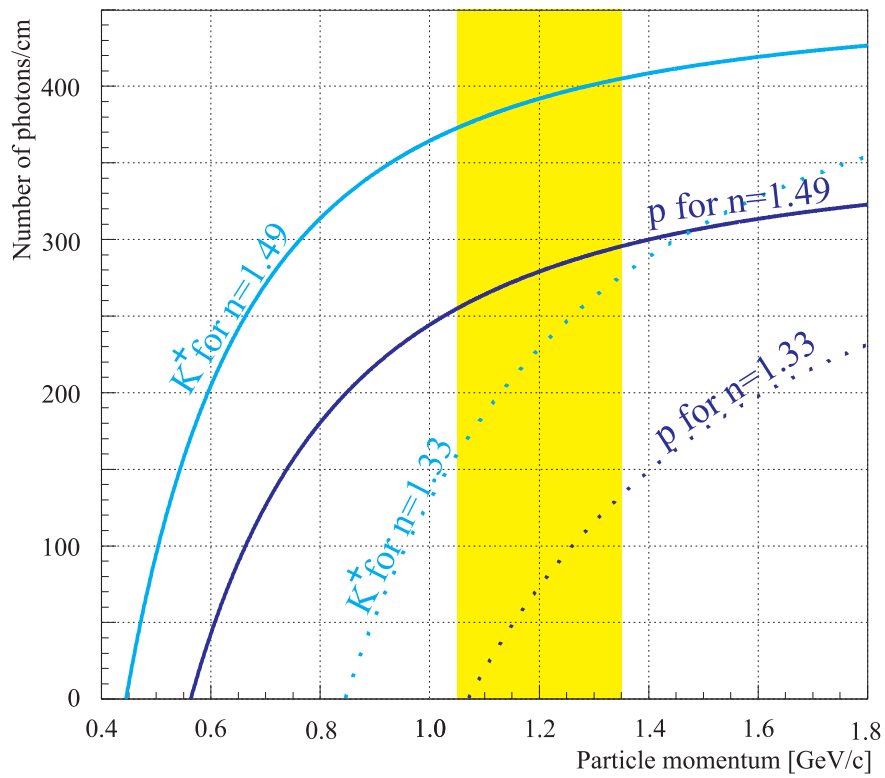
FIGURE 2.40: DEPENDENCE OF THE NUMBER OF PHOTONS PRODUCED IN ČERENKOV DETECTORS BY PROTONS AND KAONS IN WATER (N=1.33) AND ACRYLIC RADIATOR (N=1.49). COLORED REGION REPRESENTS HKS SPECTROMETER MOMENTUM ACCEPTANCE.

TABLE 2.9: HKS TRIGGER CONDITIONS.

HKS pretrigger	Setting	Comment
Unbias	HTOF	Rate, efficiency study
Pion	HTOF$\otimes WC \otimes$AC	pion selection
Proton	HTOF$\otimes \overline{WC} \otimes \overline{AC}$	proton selection
Kaon	HTOF$\otimes WC \otimes \overline{AC}$	production

trigger was $1X \otimes 2X \otimes (\overline{AC} \oplus \overline{WC})$. Kaon trigger was $1X \otimes 2X \otimes \overline{AC} \otimes WC$.

In production mode, used trigger was a combination of kaon trigger and prescaled unbiased events with prescale factor set to contribute on the level of $\smile 5\%$ of kaon trigger events.

As seen in Table 2.9, to form HKS pretrigger, first responses of each HKS detector package HTOF, WC and AC are defined. Depending on the physics motivation and running conditions detector package settings in HKS pretrigger changed. The standard detector package setting in trigger was as described:

$$HTOF = HTOF1X \otimes HTOF2X \tag{2.4}$$

$$WC = WC1 \otimes WC2 \tag{2.5}$$

$$AC = [(AC1 \otimes AC2) \oplus AC3] \oplus [(AC1 \otimes AC3) \oplus AC2]$$
$$\oplus [(AC2 \otimes AC3) \oplus AC1] \tag{2.6}$$

On the online trigger level it was not possible to isolate the real coincidence events from accidental ones because of high trigger rates of the Enge pretrigger. The real HKS and Enge coincidence events were created on the offline analysis as discussed in Section 4.1.

Grouping trigger

With this experimental setup, high trigger rates in both kaon and electron arm were expected, see Table 2.10 and Fig.2.41, much higher than data acqui-

TABLE 2.10: CALCULATED SINGLES RATES OF PARTICLES EXPECTED IN HKS AND ENGE DETECTORS. VALUES USED IN CALCULATION: $30\mu A$ BEAM, 100 MG/CM^2 TARGET THICKNESS, ANGLE OF SCATTERED KAON $\theta_K^+ = 7°$ AND $\theta_e' = 4.5°$ FOR ELECTRON.

Target	HKS				Enge	
	e$^+$ [kHz]	π^+ [kHz]	K$^+$ [kHz]	p [kHz]	e$^-$ [kHz]	π^+ [kHz]
^{12}C	-	420	0.38	150	1000	2.8
^{28}Si	-	420	0.32	130	1900	2.8
^{51}V	-	410	0.29	120	2650	3.0

sition could handle. This introduced an issue of accidental kaon overkilling (suppression) which was solved with grouping trigger. .

The grouping idea involved the segmentation of detector layers in the HKS detector package. With Monte Carlo simulation detector planes were segmented in six groups, see Fig2.42. With grouped trigger, the setup kaon overkill was avoided because AC veto signals could only veto coincidence signal $HTOF \otimes WC$ from the same group (AC veto from G3 will not veto kaon trigger event from G1, G2, G4, G5 or G6). With the HKS spectrometer system momentum and angle acceptance it was not possible to have clean separation of groups and there was an overlap to make sure Kaons are not rejected.

As a reference, grouping definition for the real event distribution on the HTOF1X and 2X are represented in Fig. 2.27, and shows an availability of the grouping trigger introduction. Group trigger was implemented with programmable logic module, Tohoku Universal Logic module (TUL-8040).

Trigger logic

Trigger logic with defined kaon, proton and pion particle pretriggers, as used in the E01-011 experiment, is shown in Fig.2.43. Each of the particle pretriggers used signals from HKS hodoscopes, Aerogel and Water Čerenekov
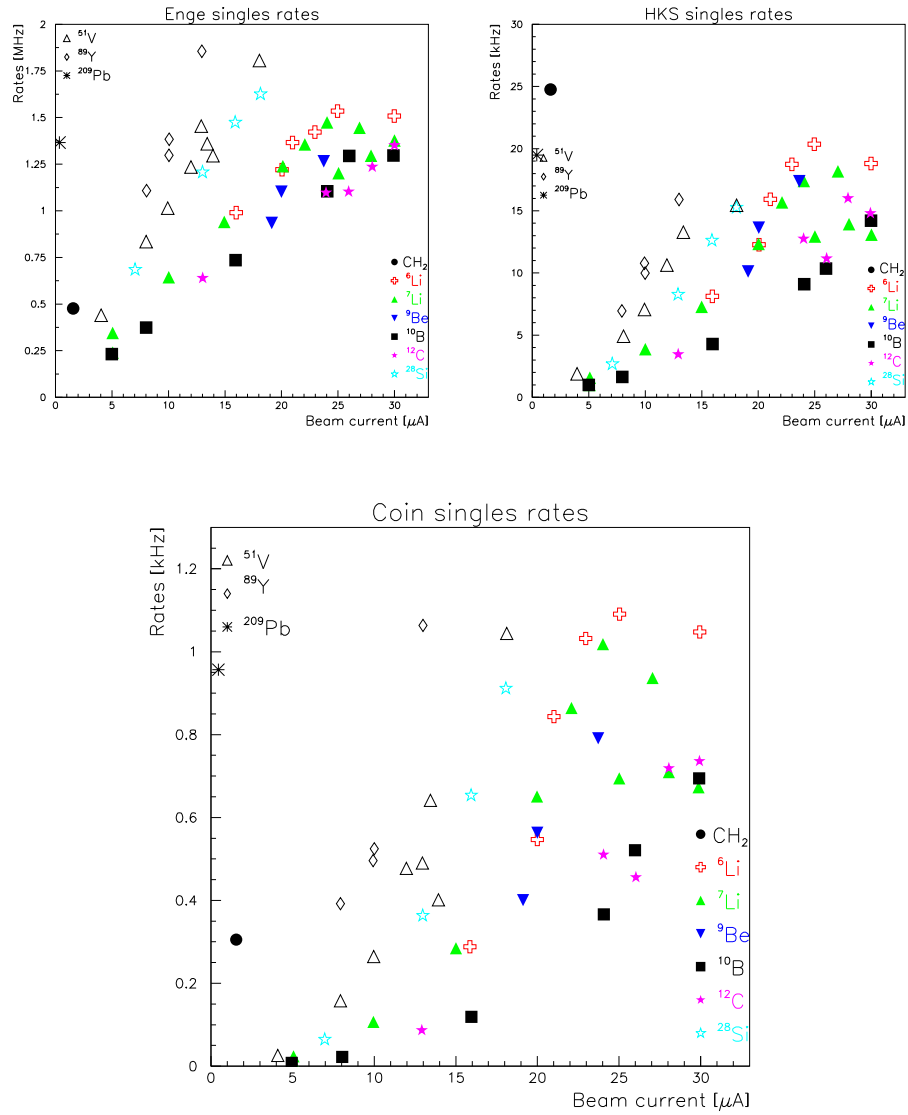
FIGURE 2.41: TYPICAL TRIGGER RATES OF ENGE AND HKS PRETRIGGERS (*Top*) AND COINCIDENCE TRIGGER (*Bottom*) IN E01-011 FOR USED TARGET AND BEAM CURRENT SETTINGS.
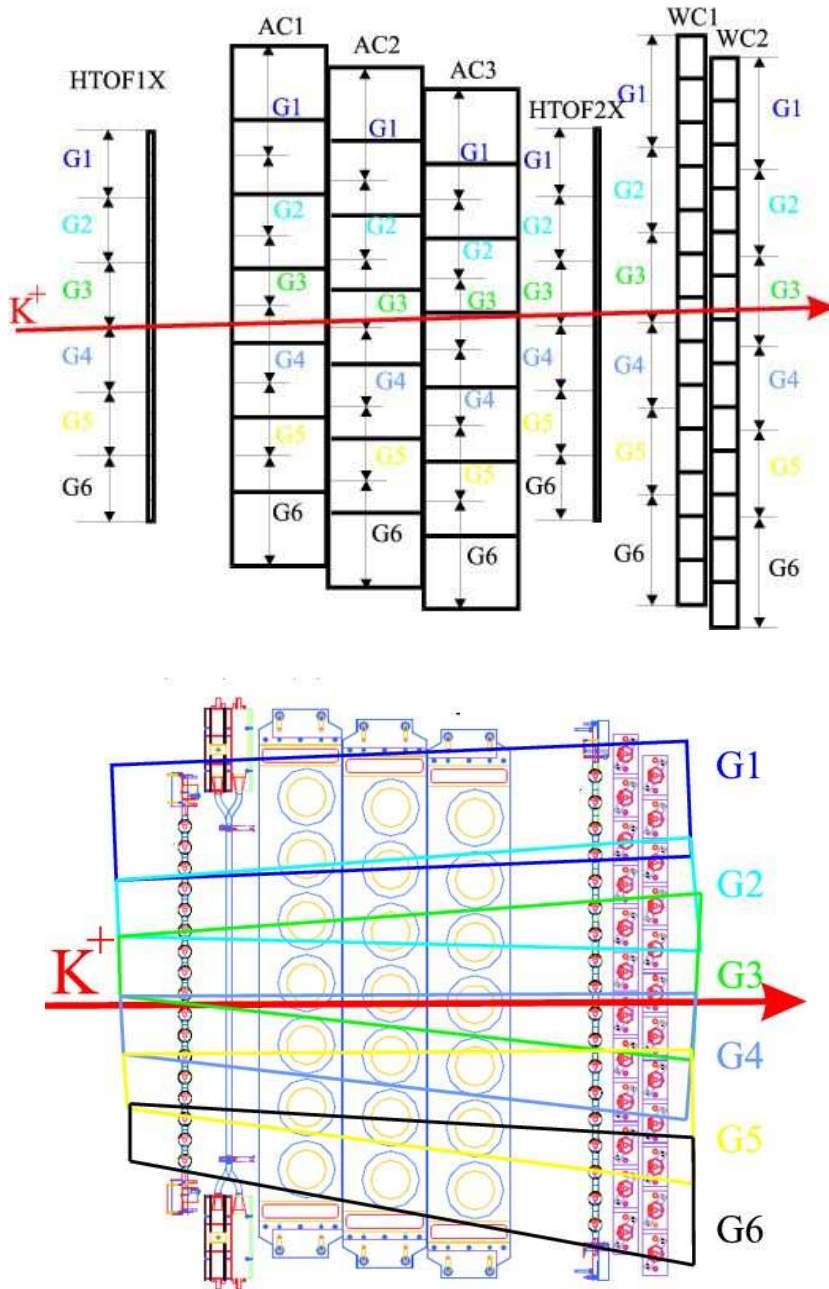
FIGURE 2.42: GROUPING TRIGGER FOR THE HKS DETECTOR PACKAGE AND DEFINED SEGMENTATION OF LAYERS.
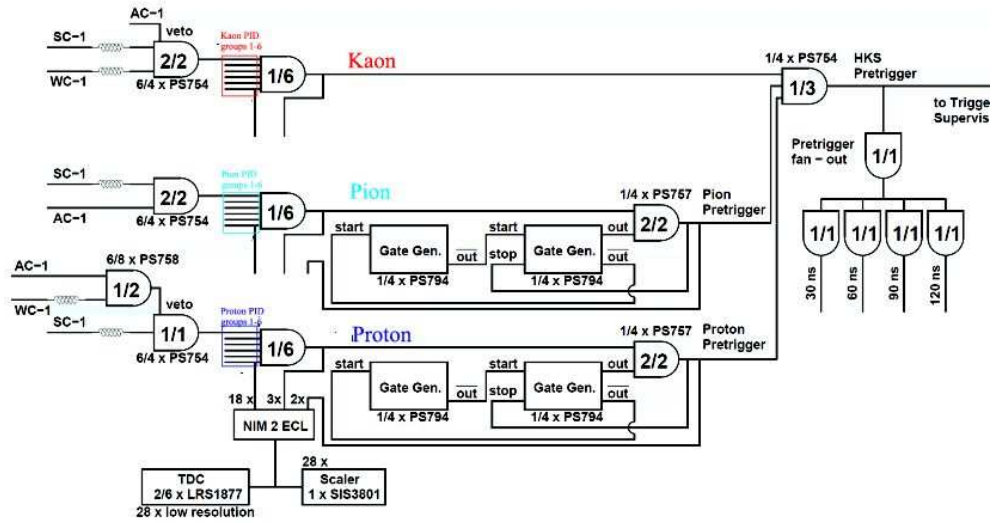
FIGURE 2.43: THE HKS TRIGGER LOGIC.

detectors as shown in the figure.

2.5.4   Data summary

Data taking for the E01-011 experiment took place in 2005 from June to October. In that period data was taken for 10 targets, as listed in Table 2.11. During the experiment, as conditions changed so did data trigger settings, as seen in Table 2.11. There were three important changes. First, introduction of grouped trigger from run 56283, data sets one, seven and eight used ungrouped trigger. Second, the HKS hodoscope layer HTOF1Y was part of the trigger from run 57729. Third, introduction of adder in WC signal (signals from both tubes of the WC segment were summed). Since Čerenkov detectors were the best tool for the reduction of proton and pion rates, their settings frequently changed during the experiment for rate and trigger control and study. Data summary for each target is shown in Table 2.12.

Target	Data Set	Beam Charge [mC]	Current Ave [μA]	Trigger ENGE⊗1X⊗2X⊗	Group.	Runs
CH$_2$	#1	149.99	1.44	WC(T⊕B)⊗$\overline{AC(T \otimes B)}$	OFF	55838-56163
	#2	246.24	1.38	WC(T⊗B)⊗$\overline{AC(T \oplus B)}$	ON	56283-57334
Li$_6$	#3	2543.6	21.0	1Y⊗WC(T⊕B)⊗$\overline{AC(T \otimes B)}$	ON	60623-61035
Li$_7$	#4	3764.6	25.2	1Y⊗WC(T⊕B)⊗$\overline{AC(T \otimes B)}$	ON	60235-61065
Be$_9$	#5	2267.2	17.9	WC(T⊗B)⊗$\overline{AC(T \oplus B)}$	ON	56476-57528
	#5	9.5	18.9	WC(T⊗B)⊗$\overline{AC(T \otimes B)}$	ON	57529-57538
	#5	6.8	17.2	WC(T⊕B)⊗$\overline{AC(T \otimes B)}$	ON	57542-57545
	#6	1311.8	18.0	1Y⊗WC(T⊕B)⊗$\overline{AC(T \otimes B)}$	ON	59316-59800
B$_{10}$	#7	3248.2	26.3	1Y⊗WC(T⊕B)⊗$\overline{AC(T \otimes B)}$	ON	60812-60961
C$_{12}$	#8	499.4	13.2	WC(T⊕B)⊗$\overline{AC(T \otimes B)}$	OFF	55911-56230
	#8	19.4	16.7	WC(T⊗B)⊗$\overline{AC(T \otimes B)}$	OFF	56229-56230
	#9	187.0	11.3	WC(T⊗B)⊗$\overline{AC(T \oplus B)}$	OFF	56231-56278
	#10	6046.5	22.9	WC(T⊗B)⊗$\overline{AC(T \oplus B)}$	ON	56355-57200
	#11	1130.7	19.6	WC(T⊗B)⊗$\overline{AC(T \otimes B)}$	ON	57547-57727
	#12	646.3	20.4	1Y⊗WC(T⊗B)⊗$\overline{AC(T \otimes B)}$	ON	57729-58409
	#13	6223.1	23.4	1Y⊗WC(T⊗B)⊗$\overline{AC(T \otimes B)}$	ON	58410-60561
Si$_{28}$	#14	2648.7	16.7	1Y⊗WC(T⊗B)⊗$\overline{AC(T \otimes B)}$	ON	57249-58394
	#15	8542.2	11.3	1Y⊗WC(T⊕B)⊗$\overline{AC(T \otimes B)}$	ON	58720-59869
	#16	2650.0	16.2	1Y⊗WC(T⊕B)⊗$\overline{AC(T \otimes B)}$	ON	59995-60756
V$_{51}$	#17	779.0	13.1	1Y⊗WC(T⊕B)⊗$\overline{AC(T \otimes B)}$	ON	60026-60418
Y$_{89}$	#18	585.7	10.8	1Y⊗WC(T⊕B)⊗$\overline{AC(T \otimes B)}$	ON	60063-60439
Pb$_{208}$	#19			1Y⊗WC(T⊕B)⊗$\overline{AC(T \otimes B)}$	ON	

TABLE 2.11: DATA ACQUISITION SETTINGS DURING THE E01-011 EXPERIMENT.

Target	Thickness [mg/cm^2]	Beam Charge [mC]	Note
CH$_2$	460	366.3	for mass calibration
Li$_6$	164	2545.1	production
Li$_7$	189	3828.7	production
Be$_9$	188	3657.8	production
B$_{10}$	114	3249.1	production
C$_{12}$	100	14940.8	for mass calibration and production
Si$_{28}$	65	13859.8	production
V$_{51}$	59.6	779.0	for QF rate study
Y$_{89}$	56	585.7	
Pb$_{208}$	283		

TABLE 2.12: THE E01-011 TARGET DATA SUMMARY.

Chapter 3

DETECTOR CALIBRATION AND PERFORMANCE

3.1 Overview

The raw data file, produced by CODA, contains the information read out from detector (end-front) electronics when trigger (event) is accepted. Each raw file contains one thousand pedestal events, settings of the accelerator magnets and monitors, scalers and detector ADCs and TDCs. The raw information, TDC, ADC and scalers are decoded and analyzed and then turned into physics observables by the reconstruction program. The reconstruction program was also used during the E01-011 data taking to oversee detector performances on the run by run basis in order to identify possible problems on time.

The E01-011 analysis software was a modified version of Hall C analysis software ENGINE [93] [3] [110] [92] consisting of four basic parts: initialization package, HKS reconstruction, ENGE reconstruction and coincidence part. The modifications made for the electron side, the ENGE arm, were significant because of the introduction of the Honeycomb drift chamber in the Enge detector package. Hodoscopes setup was similar to the one in the HNSS. The Honeycomb drift chamber, not used in HNSS, was a completely

new detector and so the code needed to be written for them. For the HKS drift chamber except for parameter files change, the number of wires and the active area were different from SOS drift chambers, tracking code itself had to be changed. The original tracking code could not properly handle high rates and multiplicity issues in each event caused by high rates seen by drift chambers, up to 10MHz, much higher than in previous experiments. The HKS TOF system had three planes of hodoscopes (1X1Y2X), instead of SOS four (1X1Y2X2Y), and therefore part of the code involving 2Y was removed from the SOS software. The SOS AC code was modified to include the three planes and the segmentation of the detectors. The HKS WC code was written from the SOS Lucite Čerenkov code.

3.2   Event Reconstruction

The E01-011 ENGINE event reconstruction procedures are shown in Fig.3.1 flow chart. The first step is the initialization of the parameters such as input and output file names, detector maps, kinematics parameters, detector positions; TDC and ADC windows, conversions, templates, histograms, ntuples... The file parameters are set by the REPLAY.PARM and detector information and signal processing parameters by the e01011.database file. The raw data file is opened and detector variables for the red event are filled according to the detector map file. With the detector variables filled, physical analysis starts. In each run the first one thousand events are pedestals used in the ADC reconstruction.

First, hodoscope timing information is extracted because this information is used in determination of drift chamber start time used in tracking for calculation of drift time values. To obtain accurate timing information the hodoscope raw TDC values undergo pulse height correction, correction for time offset caused by cable delays and light propagation inside the scintillator. Start time, the time at which a particle passes the focal plane, is calculated from the corrected hodoscope timing that undergoes additional path length correction since particle travel a certain time from focal plane to hodoscope.
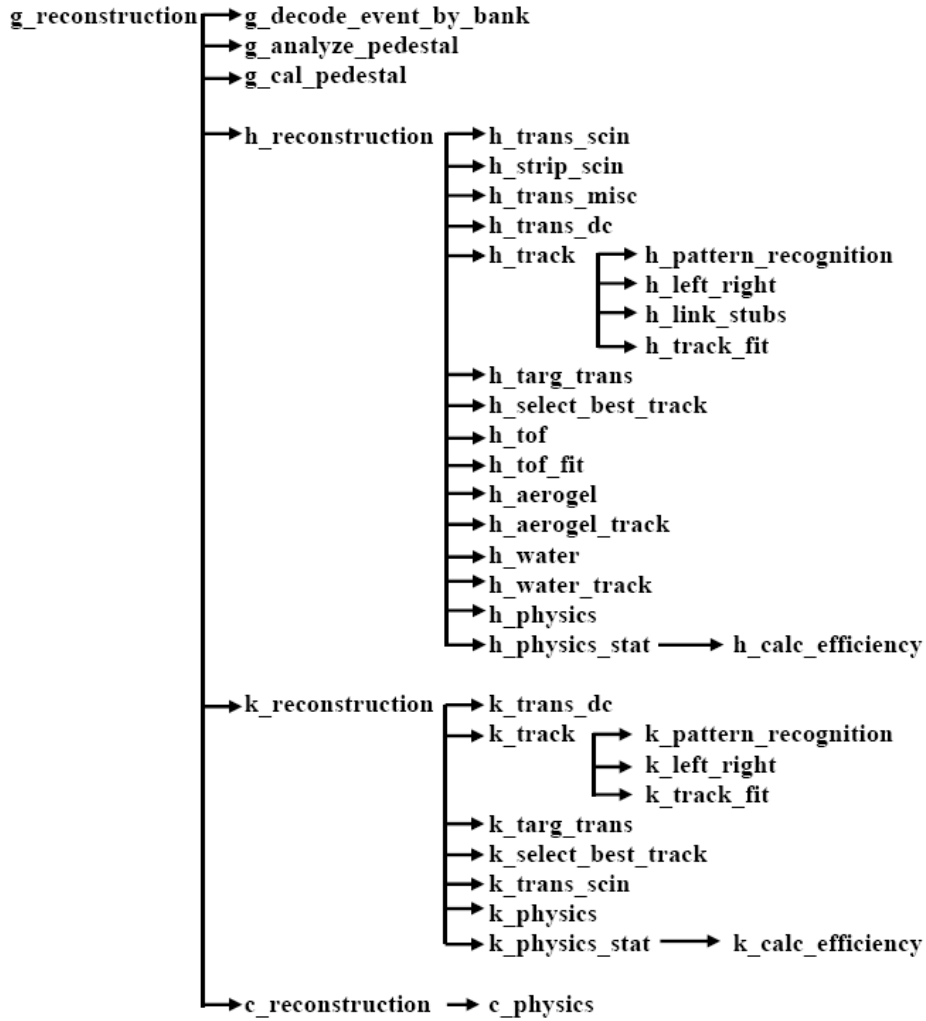
FIGURE 3.1: EVENT RECONSTRUCTION FLOW CHART. THESE ARE THE NAMES OF THE PROCEDURES IN ORDER OF EXECUTION. THE INITIAL LETTERS REFER TO DIFFERENT PARTS OF THE EXPERIMENT: G FOR GENERAL, H FOR HKS, K FOR ENGE, AND C FOR COINCIDENCE.

Without tracking information, it is assumed that all particles have the same momentum and that their trajectories follow the central ray. Start time, calculated at this stage, represents an average value of all hodoscope hits, within a predefined window of 60ns to reduce random hits. For high rates, start time obtained at this stage is (usually) not a correct value because on average each hodoscope layer has more than one hodoscope hit.

Furthermore, drift chamber information is decoded and drift time calculated from the decoded DC time and hodoscope start time. The drift time is converted into drift distance by drift time-to-drift distance map. While Enge part of the code is done, before going to drift chamber tracking code, HKS code still has to decode Čerenkov detectors, Aerogel and Water, and calculate track independent quantities.

Once tracks are formed all track dependent quantities, such as focal plane time, time of flight β_{ToF} and Čerenkov detectors on track are calculated. Finally, coincidence physics is calculated and all histograms and NTUPLES are filled.

3.2.1   Tracking

The purpose of drift chambers, EDC for electrons and HDC for kaons, is to determine particle trajectory through the spectrometers to reconstruct target quantities (momentum and angles). Every track can be uniquely reconstructed from focal plane coordinates X, Y and the tangents of the in-plane and out-of-plane angles XP, and YP which are reconstructed by tracking code from drift chamber information. Since EDC and HDC are two different types of drift chambers they have separate and different tracking codes.

HDC tracking

With the wire number and drift distance information from each plane of the two HKS drift chambers, particle trajectory can be calculated by the tracking algorithm working with the assumption that particle trajectories are perpendicular to the drift chamber planes and have a small angle spreading in

the focal plane [17]. In HKS, for most particles and for all kaons of interest, the angle spreading in the bending direction was within $\pm 14°$ and in the out-of-plane direction within $\pm 2°$, see Fig.3.18. Quantities determined by tracking algorithm are position and direction of a particle at the focal plane: $(x_f.x'_f, y_f.y'_f)$ and their typical distributions are shown in Fig.3.18.

Tracking algorithm can be decomposed into following fundamental steps:

- pairs - each two non-parallel wires form a pair with their intersection giving x and y coordinate. Only wire information is used.

- combinations - pairs are assigned to the same combination if the squared distance between intersections are less than space point criterion

- space point - combinations are assigned to the same space point if the squared distance between combinations is less than space point criterion. More than two combinations can be in the space point.

- stub - track obtained by fitting space point hits from only one chamber. Drift distance used and accompanying left-right ambiguity is solved: by requiring the hit point to be located between the two wire centers if both primed and unprimed planes fire or in the case of one of the two planes missing a track with the best χ^2 is chosen.

- trajectory - stubs from two chambers are combined into tracks if the difference of their focal plane parameters is less than the test criterion and trajectory hits are formed from space point hits of the two stubs.

Finally, tracks are fitted from all the space points by minimizing χ^2 and the track with the lowest χ^2 is chosen as the true track. For a detailed overview of the tracking algorithm see [17].

With the high rates seen in the E01-001 experiment the code was changed to deal with the fact that space point usually had more than optimal six wire hits, one wire per plane, and that multiple hodoscopes that were not on the track had a good TDC hit which resulted in wrong start time calculation. Although wrong start time effect is up to few tenths of nanoseconds, this effect in momentum reconstruction can be up to 300 keV.

Wrong start time was resolved by going through the tracking code twice, once with the initial start time and the second time with start time obtained only from hodoscopes that were on the track obtained after the first loop. Multiple same plane hits in the space point issue were solved by creating all possible combinations, especially those that can resolve the left-right ambiguity, and choosing the one that produced the track with the smallest χ^2.

3.2.2   Hodoscope timing measurement

Both, Enge and HKS detector package consist of time of flight hodoscope layers used on both sides with the same purpose, online creation of triggers and offline as a part of particle identification and target quantity reconstruction. Apart from the mentioned start time information obtained from hodoscopes used in both Enge and HKS drift chambers, they have one more common purpose: they are used in focal plane time calculation. Focal plane time represents the time when particle passes the focal plane, the same definition as start time, and as such is used in the calculation of coincidence time between HKS and Enge particles.

There is one additional purpose of HKS hodoscopes: calculation of time of flight β, extremely useful PID tool. This is not important for Enge side since there are no other particles besides electrons present and in the momentum acceptance of Enge spectrometer β for all electrons can be set to one.

The time of flight β calculations follow tracking code which allows calculation of β for each track. For each track, only the hits that come from the scintillators that are on the track are used in calculation. Drift chamber tracks are projected on the hodoscope planes and from each plane only scintillator hits used are the ones coming from scintillators on the projected track. With the knowledge of hit position on the scintillator, intersection of the track and the scintillator, and the speed of the light in the scintillator, hodoscope TDCs were corrected for light propagation in the scintillator. Other corrections used were pulse height and cable delay correction. Since each hodoscope had two PMTs, one on both ends, after the corrections were done, the final time used for time of flight was the average time of both

PMTs. Now time of flight (ToF) was calculated, ToF - difference between time information obtained from hodoscopes from two different planes.

The time of flight β can be calculated from hodoscope time of flight and distance traveled by the particle between the two hodoscope planes. The distance is calculated from particle coordinates and angles at focal plane obtained from drift chamber code. ToF beta was used to select real electron events on the Enge side and on the HKS side as a part of particle identification tools, because β is directly related to particles mass, see Equation 3.1.

$$\beta = p/\sqrt{p^2 + m^2}. \tag{3.1}$$

3.2.3 Čerenkov detectors

The ADC signals from Aerogel and Water Čerenkov detectors were converted into a number of photoelectrons. With expected high rates Čerenkov detector planes, three Aerogel and two Water planes, were segmented to avoid accidental vetoes from pions and to have a better particle ID for multiple track events. Each aerogel segment had two PMTs so the final number of photoelectrons is the sum of the number of photoelectrons from both.

HDC tracks are now projected to Čerenkov detector planes and only signals from the segments traversed by the track are summed and later used in PID. The signals of the AC segments (or the WC planes) are summed. Then, they are sent to a discriminator whose threshold is set accordingly to a preset level which vetoes particles in the trigger (-31 mV for AC and -150 mV for WC). In the off-line analysis, the number of photoelectrons produced in the Čerenkov detectors is used to clean kaon events from pions and protons.

3.3 Detector Calibration

Detectors must be calibrated to give meaning and proper values to the physical quantities that are measured. These calibrations set the required manipulation of the output signals to translate them into physical parameters, e.g.,

a TDC channel into time or an ADC signal into number of photoelectrons. The detectors or the entire system (in the case of optics calibrations) are exposed to a known radiation or condition, independent of the experiment itself, and their output signals are analyzed to establish the procedure to treat the data. Calibration also refers to set the optimal conditions for the detectors, i.e. establish the operational voltages, thresholds, currents, etc., as well as corrections for hardware or cable delays.

3.3.1   Hodoscope Timing Calibration

With hodoscope timing information being used in the reconstruction of particle trajectories, coincidence time and part of particle identification (PID) (β_{ToF}) each hodoscope scintillator, both on Enge and HKS side, had to be calibrated carefully.

Calibration procedure involved the following steps:

- obtaining operational settings: PMT high voltage and discriminator threshold

- pulse height correction: time walk from pulse height variations relative to the fixed discriminator threshold, see Fig3.2

- traveling time - light propagation in scintillator; PMT signals were sent through long cables to Hall C counting house

Operational settings, plateau regions for both high voltage and discriminator voltage, were obtained by testing all the hodoscopes with cosmic rays or a radioactive source (e.g., ^{60}Co). For each voltage setting efficiency, defined as the ratio of hodoscope events and the number of triggers, was calculated. Typical plateau curves for both high voltage and discriminator threshold are shown in Fig.3.3

Final high voltage operating setting for individual PMTs was selected in plateau region with a requirement that all PMTs are gain matched within $\pm 10\%$. Gain matching was tested by putting ^{60}Co source in the middle of
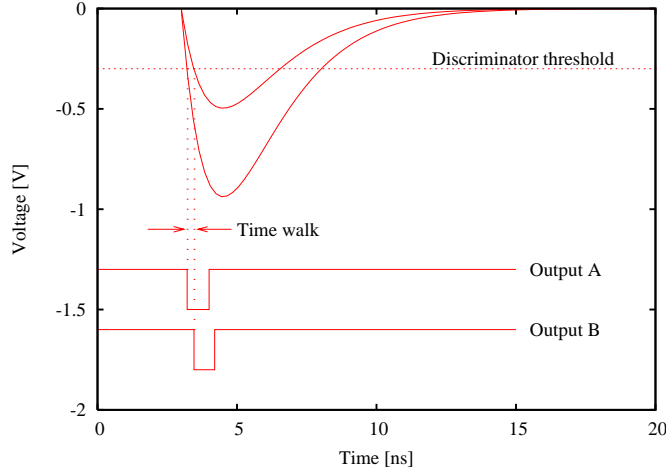
FIGURE 3.2: TIME WALK EFFECT ON RECORDED HODOSCOPE TDC DUE TO DIFFERENCE IN PULSE HEIGHT.

each scintillator and high voltage was being changed until ADC peak position was at designated setting. Discriminator threshold settings were changed in the plateu region during the experiment to balance high rates observed.

The time walk happens when signals with different pulse shape and height are discriminated with fixed discriminator threshold, as seen in Fig.3.2. The function used to correct the time walk effect caused by pulse height was:

$$\Delta t_{corrected} = t_{raw} + P_1 + \frac{P_2}{\sqrt{ADC - pedestal}} \qquad (3.2)$$

where ADC is the raw ADC from the corresponding scintillator PMT. Parameters P_1, P_2 were obtained for each PMT by fitting the equation to the calibration data.

Time offsets caused from signal propagation through cables and hardware were calibrated on Enge side by comparing the time with respect to the third scintillator in the back of the detector package. HKS hodoscope time walk correction and offset calibration was done by using shoe string algorithm, by comparing the time differences between 1X-1 to 2X-1, 2X-2 to 1X-1, etc. keeping the differences with respect to the time of counter 1X-6 (absolute reference).
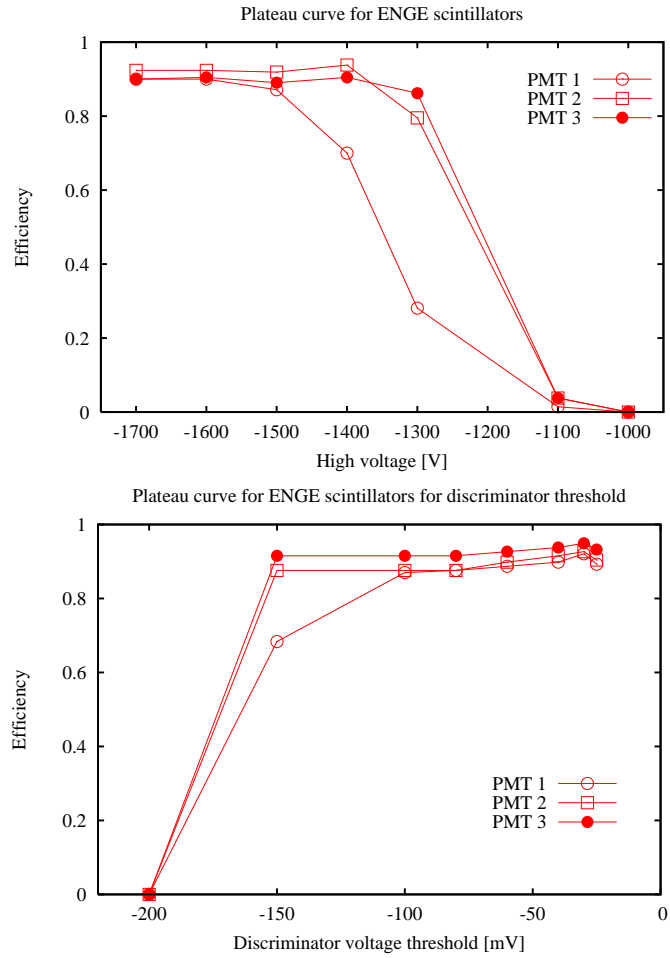
FIGURE 3.3: PLATEAU CURVES FOR ENGE HODOSCOPES. *Left* HIGH VOLTAGE PLATEAU CURVE. *Right* DISCRIMINATOR THRESHOLD PLATEAU CURVE.
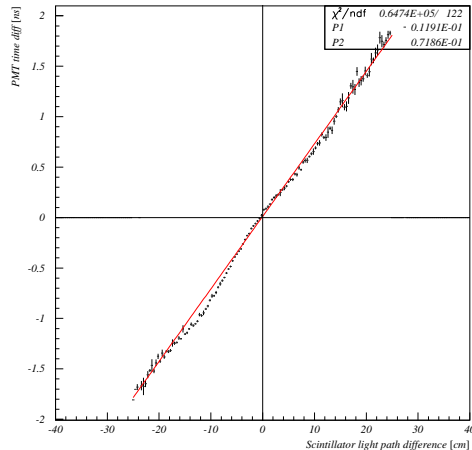
FIGURE 3.4: TYPICAL SCINTILLATOR CORRELATION OF PMT TIME DIFFERENCE
AND LIGHT PATH LENGTH DIFFERENCE, HTOF- LAYER 1X -TUBE 6.

Calibration of light propagation speed through scintillator detectors was
calibrated with tracking information used to determine the exact position
of the particle at scintillator detector. Since light produces signals in both
scintillator PMTs, their time difference is calculated as well as difference be-
tween paths of light from position of the particle at scintillator detector to
individual PMTs. Typical correlation between time and path length differ-
ence is shown in Fig.3.4 and by fitting this dependence with linear regression
light speed propagation is obtained.

Time walk parameters, scintillator light speed and delay offsets are re-
corded in parameter files and used by the ENGINE in timing reconstruction.
Time offsets tend to change when counting rates change significantly.

To have a valid calibration parameters particle velocity β needs to be
calculated from the momentum and known mass (and without TOF infor-
mation) of the particle, for this reason single type of particle is used in
calibration. Kaon events should be used to calibrate pulse height correc-
tion for kaons. Hodoscope calibration procedure uses tracking information,
scintillator positions and reconstructed β from momentum.

3.3.2   HKS drift chamber

Particle trajectories for the particles passing through the HKS detector package (mostly proton, pion and kaon) were obtained with the set of two drift chambers. Quantities determined were position and direction of a particle at the focal plane: $(x_f.x'_f, y_f.y'_f)$. If spectrometer system is well understood, focal plane variables are used to reconstruct momentum and angle of the particle at the target (dp, x'_t, y'_t). Detailed description of the target quantities reconstruction is in Section 4.4.

The information extracted from TDC information is drift time, time needed for drifting electron to arrive to sense wire from the point of ionization, see Fig.3.5.

The information needed to be extracted from drift time information is drift distance so that the exact position where particle went through the HDC plane can be calculated. To obtain a time-to-distance map two things are needed:

- First, for each plane the start time offset of drift time needed to be set so that the front edge of the drift time distribution is at zero.

- Second, drift distance distribution should be uniform in the cell range, as shown in Fig.3.6, if the chamber is uniformly illuminated and has constant drift velocity.

The second point holds for HDCs since HDC is a plane-type drift chamber and thus its electrical field distribution should be symmetrical and totally uniform. With these two requirements the time-to-distance map is obtained with:

$$D(T) = D_{max} \frac{\int_{t_{min}}^{T} F(\tau)d\tau}{\int_{t_{min}}^{t_{max}} F(\tau)d\tau}, \tag{3.3}$$

D - drift distance, D_{max} - maximum drift distance (size of half drift cell- 0.5 cm), T - drift time, $F(\tau)$ - drift time distribution and the inter-
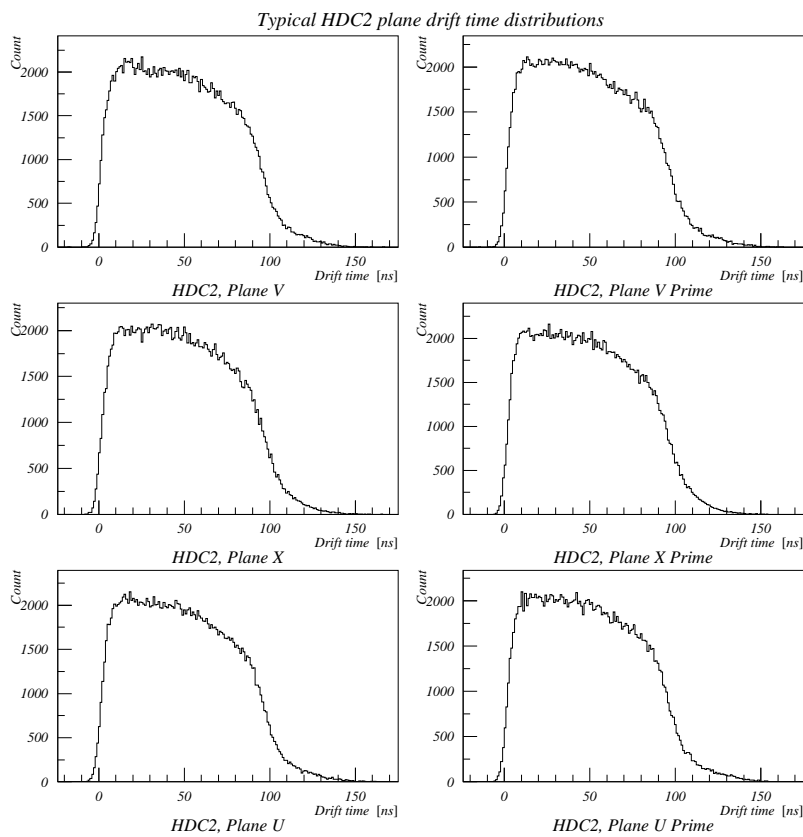
FIGURE 3.5: TYPICAL HDC DRIFT TIME DISTRIBUTION FROM THE CH$_2$ DATA. DRIFT TIME WAS USED IN TIME-TO-DISTANCE MAP CALIBRATION.
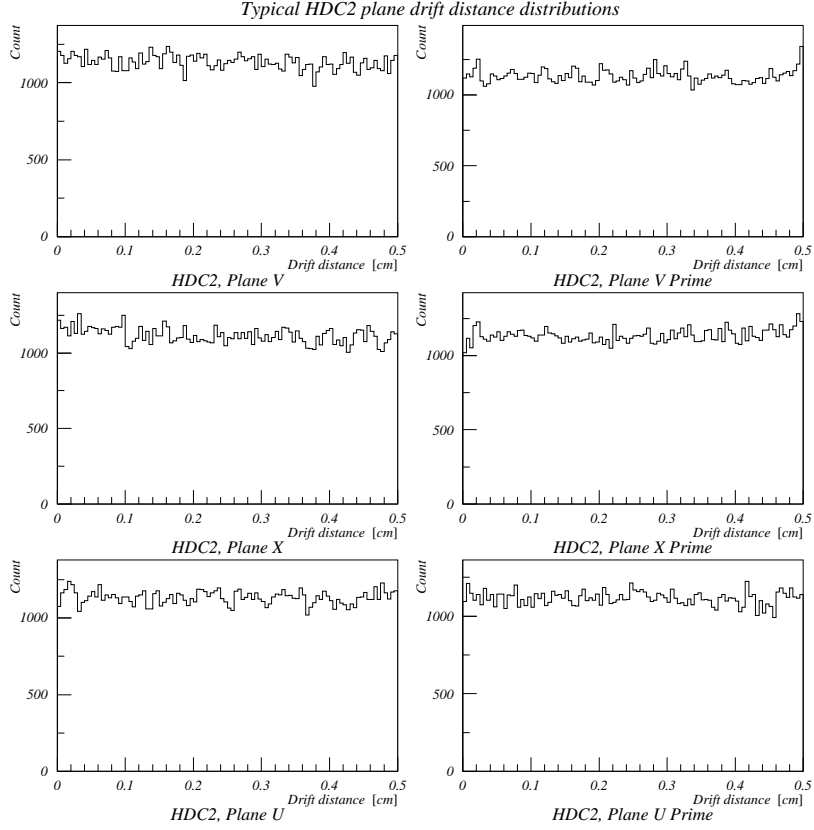
FIGURE 3.6: TYPICAL HDC DRIFT DISTANCE DISTRIBUTION AFTER THE CALI-
BRATION OF TIME-TO-DISTANCE MAP.

val $[t_{min}, t_{max}]$ is selected to reject noise hits. With time-to-distance map,
the obtained correlation of drift distance and drift time is shown in Fig. 3.7.

3.3.3   Enge drift chamber

As in the case of HDC, the EDC calibration procedure involves obtaining
start time offsets and time-to-distance map as well. Since EDC is honeycomb
and HDC is a plane type of drift chamber the procedures to obtain time-to-
distance maps are different. Because EDC has a honeycomb cell structure
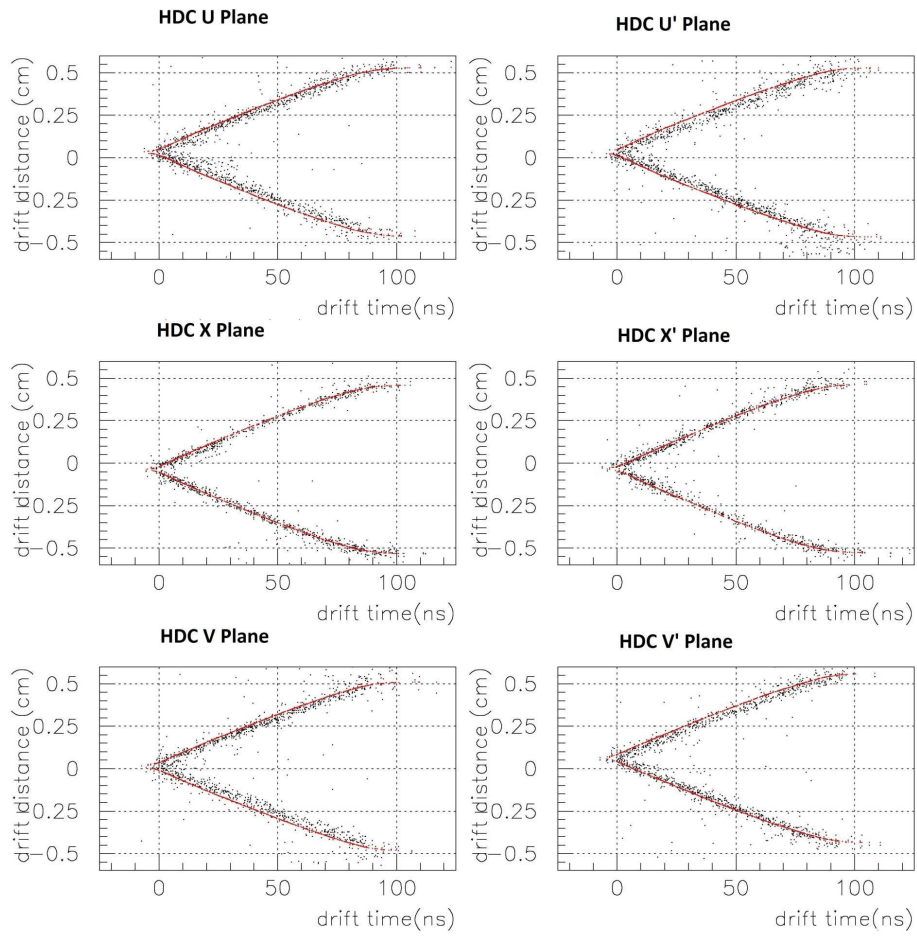
FIGURE 3.7: CORRELATION BETWEEN DRIFT DISTANCE AND DRIFT TIME. DATA WAS FITTED BY SECOND ORDER POLINOM.
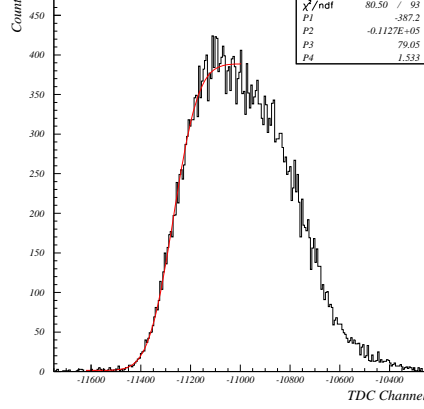
FIGURE 3.8: TYPICAL EDC DRIFT TIME DISTRIBUTION FROM CH$_2$ DATA. DRIFT TIME WAS USED IN TIME-TO-DISTANCE MAP CALIBRATION.

the electrical field distribution should be symmetrical but not uniform (we can say it is close to uniform but not totally uniform) so uniformity of drift distance can not be used in calibration.

Start time offsets are obtained by fitting TDC distribution from EDC wires with signal that belong to a track with:

$$N(x) = A - B * Freq(\frac{x - C}{D}) \qquad (3.4)$$

as shown in Fig.3.8. Time offset value corresponds to parameter C of the fitting function.

Time-to-distance map is obtained in an iterative procedure involving EDC tracking algorithm. Although EDC does not have a uniform field, the initial time-to-distance map can be obtained by the HDC calibration procedure. This map is now used in tracking algorithm for the calculation of drift distance in order to obtain particle trajectories. They are then projected on each EDC plane and new ('real') drift distances are calculated. New map is then created by fitting dependence of this trajectory based drift distance on drift time with the third order polynomial. Typical dependence of drift distance on drift time for EDC is shown in Fig.3.9
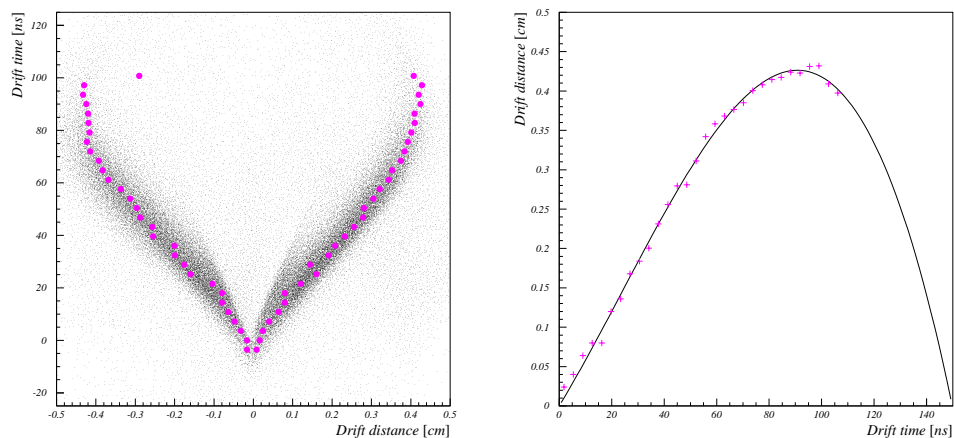
FIGURE 3.9: TYPICAL EDC DRIFT DISTANCE-DRIFT TIME DEPENDENCE. *Left* OBTAINING POINTS FOR MAP CALIBRATION. *Right* FITTING OF THE THIRD ORDER POLYNOMIAL.

3.3.4   Čerenkov detectors

Water Čerenkov detector was an intricate part of the HKS pretrigger and particle identification tool in the offline analysis, as discussed in Section 2.5.2. For the offline analysis the ADCs from Čerenkov counters were converted into number of photoelectrons.

TABLE 3.1: TIME RESOLUTIONS (σ) OF THE HKS HODOSCOPE PLANES.

Plane	HTOF1X	HTOF1Y	HTOF2X
Time Resolution σ (ns)	0.125	0.284	0.163

3.4 Detector performance

With the data taking period of the experiment E01-011 of full two months, involving data taking on ten different targets and numerous beam currents and high magnet fringe fields, detectors showed changes in their properties. Some of the issues that had to be dealt with, during data taking and/or data analysis were:

- ToF hodoscope, HDC and EDC rate dependence.

- Aerogel Čerenkov: HKS dipole fringe field effect on AC PMTs.

- Water Čerenkov: decay of wavelength shifter properties.

These issues had either a direct influence on data taking or data analysis (PID, kaon survival, detector efficiencies..) and here, to some length, we will discuss/explain their cause and show how they were solved.

3.4.1 Hodoscopes

Hodoscope timing information is used for calculation of particle speed, time of flight β (β_{ToF}), (as well as start time for drift chambers and coincidence time calculation) which is then used in kaon PID, it is important to have a good time resolution. Typical time resolution of HKS hodoscope planes (time resolution of a hodoscope plane is the average of all its elements) is shown in Fig.3.10. Time resolutions of each HTOF plane are listed in Table 3.1.
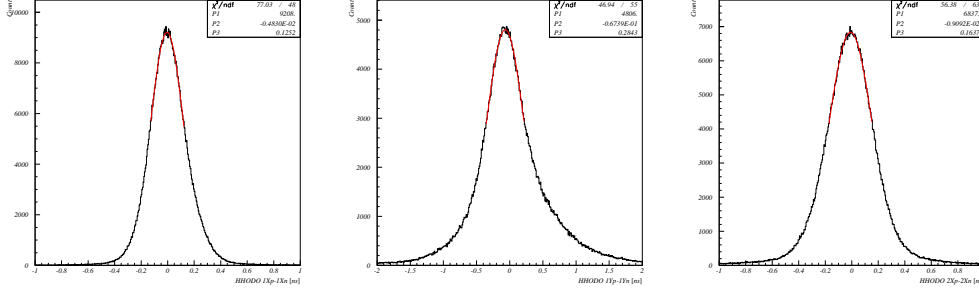
FIGURE 3.10: TYPICAL TIME RESOLUTION OF HKS HODOSCOPE PLANE.
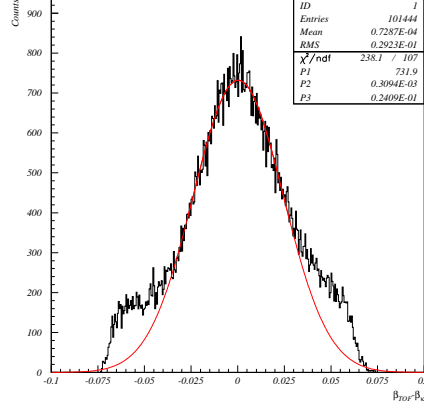
FIGURE 3.11: HKS KAON $\Delta\beta = \beta_{TOF} - \beta_K$ DISTRIBUTION FOR THE CH$_2$ DATA.

Particle velocity (TOF β) calculation depends on HTOF calibration para-
meters and if these calibration were done properly then the difference between
TOF β_{ToF} and β_K (β_K is the β calculated by assuming kaon mass and using
the known momentum from tracking, see Eqn 3.1), $\Delta\beta = \beta_{TOF} - \beta_K$, will
be a momentum independent Gaussian centered at zero.

In the HKS experiment $\Delta\beta$ resolution (σ) for kaon particle was $\sigma =$
0.0241, as shown in Fig. 3.11. In obtaining this plot kaon PID cuts (Aerogel
and Water Čerenekov cuts, $\Delta\beta$) were applied, detailed discussion on PID
cuts is in Section 4.2. This distribution is not a perfect Gaussian because of
some residue of protons and pions on the edges.
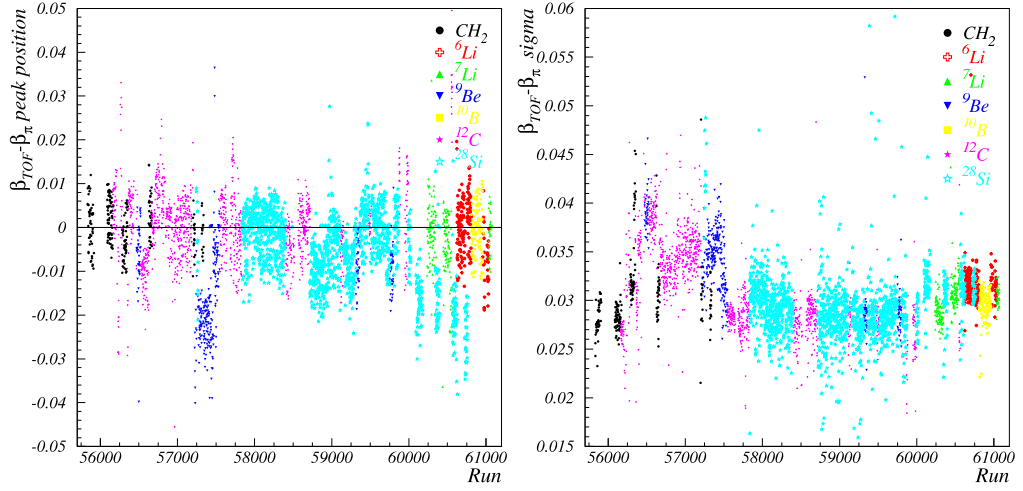
FIGURE 3.12: *Left* $\Delta\beta_\Pi$ PEAK CENTER VALUE AS A FUNCTION OF RUN NUMBER. *Right* $\Delta\beta_\Pi$ RESOLUTION (GAUSS σ) AS A FUNCTION OF RUN NUMBER.

In data analysis it was noticed that even on the run to run basis there are offsets $\Delta\beta_\Pi$ peak center (correspond to Mean of a Gaussian fit) and fluctuations in resolution (Gauss σ), as shown in Fig.3.12. This effect is also seen in $\Delta\beta_K$ but due to a much smaller number of kaons in each run it can not be represented/ (corrected) on run to run basis. There are three likely and connected reasons for this effect. First, fluctuation of beam from run to run (and even in the same run) which effects pedestal levels of HTOF ADCs and introduces offsets in timing calculation. Second, first 1000 triggers were used for pedestal calculation in each run and with a higher number of pedestal triggers more stable pedestal would be achieved. Third, pileup effects in HTOF ADCs connected with higher currents which also effect pulse height correction of the TDC signal.

3.4.2   ENGE drift chambers

The information obtained from EDC are electron particle trajectories represented in the form of the so called focal plane quantities: X, X_p, Y, Y_p. Focal plane represents an imaginary plane in the middle of EDC. Typical distributions of the EDC focal plane variables are shown in Fig.3.13.
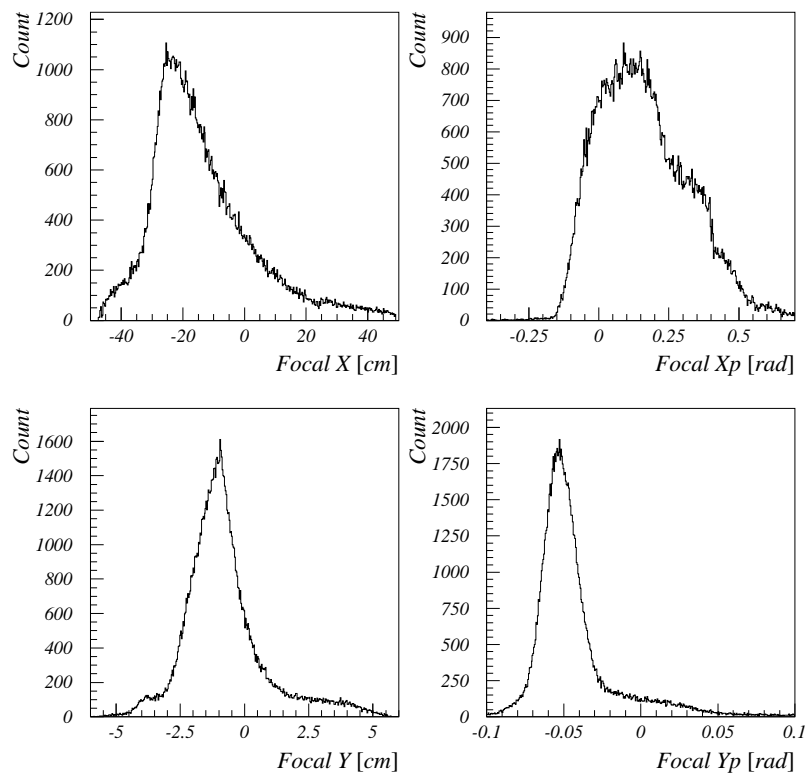
FIGURE 3.13: TYPICAL DISTRIBUTION OF EDC FOCAL PLANE QUANTITIES FOR CH_2 TARGET. *Top Left* FOCAL PLANE X POSITION. *Top Right* FOCAL PLANE X' POSITION.*Bottom Left* FOCAL PLANE Y POSITION.*Bottom Right* FOCAL PLANE Y' POSITION.
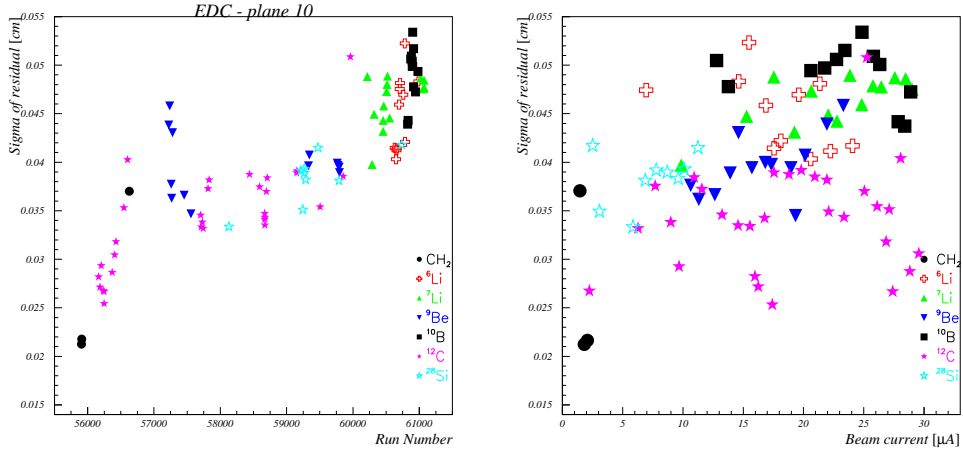
FIGURE 3.14: *Left* EDC RESIDUAL DISTRIBUTION FOR USED TARGETS DURING THE DATA TAKING PERIOD. *Right* EDC RESIDUAL DISTRIBUTION FOR USED TARGETS AND BEAM CURRENTS.

Residual, the difference between measured plane coordinate and the coordinate obtained by tracking code, distribution gives plane resolution of drift chamber. The expected resolution, Gauss σ of the residual, was 300 μ. This spatial resolution of Enge drift chamber directly influences the resolution of target quantities through dependence on focal plane variables. The expected spatial resolution is worse than one expects in EDCs because of higher rates seen by EDC and a more compact design (separation between in the first and the last plane is much smaller than in the case of HDC). Shape of Residual and Chi2 distributions for both Enge and HKS drift chambers, EDC and HDC, are similar and for HDC are represented in Fig.3.19.

As shown in Fig.3.14, for most of the data taking period the expected resolution was achieved. At the last stage of the data taking resolution of EDC worsened to 550μm. This effect might be the result of a two month exposure of EDC and EHODO to radiation.

EDC Chi2 distribution is not uniform across Enge focal plane, as it is clearly seen from Fig.3.15 where Chi2 distribution- Mean, RMS and peak position, are plotted as function of Enge focal X. Lower momentum side,
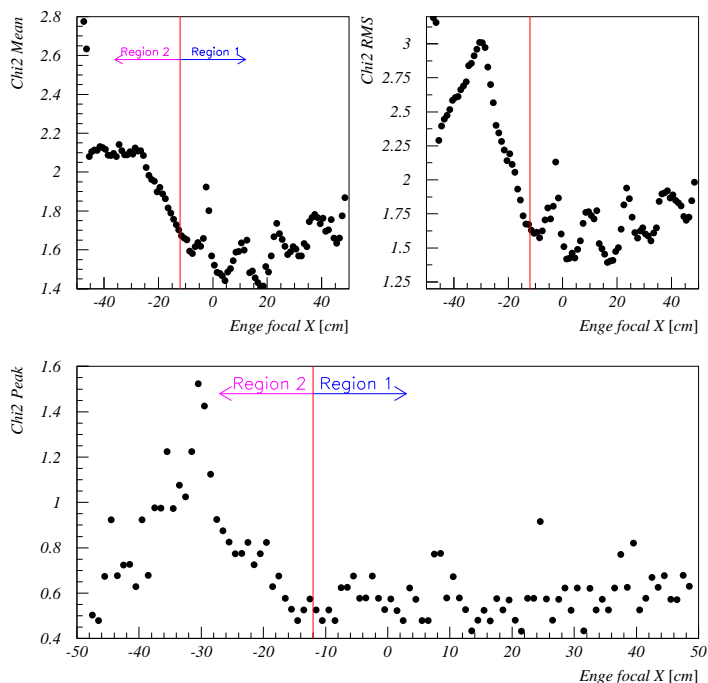
FIGURE 3.15: EDC CHI2 DISTRIBUTION. *Top Left* CHI2 MEAN OVER ENGE
FOCAL PLANE. *Top Right* CHI2 ROOT MEAN SQUARE (RMS) OVER ENGE FOCAL
PLANE. *Bottom* CHI2 PEAK POSITION OVER ENGE FOCAL PLANE.

corresponding to negative focal X, was subjected to higher rates resulting
in worse EDC track reconstruction directly seen in track Chi2. This off
course, through reconstruction of target quantities from focal plane variables,
influences resolution of hypernuclear states. With production data, from CH_2
and ^{12}C targets, being included in the calibration of optics lower momentum
side would influence resolution of high momentum side that intrinsically has
better track resolution. To avoid this effect, the data was divided into two
sets (regions) as shown in Fig.3.15 and the calibration of optics was done
separately for each of these regions. Detailed discussion on the calibration of
optics is in Sec.4.4.

EDC Tracking efficiency

Tracking efficiency, defined as the ratio of the number of the reconstructed
particle trajectories by drift chamber and the number of passing particles, is
an important factor describing performance of drift chambers (as well as the
spatial resolution discussed in previous section). The number of total pass-
ing particles is assessed by using Enge hodoscopes. By noting that there is
a clear correlation between EHODO1X and EHODO2X for trackable events,
as shown in Fig.3.16, total number of passing particles (trajectories, tracking
candidate) is obtained by counting EHODO1X-EHODO2X counter combi-
nations that satisfy:

- $0 =< (CounterID(Ehodo1X) - CounterID(Ehodo2X)) <= 1$

- $abs(Ehodo1XTime - Ehodo2XTime) < 1ns$

- counters surrounding EHODO1X and EHODO2X counters did not pro-
  duce a signal.

With these three conditions satisfied, over counting in the number of
trajectories is avoided.

From total number of tracking candidates we need to calculate the number
of those that are found by EDC. This is done by projecting EDC obtained
tracks on hodoscope planes and checking if selected EHODO1X-EHODO2X
counter combination is on EDC track. Finally the EDC tracking efficiency
is calculated by this expression:

$$EDC\ tracking\ efficiency = \frac{Ehodo1X \otimes Ehodo2X \otimes EDCtrackON}{Ehodo1X \otimes Ehodo2X}$$

(3.5)

The results of the EDC tracking efficiency study are shown in Fig.3.17
which shows overall tracking efficiency for all targets used during the data
taking period. In the evaluation of the tracking efficiency very loose cuts on
EDC track Chi2 were set. The dependence of the EDC tracking efficiency
on Chi2 cut condition is studied in Section 4.7.3.
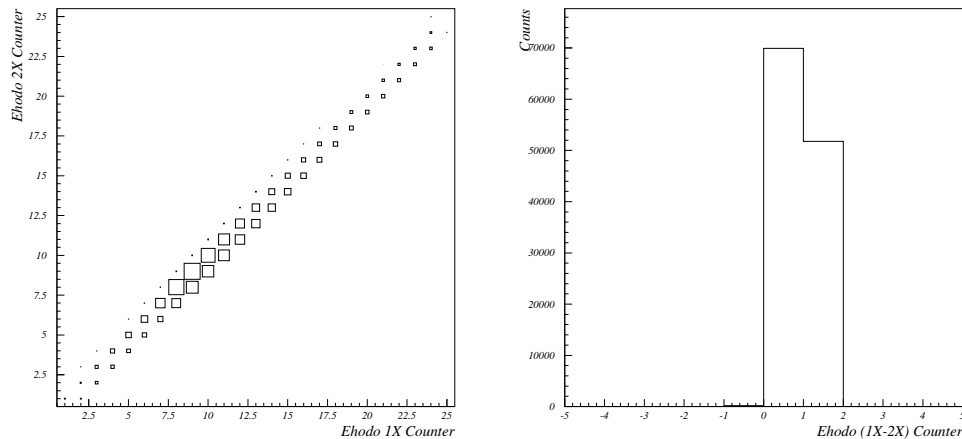
FIGURE 3.16: ENGE HODOSCOPE EHODO1X AND EHODO2X COUNTER NUM-
BER CORRELATION FOR EDC TRACKABLE EVENTS.

3.4.3 HKS drift chambers

As in the case of EDC, the information obtained from HDC are particle
trajectories (in HKS case: kaon, pion, proton, positron) represented in the
form of the so called focal plane quantities: X_f, X_{fp}, Y_f, Y_{fp}. Focal plane
represent an imaginary plane positioned in the middle of the two HKS drift
chambers. Typical distributions of the HDC focal plane variables are shown
in Fig.3.18.

Position resolution of the HDCs, averaged per plane, is given in terms of
the HDC residual, the difference between the measured coordinate and the
one obtained by tracking code. Typical residual distribution and tracking
χ^2 per degree-of-freedom are shown in Fig.3.19 and HDC residual distribu-
tion for used targets and beam currents in Fig.3.21. Typical values of the
residual Gaussian fit for each HDC plane are shown in Fig.3.20. It follows
that alignment of individual planes and residual offsets between the planes in
the parameter files were done correctly since Gaussians are centered around
zero. Also, it shows that HDC1 planes had a bit worse resolution and this
is because they suffered higher background rates. During the E01-011 expe-
riment, the performance of HKS drift chambers and their tracking residues,
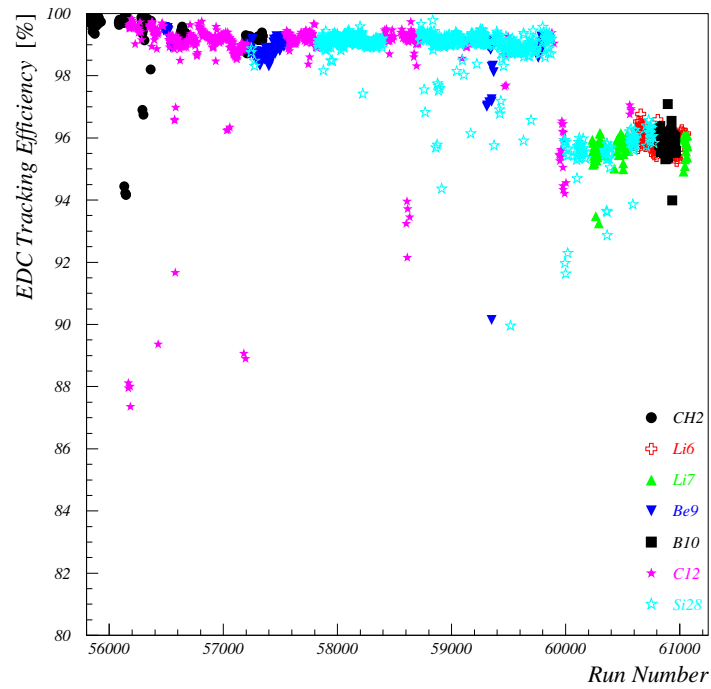
FIGURE 3.17: TRACKING EFFICIENCY OF ENGE DRIFT CHAMBER FOR TARGETS USED DURING THE DATA TAKING PERIOD. ALL TRACKS WITH CHI2 PER D.O.F (DEGREE OF FREEDOM) LESS THAN 750 WERE USED IN THE EFFICIENCY CALCULATION.
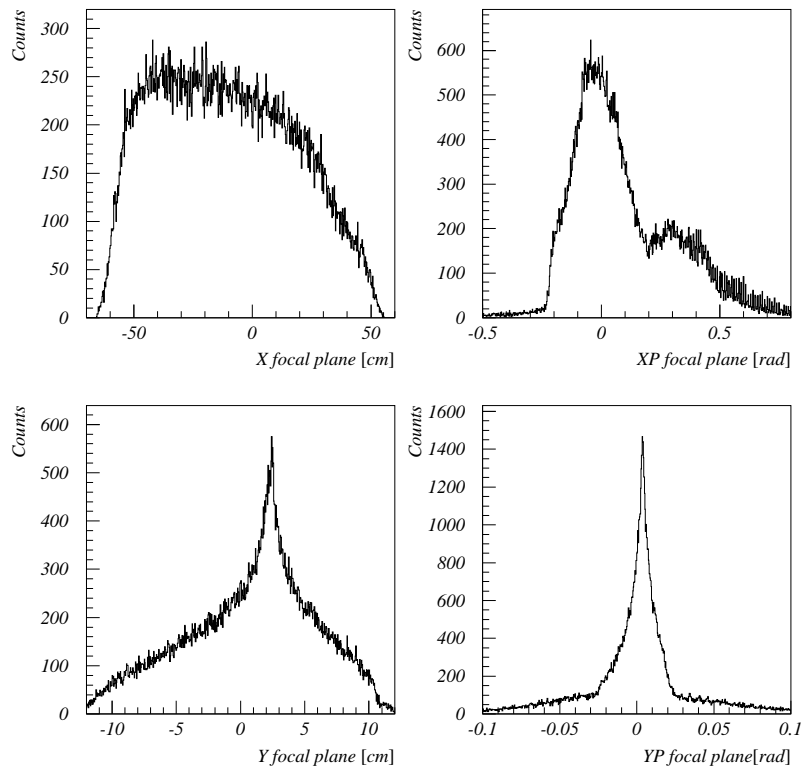
FIGURE 3.18: TYPICAL DISTRIBUTION OF HDC FOCAL PLANE QUANTITIES FOR UNBIASED EVENTS OF ^{12}C TARGET. *Top Left* FOCAL PLANE X POSITION. *Top Right* FOCAL PLANE X' POSITION. *Bottom Left* FOCAL PLANE Y POSITION. *Bottom Right* FOCAL PLANE Y' POSITION.
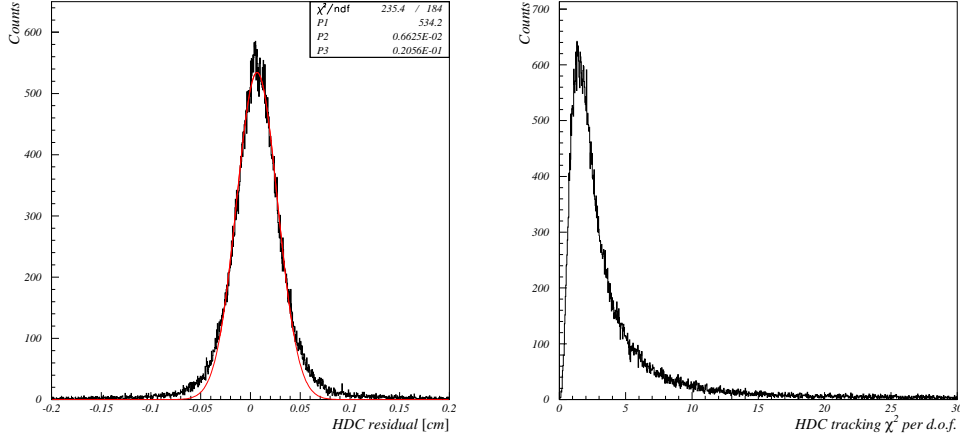
FIGURE 3.19: TYPICAL DISTRIBUTION OF HDC TRACKING. *Left* HDC RESID-
UAL: THE DIFFERENCE BETWEEN MEASURED COORDINATE AND THE ONE OB-
TAINED BY TRACKING CODE. *Right* CHI2 DISTRIBUTION PER DEGREE OF FREE-
DOM (D.O.F) FOR THE HDC TRACKS.

for all chamber planes, were at the expected level of 0.02 cm in σ and that
alignment (combination of hardware and parameter setting) of the chambers
was done properly, as seen on the right plot of Fig.3.20.

Fig.3.21 shows dependence of plane resolution (sigma value of the residual
Gaussian fit) of the two HDC planes for targets used as a function of beam
current. For individual target there is no current dependence of HDC plane
resolution. For ^{6}Li,^{7}Li and ^{10}B targets, plane resolution was a bit worse
probably due to long detector exposure to radiation since data on these
targets was taken at the end of the data taking period with the highest
possible particle rates.

Fig.3.22 shows properties of track Chi2 distribution across HKS focal
plane such as peak position (*Bottom*), RMS (*Top Right*) and Mean(*Top Left*).
The best Chi2 achieved (the lowest RMS, Mean) was centered around the
central trajectory. All three Chi2 variables :peak position, RMS and Mean
were consistent (relatively) across HKS focal plane except on the boundary
regions probably due to higher rates.
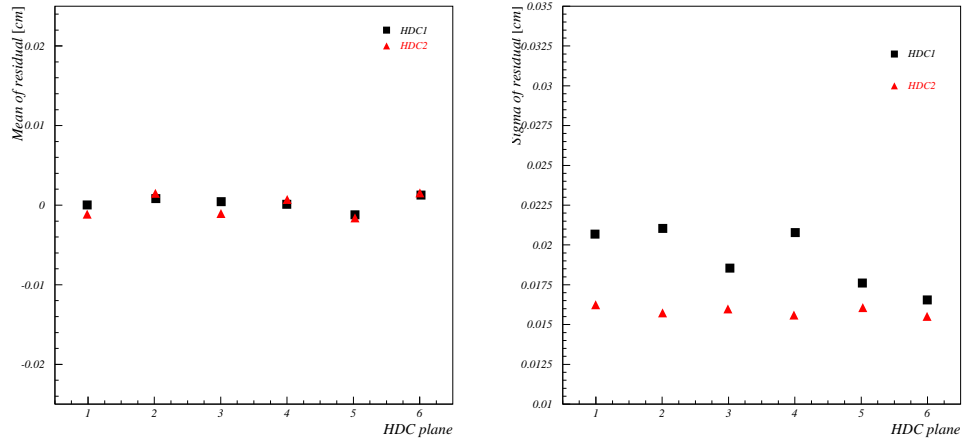
FIGURE 3.20: TYPICAL PLANE DEPENDENCE OF THE HDC RESIDUAL FOR CH_2 TARGET. *Left* MEAN VALUE OF THE RESIDUAL GAUSSIAN FIT. *Right* SIGMA VALUE OF THE RESIDUAL GAUSSIAN FIT.
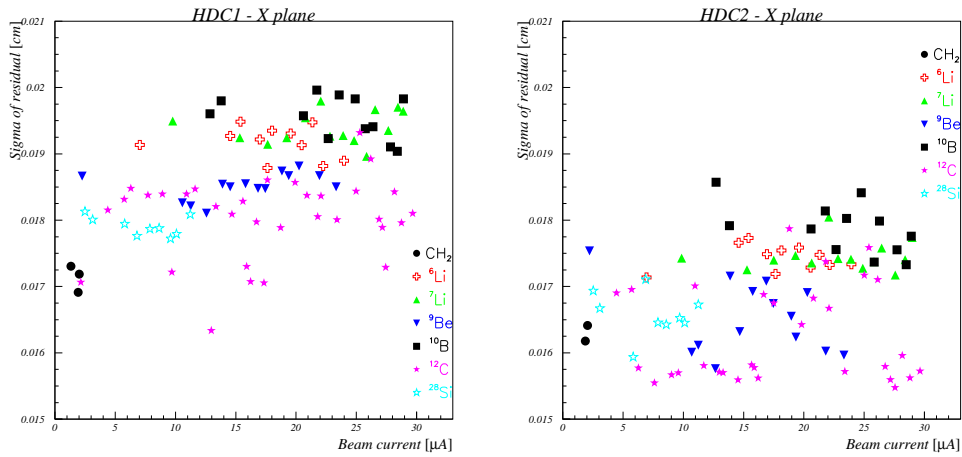
FIGURE 3.21: HDC RESIDUAL DISTRIBUTION FOR USED TARGETS AND BEAM CURRENTS. SIGMA VALUE OF THE RESIDUAL GAUSSIAN FIT.
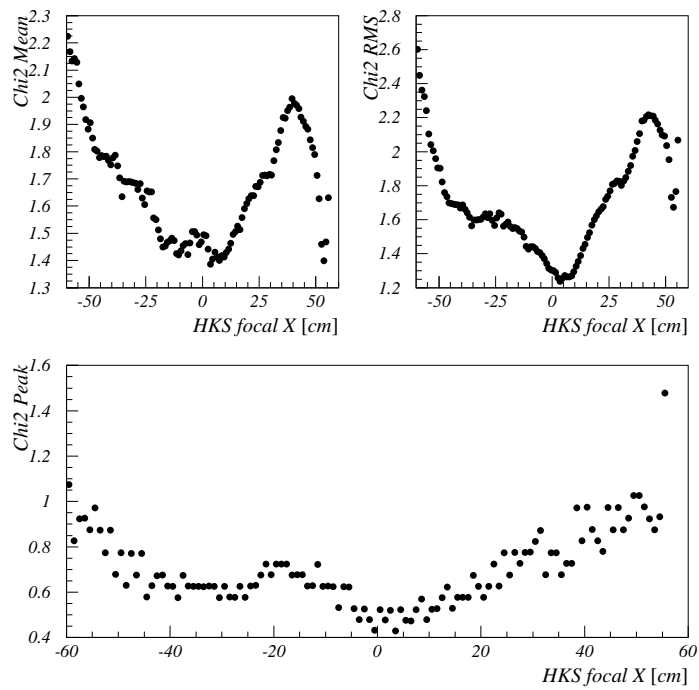
FIGURE 3.22: HDC CHI2 DISTRIBUTION. *Top Left* CHI2 MEAN OVER THE HDC FOCAL PLANE. *Top Right* CHI2 ROOT MEAN SQUARE (RMS) OVER THE HDC FOCAL PLANE. *Bottom* CHI2 PEAK POSITION OVER THE HDC FOCAL PLANE.
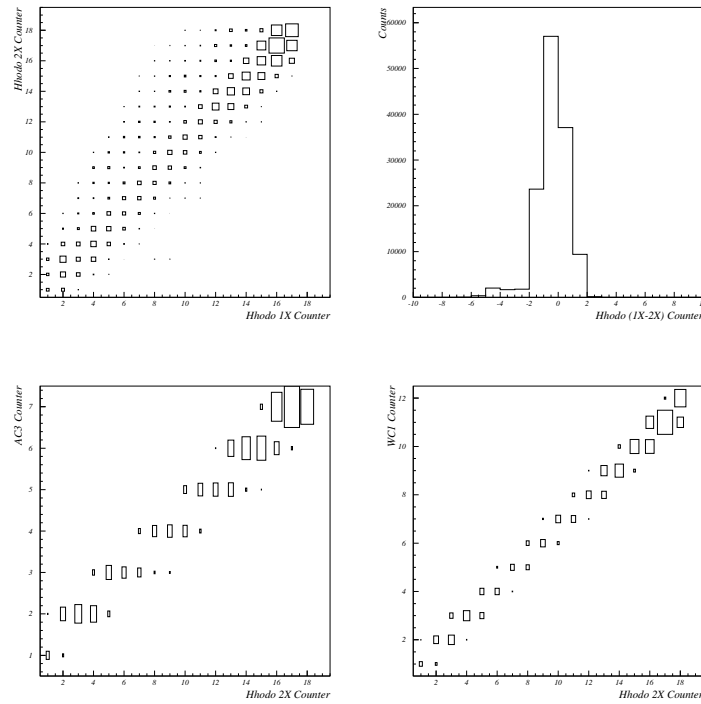
FIGURE 3.23: CORRELATION BETWEEN HKS DETECTORS FOR TRACKABLE EVENTS.

HDC Tracking efficiency

Basic idea in calculating the HDC tracking efficiency is similar to the one used for the EDC efficiency calculation with extension that there are three different detector types: Hodoscopes, Water and Aerogel Čerenkov forming an overall of nine detector planes on the HKS side. With well defined correlation between counter IDs of different HKS detectors for trackable events, as shown in Fig.3.23, total number of tracks can be evaluated.

For the EDC efficiency calculation,with Ehodo1X and Ehodo2X planes being much closer than in the case of HKS hodoscopes, there is a cleaner correlation between hodoscope counter IDs of different planes than in the case of HDCs, compare Fig.3.16 and Fig.3.23. Using counter ID correlations only will clean total number of tracks from accidental coincidences. For this

reason a primitive tracking was done from hodoscope information:

- X direction: from hodoscope counter x-position and width informa-
  tion a set of possible trajectories in XZ-plane between HTOF1X and
  HTOF2X are calculated. Trajectories that do not lie in the geometri-
  cal acceptance of HDC, AC and WC or whose Xp coordinate (obtained
  from HTOF1X and HTOF2X tracking) is outside the typical region are
  discarded.

- Y direction: very good HKS hodoscope timing resolution allows calcu-
  lation of hit position in y-direction, see Fig.3.24, directly from time dif-
  ference between top and bottom PMTs. From y-positions of HTOF1X
  and HTOF2X a set of possible trajectories in YZ-plane are calculated.
  Trajectories that do not lie in the geometrical acceptance of HDC, AC
  and WC or whose Yp coordinate is outside the typical region are dis-
  carded.

- detectors on track: tracks are projected on HTOF1Y, AC and WC
  planes and information from each detector is collected and later used
  in PID and accidental track separation.

- checking if selected HTOF1X-HTOF2X counter combination is on HDC
  track.

The Y coordinate resolution, the difference between Y-coordinate hit po-
sition at hodoscope layer obtained from HDC tracking and the one obtained
directly from time difference between top and bottom hodoscope counter
PMTs, is shown in Fig.3.24.

With tracking created in this way, tracking efficiency for both pion and
proton events can be calculated by doing PID analysis (ToF, WC and AC cut
conditions). Finally, the HDC tracking efficiency for pion events is calculated
by this expression:

$$HDC\ pion\ efficiency = \frac{HTOF1X \otimes HTOF2X \otimes WC \otimes AC \otimes HTOF1Y \otimes HDCtrackON}{HTOF1X \otimes HTOF2X \otimes WC \otimes AC \otimes HTOF1Y} , \quad (3.6)$$
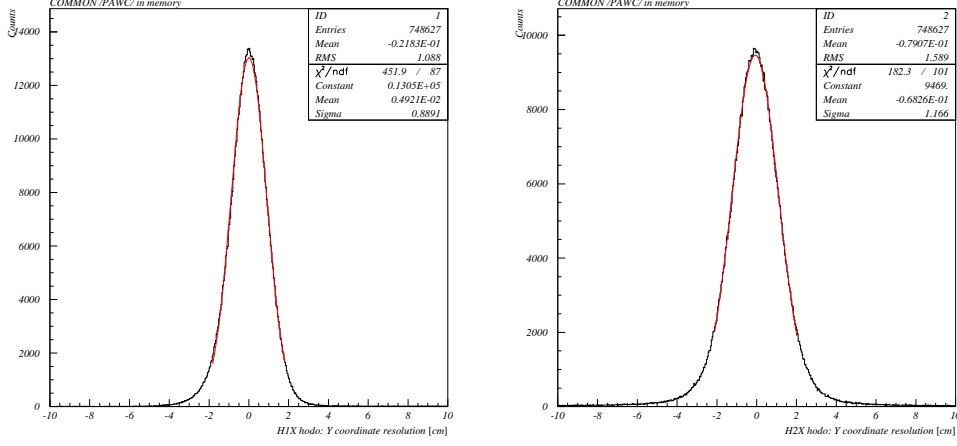
FIGURE 3.24: 1X AND 2X HODOSCOPE Y COORDINATE RESOLUTION CALCU-
LATED WITH HODOSCOPE TIMING INFORMATION WHEN COMPARED TO THE HDC
OBTAINED ONE.

and HDC tracking efficiency for proton events by:

$$HDC\ proton\ efficiency = \quad (3.7)$$

$$\frac{HTOF1X \otimes HTOF2X \otimes WC \otimes \overline{AC} \otimes HTOF1Y \otimes HDCtrackON}{HTOF1X \otimes HTOF2X \otimes WC \otimes \overline{AC} \otimes HTOF1Y}$$

HDC tracking efficiency for both pion and proton events has been calcu-
lated on run to run basis and results are shown in Fig.3.25. HDC tracking
efficiency was stable for both types of particles. Tracking efficiency for pion
events is slightly better than proton efficiency because, for pions, it is re-
quired that all detectors on the trajectory produce a signal. This reduces
accidental events that form fake HTOF1X-HTOF2X tracks and increase effi-
ciency. This type of accidental/fake tracks is highly dependent on event rate
and increasing the rates the number of fake tracks will also increase leading
to wrong calculation of the HDC tracking efficiency. This is clearly seen in
Fig.3.25 since at the earlier stages of the experiment the used beam currents
were lower leading to a better HDC efficiency for proton events than at the
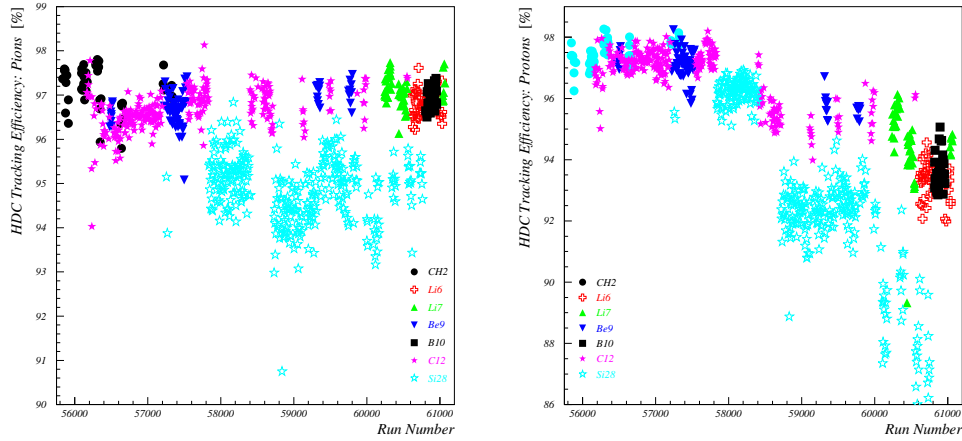
FIGURE 3.25: EFFICIENCY OF HKS DRIFT CHAMBER TRACKING. *Left* PION
EVENTS. *Right* PROTON EVENTS.

latter stage when data was taken at higher currents.

Typical dependence of the HDC tracking efficiency for targets and beam
currents used in the E01-011 experiment is shown in Fig.3.26. It has to be
taken into account that beam current information used in this plot represents
average current in each run and that there were significant fluctuations of
beam current even in the same run.

Fig.3.27 shows HDC tracking inefficiency for pion type of events across
HTOF1X and HTOF2X hodoscope planes. There is a rise in the HDC track-
ing inefficiency at the low and high side of HTOF layers due to increased
rates of protons at low side and positrons at high side. High rates cause too
many HDC wires producing a signal and for this reason events tracking code
can not produce a good trajectory.

As mentioned, the same type and design of the drift chambers were used
in both HNSS and E01-011 experiments and so in the E01-011 track recon-
struction the used algorithm was the same as for HNSS. While doing studies
on drift chambers calibration procedure, performance, reconstruction and
resolution it was noted that the existing tracking algorithm does not handle
well the high rates such as seen in the E01-011 experiment. This inefficiency
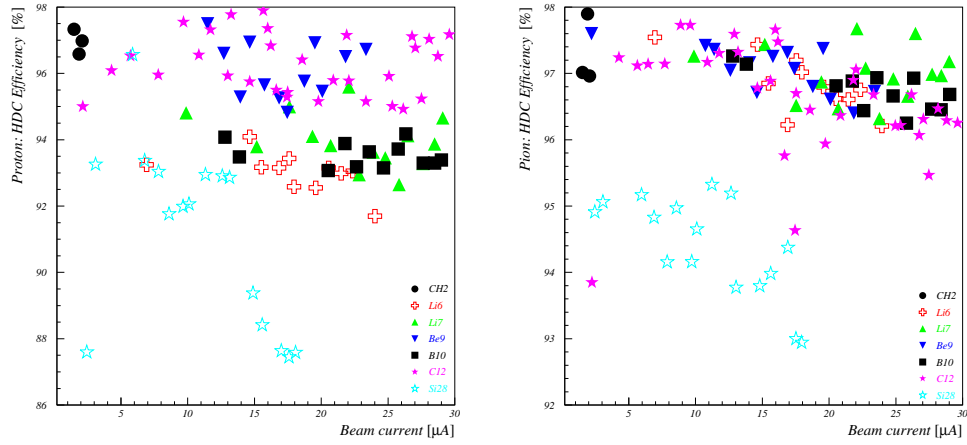
FIGURE 3.26: TRACKING EFFICIENCY OF THE HDC FOR THE USED TARGETS
AND TYPICAL CURRENTS. *Top* EFFICIENCY OF PROTON EVENT SELECTION *Bottom* EFFICIENCY OF PION EVENT SELECTION.
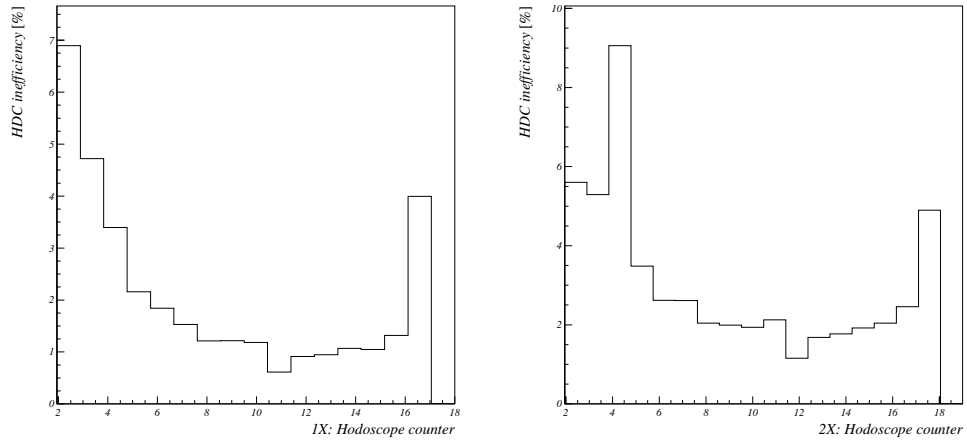
FIGURE 3.27: HDC TRACKING INEFFICIENCY ACROSS HTOF1X AND HTOF2X
HODOSCOPE PLANES FOR THE CH_2 TARGET.

led to both inefficiency in the number of reconstructed tracks and spatial resolution of the reconstructed focal plane quantities. Comparison of the tracking efficiencies with original the HKS code and high rate optimized is shown in Fig.3.28.

3.4.4   Aerogel Čerenkov

As discussed in Section 2.5.2, fringe field of the HKS magnets had a severe effect on the performance of Aerogel Čerenkov PMTs. The effect is clearly seen in Fig.3.29, AC phototubes were tested with light produced by LED w/wo magnetic shield, with/without (w/wo) HKS magnets turned ON and w/wo coil current ON. Clearly two things can be concluded: First, AC PMTs are severely affected by fringe field; Second, by setting up coils around individual PMTs their performance recovered and for some almost to the level they performed with the HKS magnets turned OFF.

The recovery of Aerogel Čerenkov PMT performance as a function of applied current on coils is shown in Fig.3.30. As expected, there is no shift in pedestal (*Top left*) or change in single electron peak position (*Top right*) with increasing current. The recovery of a number of photoelectrons (NPE) produced by LED in AC while HKS magnets are ON, (*Bottom*), is represented by comparing means of LED NPE distributions when magnets are ON and OFF. By using coils to counter effect of the fringe field and recover PMT performance worked much better for AC2 layer (almost 100% recovery) than for AC1 layer (only 40% recovery). This difference in performance of the two layers is due to different PMTs used : Hamamatsu tubes (PMTs) were used for AC1 layer and Photonis tubes were used for AC2 and AC3 layers.

The number of photolectrons produced in Čerenkov detectors depends on particle speed and with HKS momentum acceptance in the range $1.2 geV \pm 10\%$ individual AC tubes produced different (speed/momentum dependent) NPE distributions. The usage of different types of PMTs and fringe field effect also influenced NPE distributions since the recovery with coil setup was not at the same level for different tubes, as shown in Fig.3.30. Fig.3.31 shows typical AC NPE distributions for unbiased events (PID detectors were
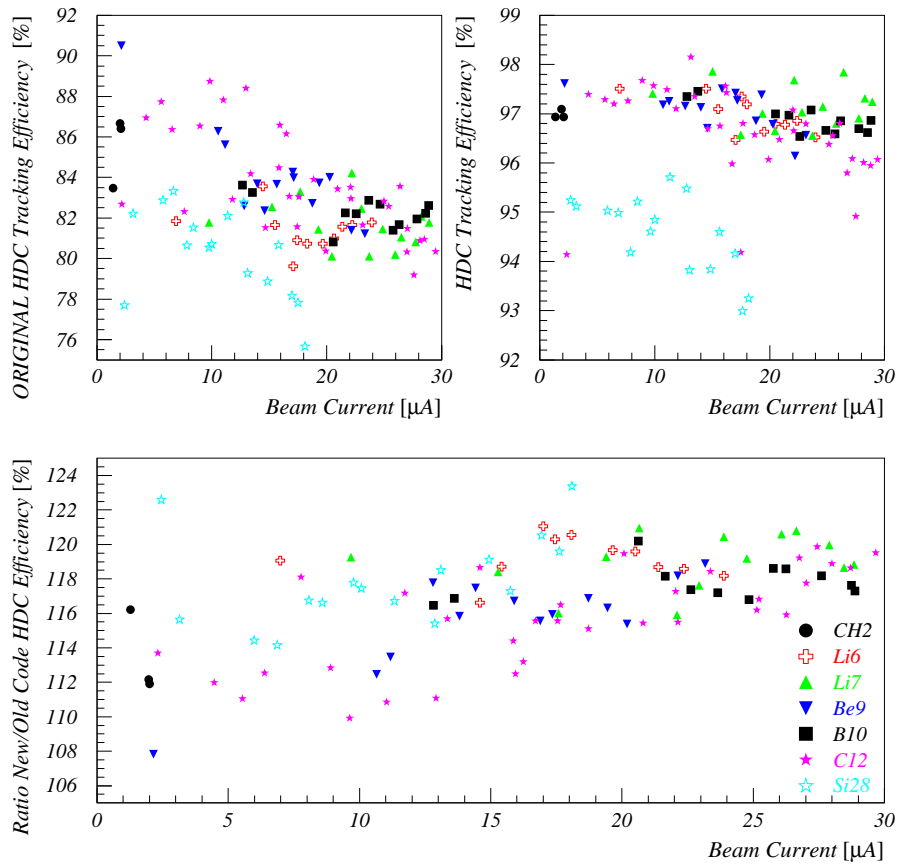
FIGURE 3.28: COMPARISON OF THE HDC TRACKING EFFICIENCY AS A FUNC-
TION OF BEAM CURRENT FOR THE USED TARGETS OBTAINED WITH HNSS CODE
AND E01-011 OPTIMIZED CODE. *Top Left* HDC TRACKING EFFICIENCY WITH
THE ORIGINAL (HNSS) CODE. *Top Right* HDC TRACKING EFFICIENCY WITH
THE CODE OPTIMIZED FOR HIGH RATE E01-011 DATA. *Bottom* RATIO OF THE
NUMBER OF TRACKS RECONSTRUCTED BY OPTIMIZED AND HNSS CODES ON THE
SAME DATA SET.
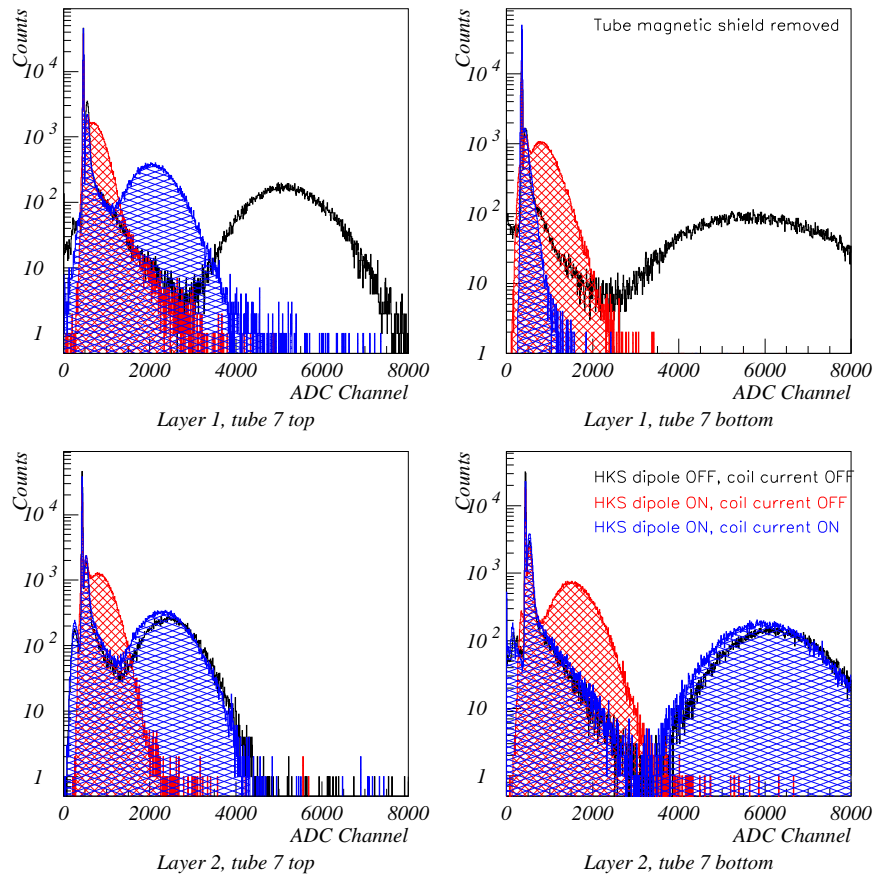
FIGURE 3.29: RESPONSE OF AC PHOTOTUBES IN THE FRINGE FIELD OF THE HKS DIPOLE. LIGHT WAS PRODUCED BY LED AND SINCE TURNED TOWARDS THE BOTTOM TUBES, THEY GAVE MORE LIGHT. *Top right* MAGNETIC SHIELD OF THIS TUBE HAS BEEN REMOVED FOR TESTING PURPOSES.
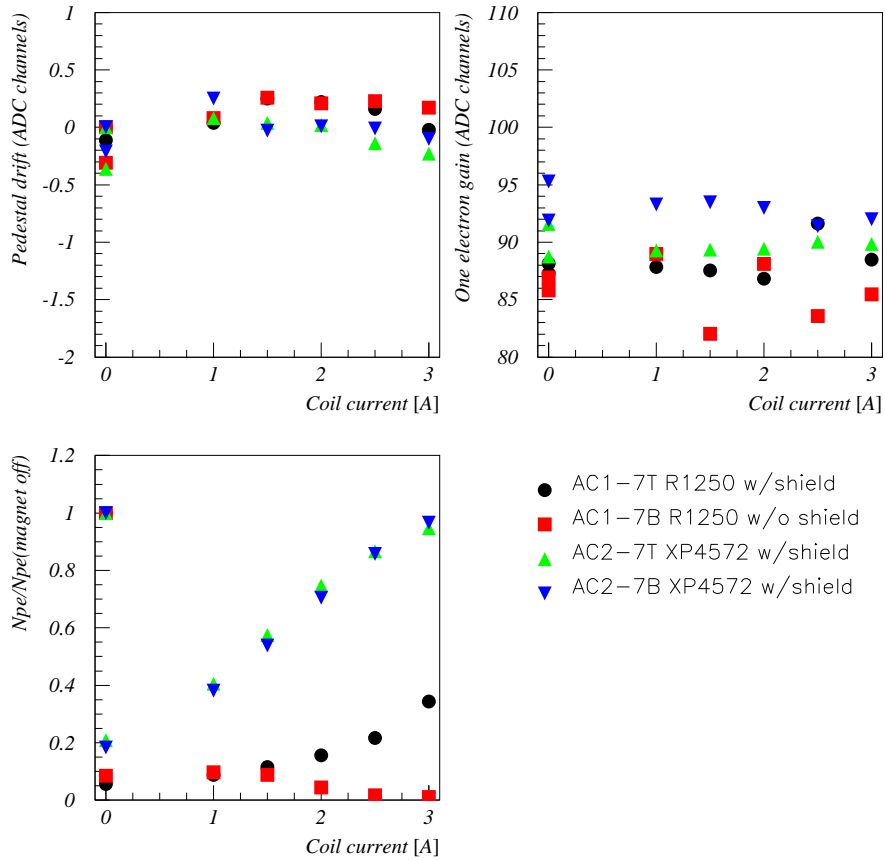
FIGURE 3.30: RECOVERY DEPENDENCE OF THE AC TUBES IN HKS MAGNETS FRINGE FIELD ON COIL CURRENT. LIGHT WAS PRODUCED BY LED. VALUES NORMALIZED TO NO FIELD VALUES. *Top left* PEDESTAL SHIFT *Top right* SINGLE PHOTOELECTRON PEAK GAIN *Bottom* RECOVERY OF THE LED PHOTOELECTRON DISTRIBUTION MEAN.
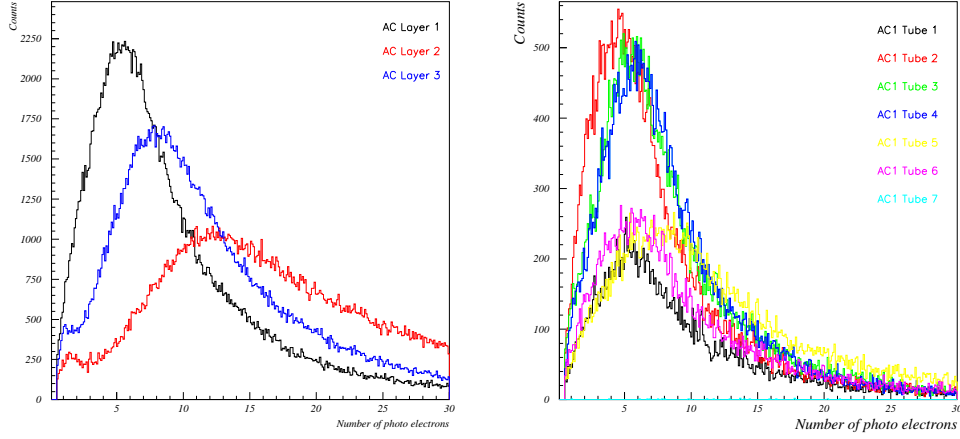
FIGURE 3.31: DISTRIBUTIONS OF AEROGEL ČERENKOV NUMBER OF PHOTO-
ELECTRONS FOR UNBIASED ^{7}Li EVENTS. *Left* NPE DISTRIBUTIONS OF ALL AC
LAYERS. *Right* NPE DISTRIBUTIONS OF AC1 TUBES.

not used in forming of the trigger) of ^{7}Li data set with clear differences in
performance between layers and individual tubes.

3.4.5   Water Čerenkov

During the data taking it was noted that light output of WC counters de-
cayed with time, as shown in Fig.3.32 and Fig.3.33. This could possibly
influence both kaon overkill on the trigger level (WC are in the AND mode)
and also reflect in worse p/K$^+$ separation in offline level. Fig.3.33 shows peak
of number of photoelectron distributions produced in WC layers by kaons.
Peak value is obtained by fitting NPE distribution in the neighbourhub of
maximum with Gaussian function and taking the peak to correspond to the
value of the mean of Gaussian fit. For this decay in number of NPE (calcu-
lated from WC ADC values) not to be the cause of kaon overkill on trigger
level, signal discrimination was done on summed ADC pulses from top and
bottom PMTs from run 58410. ADC summation was done by analog signal
adders. For run period up to run 58410 signal discrimination was done on
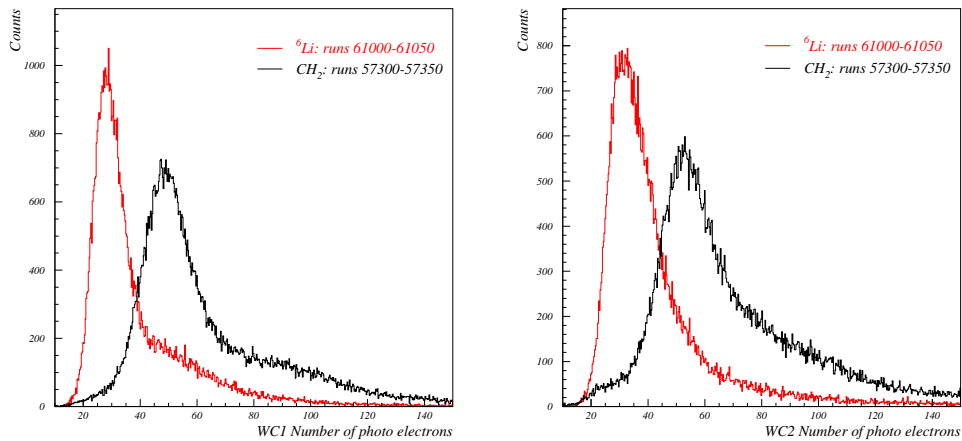
FIGURE 3.32: TYPICAL KAON NPE DISTRIBUTION IN WATER ČERENKOV DE-
TECTORS *Left:WC1, Right:WC2.* DECAY IN PERFORMANCE IS OBVIOUS.

ADC pulses of individual PMTs. Probable cause of the NPE decay was due
to the chemical instability of the wave length shifter.

Fig.3.33 shows the ratio of the width and mean of the kaon WC distribu-
tions corresponding to sigma and mean of the Gaussian fit. This plot shows
that before the introduction of signal adder in the experimental configura-
tion, decrease in produced NPEs also resulted in worse ratio of distribution
width and peak position. This will result in worse p/K^+ separation because
with the reduction of NPEs it follows that p and K^+ distributions are getting
closer and with slower decrease in NPE widths their overlap is getting bigger.

By analyzing the performance of individual WC counter PMTs it was
noted that there was a difference in NPE distributions between the counters
because of different gains of the counters (and partly because of different
particle speeds across WC plane). This is shown in Fig.3.35.
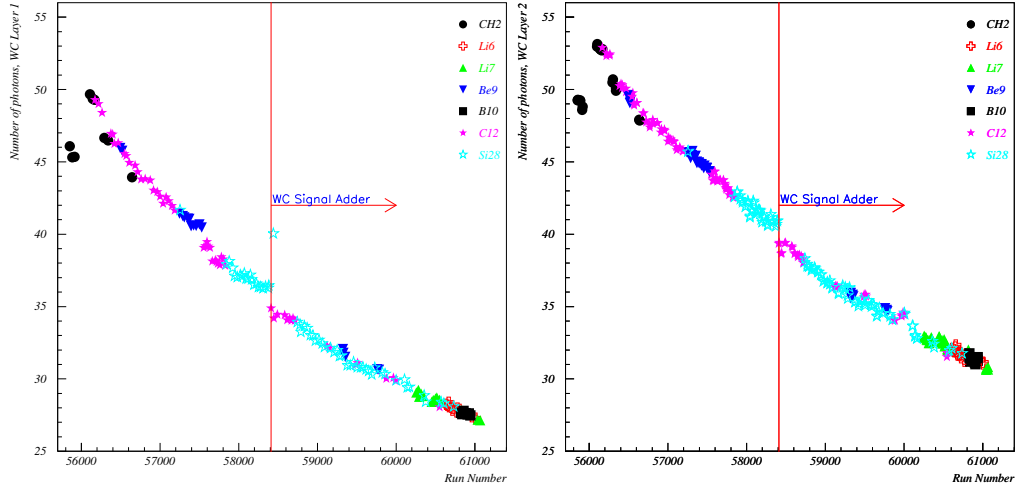
FIGURE 3.33: THE MEAN VALUE OF THE NUMBER OF PHOTOELECTRONS PRO-
DUCED IN WC LAYERS BY K^+ DURING THE EXPERIMENT.
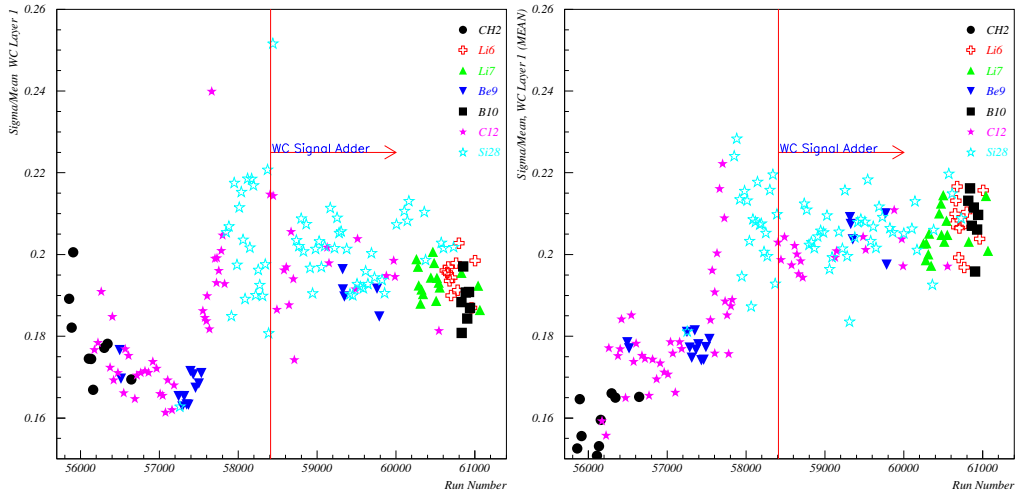
FIGURE 3.34: QUOTIENT OF SIGMA AND MEAN OF PHOTOELECTRONS DISTRIBU-
TION IN WC LAYERS. THE MEAN (SIGMA) VALUE CORRESPONDS TO THE MEAN
(SIGMA) OF THE GAUSSIAN FIT OF THE KAON EVENTS.
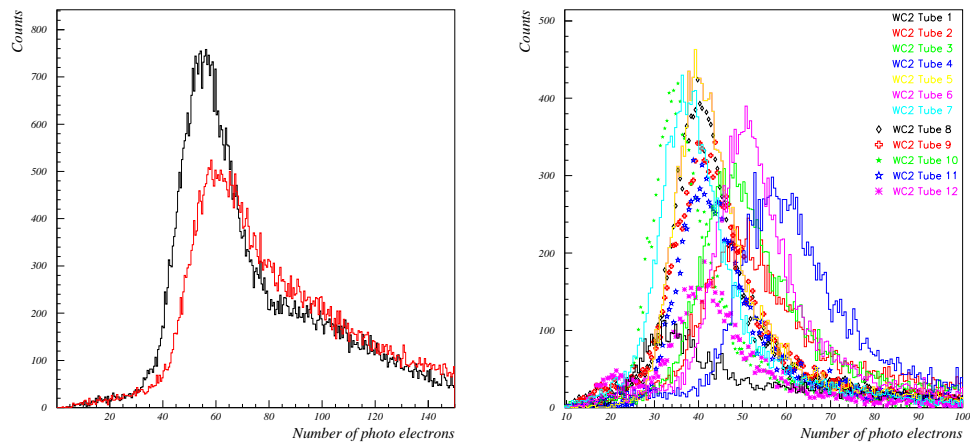
FIGURE 3.35: WATER ČERENKOV NUMBER OF PHOTOELECTRONS DISTRIBU-
TIONS FOR UNBIAS ^{7}LI EVENTS. *Left* NPE DISTRIBUTIONS OF THE WC LAYERS.
Right NPE DISTRIBUTIONS OF THE WC2 TUBES.

Chapter 4

DATA ANALYSIS

The overview of Hall C analysis software package, ENGINE 3.1, was provided in Section 3.1. The details of the used calibration procedures are covered in Section 3.3. The performance of the detector package (drift chambers, hodoscopes and Čerenkovs) is in detail described in Section 3.4. With all this at hand, data analysis can be done.

In this chapter detailed discussion on all aspects of data analysis needed to obtain missing mass spectra and extract cross sections of Λ hypernuclear states is presented. The process of data analysis can be summarized in the following points:

- K^+ identification (Section 4.2)

- e' and K^+ coincidence (Section 4.1)

- calculation of missing mass spectra (Section 4.3)

- calibration of optics and kinematics (Section 4.4)

- information needed for cross section calculation (Section 4.7)

4.1   Two arms in coincidence

In order to get to physics plots, meaning Missing Mass (MM) spectra, electron and kaon that belong to the same scattering event must be linked together. This is done by using the so called coincidence time (t_{coin}). It represents target time of the (e,e'K$^+$) reaction. Coincidence time is obtained when Enge and HKS focal plane times are corrected for the path length time from the target, as described in Eqn.4.1.

$$t_{coin} = t_{HKS}(focalplane) - \delta t_{HKSpath} - t_{Enge}(focalplane) + \delta t_{Engepath} \quad (4.1)$$

Typical coincidence time distributions before particle ID tools are used is shown in Fig.4.1 and coincidence time for kaon events in Fig.4.2. Fig.4.1 as expected shows that data is dominated with high number of proton and pion events with their numbers being controlled by WC and AC thresholds, respectively. π leakage into real K$^+$ coincidence peak is clearly seen and without good PID separation they could not be clearly separated.

Fig.4.2 shows coincidence time distribution for K$^+$ particle with real (e',K$^+$)coincidences centered around zero. Coincidence time distribution, with local maximums/minimums being 2ns apart, is due to 2ns structure of the electron beam. Other maxima/peaks correspond to accidental coincidences between e' and K$^+$ coming from different beam bunches. Maximums at 2ns and 4ns are the highest because it was not possible to completely separate π from K$^+$ since their $\Delta\beta$ significantly overlap, see Fig.4.5. The overlap in $\Delta\beta$ of protons and K$^+$ is less pronounced.

To extract real coincidence events cut conditions are applied to coincidence time. With real K$^+$ coincidence peak centered around zero and 2ns electron beam structure, coincidence cut used is:.

$$|Coincidence\ time| \leq 1ns \quad (4.2)$$

The effect of the coincidence cut on the real coincidence kaon survival and leakage of the events from the surrounding coincidence peaks are shown in
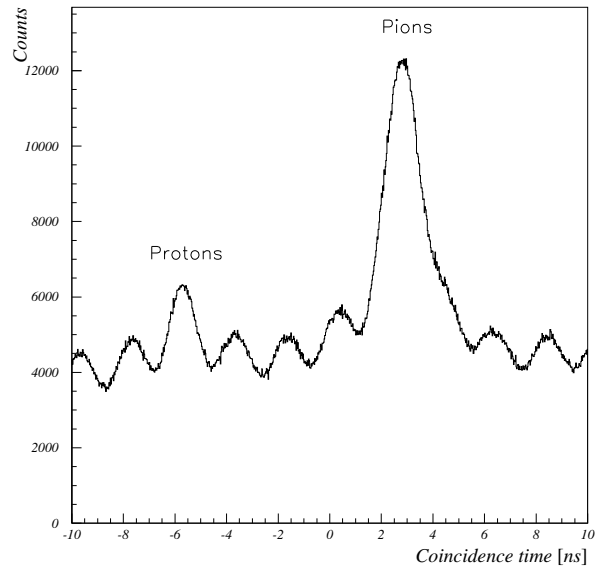
FIGURE 4.1: COINCIDENCE TIME DISTRIBUTION - KAON PID WAS NOT USED.
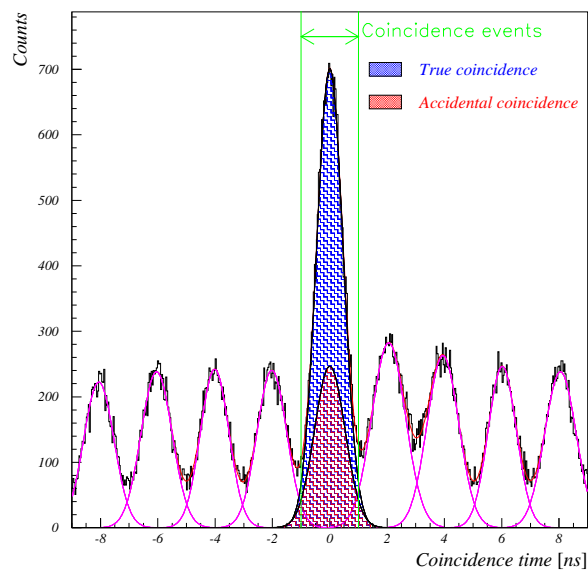
FIGURE 4.2: COINCIDENCE TIME DISTRIBUTION WITH APPLIED KAON PID FOR CH_2 DATA. REAL COINCIDENCE PEAK IS CLEARLY SEEN.

Fig.4.3. Coincidence distribution was fitted with a set of Gaussian functions, one for real coincidence peak and eight for accidental peaks. Real coincidence peak, as shown in Fig.4.2, consisted of true K^+ coincidence events and accidental coincidence events since they contribute to all peaks including the real coincidence peak.

With applied coincidence cut, see Eqn.4.2, survival of the true coincidence K^+ was $98.0 \pm 0.2\%$. Contribution of accidental coincidence events in the real coincidence peak was $\approx 40\%$ with chosen PID cuts. Leakage of the K^+ accidental coincidence to the real coincidence peak was $3.0 \pm 0.3\%$ with 2/3 coming from +2ns peak because π/K^+ separation could not be done at 100% level.

4.2 Particle identification

The first task of data analysis was to select kaon events produced in elementary process $p(e, e'K^+)\Lambda$ and detected by experiments detector package. Kaon events produced by electroproduction were dominated by huge background of protons, pion and positrons because of the small cross section. These background events have to be excluded. This is done by using the information from ToF hodoscope, Water and Aerogel Čerenkov detectors. In this section the definition of PID tools is explained as well as how data was manipulated to achieve the best possible kaon identification. Also, PID analysis by two complementary methods : using β spectrum and two arms coincidence time distribution is described.

4.2.1 PID Tools

$\beta_{TOF} - \beta_{K^+}$ **spectrum**

As discussed in Sec3.4.4, shifts in $\beta_{TOF} - \beta_\pi$ spectrum were noticed on the run to run basis. These shifts also translate into $\Delta\beta_K = \beta_{TOF} - \beta_{K^+}$ spectrum. With limited kaon statistics in each run this offset can not be corrected by simply shifting kaon $\Delta\beta_K$ distribution.
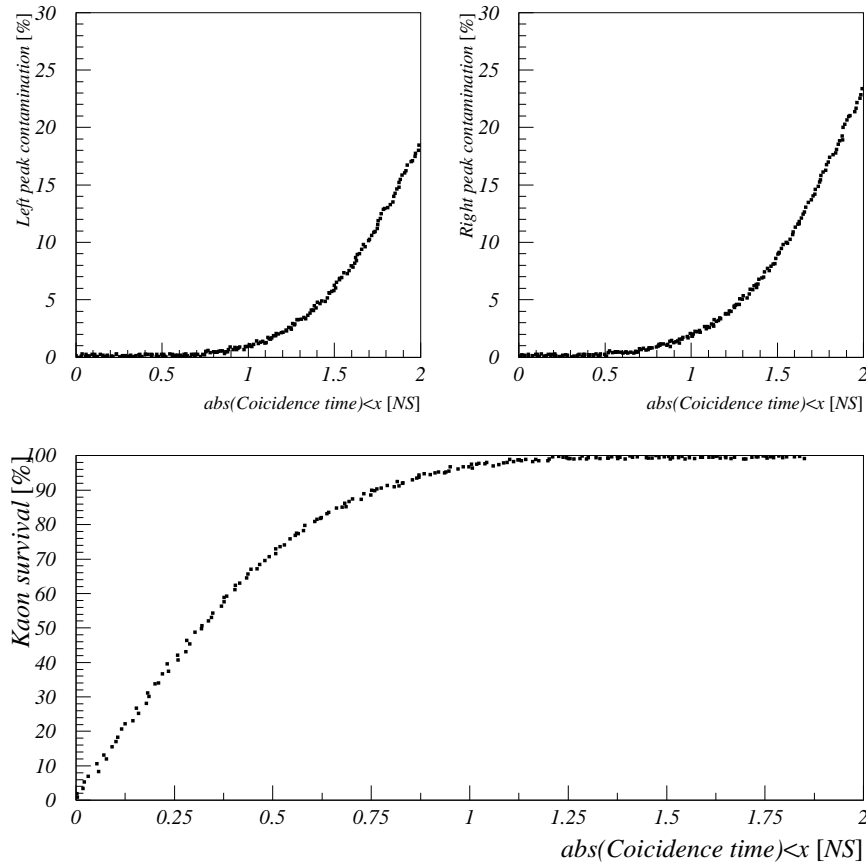
FIGURE 4.3: CH$_2$ DATA COINCIDENCE CUT PARTICLE SURVIVAL. *Top Left* CON-
TAMINATION OF REAL K$^+$ COINCIDENCES FROM LEFT SIDE. *Top Right* CONTAM-
INATION OF REAL K$^+$ COINCIDENCES FROM RIGHT SIDE. *Bottom* REAL COINCI-
DENCE KAON SURVIVAL DEPENDENCE ON COINCIDENCE TIME CUT CONDITION.
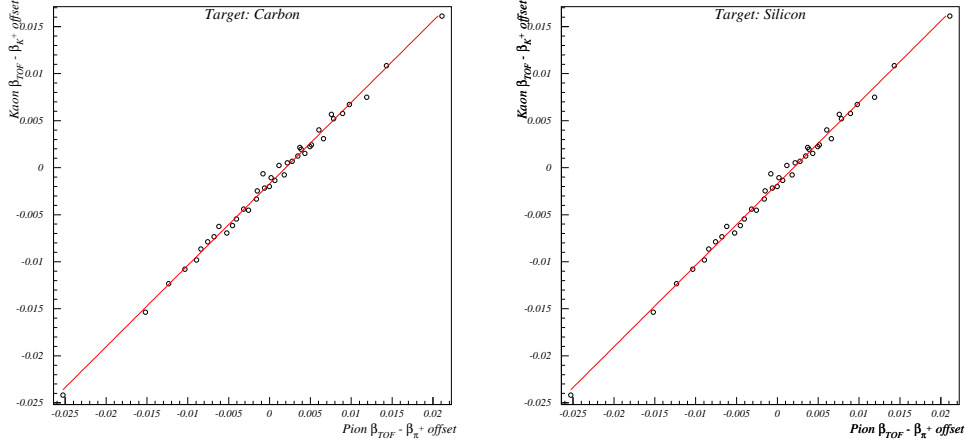
FIGURE 4.4: DEPENDENCE OF THE KAON BETA OFFSET ON PION BETA OFFSET. THIS CORRECTION WAS USED TO GET BETTER KAON/PION SEPARATION.

Corrections on kaon events were done by extrapolating correlation between $\Delta\beta_\pi$ and $\Delta\beta_K$ offsets. First, $\Delta\beta_\pi$ distributions were fitted with Gauss function. Second, runs with similar $\Delta\beta_\pi$ offsets were grouped to accumulate/increase kaon statistics. Third, for these grouped runs $\Delta\beta_K$ and $\Delta\beta_\pi$ distributions were fitted and corresponding $\Delta\beta$ offsets were obtained. Finally, the correlation between $\Delta\beta_K$ offset and $\Delta\beta_\pi$ offset was calculated. The correlation between $\Delta\beta_K$ and $\Delta\beta_\pi$ offsets for ^{12}C and ^{28}Si targets is shown in Fig.4.4. The correlation is represented by linear function.

With calculated $\Delta\beta_\Pi$ offset for each run and known $\Delta\beta_K$ offset-$\Delta\beta_\Pi$ offset correlation, $\Delta\beta_K$ shift is calculated for each run. This correction allows better pion/kaon separation leading to a cleaner MM spectra and better S/A ratio. In the $|\beta_{TOF} - \beta_{K^+} - offset| \leq X$ spectrum, with kaons centered around zero, protons and pions can be identified, see Fig.4.5. Beta PID cut used can be written in the form: $|\beta_{TOF} - \beta_{K^+} - offset| \leq X_\beta$. With protons centered in the region > -0.1 and typical particle velocity β_{ToF} resolution better than 0.025, see Fig.4.5, most protons are excluded if the used beta cut is set to $X_\beta = 0.07 (\approx 3\sigma)$ but this is not the case for pions.
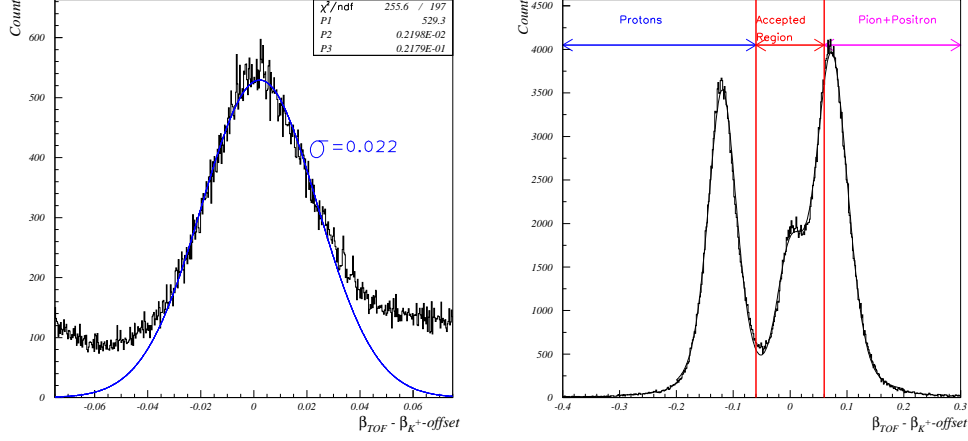
FIGURE 4.5: PARTICLE VELOCITY ($\beta_{TOF} - \beta_{K^+} - offset$) RESOLUTION (*Left*) AND TYPICAL DISTRIBUTION (*Right*) WITH DEFINED PID REGIONS FOR CH_2 DATA SET.

Aerogel Čerenkov

Aerogel Čerenkov, as discussed in Sec.3.4.4, performed differently for each tube/layer. Since NPE sum of all three layers is used for K^+/π separation, a single cut condition will for certain tube combinations let in more π and for some kill K^+.

Normalization of the NPE distributions was done so that all AC tubes have equal effect in the AC cut condition and as a result giving better PID, S/A ratio and less background events due to π leakage into real coincidence peak. For normalization, pions from unbiased data were used. First, NPE distribution peak positions were obtained for each AC tube. Within the same layer individual tube NPEs were normalized, with respect to the same tube, according to:

$$NPE_N(AC : i - k) = \frac{NPE_{peak}(AC : i - m)}{NPE_{peak}(AC : i - k)} NPE(AC : i - k), \quad (4.3)$$

NPE_N - normalized number of photoelectrons; i-layer number; k-tube; m-

FIGURE 4.6: REAL L𝙸7 DATA AEROGEL ČERENKOV NUMBER OF PHOTOELEC-
TRONS DISTRIBUTIONS FOR ALL AC1 LAYER TUBES. *Left* REAL DATA DISTRIBU-
TIONS. *Right* DISTRIBUTIONS AFTER TUBE NORMALIZATION.

tube set as ethalon. The results of tube normalization within a layer are
shown in Fig.4.6.

With tube NPE normalization within the same layer a more uniform layer
NPE distributions were obtained.

Second, NPE_N distributions of the layers AC1 and AC3 were normalized to
the AC2 NPE_N distributions. AC1 (AC3) NPE_N value X has equal weight
as AC2 NPE_N value Y if the number of pions that have $NPE_N < X(Y)$
is equal. The normalization between layers is now simply done by assigning
Y value to X. This was done since number of pions passing through each
layer was the same and so AC layers should all have (produce) very similar
(equal) NPE distributions. The results are that all three layers now have the
same normalized distributions (See Fig.4.7) and equally contribute to the cut
conditions. Two different approaches in AC tube and layer normalizations
are due to different types of tubes used in the layers, also layers AC1 and
AC2 had newer Aerogel Silica than AC3.

Finally, AC PID cut used for K^+/π separation can be written in the
form: $AC1norm + AC2norm + AC3norm < X_{AC}$. Typical distributions of
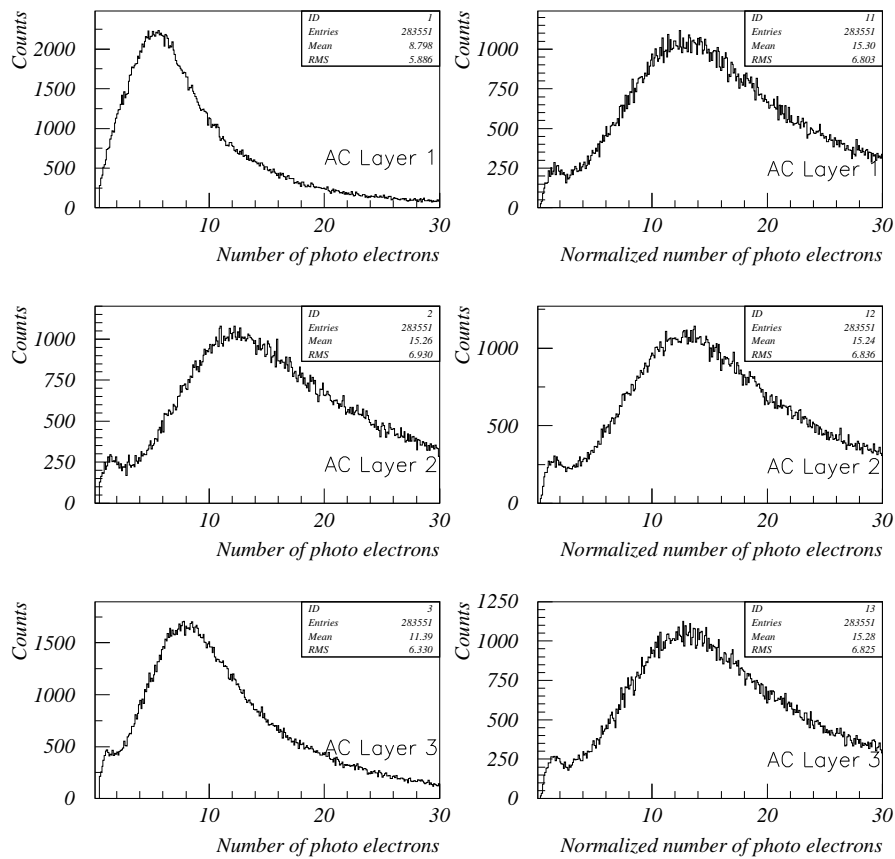
FIGURE 4.7: REAL Li₇ DATA-AEROGEL ČERENKOV NUMBER OF PHOTOELEC-
TRONS DISTRIBUTIONS FOR ALL THREE LAYERS. *Left* REAL DATA DISTRIBUTIONS.
Right NORMALIZED DISTRIBUTIONS.
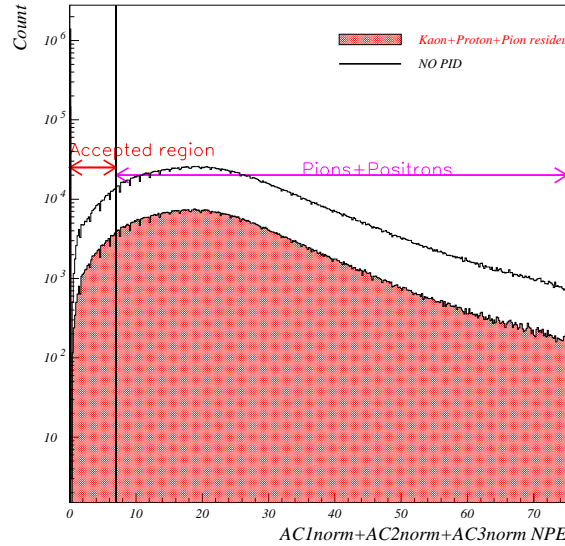
FIGURE 4.8: TYPICAL NORMALIZED AC NUMBER OF PHOTOELECTRONS DISTRIBUTION WITH/WITHOUT WC AND β KAON PID SELECTION.

$AC1norm + AC2norm + AC3norm$, with/without WC and β kaon imposed PID selection, are shown in Fig.4.8.

Fig.4.9 shows contour plot of the normalized AC number of photoelectrons vs $\beta_{TOF} - \beta_{K^+} - offset$. The separation of pions from kaons and protons is evident, since protons and (most) kaons do not produce a signal in AC. Typical cut condition set was $AC1norm+AC2norm+AC3norm < 7$ because most π's are removed by this cut as shown in scatter plot in Fig.4.10.
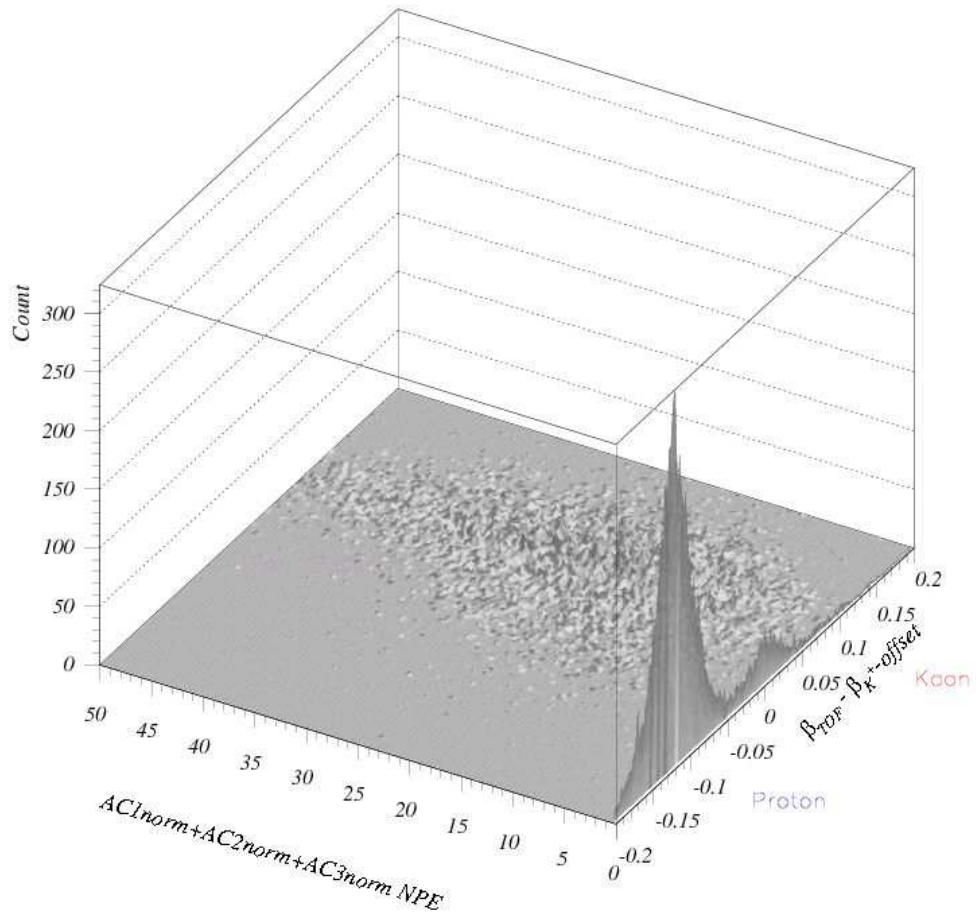
FIGURE 4.9: SURFACE PLOT OF THE NORMALIZED AC NUMBER OF PHOTOELEC-
TRONS VS $\beta_{TOF} - \beta_{K+} - offset$.
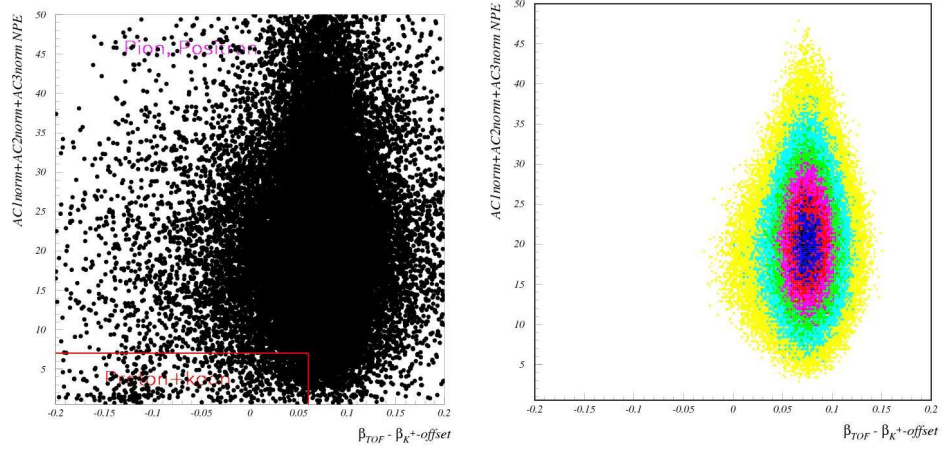
FIGURE 4.10: SCATTER PLOT OF THE NORMALIZED AC NUMBER OF PHOTO-
ELECTRONS VS $\beta_{TOF} - \beta_{K^+} - offset$. *Left* NO PID. *Right* COLOUR PLOT FOR
π EVENTS.

Water Čerenkov

Water Čerenkov, as discussed in Sec.3.4.5, experienced a reduction in the
NPE production with time. This effect was corrected by the normalization
of measured WC NPE distribution with respect to kaon events. This was
done by grouping runs from same time period and applying kaon PID cuts
(AC, $\delta\beta(K^+)$) on the WC1 (WC2) distributions, which then represent kaon
signature in WC1(WC2), see Fig.3.32. Kaon peak position for each layer is
extracted (Gaussian fitting in the region of the peak) and WC NPE is than
normalized:

$$NPE_N(WC : i - k) = 50 \frac{NPE(WC : i - k)}{NPE_{K^+peak}(WC : i)} \qquad (4.4)$$

Finally, differences in the tube performance were removed by finding kaon
peak in the time decay corrected distribution by, again, using Eqn.4.4. The
two corrections could not be done at the same time because of insufficient
kaon statistics in the small time periods. The results of this two step proce-
dure are shown in Fig.4.11 where kaon peak position in the measured, decay
corrected and tube corrected WC1(2) spectra are shown.
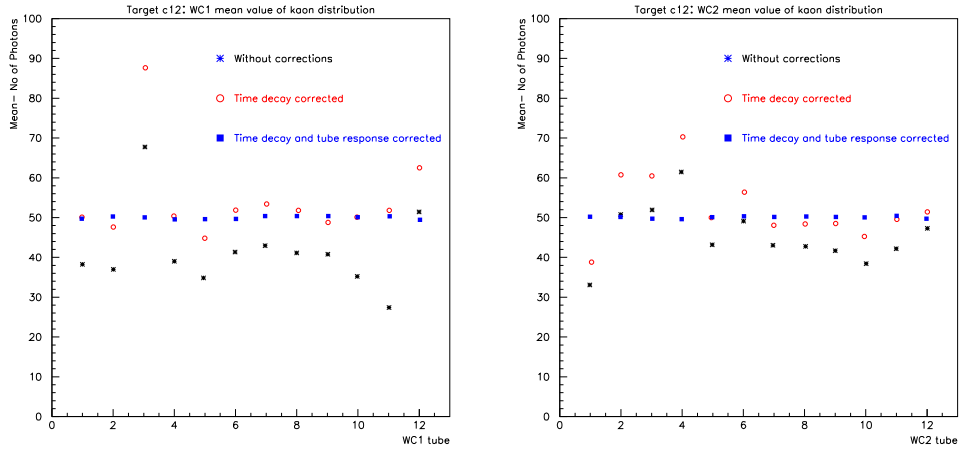
FIGURE 4.11: RESPONSE OF THE WATER ČERENKOV COUNTERS, AS MEASURED AND AFTER TIME DECAY AND TUBE BY TUBE CORRECTIONS. THE MEAN VALUE CORRESPONDS TO THE MEAN OF THE GAUSSIAN FIT OF THE KAON EVENTS.

PID, K^+/p separation, is now done on the sum of the two normalized distributions and the cut condition is: $WC1norm + WC2norm > X_{WC}$. The normalized WC sum is shown in Fig.4.12 with prominent and separate pion and proton peaks. Kaon WC distribution (AC and β cuts are applied) is also shown with K^+ peak set at 100 (as normalized) and clear proton residue that has to be removed by imposing WC cut.

Fig.4.13 shows scatter plot of the normalized WC number of photoelectrons and $\beta_{TOF} - \beta_{K^+} - offset$ with clear π/p separation (left plot). Events that satisfy AC and $\delta\beta$ kaon PID cuts, kaons and proton residue, are shown on the right plot.
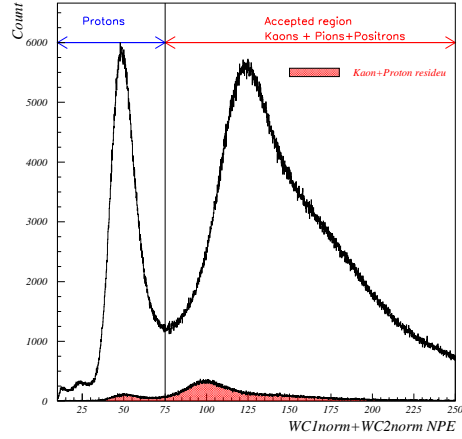
FIGURE 4.12: SUM OF WATER ČERENKOV NORMALIZED NPE DISTRIBUTIONS, AFTER TIME DECAY AND TUBE BY TUBE CORRECTIONS. WITHOUT PID π AND PROTONS DOMINATE. *Red* WC DISTRIBUTION AFTER K$^+$ AC AND β APPLIED CUTS.
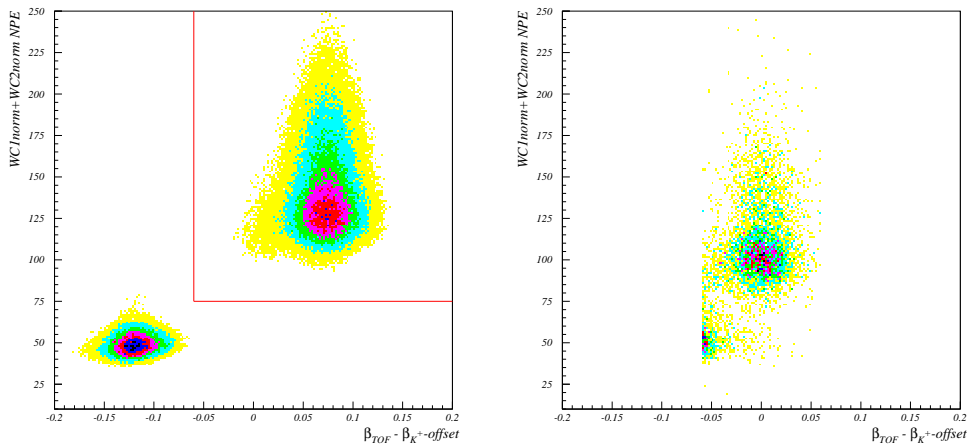
FIGURE 4.13: SCATTER PLOT OF THE NORMALIZED WC NUMBER OF PHOTO-ELECTRONS AND $\beta_{TOF} - \beta_{K^+} - offset$. *Left* WITHOUT USING PID. *Right* WITH USED KAON PID.

4.2.2 PID analysis

There are two major points to be considered when selecting PID cut criteria on Aerogel/Water Čerenkov and $\beta_{ToF} - \beta_{K+}$:

- maximizing K$^+$ survival resulting in higher statistics in hypernuclear states

- minimizing proton/pion background leading to better Signal / Background ratio

both points are addressed in this section and section that follows.

The cut efficiency, defined as the ratio of the number of kaon events below the set AC cut (above WC cut)to that without AC(WC) cut, was studied on the β_{ToF} spectrum. Since kaon/proton and kaon/pion $\beta_{ToF} - \beta_{K+-offset}$ distributions overlap, β_{ToF} spectrum was fitted with two pseudo-Voigt functions and one Gaussian, as shown in Fig.4.14 and described in Eqn.4.5. Pseudo-Voigt functions (see Eqn.4.6) were used to evaluate the number of pions and protons while Gaussian was used to evaluate the number of kaons.

$$Y(x) = Voigt(x)_{Proton} + Gaussian(x)_{Kaon} + Voigt(x)_{Pion} \qquad (4.5)$$

$$Voigt(x) = C_1 \left[\frac{2}{\pi} \frac{C_2 C_3}{4(x - C_4)^2 + C_3^2} + (1 - C_3) \frac{\sqrt{4Ln2}}{\sqrt{\pi}C_3} e^{-\frac{4Ln2}{C_3^2}(x - C_4)^2} \right] \qquad (4.6)$$

where $x = \beta_{ToF} - \beta_{K+-offset}$ and Y(x) represents counts.

Effects of applied AC and/or WC cuts are represented in Fig.4.15. As expected, the applied AC cut does separate kaons from pions by removing pions from β_{ToF} spectrum when used in the form $AC1_{norm} + AC2_{norm} + AC3_{norm} < X_{AC}$. Similarly, by using WC cut condition in the form $WC1_{norm} + WC2_{norm} > X_{WC}$, the separation of kaons from protons was done by removing protons. Complete kaon/proton and kaon/pion separations by using
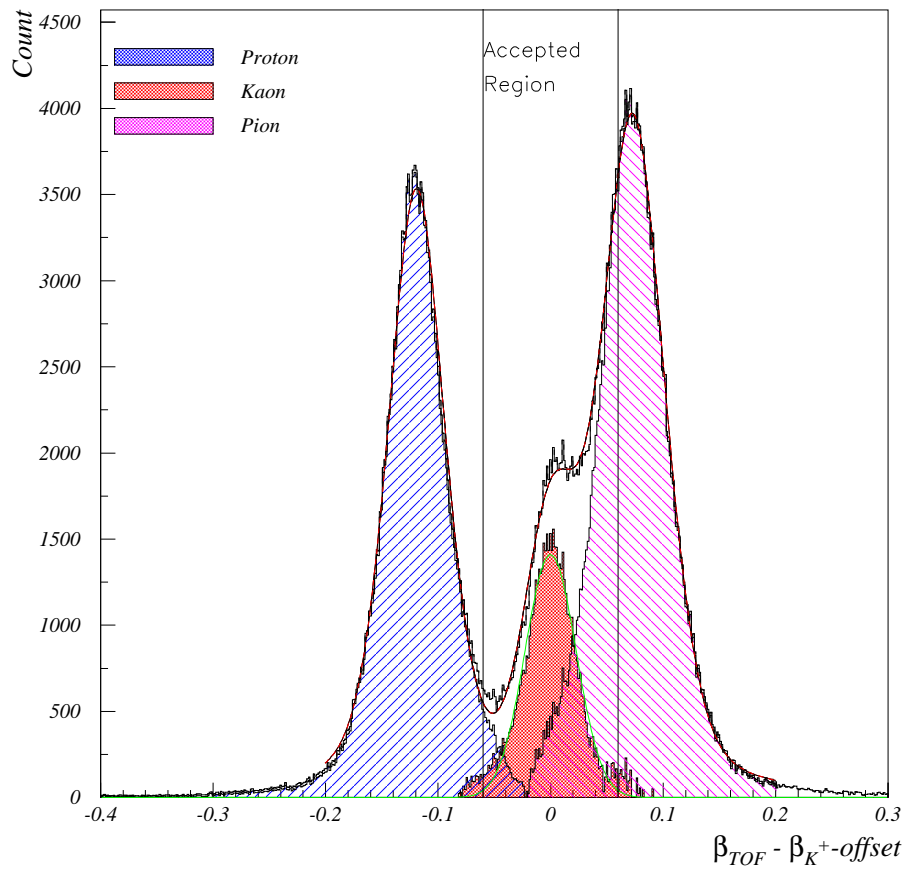
FIGURE 4.14: $\beta_{TOF} - \beta_{K^+} - offset$ DISTRIBUTION FITTED WITH TWO PSEUDO-VOIGT AND ONE GAUSSIAN FUNCTION.

only Aerogel and Water Čerenkov cut conditions, in the form mentioned, were not possible. Additional cut condition imposed on β_{ToF} spectrum in the form $|\beta_{TOF} - \beta_{K^+} - offset| < X_\beta$ was also necessary.

Aerogel Čerenkov

The AC cut efficiency was evaluated by applying AC cuts in the form $AC1norm + AC2norm + AC3norm < X_{AC}$ then fitting β_{ToF} distribution to calculate the number of protons, kaons and pions. Proton survival and pion rejection dependence on the AC cut condition are shown in Fig. 4.16, plotted is the ratio of the number of protons(pion) after the applied cut condition and the number of protons(pion) with the applied final PID AC condition. Number of protons was stable and did not significantly change in the AC cut region $X_{AC} \geq 2.5$. Small percentage of proton had on their trajectories AC with $NPE > 0$ due to high pion rates producing a drop in proton survival in the region $X_{AC} < 2.5$. As expected, the biggest influence of the AC cut was seen in pion survival, as shown in Fig.4.16(b). Fig. 4.16(c) shows kaon survival efficiency as a function of applied AC cut condition. The results of the kaon survival efficiency vs AC cut condition for the used targets are summarized in Table 4.5.

Water Čerenkov

The WC cut efficiency was evaluated by applying WC cuts in the form $WC1norm + WC2norm > X_{WC}$ then fitting β_{ToF} distribution to calculate the number of protons, kaons and pions. Proton rejection and pion survival dependence on the WC cut condition are shown in Fig. 4.17, plotted is the ratio of the number of protons after the applied cut condition and the number of protons with the applied final PID WC condition. Bottom plot of Fig. 4.17 shows kaon survival efficiency as a function of applied AC cut condition. The results of the WC cut condition kaon survival efficiency for the used targets are summarized in Table 4.6.
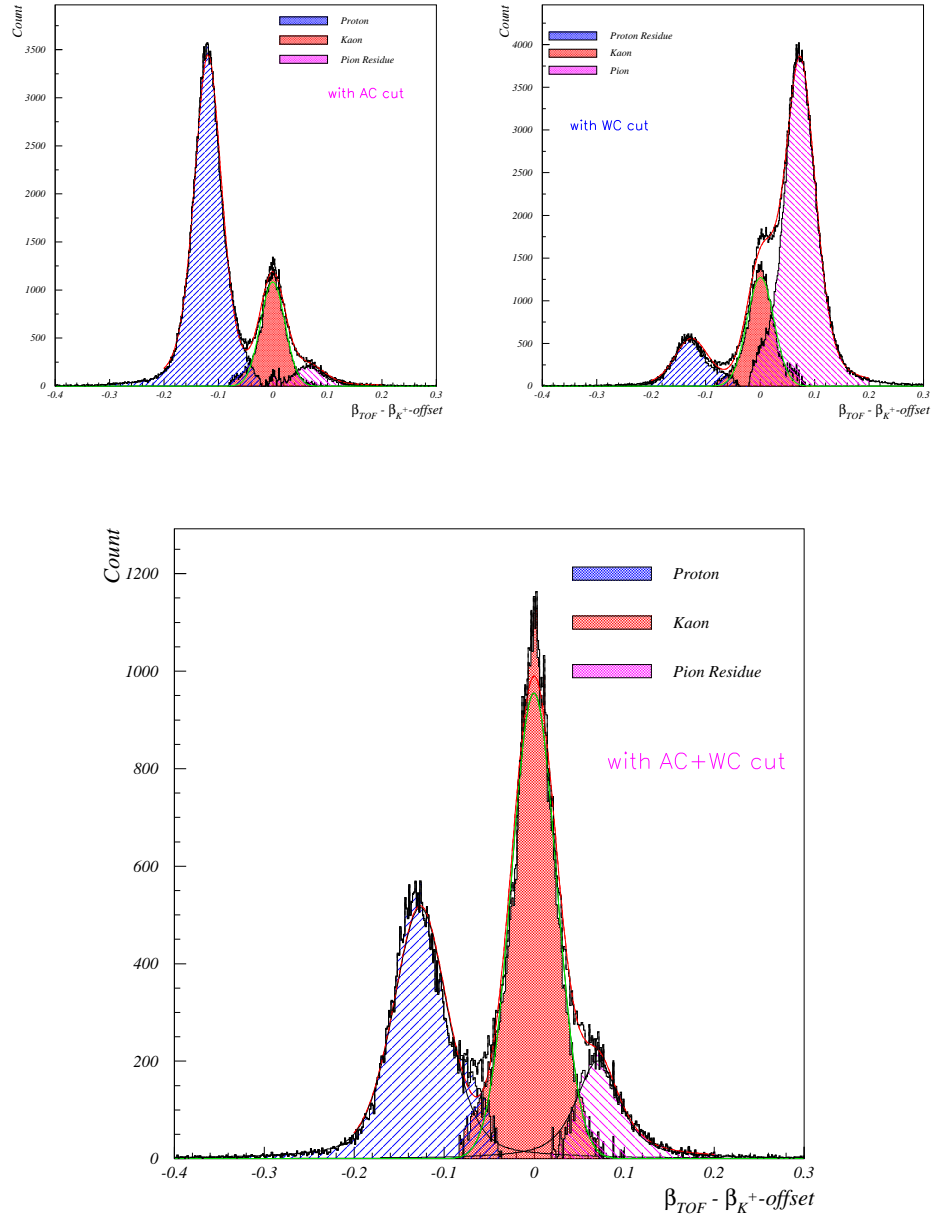
FIGURE 4.15: β_{ToF} SPECTRUM WITH APPLIED AEROGEL AND/OR WATER ČERENKOV CUTS. *Top Left* AC CUT $X_{AC} = 6$ WAS USED. *Top Right* AC CUT $X_{WC} = 80$ WAS USED. *Bottom* BOTH AC AND WC CUTS WERE APPLIED. ANALYSIS ON CH_2 DATA.
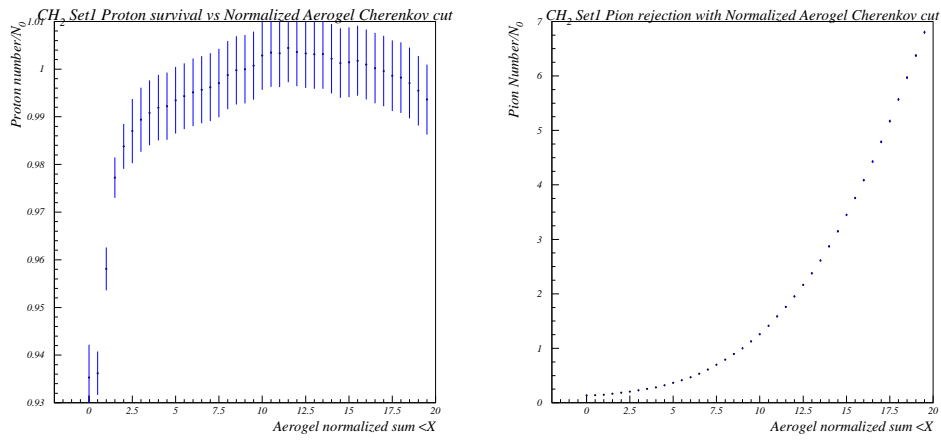
(a) Protonsurvival

(b) Pion rejection efficiency
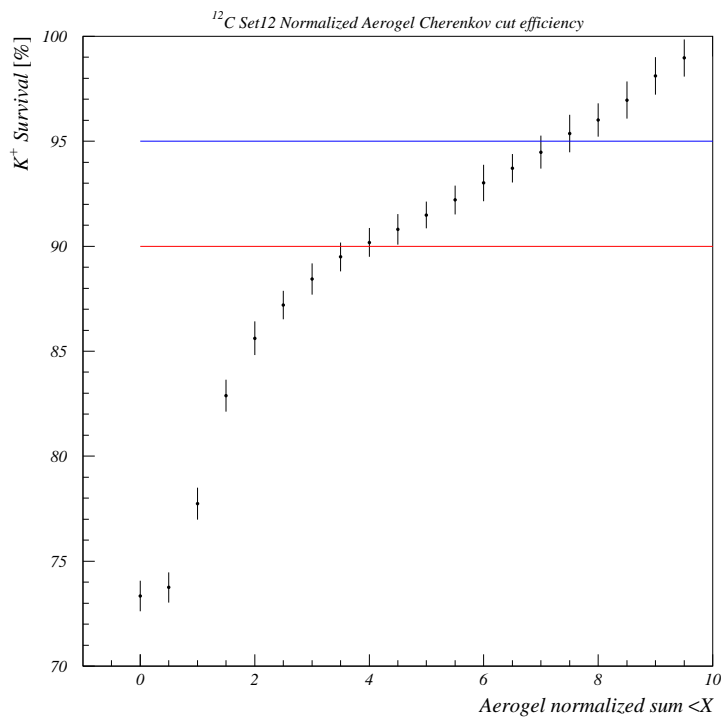
(c) Kaon survival efficiency

FIGURE 4.16: PROTON AND KAON SURVIVAL, PION REJECTION EFFICIENCY VS APPLIED AC CUT CONDITION. PION(PROTON) COUNT WAS NORMALIZED WITH THEIR NUMBER AT FINAL PID CUT CONDITION. ERRORS ARE STATISTICAL ONLY.
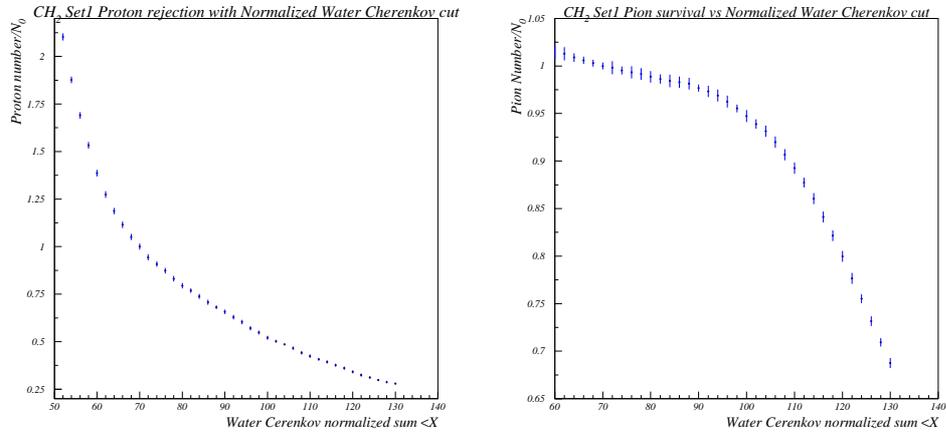
(a) Proton rejection efficiency

(b) Pion survival
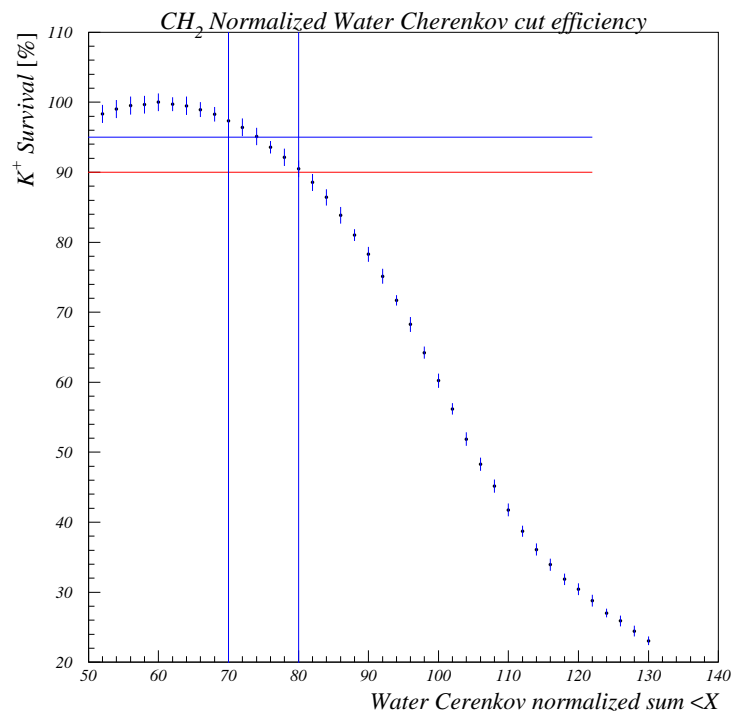
(c) Kaon survival efficiency

FIGURE 4.17: PION AND KAON SURVIVAL, PROTON REJECTION EFFICIENCY VS APPLIED WC CUT CONDITION. PION(PROTON) COUNT WAS NORMALIZED WITH THEIR NUMBER AT FINAL PID CUT CONDITION. ERRORS ARE STATISTICAL ONLY.

Time of flight β

Once Aerogel and Water Čerenkov PID cuts are finalized, time of flight β cut efficiency was calculated. By fitting β_{ToF}, with the applied AC and WC finalized cuts, proton, pion and kaon distribution in β spectrum are obtained. Proton and pion β distributions are then subtracted from β spectrum. The remaining events represent total number of kaons N_{0_β}.
Kaon distribution is now subjected to β cut condition in the form $|\beta_{TOF} - \beta_{K^+} - offset| < X_\beta$ and for set X_β value the number of remaining kaons N_{X_β} is calculated. The β cut efficiency is defined as the ratio of the number of kaons N_{X_β} with β cut and the number of kaons N_{0_β} before β cut. The results of the β cut condition and corresponding kaon survival efficiency for the used targets are summarized in Table 4.7.

PID analysis with coincidence time

Proton, kaon and pion distributions in coincidence time spectrum are clearly separate if, even loose, kaon cut conditions on AC, WC and β_{ToF} are used, as shown in Fig.4.1 and Fig.4.2. With protons centered around $-6ns$ and pions around $2ns$ they mostly contribute (especially protons) to real kaon coincidence peak, centered around $0ns$, through accidental coincidences.

PID analysis with coincidence time is done by fitting coincidence time distribution, the true coincidence peak and eight accidental coincidence bunches, with the combination of nine Gaussian functions. By integrating Gaussian functions, the number of events in each peak is calculated. The number of kaons in true coincidence peak is then extracted as:

$$N_{K^+} = N_{True} - \frac{1}{8} \sum_{i=1}^{8} N_{Accidental,i} \tag{4.7}$$

where N_{True} is the number of real coincidence events, $N_{Accidental,i}$ is the number of events in ith accidental peak.

By repeating this procedure for each combination of PID cut conditions $(X_\beta, X_{AC}, X_{WC})$ dependence of the number of kaons and dependence of the

signal to accidental ratio on PID cut conditions can be obtained, as shown in Fig. 4.18.

The advantage of this method over β cut lies in the clear separation of proton, kaon and pion distributions, consistent shape of the coincidence time and clear accidental and true coincidence peak separation that can be represented by nine Gaussian function. The overlap between pion/proton and kaon distributions in β spectrum is more pronounced, compared to their distributions in coincidence time. As a result of this and time fluctuations of β_{ToF} (see Fig.3.12) fitting β spectrum with the combination of two pseudo-Voigt and one Gaussian function PID analysis on β spectrum, as shown in Fig.4.14, might not result in a physically reasonable fit. The disadvantage of using coincidence time in PID analysis mostly comes from small kaon statistics in true coincidence peak because kaon events are now divided in multiple peaks. Also, since only eight accidental peaks are used in derivation of the number of events in accidental background, overestimation of background leading to underestimation of real coincidences is possible at PID cuts that allow high statistics of pions/protons. Kaon statistics is higher when using β spectrum because single arm analysis does not involve information from Enge side, including coincidence time. Both analyses are used simultaneously for the already mentioned reasons but also to cross check the obtained results.

PID check on Λ,Σ peaks

Combined statistics of Λ and Σ peaks, produced in elementary process $p(e,e'K^+)\Lambda/\Sigma$ on CH_2 target, was ≈ 3300 with ≈ 2700 counts in Λ peak and ≈ 600 counts in Σ peak. Other hypernuclear states had only few hundred counts. With such statistics in Λ and Σ peaks they can be used to check/confirm PID cut efficiencies obtained by analyzing β spectrum as described in Section 4.2.2. Missing mass spectra from CH_2 target was fitted by 2nd order polynom and pseudo-Voigt function multiplied by polynom. 2nd order polynom represents background due to accidental coincidences and quasi free contribution. The combination of pseudo-Voigt and polynom (also 2nd order) represents real Λ/Σ events. Subtracting the background from MM
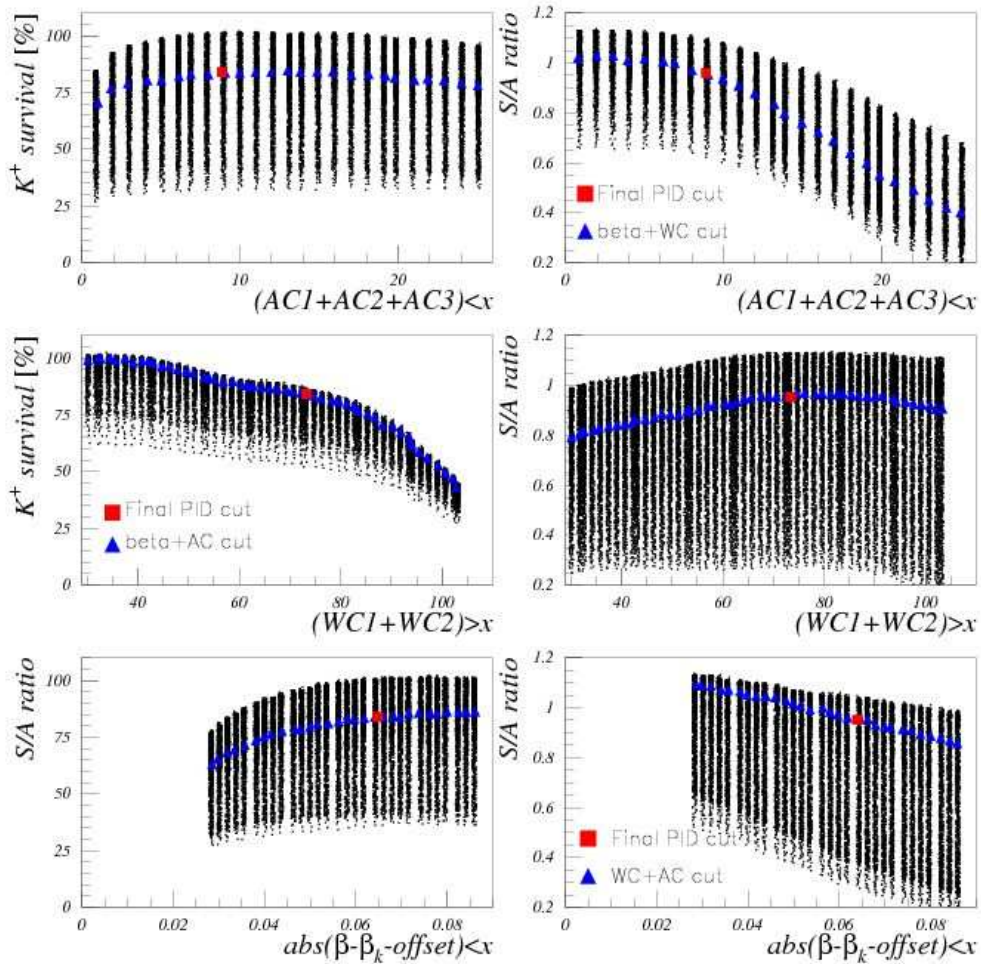
FIGURE 4.18: OPTIMIZATION OF PARTICLE IDENTIFICATION (PID) CUTS: AERO-GEL AND WATER ČERENKOV, TIME OF FLIGHT BETA WITH COINCIDENCE TIME DISTRIBUTION. CUTS WERE CHOSEN TO MAXIMIZE NUMBER OF REAL CONCI-DENCE EVENTS AND AND SIGNAL/ACCIDENTAL RATIO OBTAINED BY FITTING COINCIDENCE TIME DISTRIBUTION. DATA FROM ^{12}C TARGET.

(missing mass) spectra, the number of events in Λ and Σ peaks was extracted. MM spectra was plotted and number of events in Λ and Σ peaks extracted for numerous Aerogel Čerenkov, Water Čerenkov and β_{ToF} cut conditions. The efficiency of each cut selection was defined as ratio of the number of $\Lambda+\Sigma$ events with the applied cut condition and initial number of $\Lambda+\Sigma$ events. The calculation of missing mass spectra is explained in Section 4.3. Missing mass spectra obtained from CH_2 data, Λ and Σ peaks, are shown in Fig.4.23.

The importance of Λ and Σ peaks lies not only in showing that the designed experimental configuration works but more importantly in the calibration of spectrometer optics and kinematic conditions, a detailed discussion on this subject is in Section 4.4. To reconstruct optic and kinematic conditions, as close as possible to experimental settings, events in Λ and Σ peaks should come only from kaons, have the highest possible statistics and the best possible signal to background ratio. Signal to background ratio is defined as a ratio of the number of real Λ and Σ events to the number of events from background that contribute to Λ and Σ peaks.

For each AC (WC or β) cut condition all possible combinations of the other two PID tools were used and for all AC, WC and β cut condition calculated were: number of Λ and Σ events, signal to accidental background (S/A) ratio and signal to background (accidental background + quasi-free) (S/B) ratio. Fig.4.19, *Left* plots show number of events in Λ and Σ peaks once the accidental background is subtracted as a function of applied PID cut *Right* plots show signal to accidental background ratio as a function of the applied PID cut condition with at least 3300 events. Fig.4.20, *Left* plots show the number of events in Λ and Σ peaks once background (accidental + quasi-free) is subtracted as a function of the applied PID cut *Right* plots show signal to background ratio as a function of the applied PID cut condition with at least 2900 events. In both cases similar performance, with a tighter kaon cut number of kaons decreases and signal to background ratio increases until only kaons are left at which point this ratio becomes constant.

Fig.4.21 shows kaon survival efficiency as a function of applied PID cut condition. If we compare the final X_{AC}, X_{WC} and X_β and kaon survival efficiency, as shown in Fig.4.21, are compared to values obtained from β
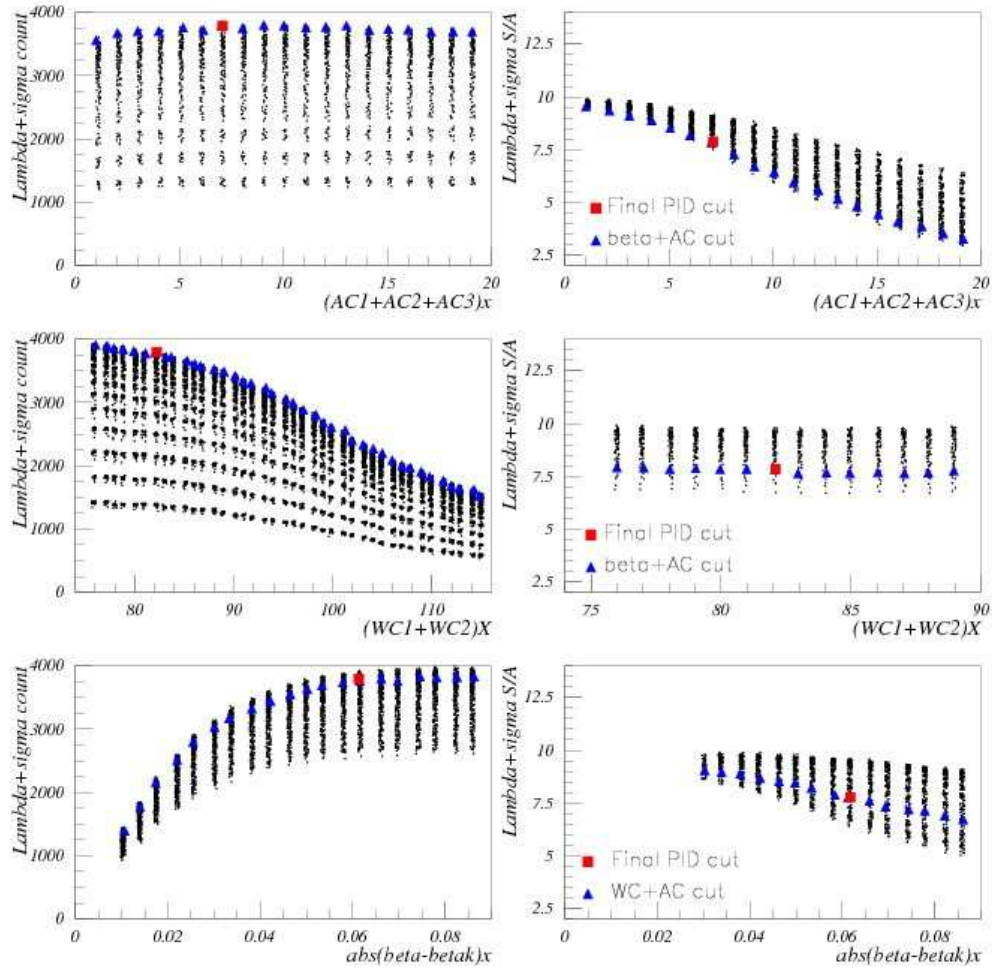
FIGURE 4.19: OPTIMIZATION OF PARTICLE IDENTIFICATION (PID) CUTS: AERO-GEL AND WATER ČERENKOV, TIME OF FLIGHT BETA WITH CH_2 DATA. CUTS WERE CHOSEN TO MAXIMIZE NUMBER OF THE EVENTS IN Λ AND Σ PEAKS AND SIGNAL/ACCIDENTAL RATIO.
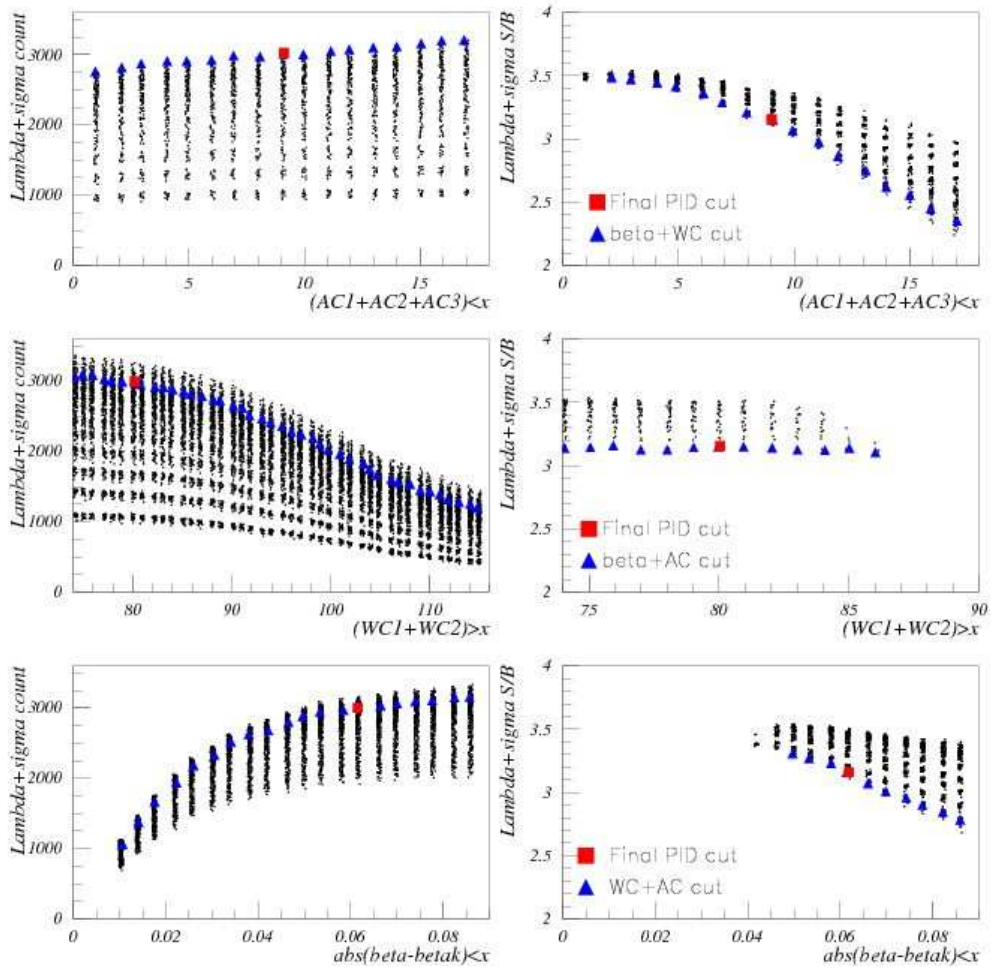
FIGURE 4.20: OPTIMIZATION OF PARTICLE IDENTIFICATION (PID) CUTS: AERO-GEL AND WATER ČERENKOV, TIME OF FLIGHT BETA WITH CH_2 DATA. CUTS WERE CHOSEN TO MAXIMIZE THE NUMBER OF EVENTS IN Λ AND Σ PEAKS AND SIGNAL/BACKGROUND RATIO.
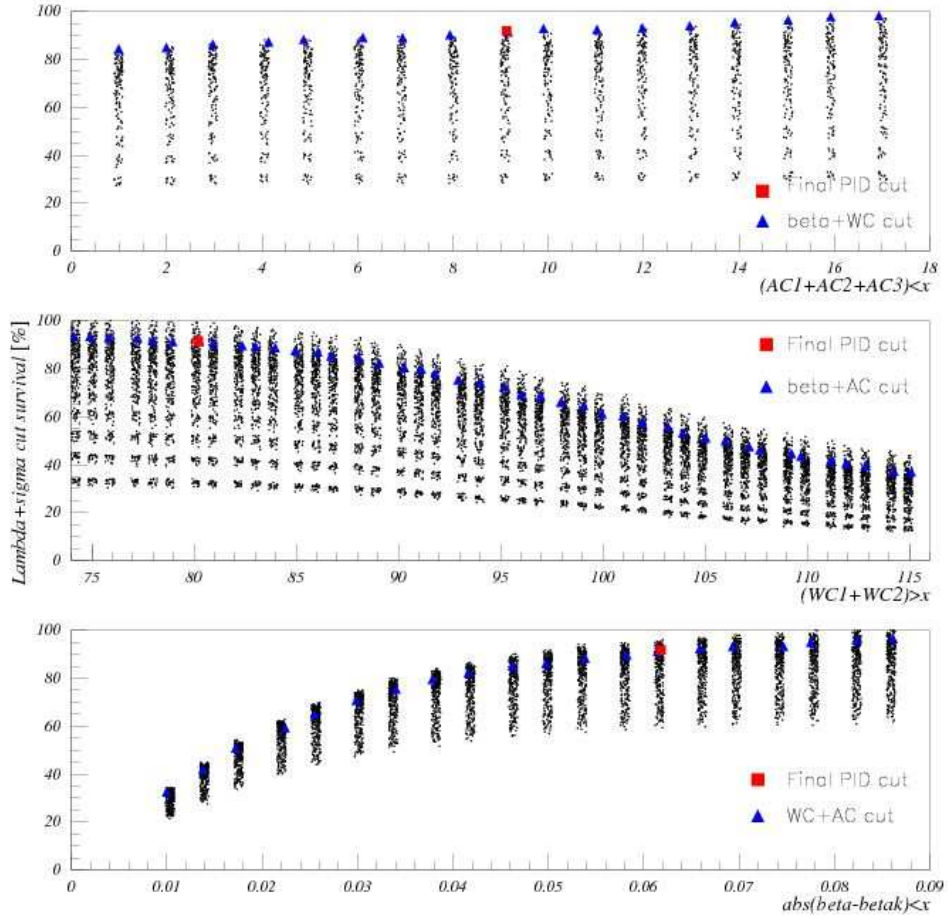
FIGURE 4.21: SURVIVAL OF KAONS, IN Λ AND Σ PEAKS FOR CH_2 DATA, AS A FUNCTION OF PARTICLE IDENTIFICATION (PID) CUTS: AEROGEL AND WATER ČERENKOV, TIME OF FLIGHT BETA.

spectrum, see Tables 4.5, 4.6 and 4.7, we see that they are consistent.

4.3   Missing mass spectra

Missing mass of Λ hypernuclei ($M_{X\Lambda}$) can be obtained from the conservation laws of energy and momentum if:

- ingoing electron momentum p_e

- nuclear mass of target nuclei M_A

- K^+ scattering angles θ_{K+}, ϕ_{K+} and momentum p_{K+}

- e' scattering angles $\theta_{e'}$, $\phi_{e'}$ and momentum $p_{e'}$

are known. Electron beam energy was well defined and known. Scattered electron and kaon, momenta and angles were reconstructed from focal plane quantities. Definition of coordinate system and scattering particle angles, defined with respect to electron beam direction, is shown in Fig.4.22. With all these variables known, $M_{X\Lambda}$ can be calculated if Eqn.4.8 is used.

$$
\begin{aligned}
M_{X\Lambda} &= (E_e + M_A - E_{e'} - E_{K+})^2 - p_e^2 - p_{e'}^2 - p_{K+}^2 \\
&+ 2p_e p_{e'} cos\theta_{e'} + 2p_e p_{K+} cos\theta_{K+} - 2p_{e'} p_{K+} cos\theta_{e'K+} \quad (4.8)
\end{aligned}
$$

Aside from the measured (reconstructed) momenta and angles, we also need masses of the particles involved in (e,e'K^+) reaction. Masses of the elementary particles are listed in Table 4.1. Nuclear masses of used targets, masses of the nuclear core of the corresponding hypernuclei and threshold energy for the reaction are listed in Table 4.2. Values in Table 4.2 were obtained from paper by G.Audi et al. [4] and nuclear mass equation 4.9.

$$
\begin{aligned}
M_{Nuclear} &= M_{Atom} - m_{electron}Z + B_{electron} \\
B_{electron} &= 14.4381 Z^{2.39} + 1.55468 Z^{5.35} 10^{-6} [eV], \quad (4.9)
\end{aligned}
$$
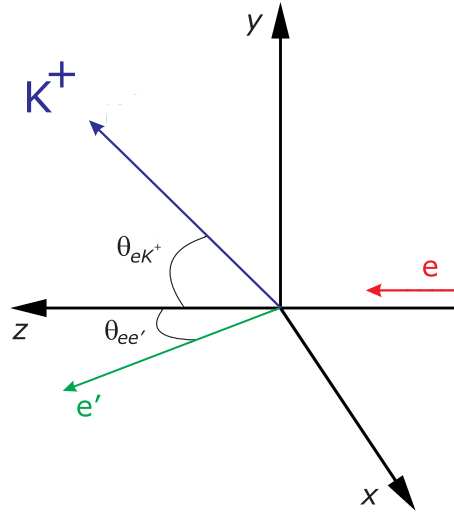
FIGURE 4.22: COORDINATE SYSTEM AND ANGLE DEFINITION USED IN MISSING MASS CALCULATION.

Particle	Mass [MeV/c^2]
electron	0.511
K$^+$	493.667
proton	938.272
neutron	939.565
Λ	1115.683
Σ	1192.642

TABLE 4.1: PARTICLE NUCLEAR MASS REFERENCES [4].

Target	Mass [MeV/c^2]	Nuclear core	Mass [MeV/c^2]	Hypernuclear state	Threshold Energy [MeV/c^2]
CH$_2$	938.272	-	-	Λ	1115.683
(proton)	938.272	-	-	Σ	1192.642
^6Li	5601.518	^5He	4667.831	$^6_\Lambda He$	5783.514
^7Li	6533.834	^6He	5605.537	$^7_\Lambda He$	6721.220
^9Be	8392.751	^8Li	7471.366	$^9_\Lambda Li$	8587.049
^{10}B	9324.437	^9Be	8392.750	$^{10}_\Lambda Be$	6721.220
^{12}C	11174.864	^{11}B	10252.548	$^{12}_\Lambda B$	11368.231
^{28}Si	26053.195	^{27}Al	25126.506	$^{12}_\Lambda Al$	26242.189

TABLE 4.2: NUCLEAR MASS REFERENCES [4] FOR THE E01-011 TARGETS.

$B_{electron}$-electron binding energy, Z-atomic number, $m_{electron}$-electron mass.

Missing mass plot from CH_2 data with clear evidence of Λ and Σ peaks with overlaid missing mass accidental background due to accidental coincidences in real coincidence peak is shown in Fig.4.23. Accidental background shows averaged missing mass spectra of the accidental coincidence events from total eight bunches with selection criteria as:

$$1[ns] < |Coincidence\ time| \leq 9[ns] \tag{4.10}$$

4.3.1 Accidental background analysis

Accidental background becomes relevant when one decides to calculate the hypernuclear cross section. To calculate the cross section accidental background has to be subtracted from missing mass spectra because in the real coincidence peak aside from the true coincidence events there is always a contribution of accidental coincidences as discussed in Sec.4.1 and shown in Fig.4.2.

Because accidental background has to be subtracted from missing mass spectra the statistical fluctuations in accidental background influence cross section calculation and therefore the background fluctuations should be minimized. To get accidental background with high statistics and small fluctuations we use mixed event analysis. A principle of mixed event analysis is described in Fig. 4.24. Events used in mixed event analysis are those that satisfy kaon PID cut conditions and belong to accidental coincidence peaks, see Fig. 4.2, and selected as written in Eqn. 4.10. Each event contains information on momenta and emission angles (p, x', y') of kaon and scattered electron. Mixed event analysis to each kaon momentum and emission angles $(p_{K^+}, x'_{K^+}, y'_{K^+})$ randomly assigns up to N (total number of events in accidental background) electron momenta and emission angles $(p_{e'}, x'_{e'}, y'_{e'})$. The result of mixed event analysis is increased accidental background statistics, from N counts in real data, to N^2 counts leading to smooth accidental background shape, as shown in Fig. 4.25, and smaller statistical error.
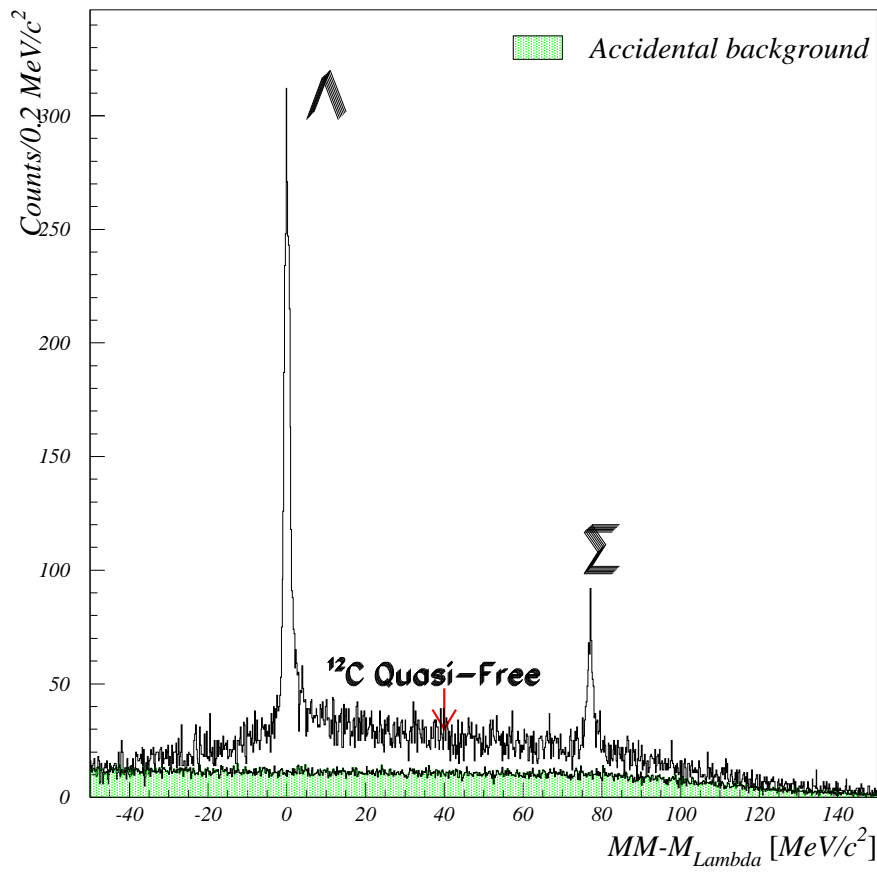
FIGURE 4.23: MISSING MASS SPECTRA FROM CH_2 DATA. Λ AND Σ PEAKS ARE CLEARLY SEEN. ACCIDENTAL COINCIDENCES AND QUASI-FREE CONTRIBUTION FROM ^{12}C ARE ALSO SHOWN.
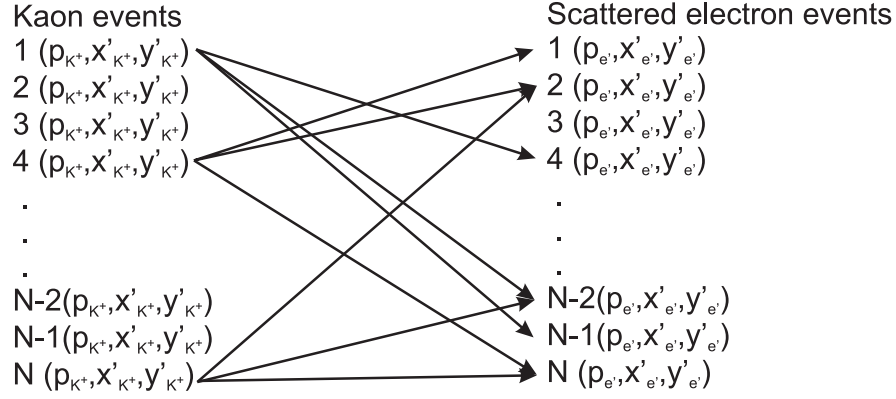
FIGURE 4.24: MIXED EVENT PRINCIPLE FOR ACCIDENTAL BACKGROUND ANAL-
YSIS.

4.4   Optics and kinematics calibration

Uniqueness of the E01-011 spectrometer system as well as procedures devel-
oped for the spectrometer optics and kinematics calibration are presented in
this section.

As described in Section 4.3 and Eqn. 4.8, to calculate missing mass
of Λ hypernuclei the kinematics of the reaction: beam energy, scattered
electron and kaon momenta $(p_{e'}, \theta_{ee'}, \phi_{ee'})$ and angles at the target point
$(p_{K^+}, \theta_{eK^+}, \phi_{eK^+})$ must be precisely known. In terms of the E01-011 expe-
riment this addresses: the absolute beam energy, spectrometer kinematics
(central momenta and angles of the two spectrometers) and spectrometer
optics (relative momentum and angles).

Once spectrometer optics and kinematics are well established, particle
momenta and target emission angles are reconstructed from focal plane vari-
ables by transfer matrices (M_{F2T}) that describe spectrometer optics and cen-
tral momenta and angle values. Transfer matrices are described with 6th
order polynomial in focal plane variables, see Eqn.4.11.
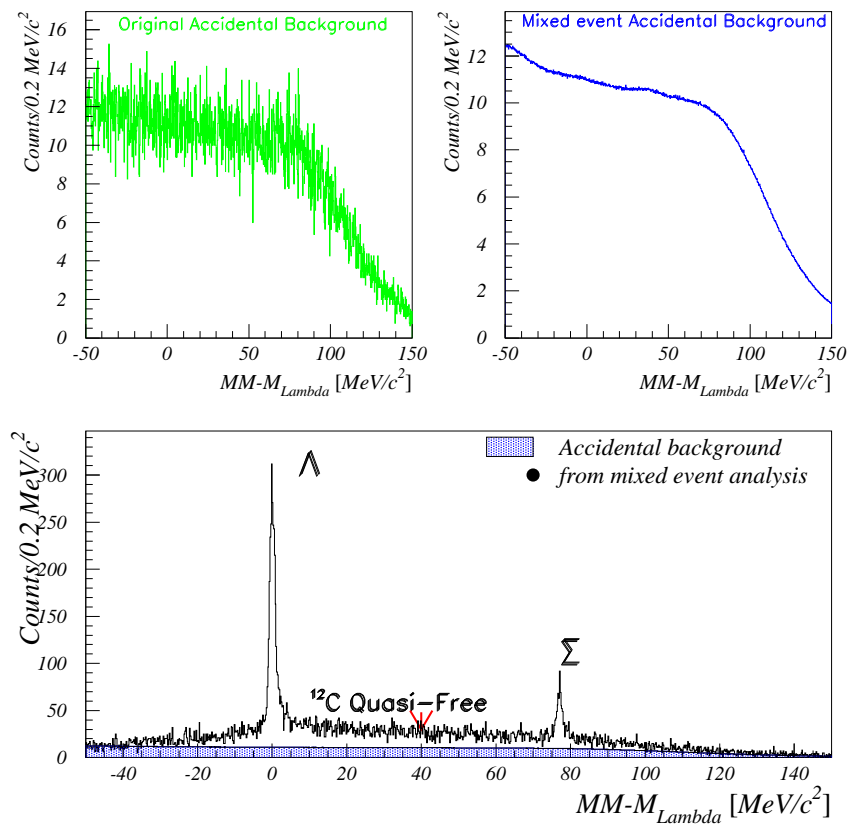
FIGURE 4.25: MIXED EVENT ANALYSIS OF ACCIDENTAL BACKGROUND ON Λ MISSING MASS SPECTRA. *Top Left* ACCIDENTAL BACKGROUND FROM REAL DATA. *Top Right* ACCIDENTAL BACKGROUND FROM MIXED EVENT ANALYSIS. BOTTOM MM SPECTRA WITH MIXED EVENT ACCIDENTAL BACKGROUND.

$$X_{Target} = \begin{pmatrix} dp \\ x\prime_t \\ y\prime_t \end{pmatrix} = M_{F2T} X_{Focal}$$

$$= \sum_{i+j+k+l=1}^{6} A_{ijkl} x_f^i x'^j_f y_f^k y'^l_f \qquad (4.11)$$

with particle momentum dp ($dp = (p - p_c)/p_c \times 100$), particle emission angles $x\prime_t, y\prime_t$ expressed as tangent of their X and Y component: $x\prime_t = P_x/Pz, y\prime_t = P_y/Pz$.

E01-011 spectrometer system

As described in Section 2.2 and 2.4, the so called Splitter magnet was part of the E01-011 spectrometer system. Splitter magnet was an on-target dipole magnet used for bending particles with opposite charge in different directions and at the same time enabled detection of very forward angle scattering particles connected with high virtual photon flux at small angles as shown in Fig. 2.4. Fig. 4.26 shows schematic view of magnetic optical properties of normal double arm spectrometer system and spectrometer system with an on-target dipole magnet (Splitter), as used in the E01-011 experiment.

In such a configuration, the on-target magnetic field of the splitter couples both electron and kaon arms together with the fixed beam dump line for electrons passing through target without interaction. As a result, typical spectrometer calibration procedures for momentum and angle reconstruction had to be modified. Spectrometer calibration by taking single arm electron elastic scattering data at different kinematics points can not be implemented here because of the electron and kaon arm coupling and this would change optics of the HKS spectrometer. Similarly, angle reconstruction calibration by sieve slit (collimator with an array of holes drilled on metal plate, see Fig. 4.28) had to be modified because with target being inside of the Splitter the sieve slit plate can only be mounted on the Enge and HKS dipole entrance after the Splitter, see Fig. 4.26. Thus, particle trajectories are bent by
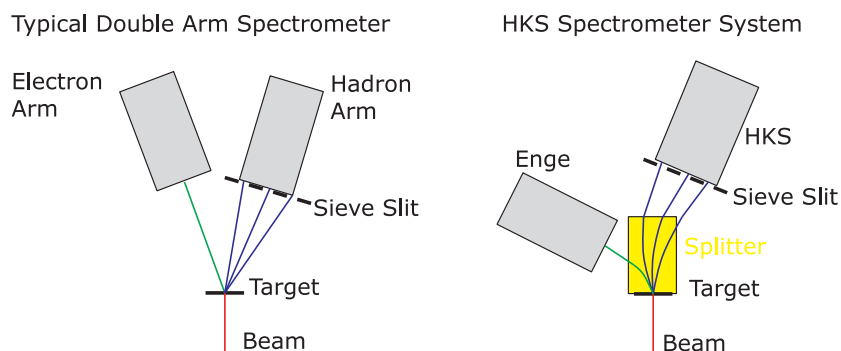
FIGURE 4.26: SCHEMATIC VIEW OF MAGNETIC OPTICAL PROPERTIES OF NORMAL DOUBLE ARM SPECTROMETER SYSTEM *(Left)* AND HKS SPECTROMETER *(Right)* WITH AN ON-TARGET DIPOLE MAGNET (SPLITTER)

the splitter field before they reach sieve slit and sieve slit holes no longer correspond to particle trajectories with fixed single angle values.

Calibration procedure

The calibration method developed [86] [85] for missing mass reconstruction in the E01-011 experiment used data taken from CH_2 and ^{12}C target and as a reference well known masses of Λ, Σ^0 hyperons and the ground state of the $^{12}_{\Lambda}B$ hypernucleus. Hypernuclear bound state is used to provide additional constraint on the optics because, compared to hyperons, contribution to missing mass error due to the uncertainty of the scattering angles of the recoiling particles is smaller. As a result, intrinsic peak width in missing mass spectrum of the $^{12}_{\Lambda}B$ hypernucleus is narrower.

A flow chart of the missing mass reconstruction procedure is shown in Fig. 4.27.

Field map: Tosca
Enge:Geant
HKS:Raytrace+Geant

⇩

Initial optics

⇩

Angle reconstruction M_{F2S} matrix
calibration:
Focal plane to Sieve Slit

⇩

Angle reconstruction M_{S2T} matrix   ⟺   Momentum reconstruction
calibration: matrix calibration
Sieve Slit to Target by MM

⇩

Kinematics calibration

⇩

Hypernuclear missing mass
spectra
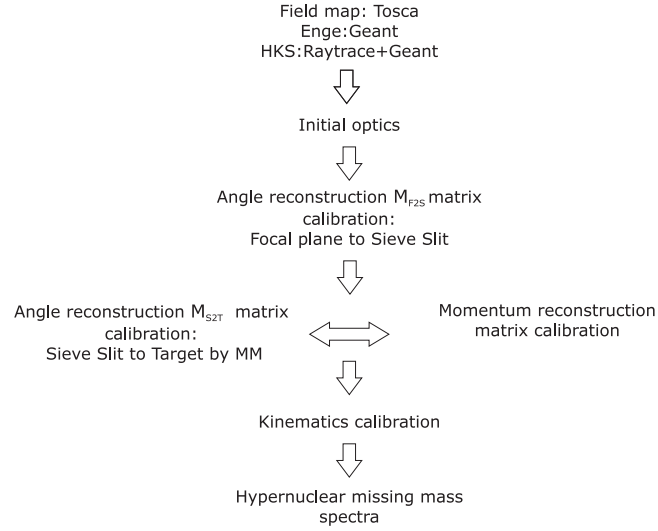
FIGURE 4.27: A FLOW CHART OF THE MISSING MASS RECONSTRUCTION PROCE-
DURE.

4.4.1   Calibration of the momentum reconstruction matrices

The momentum reconstruction matrices for the scattered e' and K^+ are
optimized simultaneously by directly minimizing a criterion function with
respect to these matrices. This also makes use of the known masses of hy-
perons like in kinematics calibration, but unlike kinematics calibration the
criterion function is defined as the sum of the squared differences between
the reconstructed masses and the predefined mass values as references for all
the events in Λ, Σ^0 peaks and the selected bound state of hypernuclei. A
set of statistical weights was given to the events from the specific state or
particle to take into account the effects of the variation of statistics and data
quality. A Nonlinear Least Square (NLS) method was used to optimize the
matrices for the electron and kaon arms simultaneously.

In this process, the mass values of Λ and Σ^0 hyperons are always their
PDG values. However, the peak positions for the bound hypernuclear states
were treated as adjustable parameters since their masses were not known.

Therefore, this procedure had to be iterated. The peak positions were fitted at each iteration and the predefined mass values were adjusted. Then the procedure was repeated until a minimum of Chisquare was reached for the current cycle of calibration. The procedure is detailed as:

1. Calculate the missing mass using the existing angular matrices, the initial momentum matrices, and the current kinematics obtained from the previous two procedures. Select events from Λ and Σ^0 peaks and the identified hypernuclear bound states peaks within event selection windows located around the centers of the missing mass peaks. (For each cycle of these documented procedures, the tightness of the event selection windows were increased following the improvement of resolution so that the data quality and so the precision was increased for the next cycle.)

2. Sum the squared mass differences Δm_i^2 between the reconstructed mass m_i^{rec} and the PDG value of Λ or Σ^0, or the predefined mass values of the bound hypernuclear states for each group of the selected events. Define the overall Chisquare as:

$$\chi^2 = \sum_i w_i \Delta m_i^2$$

where w_i is the relative weigh of Λ, Σ and bound state events.

3. The reconstructed missing mass m_i^{rec} is a function of e' and kaon momenta p_e, p_k and their scattering angles at target. The particle momenta p are in turn reconstructed by a polynomial function of measurements at spectrometer focal plane such as positions and angles with the elements of the momentum reconstruction matrix $\boldsymbol{M}$ as its coefficients. Thus the χ^2 defined above is a composite nonlinear function of the focal plane positions and angles x_{fp} with the reconstruction matrix $\boldsymbol{M}$ as parameter of the function:

$$\chi^2 = f(x_{fp}|\boldsymbol{M}).$$

The χ^2 is minimized with respect to (w.r.t.) the matrix $\boldsymbol{M}$ by the Nonlinear Least Square method to obtain the optimized Enge and HKS

momentum reconstruction matrices. Since f is a complex nonlinear
function, it has to been minimized numerically. The computer code uses
the subroutines from CERNLIB Fortran program package LEAMAX.

4. Fit the actual peak centers from the newly obtained missing mass spec-
   tra. Use the fitted values as the new predefined missing masses for the
   bound hypernuclear states. Go back to the first step and iterate until
   a minimum Chisquare is reached.

4.4.2   Calibration of the angular reconstruction matrices

As mentioned, because of the on-target splitter field, particle trajectories
passing through sieve slit hole, see Fig. 4.28, no longer have one specific
target emission angle. For this reason sieve slit run data can not (by itself)
be used for the calibration of transport matrix from focal plane variables to
target emission angles.

To calibrate angular reconstruction matrices and reconstruct target emis-
sion angles the procedure is divided into two steps: From focal plane to Sieve
slit plane (Enge or HKS) and from Sieve slit plane to target, as described
in Eqn. 4.12.

$$
\begin{array}{cccccc}
\text{Focal Plane} & & \text{Sieve Slit} & & \text{Target} & \\[4pt]
\begin{pmatrix} X_{FP} \\ X\prime_{FP} \\ Y_{FP} \\ Y\prime_{FP} \end{pmatrix} & \overset{M_{F2S}}{\Longrightarrow} & \begin{pmatrix} X_{SS} \\ Y_{SS} \\ dp \end{pmatrix} & \overset{M_{S2T}}{\Longrightarrow} & \begin{pmatrix} X\prime_{Tar} \\ Y\prime_{Tar} \end{pmatrix} & (4.12)
\end{array}
$$

Focal plane to Sieve slit calibration

The first part of angle matrix calibration, from focal plane to Sieve slit, for
both Enge and HKS spectrometers has to be done only once. Enge and HKS
collimator and Sieve slit are shown in Fig. 4.28. Focal plane patterns for

(a) Enge   (b) HKS
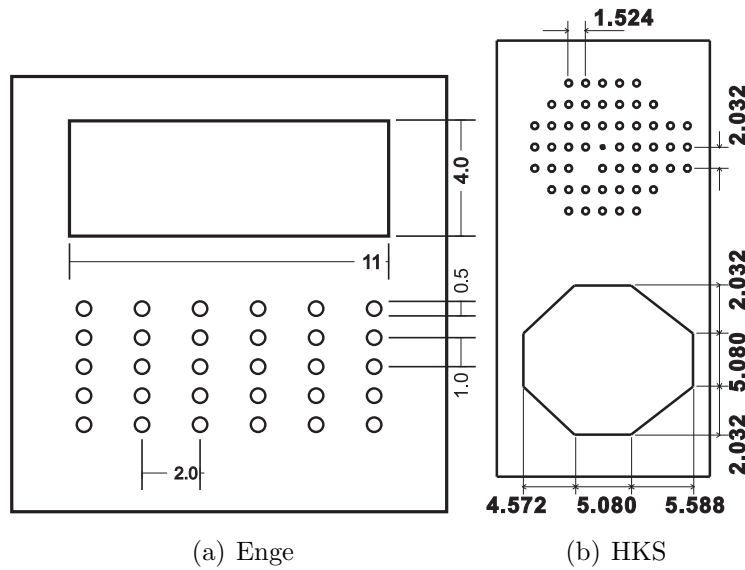
FIGURE 4.28: ENGE AND HKS COLLIMATOR AND SIEVE SLIT. UNIT IS CM.

Sieve slit run data for Enge and HKS sides are shown in Fig. 4.29. In this step of calibration, transport matrices from focal plane variables to particle trajectory position at Sieve slit plane x_{SS},y_{SS} are obtained.

Procedure for focal plane to Sieve slit calibration is:

1. Assign to each event Sieve slit hole it originated from by selection criteria on focal plane variable patterns and Geant/Raytrace simulated transport matrices.

2. Assign the SS hole center position $(x_{SS}$,$y_{SS})$ to each event that is associated with the corresponding hole.

3. Fit transfer matrix M_{F2S} from focal plane to Sieve slit plane: $(x_f$, x'_f, y_f, $y'_f) \longrightarrow (x_{SS}$,$y_{SS})$.

The results of the Sieve slit data calibration are shown in Fig. 4.30 for both Enge and HKS side. Sieve slit data transported by the M_{F2S} matrices, obtained in this calibration step, to the Enge/HKS Sieve slit plane clearly show Sieve slit patterns.
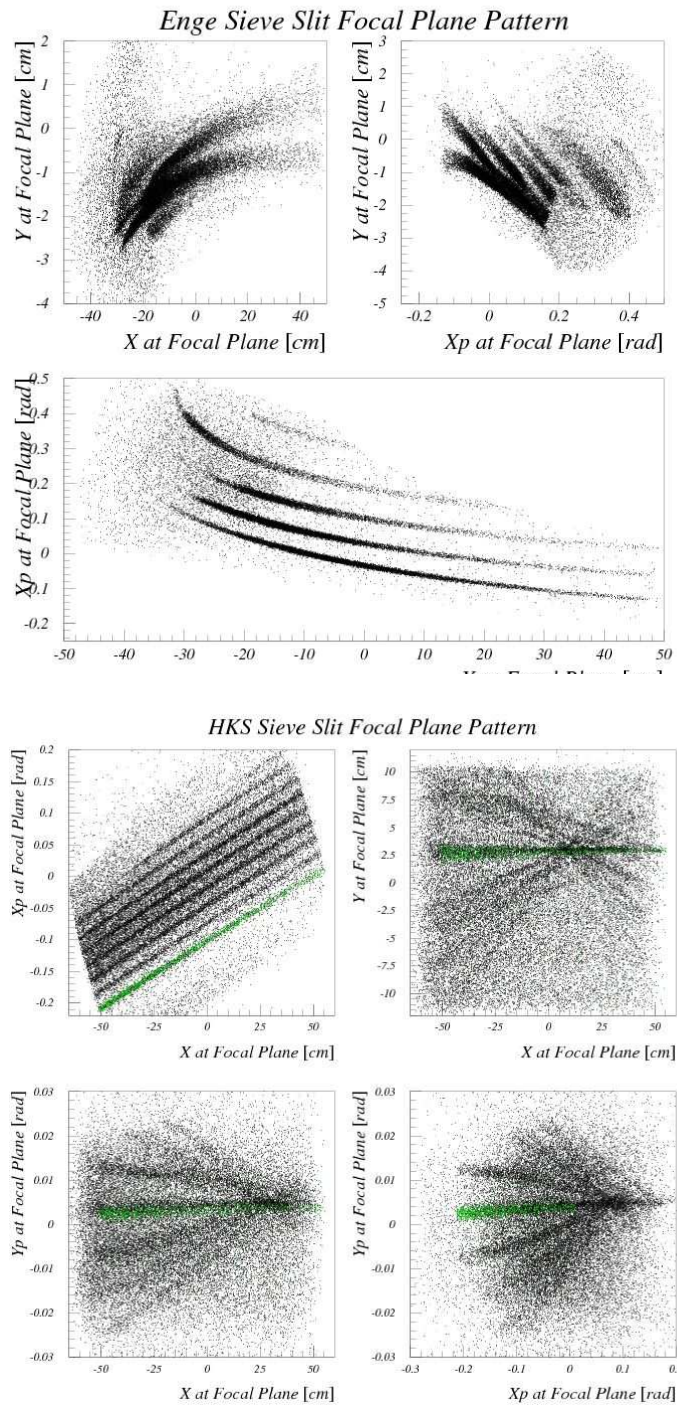
FIGURE 4.29: ENGE AND HKS FOCAL PLANE PATTERNS FOR SIEVE SLIT RUN DATA.
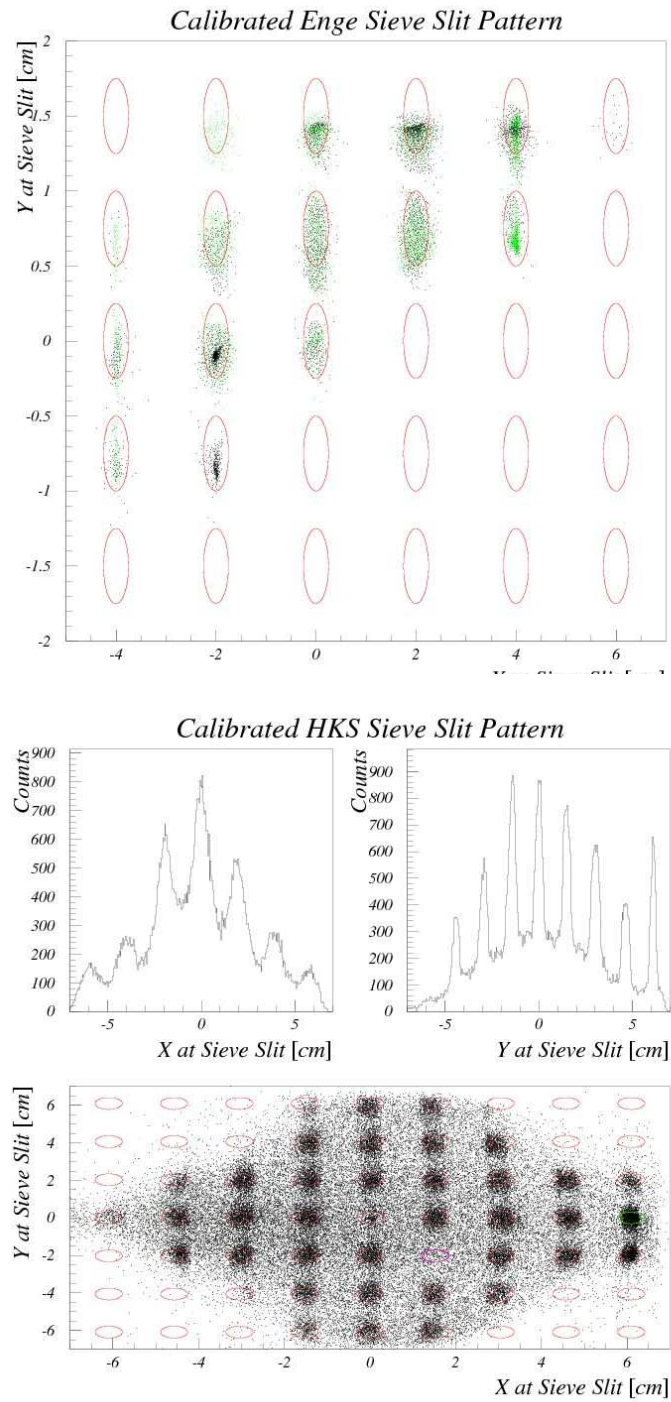
FIGURE 4.30: ENGE AND HKS CALIBRATED SIEVE SLIT PATTERN FOR SIEVE SLIT DATA RUN.

Sieve slit to target calibration

Based on the observation that there is a one to one correspondence between
the scattering angle from a point target and particle momentum and posi-
tions at Sieve slit plane, the scattering angles of particles at target can then
be calculated. Since this relation is influenced by the Splitter field, the ca-
libration can not be done with Sieve slit run data. Splitter field correction
is expected to be small because Splitter contributed $\sim 8\%$ of the total Bdl
of the e' arm or kaon arm. Initial angle reconstruction matrix M_{S2T} was
extracted from Geant simulations. Further optimization of M_{S2T} is done
by using the missing mass data for the hyperons and similar NLS method
as used to calibrate the momentum reconstruction matrix as described in
Section 4.4.1.

Procedure for Sieve slit to target part of the angle reconstruction calibra-
tion is:

1. Extract M_{S2T} from positions at Sieve slit plane, particle momentum
   and target angles based on the initial/simulated Splitter optics.

2. Reconstruct the target angles from focal plane variables from Sieve slit
   data obtained matrix M_{F2S} and M_{S2T} obtained from initial Splitter
   optics.

3. Calibrate initial M_{S2T} from reconstructed missing mass and the known
   hyperon mass values as references.

4.4.3 Calibration of spectrometer kinematics

The purpose of the kinematics calibration for the HKS spectrometer is to find
the real values of the absolute beam energy, Enge and HKS spectrometer
central momenta. They may deviate from nominal values as a result of
accelerator operation and magnetic settings of Enge and HKS spectrometer.

To find real values of kinematic setting kinematic offsets $\triangle E_{Beam}$, $\triangle p_{e'}^0$
and $\triangle p_{K+}^0$ are added to all three nominal values $E_{Beam}, p_{e'}^0$ and p_{K+}^0. The

widths of the reconstructed missing mass peaks of Λ, Σ^0 and their offsets from known masses are calculated and used in the two χ^2 functions definition:

$$\begin{array}{rcl} \chi^2_{pos} & = & w_\Lambda (m_\Lambda^f - m_\Lambda^{PDG})^2 + w_\Sigma (m_\Sigma^f - m_\Sigma^{PDG})^2 \\ \chi^2_{wid} & = & w_\Lambda \sigma_\Lambda^2 + w_\Sigma \sigma_\Sigma^2, \end{array} \qquad (4.13)$$

where the m_Λ^f and m_Σ^f are the fitted centers of Λ and Σ^0 peaks, σ's are the peak widths of Λ, Σ^0 and w_Λ and w_Σ are the weight factors. The values of the widths is chosen based on the sensitivity of different masses to the kinematics offsets and the statistics, S/N ratio and the expected resolution of these masses.

Offsets to nominal values $\triangle E_{Beam}, \triangle p_{e'}^0$ and $\triangle p_{K^+}^0$ are scanned in the region of interested with 50KeV step and at each combination (scanning point) χ^2 function, as defined in Eqn.4.13, are calculated.

Kinematic variables V_{Kin} defined as:

$$V_{Kin} = \triangle E_{Beam} - \triangle p_{e'}^0 - \triangle p_{K^+}^0$$

is used to view χ^2 dependence on kinematic parameters. Fig.4.31 shows dependence of the two χ^2 functions on kinematic offset V_{Kin}. The error bars represent χ^2 errors caused by the error in the hyperon peak fit. Both plots show clear χ^2 dependence on kinematic parameters.

The kinematic point which minimizes χ^2_{wid} and has χ^2_{pos} below a certain value is selected as the correct kinematic point. The limiting value of χ^2_{pos} depend on the fitting error of the peak centers and specific kinematic of the spectrometer, which has been determined from simulation in the HKS case. This criterion of minimizing χ^2_{wid} is better as it decouples kinematic offsets from effect of optical distortion because it is independent from optical calibration which also utilized the mass offsets from references on a event by event basis as criterion to determine the correct optics.
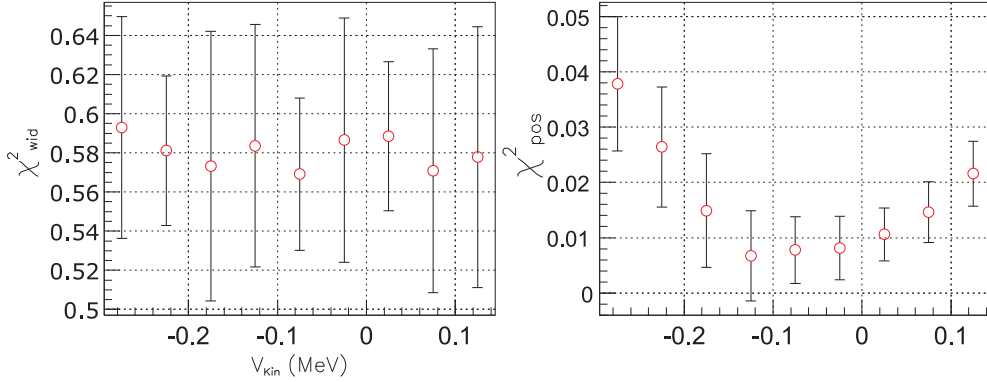
FIGURE 4.31: χ^2_{pos} AND χ^2_{wid} AS FUNCTIONS OF KINEMATICS OFFSET V_{Kin}. THE ERROR BARS REPRESENT THE ERROR OF THE χ^2 CAUSED BY THE ERROR IN THE HYPERON PEAK FIT.

4.4.4   Beam shift correction

Offset of the beam from expected central trajectory at designated positions is what BPMs measure. Fig.4.32 shows stability of beam position (trajectory) during the E01-011 experiment as measured by Hall C Arc Beam Position Monitors (BPM). The most stable BPM readouts were obtained form IPMC07y, IPMC12y and IPMC17x. BPMs IPMC07x, IPMC12x and IPMC17y showed noticeable shifts and/or spreads in beam position measurement.

With beam steering magnets producing stable magnetic field the reason for this offsets is due to (small) beam energy changes. These beam energy shifts then lead to shifts in MM spectra, see Eqn.4.8, as clearly represented in Λ MM spectra in Fig.4.33.

This effect was studied on CH_2 data - Lambda peak because it had the highest statistics from all measured hypernuclear states. Beam energy shifts are best represented with the measured beam positions from following three BPMs: IPMC07x, IPMC12x and IPMC17y. Beam energy shift dependence on the BCM measured beam position is of linear type, as described in Eqn.4.14:

$$\frac{\delta E}{E} = C_0 + C_1 \frac{dX_7}{R_0} + C_2 \frac{dX_{12}}{R_0} + C_3 \frac{dY_{17}}{R_0}, \qquad (4.14)$$
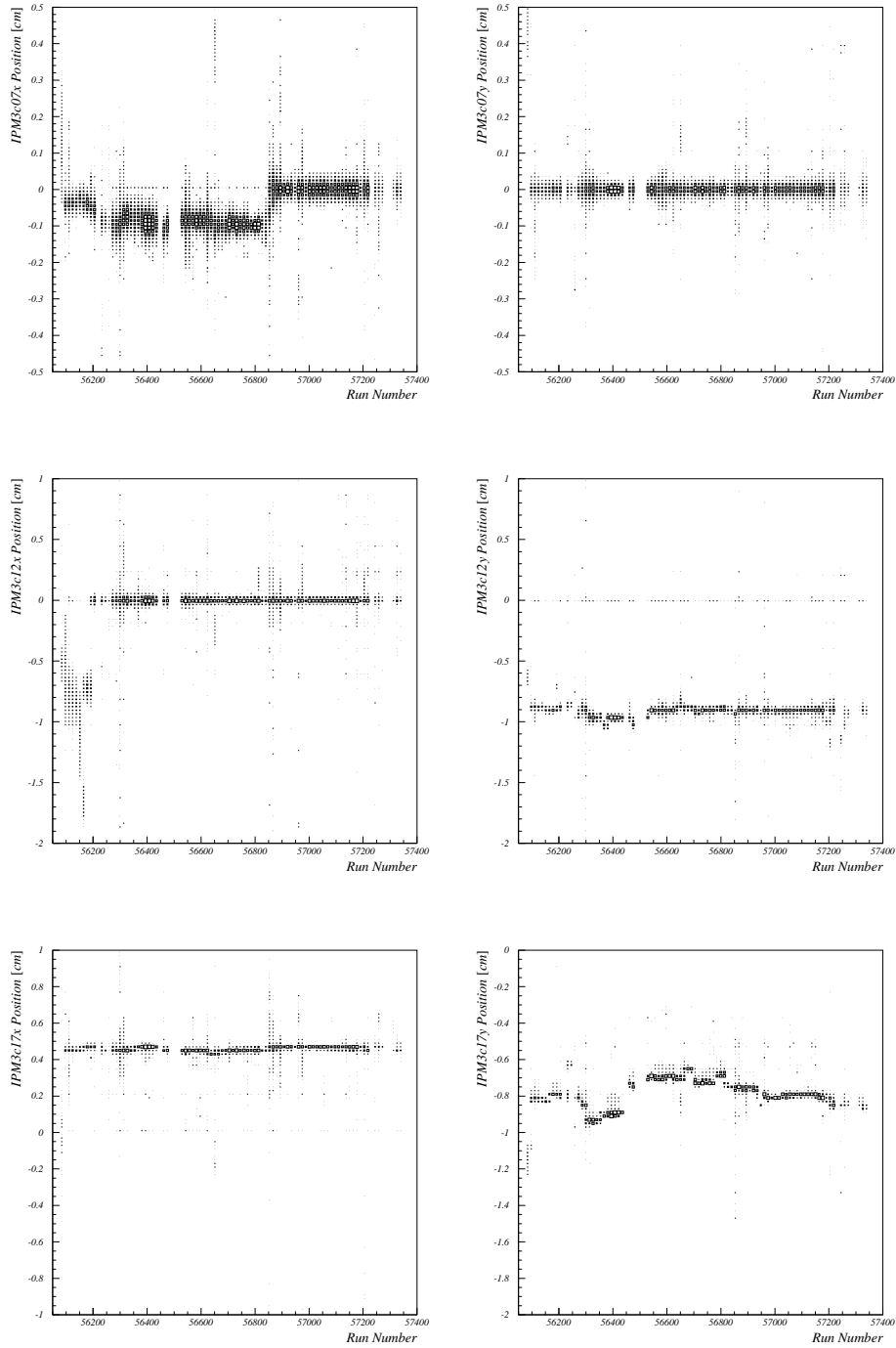
FIGURE 4.32: HALL C ARC BEAM POSITION MONITORS (BPM) READOUT.
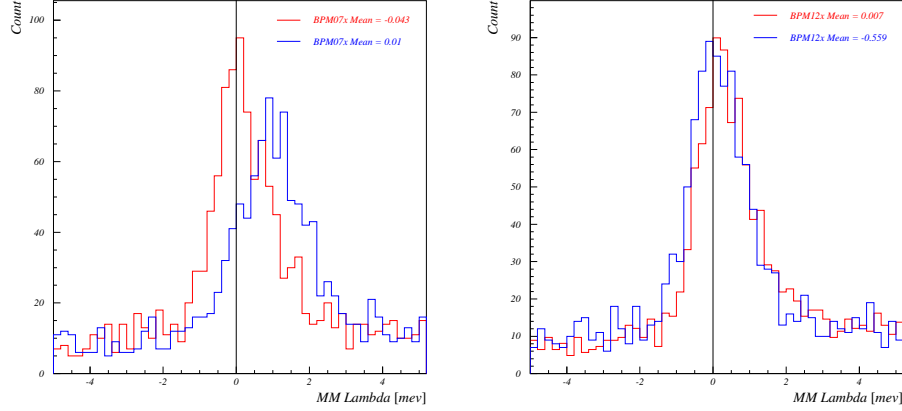
FIGURE 4.33: LAMBDA MM SPECTRA FOR TWO CH_2 DATA SETS WITH DIFFER-
ENT BPM CONDITIONS. MASS OF Λ SUBTRACTED FROM MM SPECTRA. *Left*
BPM-IPM307x *Right* BPM-IPM312x

where δE is beam shift; E=1853MeV nominal beam energy; dX_7, dX_{12}, dY_{17}
are beam shifts measured by IPMC07x, IPMC12x, IPMC17y, respectively;
R_0=40.09 m Hall C Arc radius.

The four unknowns are the coefficients $C_0 - C_3$ so CH_2 data was divided
into four data sets. For each set values of the Λ mass offsets from PDQ value
and averages of the dX_7, dX_{12} and dY_{17} are extracted. This gave four sets of
equations with four unknowns. The calculated values of the coefficients are:
$C_0 = 0.00207$, $C_1 = 34.32$, $C_2 = 3.25$ and $C_3 = 5.06$.

The obtained beam energy correction was used on data from all targets.
The beam energy correction effect on the Λ peak is shown in Fig.4.34. The
correction influences Λ peak twofold: First, peak with correction is clearly
centered around zero, as expected since this plot shows: MM spectra-M_Λ;
Second, peak with correction became more prominent (higher with a smaller
width). The difference in the two Λ peak positions is 350 keV.
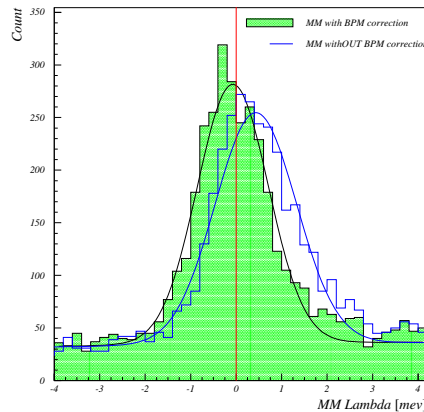
FIGURE 4.34: LAMBDA MM SPECTRA FOR TWO CH_2 DATA SETS WITH DIF-
FERENT BPM-IPM307x CONDITIONS. MASS OF Λ SUBTRACTED FROM MM
SPECTRA.

4.5 HDC resolution

Resolution of the HKS drift chambers can be studied once optical proper-
ties of the spectrometer system and kinematic settings are established as
described in Sec.4.4. HDC performance is in detail described in Sec.3.4.3
and here, with the known residual and Chi2 distributions of the HDC, the
resolution of the track reconstructed focal plane quantities as well as the
resolution of the reconstructed particle momentum are discussed.

HDC resolution was studied on CH_2 data with selected kaon events. Kaon
trajectories were projected onto each HDC plane and HDC wire numbers
and drift distances obtained. Monte Carlo simulated offsets (corresponding
to residual information) were added to drift distance values at each plane ac-
cording to residual distributions measured in the E01-011 experiment. Sim-
ulated HDC events were reconstructed by HDC tracking code producing a
new set of focal plane X_f, X_{fp}, Y_f, Y_{fp} values. For each kaon event a few hun-
dred tracks with simulated drift distance errors were calculated. In addition,
the resolution of HDC when only ten or eleven of HDC planes are used in
reconstruction of the HKS focal plane variables was also studied.

For each simulated event differences $\delta X_f, \delta X_{fp}, \delta Y_f, \delta Y_{fp}, \delta p$ between simulated and real data, HDC focal plane X_f, X_{fp}, Y_f, Y_{fp} and particle momentum values were calculated. X_f, X_{fp}, Y_f, Y_{fp} resolutions correspond to the sigma values of the Gaussian fit of the $\delta X_f, \delta X_{fp}, \delta Y_f, \delta Y_{fp}$ distributions. Momentum resolution corresponds to the value of the parameter C_3 (Voigt sigma) when δp distribution is fitted with pseudo-Voigt function. HDC momentum resolution did not have Gaussian distribution because dependence between particle momentum and focal plane variables was described with 6th order polynomial producing pseudo-Voigt type of distribution from initial Gaussian like ones. Fig.4.35 shows dependence of the focal plane variable resolutions on the number of HDC planes used in the reconstruction. As expected, the resolutions became worse when less planes in track reconstruction were used.

Typical distribution of the momentum shift for simulated data for the events in the central trajectory region is represented in Fig.4.36. Non-Gaussian shape is clearly seen.

With real data hypernuclear states Λ, Σ and $^{12}_{\Lambda}B$ used in calibration of the E01-011 spectrometer system, as described in Sec.4.4, focal plane regions with higher statistics had the best resolution. This effect is clearly seen in Fig.4.37 since the best HDC momentum resolution (Voigt sigma) achieved $90 \pm 5 keV$ in was in the region $0cm < Xf < 35cm$. In terms of FWHM this corresponds to 210 ± 12 keV which is close to expected HDC momentum resolution of 180 keV (FWHM). Average momentum resolution is 175 ± 5 keV. Errors are only statistical. From *Top Right* plot shows that introducing residual offsets did not produce offsets (C_4:mean of the Voigt fit) in the momentum distribution. The data of each targets was divided into two sets (regions): RegionI-$Xf_{ENGE} \leq -12cm$ and RegionII-$Xf_{ENGE} > -12cm$.

Fig.4.38 shows dependence of the momentum resolution on number of planes used in track reconstruction. Similarly as in the case of focal plane variables, events that had more planes on the track also had a better resolution.
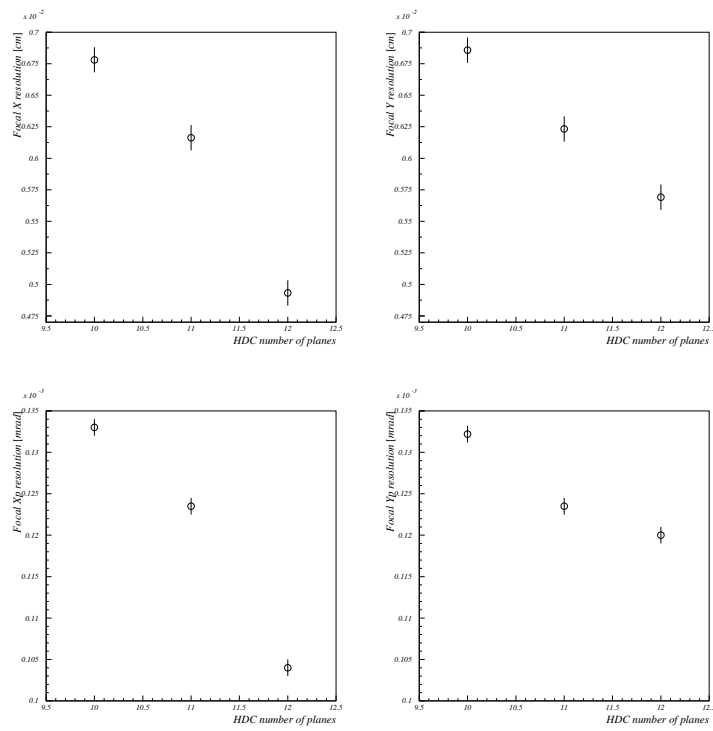
FIGURE 4.35: AVERAGE RESOLUTION OF HKS FOCAL PLANE QUANTITIES AS A FUNCTION OF THE NUMBER OF HDC PLANES USED IN TRACKING ALGORITHM. ANALYSIS WAS DONE FOR CH_2 DATA AND RESOLUTION IS DEFINED AS SIGMA OF THE GAUSSIAN.
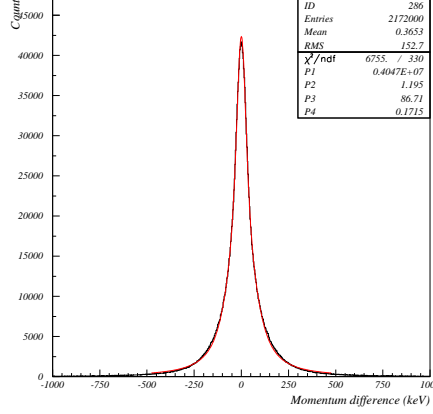
FIGURE 4.36: TYPICAL HDC MOMENTUM RESOLUTION DISTRIBUTION SIMU-
LATED FROM REAL DATA TRACKS AND RESIDUALS. PARTICLE MOMENTA ARE
RECONSTRUCTED WITH REAL OPTICS. DISTRIBUTION IS FITTED WITH VOIGT
FUNCTION.

4.6   Mass scale error

The systematic error in the mass scales was extracted by fitting Λ and Σ
peaks in the missing mass spectra obtained from CH_2 data, see Fig.4.23, by
using fitting errors in the Λ and Σ peak positions according to Eqn.4.15:

$$dM_{systematic} = \sqrt{dM^2_{\Lambda\ Peak} + dM^2_{\Sigma\ Peak}} \qquad (4.15)$$

The Λ and Σ peaks were fitted by a combination of pseudo-Voigt function
and 2nd order polynomial as described in Eqn.4.16 and Eqn.4.18. The Λ
peak is fitted by function in Eqn.4.16 and Λ peak with function defined in
Eqn.4.18. The choice of the fitting function was based on the results of
the HDC momentum resolution study, see Section 4.5, and the shape of the
background and quasi-free distribution.
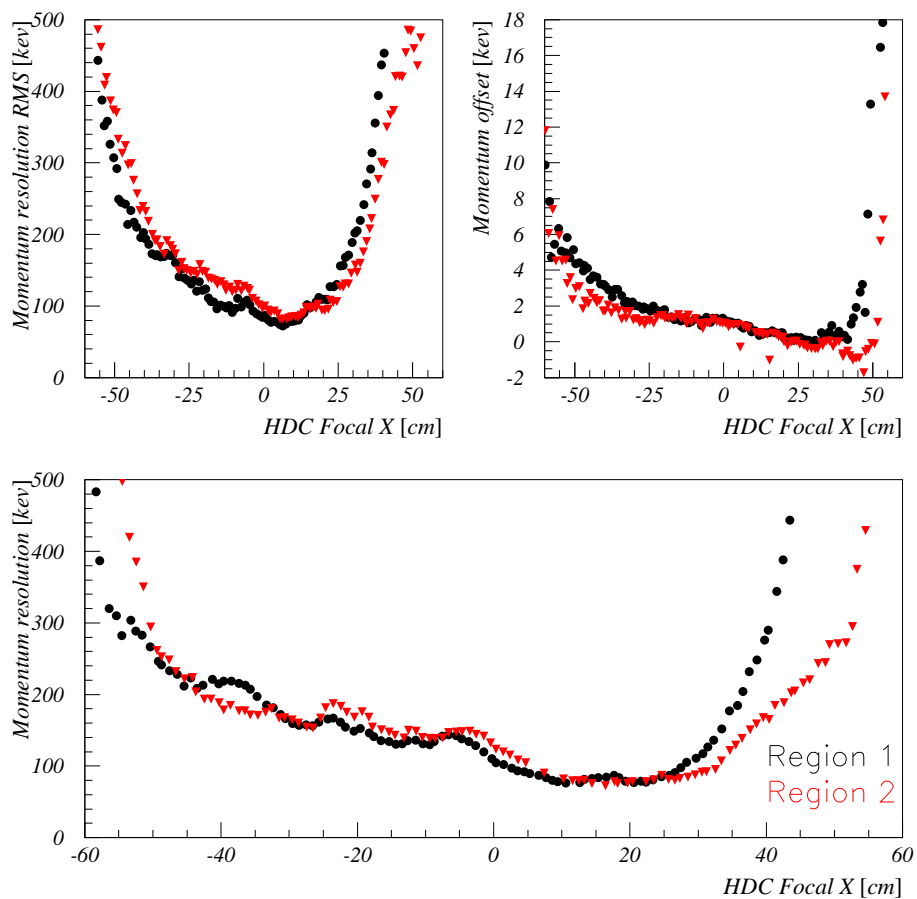
FIGURE 4.37: MOMENTUM RESOLUTION OF HDC OVER HKS FOCAL PLANE. *Top Left* MOMENTUM RESOLUTION ROOT MEAN SQUARE (RMS). *Top Right* MOMENTUM OFFSET: PEAK OF RESOLUTION DISTRIBUTION. *Bottom* HDC MOMENTUM RESOLUTION, SIGMA OF VOIGT FUNCTION, OVER HKS FOCAL PLANE.
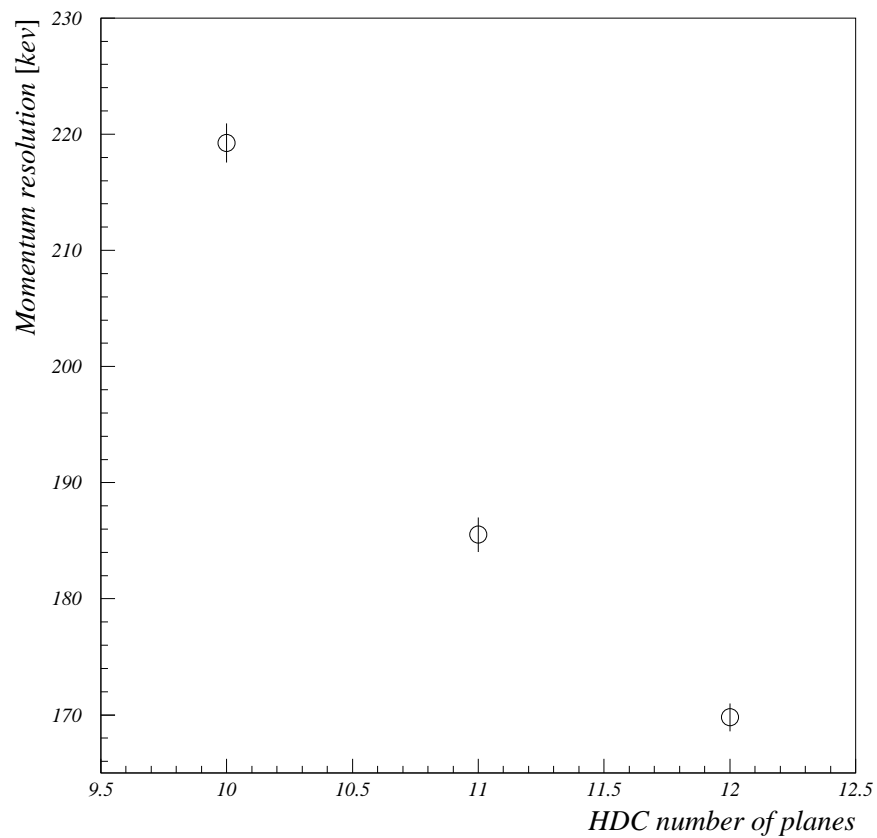
FIGURE 4.38: AVERAGE MOMENTUM RESOLUTION OF HDC FOR CH_2 DATA AS A FUNCTION OF NUMBER OF HDC PLANES USED IN TRACKING ALGORITHM. ANALYSIS WAS DONE FOR CH_2 DATA AND HDC MOMENTUM RESOLUTION IS DEFINED AS SIGMA OF VOIGT FUNCTION. ERRORS ARE ONLY STATISTICAL.

$$
\begin{aligned}
F_\Lambda(x) \;=\; & C_1 \left[\frac{2}{\pi} \frac{C_2 C_3}{4(x - C_4)^2 + C_3^2} + (1 - C_3) \frac{\sqrt{4Ln2}}{\sqrt{\pi} C_3} e^{-\frac{4Ln2}{C_3^2}(x - C_4)^2} \right] \\
& * \; \left[C_5 + C_6 x + C_7 x^2 \right] + C_8 + C_9 x + C_{10} x^2 \qquad (4.16)
\end{aligned}
$$

$$
\begin{aligned}
F_\Sigma(x) \;=\; & C_1 \left[\frac{2}{\pi} \frac{C_2 C_3}{4(x - C_4)^2 + C_3^2} + (1 - C_3) \frac{\sqrt{4Ln2}}{\sqrt{\pi} C_3} e^{-\frac{4Ln2}{C_3^2}(x - C_4)^2} \right] \qquad (4.17) \\
& * \; (1 + C_5(x - C_4) + C_6(x - C_4)^2) + C_7 + C_8(x - C_4) + C_9(x - C_4)^2,
\end{aligned}
$$

where $x = MM - M_{\Lambda/\Sigma}$; $F_\Lambda(x)$ and $F_\Sigma(x)$ represents number of counts.

The results of the Λ and Σ fit are shown in Fig.4.39 and Table 4.3. With Λ and Σ mass errors as in Table 4.3 the systematic error of the mass scale was estimated to be $\approx 0.1 MeV$. The Λ and Σ mass resolution, as listed in Table 4.3, does not represent expected resolution of the hypernuclear states in the E01-011 experiment since it is mostly due to kinematic broadening of the elementary process $p(e,eK^+)\Lambda$ which decreases with the target mass.

	MM_X-$M_{\Lambda/\Sigma}$	FWHM [MeV/c^2]
Λ	0.01±0.03	2.83±0.28
Σ	0.04±0.08	3.20±0.34

TABLE 4.3: PARTICLE NUCLEAR MASS REFERENCES.
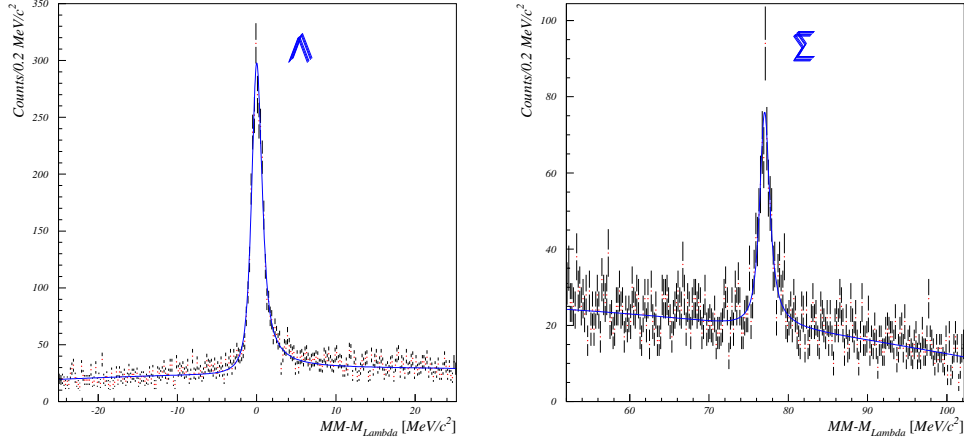
FIGURE 4.39: MISSING MASS SPECTRA OF THE $p(e, e'K^+)\Lambda/\Sigma$ REACTIONS FROM
CH$_2$ WITH FITTING RESULTS OF THE Λ/Σ PEAK BY THE POLYNOMIAL OF THE
2nd ORDER AND PSEUDO-VOIGT FUNCTION. ERRORS ARE STATISTICAL.

4.7   Cross section

The cross section of the photoproduction reaction (γ_*, K^+) is derived from
the unpolarized $(e,e'K^+)$ cross section which can be written in terms of the
virtual photon flux factor and the L/T unseparated photon absorption cross
section $\frac{d\sigma_\gamma}{d\Omega_k dp_k}$ as:

$$\frac{d^6\sigma}{d\Omega_{e'}d\omega d\Omega_{K+}dp_{K+}} = \Gamma(E_{Beam}, \omega, \theta_{ee'})\frac{d\sigma_\gamma}{d\Omega_k dp_{K+}}. \qquad (4.18)$$

In the case of discrete final nuclear states, scattering kaon momentum
p_K can be calculated from e' momentum, angle and kaon scattering angle.
The cross section dependence on kaon momentum p_k vanishes. The double-
differential photon absorption cross section $\frac{d\sigma_\gamma}{d\Omega_k dp_k}$ is reduced to $\frac{d\sigma_\gamma}{d\Omega_k}$. Thus
the yield from a discrete nuclear state is:

$$N_s = \frac{L}{A}\rho dN_e\epsilon \int_{\Delta\Omega} \int_{\Delta\omega} \Gamma d\omega d\Omega \int_{\Delta\Omega_k} \frac{d\sigma_\gamma}{d\Omega_k}d\Omega_k \qquad (4.19)$$

where ϵ is the correction factor, $N_T^{-1} = \frac{N_A}{A}\rho th$ is the effective area of one

scattering center and N_e number of electrons (N_A- Avogadro's number, A-atomic number, ρ-target density $[g/cm^3]$, th-target thickness [cm]. By replacing photon absorption cross section $\frac{d\sigma_\gamma}{d\Omega_k}$ with an average photon absorption cross section over HKS solid angel $\overline{\frac{d\sigma_\gamma}{d\Omega_k}}$ this can be simplified and so the cross section of the photoproduction reaction (γ^*, K^+) can be written as:

$$\overline{\left(\frac{d\sigma_\gamma^*}{d\Omega_{K^+}}\right)}_{1°-13°} = \frac{1}{N_{Target}}\frac{1}{N_\gamma}\sum_{i=1}^{N}\frac{1}{\epsilon_{Final}d\Omega} \qquad (4.20)$$

where N_{Target} is the number of target centers, N_γ is the number of virtual photons, $d\Omega$ is solid angle acceptance of HKS, N represents experimental yields of hyperons (Λ, Σ) or a hypernuclear state, ϵ_{Final} is a correction factor describing detector efficiencies.

Detector efficiencies that are included in the definition of the ϵ_{Final} are:

1. Hodoscope efficiency: ϵ_{Hodo}

2. HTOF1Y dead space : ϵ_{HTOF1Y}

3. Enge drift chamber tracking efficiency : ϵ_{EDC}

4. HKS drift chamber tracking efficiency : ϵ_{HDC}

5. Aerogel Čerenkov cut efficiency: ϵ_{AC}, see Sec. 4.2.2

6. Water Čerenkov cut efficiency : ϵ_{WC}, see Sec. 4.2.2

7. $\beta_{TOF} - \beta_{K^+} - offset$ cut efficiency : ϵ_β, see Sec. 4.2.2

8. Coincidence time cut efficiency : ϵ_{Coin}, see Sec 4.1

9. Computer live time : $\epsilon_{LiveTime}$

10. Kaon absorption factor : ϵ_{Abs}

11. Kaon decay factor : ϵ_{Decay}

and definition of the ϵ_{Final} can be written as:

$$\epsilon_{Final} = \epsilon_{Hodo} \cdot \epsilon_{HTOF1Y} \cdot \epsilon_{AC} \cdot \epsilon_{HDC} \cdot \epsilon_{AC} \cdot \epsilon_{WC} \cdot \epsilon_\beta \cdot \epsilon_{Coin} \cdot \epsilon_{LiveTime} \cdot \epsilon_{Abs} \cdot \epsilon_{Decay}$$
$$(4.21)$$
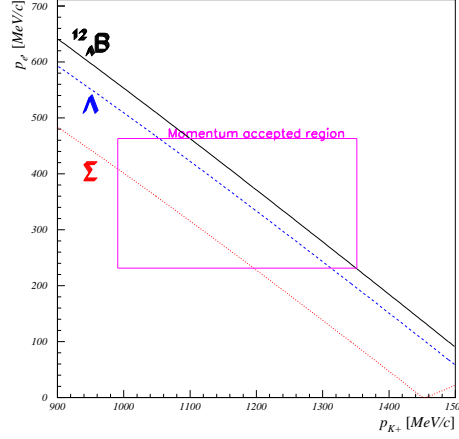
FIGURE 4.40: ENGE AND HKS MOMENTUM CORRELATION. CALCULATED FROM EQN. 4.8 FOR Λ, Σ AND $^{12}_{\Lambda}\text{B}$ GROUND STATE WITH BEAM ENERGY $E_e = 1.853$ AND SCATTERING ANGLE VALUES: $\theta_{eK+} = 0.119 rad$ AND $\theta_{ee\prime} = 0.065 rad$

4.7.1 Momentum and Solid angle Acceptance

Momentum acceptance

Momentum correlation between scattered electron ($p_{e\prime}$) and kaon can be calculated from missing mass equation, see Eqn. 4.8, if other quantities are known. Fig. 4.40 shows calculated momentum correlation between scattered electron and kaon for Λ and Σ hyperons and $^{12}_{\Lambda}\text{B}$ ground state. The calculation was done with incident beam energy $E_e = 1.853$ and target scattering angles $\theta_{eK+} = 0.119 rad$ for kaon and $\theta_{ee\prime} = 0.065 rad$ for scattered electron. Selected angle values represent central values of the scattered electron and kaon as obtained from CH_2 and ^{12}C data set, see Fig. 4.42.

Fig. 4.41 shows Enge and HKS momentum correlation as obtained from CH_2 data set. The correlation, as shown in Fig. 4.40, is also plotted on this figure. As expected, there is an agreement between real data momentum correlation and the calculated one as a result of detailed optics calibration. The Enge and HKS momentum acceptances were obtained from real data, once momentum and angle reconstruction matrices were calibrated, as $p_{e\prime} =$
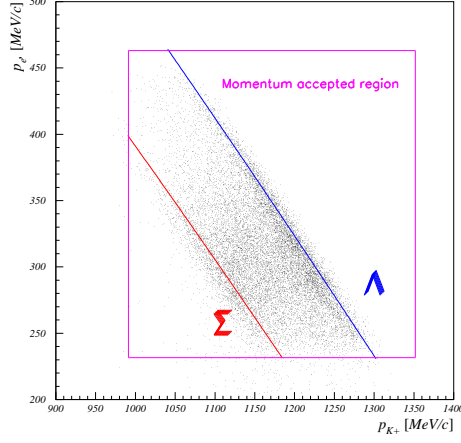
FIGURE 4.41: ENGE AND HKS MOMENTUM CORRELATION FOR CH$_2$ DATA. KAON PID SELECTION WAS DONE.

$341.7 MeV/c \pm 35\%$ and $p_{K^+} = 1202 MeV/c \pm 12.5\%$.

Solid angle acceptance

Fig. 4.42 shows correlation between reconstructed emission angles (θ, ϕ) for scattered electron and kaon from ^{12}C data with kaon PID selection.

Solid angle acceptances of Enge and HKS spectrometer systems were calculated by using RAYTRACE and GEANT. Parameters values as used in RAYTRACE/GEANT calculation are:

	Enge parameters		HKS parameters
$\triangle\theta$:	$0.05 < \theta < 0.31$ rad	$\triangle x'_{Tar}$:	$-0.27 < \theta < 0.27$ rad
$\triangle\phi$:	$0 < \phi < 2\pi$ rad	$\triangle y'_{Tar}$:	$-0.27 < \theta < 0.27$ rad
$\triangle p_{e'}$:	$188 < p_{e'} < 507$ MeV/c	$\triangle p_{K^+}$:	$950 < p_{e'} < 1450$ MeV/c

The result of the simulation is momentum dependent solid angle $SA(p_{e'}/p_{K^+})$, as defined in Eqn.4.22, calculated for both Enge and HKS spectrometers.

(a) e' angle correlation   (b) K$^+$ angle correlation
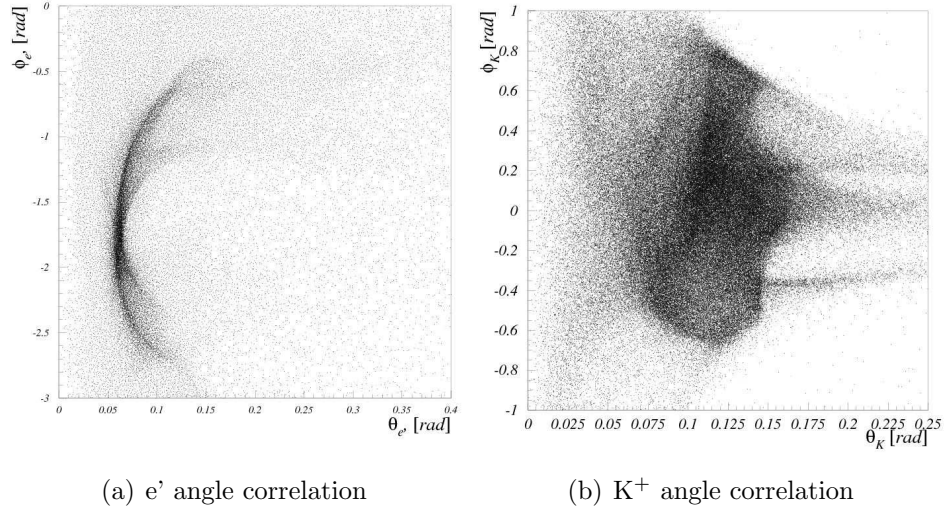
FIGURE 4.42: CORRELATION BETWEEN RECONSTRUCTED EMISSION ANGLES (θ, ϕ) FOR SCATTERED ELECTRON (*Left*) AND KAON (*Right*) FROM ^{12}C DATA WITH K$^+$ PID SELECTION.

$$SA(p_{e'}/p_{K^+}) = \triangle\Omega_{e'/K^+} \frac{Number\ of\ accepted\ events}{Number\ of\ generated\ events} \frac{\triangle p_{e'/K^+}}{p_{e'/K^+}} \qquad (4.22)$$

Ω is angular acceptance, for Enge spectrometer it represents $\triangle\theta \cdot \phi$ and in case of HKS $\triangle x'_{Tar} \cdot y'_{Tar}$.

Fig. 4.43 shows obtained momentum dependent solid angle for Enge and HKS spectrometer. Statistical error in solid angle calculation was estimated to be $\approx 1\%$.

4.7.2   Virtual photons

The number of virtual photons (N_γ) is obtained by integrating virtual photon flux $\Gamma(E_e, \omega, \theta_{ee'})$, as defined in Section 2.2 and Eqn. 2.1, as written in Eqn.4.23

$$N_\gamma = \frac{Q}{e} \int \int \Gamma(E_e, \omega, \theta_{ee'}) SA(p_{e'}) d\omega d\Omega_{e'} \qquad (4.23)$$
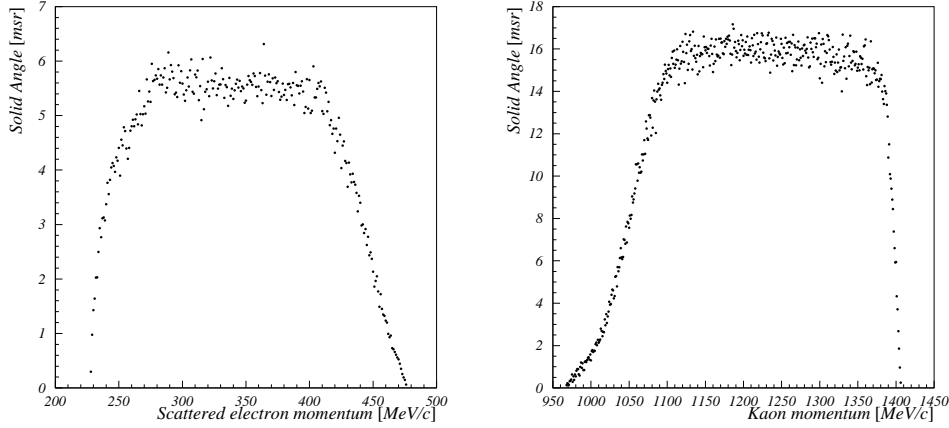
(a) Enge solid angle momentum dependence

(b) HKS solid angle momentum dependence

FIGURE 4.43: SOLID ANGLE DEPENDENCE ON PARTICLE MOMENTUM. *Left* ENGE SPECTROMETER *Right* HKS SPECTROMETER

where Q is total charge, e is elementary charge, E_e is incident electron energy (Beam energy), ω is energy of virtual photon in the range $1339 < \omega < 1604$ [MeV], $\theta_{ee'}$ is electron scattering angle and $SA(p_{e'})$ is Enge solid angle. Virtual photon flux, integrated over electron scattering angle, $\Gamma(\omega)$ dependence on scattered electron momentum is shown in Fig.4.44. The number of virtual photons per electron was calculated as $4.805 \cdot 10^{-6}$ by integrating virtual photon flux $\Gamma(\omega)$ with respect to virtual photon energy. Systematic errors to a number of virtual photons per electron are mostly due to misalignment of the magnets ($\approx 0.25mm$) estimated to be $\approx 22\%$ and from beam current monitor calibration $\approx 2\%$.

4.7.3 Correction factors

Hodoscope efficiency

With all the hodoscope layers being used in the trigger setup hodoscope trigger efficiencies (ϵ_{Hodo}) were studied with trigger events that had multiple
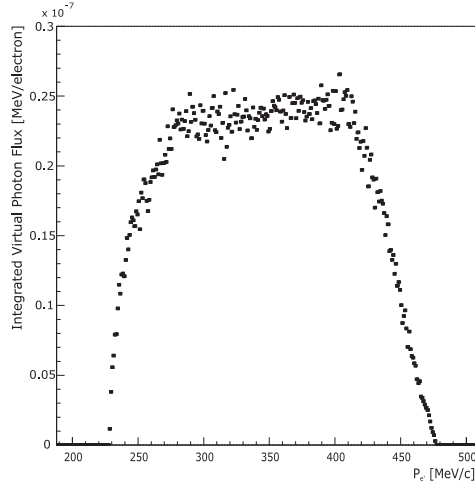
FIGURE 4.44: VIRTUAL PHOTON FLUX $\Gamma(\omega)$ INTEGRATED OVER ELECTRON SCATTERING ANGLE.

HDC tracks. For such an event one of the tracks is from particle that produces trigger and so all the hodoscope on this track will a signal. The remaining tracks are result of high rates and are not correlated with the trigger and so they can be used to estimated hodoscope efficiency. Obtained values for hodoscope trigger efficiency was $\epsilon_{Hodo} = 99.6 \pm 0.1\%$.

HKS hodoscope layer HTOF1Y was included in the trigger from run number 58410 to decrease the number of random triggers. Geometrical setup of this layer was such that it had gaps in between adjacent hodoscopes resulting in trigger dead space. Hodoscope were stacked in Y-direction. Fig.4.45 shows trackable events with tracks projected on the HTOF1Y plane, gaps in between hodoscopes are seen as trackable events dead space. The effect of HTOF1Y dead space was extracted from comparison of data with and without HTOF1Y in trigger. Result of the dead space effect on number of triggers was estimated to be $5 \pm 1\%$ ($\epsilon_{HTOF1Y} = 95 \pm 1\%$).

Drift chamber cuts

Drift chamber performance and tracking efficiency are discussed in Sec.3.4.2 and Sec.3.4.3. Acceptable EDC and HDC trajectories were selected based on
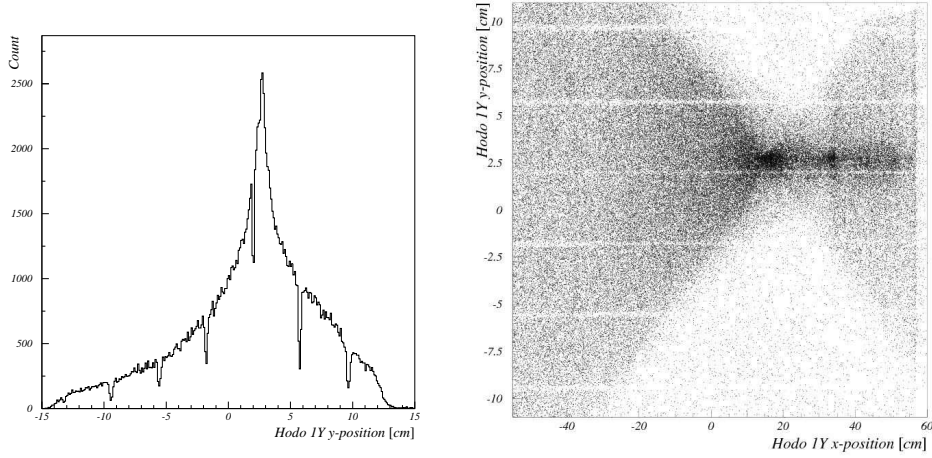
FIGURE 4.45: HODOSCOPE LAYER HTOF1Y DEAD SPACE.

their Chi2 values. Chi2 selection criterium effects EDC and HDC tracking efficiencies, as shown in Fig.4.46 and Fig.4.47. Both drift chambers exhibit similar Chi2 dependence with an obvious distinction in that HDC showed better tracking efficiency with most tracks having low Chi2 values. HDC and EDC Chi2 cuts used and their respective efficiencies for all data sets are summarized in Table4.4.

PID cut efficiencies

Detailed study of PID detectors, Aerogel and Water Čerenkov and Time of Flight hodoscopes, and their performances is discussed in Section 3.4. Definition of PID variables and the form in which they are used to separate kaons from protons and pions/positrons

- $|\beta_{TOF} - \beta_{K^+} - offset| \leq X_{ToF}$

- $AC1norm + AC2norm + AC3norm < X_{AC}$

- $WC1norm + WC2norm > X_{WC}$

is discussed in Section 4.2.1.
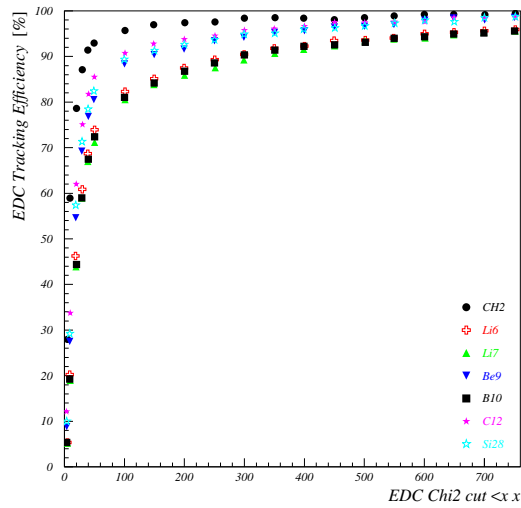
FIGURE 4.46: EDC TRACKING EFFICIENCY AS A FUNCTION OF THE APPLIED CHI2 CUT.
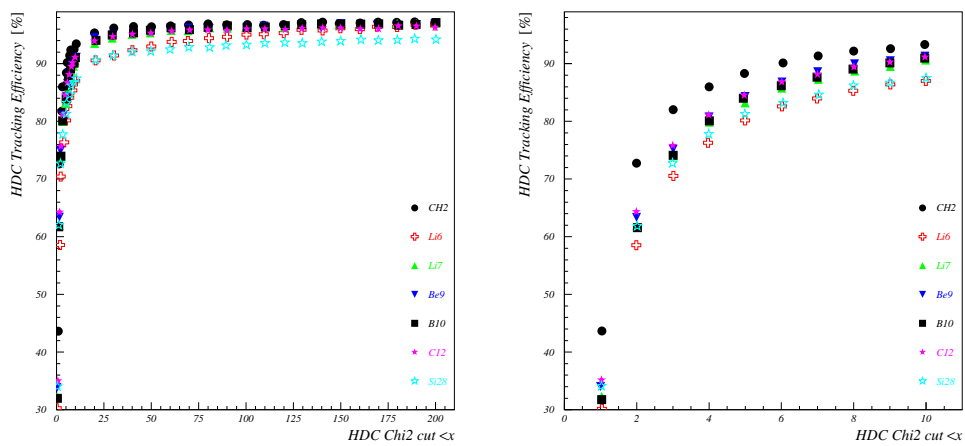
FIGURE 4.47: TRACKING EFFICIENCY OF HKS DRIFT CHAMBERS AS A FUNCTION OF THE APPLIED HDC CHI2 CUT.

Target	Data Set	Runs	EDC		HDC	
			Chi2	Efficiency	Chi2	Efficiency
CH$_2$	#1	55838-56163	50	95.2±0.8	30	96.3±0.4
	#2	56283-57334	50	90.9±0.8	30	94.6±0.7
Li$_6$	#3	60623-61035	80	80±0.3	30	92.2±0.3
Li$_7$	#4	60235-61065	90	79.8±0.5	30	94.8±0.2
Be$_9$	#5	56476-57528	70	85±0.3	30	95.1±0.1
	#5	57529-57538				
	#5	57542-57545				
	#6	59316-59800	70	86.6±0.3	30	95.0±0.4
B$_{10}$	#7	60812-60961	80	80.3±0.3	30	95.1±0.1
C$_{12}$	#8	55911-56230	50	94.0±0.3	30	95.9±0.1
	#8	56229-56230				
	#9	56231-56278	50	91.2±0.6	30	93.4±0.3
	#10	56355-57200	60	87.4±0.2	30	94.2±0.4
	#11	57547-57727	60	88.8±0.2	30	95.5±0.1
	#12	57729-58409	60	87.5±0.3	30	95.6±0.1
	#13	58410-60561	60	87.1±0.3	30	95.3±0.1
Si$_{28}$	#14	57249-58394	65	87.6±0.1	30	92.5±0.2
	#15	58720-59869	65	87.8±0.2	30	92.3±0.3
	#16	59995-60756	85	80.3±0.2	30	91.4±0.2

TABLE 4.4: EDC AND HDC TRACKING EFFICIENCY SUMMARY, CHI2 CUT CONDITIONS USED AND CORRESPONDING EFFICIENCY FOR EACH DATA SET.

Detailed discussion of the effect of the cut conditions, imposed on the three PID tools, on proton and pion rejection and kaon survival is in Section 4.2.2. Time of flight beta (β_{ToF})v cut conditions and corresponding kaon survival efficiencies are summarized in Table 4.7. Aerogel Čerenkov cut conditions and corresponding kaon survival efficiencies are summarized in Table 4.5 and shown in Fig.4.16. Water Čerenkov cut conditions and corresponding kaon survival efficiencies are summarized in Table 4.6 and shown in Fig.4.17.

Kaon Decay Correction

Kaon is an unstable particle with center of mass life time $\tau_k = 12.385 \pm 0.024$ ns [68] ($c\tau_k \sim 371.3$ cm). With central flight path of the HKS spectrometer $\approx 8.35m$ some kaons may decay in its flying path before they reach detectors and so can not be detected. Dominant kaon decay channels are listed in Table 4.8. Cross section calculation has to be corrected for kaon decay by kaon decay factor ϵ_{Decay} which actually, as defined in Eqn.4.20 and Eqn.4.21,

Target	Data Set	$X1_{AC}$ $[NPE_{Norm}]$	Survival [%]	$X2_{AC}$ $[NPE_{Norm}]$	Survival [%]
CH$_2$	#1	4.5	90.1±1.8	8.3	95.1±1.9
	#2	4.4	90.0±1.6	8.1	95.1±1.9
Li$_6$	#3	4.9	90.4±1.4	8.7	95.4±1.7
Li$_7$	#4	5.3	90.7±0.9	8.9	95.1±1.3
Be$_9$	#5	5.1	90.0±1.0	9.1	94.4±1.7
	#6	5.2	89.9±1.0	9.3	94.9±1.4
B$_{10}$	#7	5.1	90.2±1.2	8.9	94.6±1.8
C$_{12}$	#8	4.9	90.4±1.8	8.9	95.0±1.9
	#9	5.3	90.0±1.4	8.9	94.7±1.4
	#10	5.2	90.2±1.1	9.0	95.1±1.2
	#11	5.3	89.9±1.0	9.2	94.9±1.1
	#12	5.4	90.5±1.4	8.9	95.0±1.4
	#13	5.5	90.3±1.0	9.1	95.5±1.1
Si$_{28}$	#14	5.4	90.1±1.0	9.2	95.3±1.1
	#15	5.4	90.3±1.1	9.1	95.0±1.2
	#16	5.5	90.4±1.0	9.1	95.1±1.2

TABLE 4.5: AEROGEL ČERENKOV CUT EFFICIENCY.

Target	Data Set	Cut1 [Photon]	Survival [%]	Cut2 [Photon]	Survival [%]
CH$_2$	#1	82.6	90.5±1.6	73.1	95.5±2.9
	#2	83.0	90.1±1.1	74.0	95.2±1.8
Li$_6$	#3	82.1	90.1±1.3	69.6	95.6±1.7
Li$_7$	#4	84.9	90.5±1.5	73.7	95.6±2.3
Be$_9$	#5	84.1	89.9±1.3	71.1	96.0±1.2
	#6	84.5	90.1±1.5	72.1	95.4±1.5
B$_{10}$	#7	84.1	90.5±1.0	74.6	95.2±2.0
C$_{12}$	#8	82.1	90.5±1.6	76.6	95.4±2.2
	#9	85.1	90.1±1.8	74.0	94.9±2.6
	#10	83.5	90.2±0.9	73.7	95.1±1.3
	#11	82.9	90.9±1.1	72.1	96.0±1.9
	#12	84.3	90.5±1.2	75.4	95.6±2.0
	#13	82.0	90.4±1.0	73.2	95.3±1.3
Si$_{28}$	#14	83.6	90.1±1.3	73.6	95.5±1.7
	#15	85.5	89.9±1.0	76.4	95.1±1.4
	#16	84.7	90.5±1.4	75.5	94.9±1.6

TABLE 4.6: WATER ČERENKOV CUT EFFICIENCY.

Target	Data Set	Cut X$_\beta$	Survival [%]
CH$_2$	#1	0.064	99.0±1.6
	#2	0.065	98.8±1.1
Li$_6$	#3	0.068	98.0±1.3
Li$_7$	#4	0.067	98.5±1.1
Be$_9$	#5	0.07	96.9±2.1
	#6	0.069	97.2±1.7
B$_{10}$	#7	0.068	97.9±1.0
C$_{12}$	#8	0.065	96.9±1.6
	#9	0.065	97.2±1.8
	#10	0.064	97.6±1.0
	#11	0.065	98.0±1.1
	#12	0.068	98.2±1.2
	#13	0.067	98.1±1.0
Si$_{28}$	#14	0.067	98.5±1.3
	#15	0.064	98.4±1.0
	#16	0.066	98.6±1.4

TABLE 4.7: β_{ToF} CUT EFFICIENCY.

represents kaon survival ratio.

Decay modes	Branching ratio
$\mu^+\nu_\mu$	63.44±0.14
$\pi^+\pi^0$	20.92±0.12
$\pi^+\pi^+\pi^-$	5.59±0.03
$\pi^0 e^+\nu_e$	4.98±0.07
$\pi^0\mu^+\nu_\mu$	3.32±0.06
$\pi^+\pi^0\pi^0$	1.75±0.02

TABLE 4.8: SUMMARY OF K$^+$ DECAY CHANNELS [68].

The survival probability after kaon travels a distance of X is:

$$P(x) = e^{-\frac{m_k X}{p_k c \tau_k}} \tag{4.24}$$

where m_k is the kaon mass and p_k is the kaon momentum.

Kaon decay factor was obtained from Monte Carlo simulation. Generated kaon events that reach hodoscope layers (HTOF1X and HTOF2X) and are recognized by Water Čerenkov detectors as kaons are defined as detected (not decayed). Kaon survival ratio is then defined as the number of not decayed kaons and the number of generated kaons. Fig.4.48 shows momentum dependence of kaon survival ratio, Kaon decay factor ϵ_{Decay}. This correction
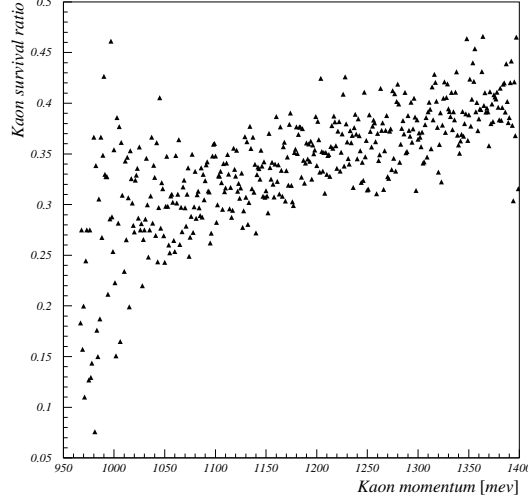
FIGURE 4.48: MOMENTUM DEPENDENCE OF KAON DECAY FACTOR (SURVIVAL RATIO).

in cross section calculation is done on event by event basis. Weighted average is $\epsilon_{Decay} = 0.345 \pm 0.001$.

Kaon Absorption Correction

Kaon produced at the target on its path passes through target, spectrometer system and detectors interacting with these materials by elastic or inelastic scattering. In the case of interaction kaon will not reach second layer of Water Čerenkov detectors and will not be detected. Assuming that N_0 particles enter material of thickness $th[cm]$ the number of absorbed particles will be:

$$N = N_0 \frac{N_A \rho \cdot th}{A} \sigma_0, \qquad (4.25)$$

where $N_A = 6.022 \cdot 10^{23} mol^{-1}$ is Avogadro's number, A is atomic number, $th[cm]$ is thickness of material and $\sigma_0[mb]$ is the absorption cross section [24]:

$$\sigma_0 = 21.065 p_{K+}^{-0.99} A^{0.79}[mb], \qquad (4.26)$$

where p_K is in unit of GeV.

Correction factor that accounts for this is kaon absorption factor defined as:

$$\epsilon_{Abs} = 1 - \frac{N_A \rho \cdot th}{A} \sigma_0 \tag{4.27}$$

The effect of kaon absorption depends on kaon momentum p_K and materials used. Summary of target properties needed for the estimation of kaon absorption is in Table 4.9. Summary of detectors and materials on kaon flight path is in Table 4.10. When both target and HKS materials, as listed in Table 4.9 and Table 4.10, are included in the calculation of factor $N_A \rho \cdot th/A$, the factor amounts to $250 - 255 \cdot 10^{-5} [mb]$. Finally, kaon absorption factor is:

$$\epsilon_{Abs} = 1 - \frac{0.221}{p_{K^+}^{0.99}} \tag{4.28}$$

Fig.4.49 shows momentum dependence of kaon survival ratio, Kaon absorption factor ϵ_{Abs}. This correction in cross section calculation is done on event by event basis.

Target	th [cm]	ρ [g/cm^3]	$N_A \rho$th/A [10^{-5}mb^{-1}]
CH$_2$	0.5008	0.92	5.934
^{6}Li	0.356	0.46	1.640
^{7}Li	0.350	0.54	1.622
^{9}Be	0.1007	1.848	1.244
^{10}B	0.041	2.16	0.533
^{12}C	0.0452	2.25	0.510
^{28}Si	0.0389	2.33	0.195

TABLE 4.9: SUMMARY OF THE E01-011 TARGET PROPERTIES.

Computer dead time

Computer dead time factor describes a situation in which trigger events are lost because DAQ is busy processing the previous event and not able to accept and process new trigger. New trigger is then vetoed by the BUSY signal from trigger supervisor. The Hall C DAQ processes the events with typical time interval of 400 μs. Computer live time ($\epsilon_{LiveTime}$)is defined as a ratio of DAQ accepted (Trigger) events and the number of pre-triggers, as described in Eqn.4.29.

	th [cm]	ρ [g/cm^3]	N$_A\rho$th/A [10^{-5}mb^{-1}]
Target chamber			
Vacuum (2 x 10"5 [Torr], 20 [°C])	$\approx$81	3.2 x 10"11	¡0.00001
Spectrometer			
Spectrometer Vacuum ($\approx 2 \cdot 10^{-5}[Torr], 20[°C]$)	-557	3.2 x 10^{-11}	¡ 0.00001
Kevlar ($C_{14}N_2O_2H_{10}$)	0.02	0.74	0.10563
Mylar ($C_{10}O_4H_8$)	0.0125	1.39	0.11979
Detector Hut			
He bag He gas	100	1.79 $\cdot 10^{-4}$	0.269
Kapton bag	0.004	1.42	0.03489
Drift chambers			
Mylar cathode	0.0176	1.39	0.16866
Ar/C$_2$H$_6$ gas	7.41	0.00154	0.08833
Sense wires	0.00003	19.3	0.001
Field wires	0.00009	19.3	0.002
Hodoscopes	6	1.032	59.95113
Aerogel Cerenkov			
Paper wall	1.8	1.42	6.45799
Silica aerogel	15	0.2	9.21408
Water Cerenkov			
Plastic wall for WC	0.9	1.19	12.56253
Water	15	1	150.42584
Air HDC2 through WC2	115	0.0012	0.57127
Light shielding			
Aluminum foil	0.312	2.7	2.11289
Plastic sheet	1.04	1.30	7.81641
Sum of all contributions			249.90142

TABLE 4.10: SUMMARY OF THE HKS MATERIALS AND THEIR PROPERTIES FOR KAON ABSORPTION CALCULATION.
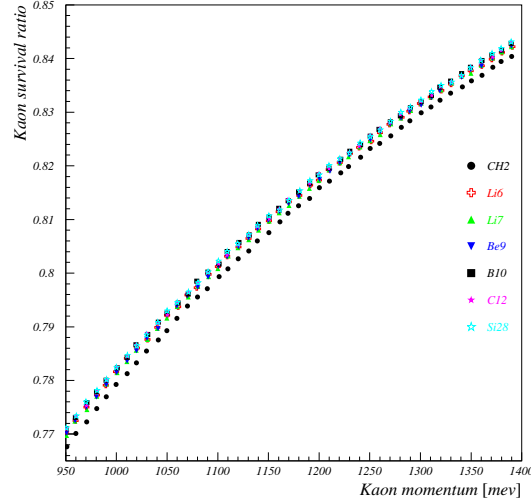
FIGURE 4.49: MOMENTUM DEPENDENCE OF KAON ABSORPTION FACTOR (SURVIVAL RATIO) DUE TO INTERACTION WITH ON PATH MATERIALS.

$$\text{Computer Live Time:} \epsilon_{LiveTime} = \frac{\text{Number of Trigger Events}}{\text{Number of Pretrigger Events}} \qquad (4.29)$$

The relation between time τ needed by DAQ to process an event and computer live time, for small dead time, is:

$$\text{Computer Live Time:} \epsilon_{LiveTime} = e^{-R\tau} \sim 1 - R\tau, \qquad (4.30)$$

where R is the pretrigger rate.

Fig.4.50 shows computer livetime as measured during the E01-011 running period. Computer live time conditions for all data sets are summarized in Table 4.11.

4.7.4   Summary of the cross section factors

All factors needed to calculate hypernuclear cross section from the experimental yields by equation 4.20 for all targets and data sets are summarized
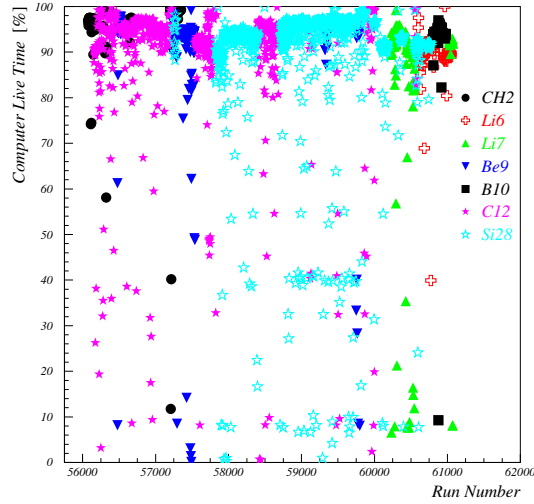
FIGURE 4.50: COMPUTER LIVE TIME AS A FUNCTION OF RUN NUMBER.

Target	Data Set	Runs	Charge [mC]	Average current [μA]	DAQ Live time [%]
CH$_2$	#1	55838-56163	95.025	1.387	96.95
	#2	56283-57334	271.259	1.388	97.95
Li$_6$	#3	60623-61035	2545.125	21.15	90.49
Li$_7$	#4	60235-61065	3828.735	25.50	91.53
Be$_9$	#5	56476-57528	2344.404	18.31	92.52
	#5	57529-57538			
	#5	57542-57545			
	#6	59316-59800	1313.366	18.10	94.26
B$_{10}$	#7	60812-60961	3249.134	26.82	94.21
C$_{12}$	#8	55911-56230	556.72	14.54	92.68
	#8	56229-56230			
	#9	56231-56282	294.301	21.19	85.10
	#10	56353-57209	6947.060	23.92	94.93
	#11	57547-57727	1191.937	20.65	92.84
	#12	57729-58409	748.642	21.27	87.70
	#13	58410-60561	5202.155	20.59	95.28
Si$_{28}$	#14	57249-58394	2667.613	11.24	92.69
	#15	58720-59869	8542.17	11.37	96.06
	#16	59995-60756	2650.039	16.20	92.36

TABLE 4.11: SUMMARY OF DATA SET AVERAGED COMPUTER LIVE TIME.

here. The number of virtual photons (per electron) was calculate by integrating virtual photon flux and the obtained value is $4.805 \cdot 10^{-6}$ photons per electron. The number of scattering centers N_T for targets used depends on target density and target thickness with values for individual targets written in Table 4.12. Other contributions in Eqn. 4.20 can be divided into kaon momentum depended quantities (HKS spectrometer solid angle $d\Omega$, kaon absorption factor and kaon decay factor) and momentum independent (detector and cut efficiencies). Fig.4.51 shows plot of product of momentum dependent factors $\epsilon_{Abs}\epsilon_{Decay}d\Omega$ in the cross section equation 4.21 as calculated for ^{12}C target. Similar results are obtained for other targets as well. Product of momentum independent quantities for all data sets is given in Table 4.12.

Target	Data Set	Runs	Charge [mC]	Run time [hour]	N_T [$\cdot 10^{22} cm^{-2}$]	$\epsilon_{p_K ind}$
CH$_2$	#1	55838-56163	95.025	19.2	5.9343	0.742±0.024
	#2	56283-57334	271.259	54.8		0.698±0.020
Li$_6$	#3	60623-61035	2545.125	33.7	1.6395	0.552±0.015
Li$_7$	#4	60235-61065	3828.735	42.4	1.6223	0.572±0.016
Be$_9$	#5	56476-57528			1.2435	0.610±0.016
	#5	57529-57538	2344.404	36.6		
	#5	57542-57545				
	#6	59316-59800	1313.366	20.4		0.633±0.017
B$_{10}$	#7	60812-60961	3249.134	34.4	0.53263	0.590±0.015
C$_{12}$	#8	55911-56230	556.720	13.0	0.50992	0.683±0.022
	#8	56229-56230				
	#9	56231-56282	294.301	8.0		0.589±0.019
	#10	56353-57209	6947.060	83.0		0.641±0.012
	#11	57547-57727	1191.937	17.1		0.652±0.013
	#12	57729-58409	748.642	10.2		0.577±0.014
	#13	58410-60561	5202.155	77.1		0.624±0.012
Si$_{28}$	#14	57249-58394	2667.613	69.7	0.19510	0.591±0.014
	#15	58720-59869	8542.17	214.1		0.610±0.012
	#16	59995-60756	2650.039	46.7		0.535±0.013

TABLE 4.12: SUMMARY OF P_{K+} INDEPENDENT CORRECTION FACTORS FOR ALL DATA SETS.
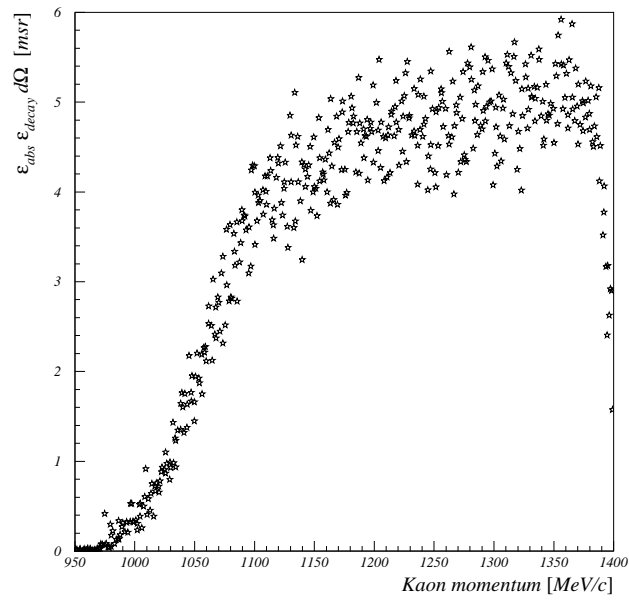
FIGURE 4.51: KAON MOMENTUM DEPENDENCE OF $\epsilon_{Abs}\epsilon_{Decay}d\Omega$ PRODUCT. CAL-CULATION WAS DONE FOR ^{12}C TARGET.

4.7.5   Error estimation

Statistical errors

The statistical errors are connected with the number of events in a bin and can be calculated as the square root of the number of counts [102] as described:

$$\triangle N = \sqrt{N} = \sqrt{S+B}, \tag{4.31}$$

N is total number of events in a bin, S is the number of real coincidence events, B is the number of events due to accidental background.

The statistical uncertainty $\triangle N$ can be made smaller if the number of events in a bin is increased by enlarging the bin width. On the other hand by increasing the bin width the resolution of the missing mass spectra and extracted cross sections decreases and so compromise has to be made.

Systematic errors

Contributions that result in the cross section calculation error are discussed in previous sections, here in Table 4.13 summary of the systematic errors is presented.

| | Systematic error [%] | |
	^{12}C	^{28}Si
Target thickness	2	5
Number of virtual photons (N_γ)	22	
HKS Acceptance	1	
Efficiency (ϵ_{Final})	3	
Optics Calibration	5	
Overall	22	23

TABLE 4.13: SUMMARY OF SYSTEMATIC ERRORS IN THE CROSS SECTION CALCULATION.

The energy resolution of the spectrometer system is derived from the FWHM of the measured $^{12}_{\Lambda}$B ground state. The deduced energy resolution is 0.47 MeV (FWHM) with detailed description in Chapter 5.

Chapter 5

RESULTS AND DISCUSSION

Second generation of the Λ hypernuclear spectroscopy experiment with the $(e, e'K^+)$ reaction (E01-011) was successfully running from June to September 2005 in the experimental Hall C at Thomas Jefferson National Accelerator Facility (TJNAF, JLab). In this chapter the performance of the new electron arm, the so called "Tilt method", and new high resolution kaon spectrometer system (HKS) in terms of particle rates, experimental yields and resolution of hypernuclear states are discussed and compared to the HNSS experiment.

The measured hypernuclear mass spectra of $^{12}_{\Lambda}B$ are shown in Fig.5.1. The experimental results are presented in terms of observed experimental yields (counts) and/or extracted cross sections averaged over HKS spectrometer angular acceptance. Cross section is calculated as described in Eqn. 4.20. Calculated cross sections for observed states are compared to previous experimental results and theoretical predictions.

Two energy scales are used in the presentation of spectra: binding energy (B_{Λ}) and excitation energy (E_x). The excitation energy represents energy excess with respect to the hypernucleus ground state. Binding energy is defined as:

$$B_{\Lambda} = M_{\Lambda} + M_A - M_{HY} \tag{5.1}$$

where M_{Λ} is mass of Λ hyperon, M_A is mass of core nucleus in its ground

state and M_{HY} is mass of the hypernucleus.

Background from accidental coincidences was evaluated from mixed events analysis as described in Section 4.3.1. Increased statistics resulted in a much smaller statistical error when compared to real and measured accidental coincidence events.

5.1   E01-011 performance overview

To fully use capabilities and unique characteristics of the $(e, e'K^+)$ reaction for the hypernuclear spectroscopy, especially for heavier systems, high background flux of bremsstrahlung electrons that limited hypernuclear yields in the HNSS experiment had to be reduced. To achieve this for the HKS experiment new electron arm configuration, the so called "Tilt method" was introduced. The expected benefits are smaller rates of scattered electrons in the Enge spectrometer by limiting flux of bremsstrahlung electrons, better signal to accidental ratio (S/A) and higher production rates. As a result heavier targets with higher on target beam currents can be studied. New kaon spectrometer system (HKS) with bigger solid angle and better momentum resolution was designed and built.

The effect of the E01-011 experimental configuration and the comparison of the performance of E89-009 and E01-011 experiments is discussed here. Information for the HNSS experiment was taken from references [56], [110] and [92].

Results from the E01-011 data from CH_2 target when compared to E89-009 showed improvement in number of Λ counts above accidental background and ^{12}C quasi-free and S/A ratio in coincidence time distribution. From CH_2 data taken in roughly 84 hours there are ≈ 2700 counts in Λ peak compared to ≈ 210 counts from 170 hours of data taking obtained from the E89-009 experiment. Fig.5.2 shows comparison of coincidence time distributions and a clear improvement with ≈ 2.5 better S/A ratio in the E01-011 data. Fig.5.3 shows comparison of missing mass spectra with E01-011 having higher statistics and ≈ 6 times better signal to accidental background ratio.
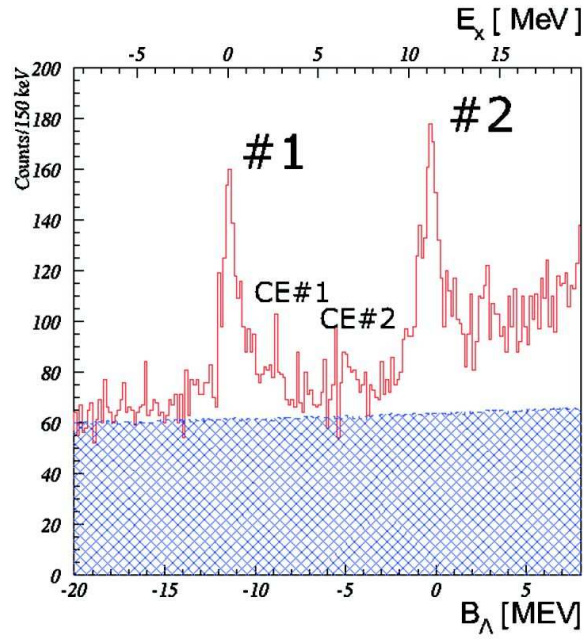
(a) The experimental counts
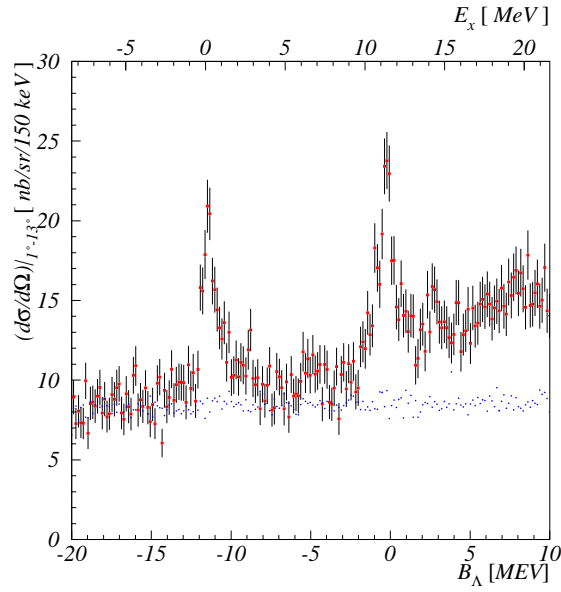
(b) The cross section

FIGURE 5.1: $^{12}_{\Lambda}B$ HYPERNUCLEAR MASS SPECTRA OBTAINED FROM ^{12}C TARGET. THE SPECTRUM FROM ACCIDENTAL COINCIDENCE EVENTS IS OVERLAYED ON BOTH PLOTS. ERRORS ARE STATISTICAL.
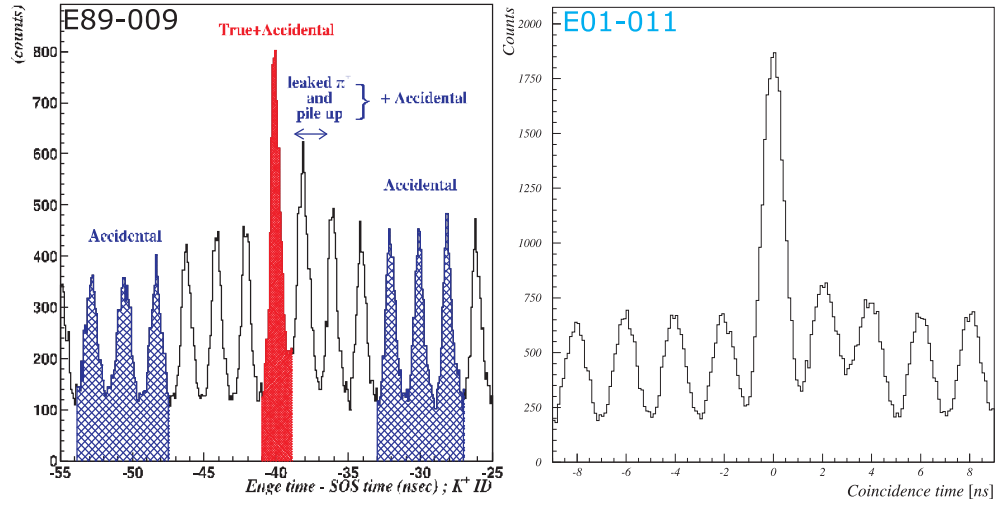
FIGURE 5.2: COMPARISON BETWEEN E89-099 AND E01-011 COINCIDENCE TIME
DISTRIBUTIONS. DATA FROM CH_2 TARGET.
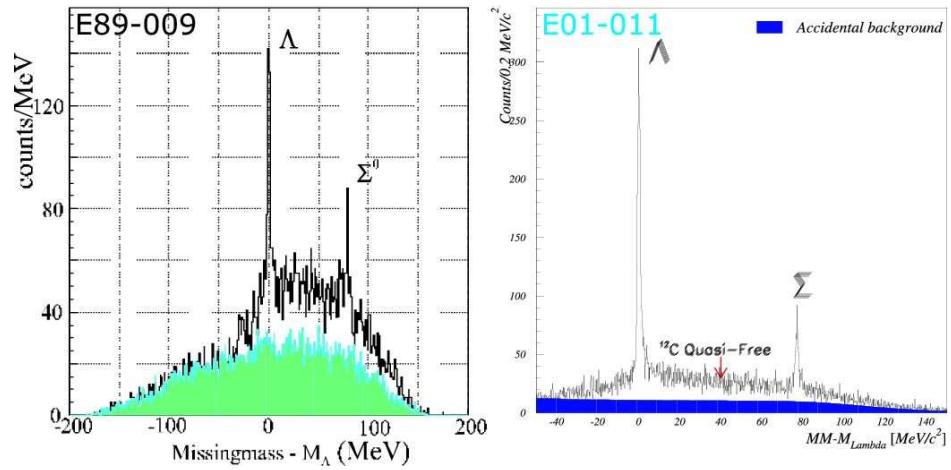
FIGURE 5.3: COMPARISON BETWEEN E89-099 AND E01-011 MISSING MASS
SPECTRA FROM CH_2 TARGET.

The comparison of key performance factors between E089-009 [56] [39] and E01-011 experiment are summarized in Table 5.1. Missing mass spectra of the $^{12}_{\Lambda}$B hypernucleus with overlayed accidental background are compared in Fig.5.4. The number of counts in the $^{12}_{\Lambda}$B ground state doublet above accidental background for 200 hours of the E01-011 data taking is estimated to be ≈ 620 compared to ≈ 165 counts for 440 hours in the E89-009 experiment.

	E89-009	E01-011	Gain
Scattered electron momentum acceptance [MeV/c]	120	320	2.6
Solid angle of kaon arm [msr]	5	16	3.2
Kaon survival	0.37	0.34	0.94
	^{12}C target		
Beam current [μA]	0.66	22.0	33.3
Target thickness [mg/cm^2]	22	100	4.5
Virtual photon flux ($\cdot 10^{-6}$)	370	4.8	0.013
Singles rates of e' arm	>100MHz	1.2MHz	0.012
$^{12}_{\Lambda}$B ground state doublet count	165	620	3.8
Yield rate of $^{12}_{\Lambda}$B ground state doublet [Hz]	$1.0 \cdot 10^{-4}$	$8.3 \cdot 10^{-4}$	8.3
S/A ratio of $^{12}_{\Lambda}$B ground state doublet	0.6	1.4	2.3
Width of $^{12}_{\Lambda}$B ground state doublet [keV]	900	465$\pm$97	

TABLE 5.1: COMPARISON OF HNSS (E89-009) [56] [39] [92] [110] AND HKS (E01-011) EXPERIMENT PERFORMANCE FOR ^{12}C TARGET.

From the information listed in Table 5.1 and Figures 5.2, 5.4 and 5.4 conclusion is that experimental configuration of the E01-011 experiment with implemented HKS spectrometer and "Tilt method" resulted in decrease of the rates seen by electron arm resulting in better S/A ratio, higher hypernuclear yields and as a result hypernuclear spectroscopy with higher statistics and high resolution was realized.
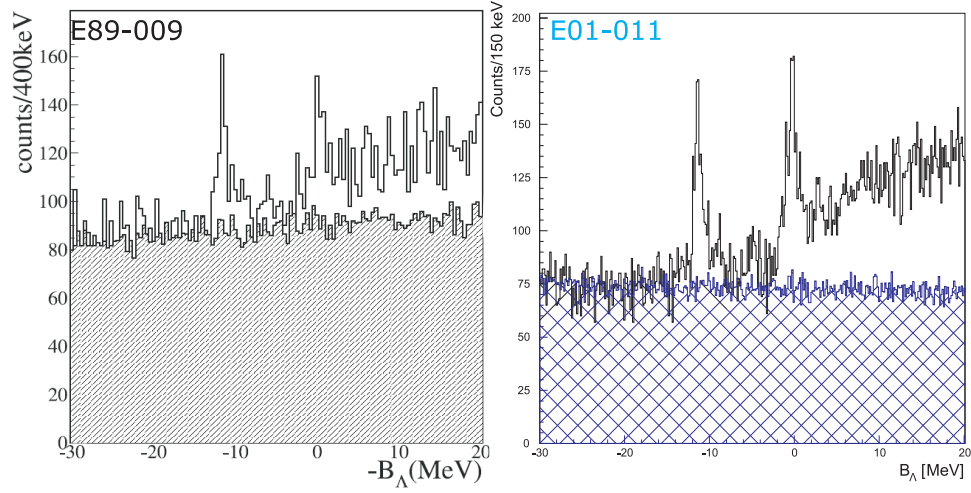
FIGURE 5.4: COMPARISON BETWEEN E89-099 [56] [39] AND E01-011 $_\Lambda^{12}$B SPEC-
TRA.

5.2   Spectroscopy of the $_\Lambda^{12}B$ hypernucleus

5.2.1   Experimental results

Fig.5.1 shows measured hypernuclear mass spectra of $_\Lambda^{12}B$ in terms of ob-
served experimental yields and extracted cross section (averaged over HKS
spectrometer angular acceptance). The hypernuclear mass spectrum, in
terms of cross section with subtracted background is shown in Fig.5.8. High
statistics study of the background by mixed events analysis was done, limit-
ing statistical errors from the background subtraction to final cross section.
The error bars represent statistical uncertainties including the contribution
from background subtraction.

Two prominent peaks, one at $B_\Lambda \approx -11.5 MeV$ and the other near the
Λ emission threshold $B_\Lambda \approx 0 MeV$, are clearly evident in the spectrum.
They correspond to proton-hole Λ-particle configuration, s_Λ ground state
$^{11}B(3/2^-) \otimes s_{\Lambda 1/2}$ and p_Λ substitute states $^{11}B(3/2^-) \otimes p_{\Lambda 1/2}$ and $^{11}B(3/2^-) \otimes$
$p_{\Lambda 3/2}$ [94] [95].

Additionally, two peaks have been observed between ground state and

composite p-shell peaks. The origin of these peaks is in the coupling of the ^{11}B core excited states and Λ hyperon. The observed core excited states of $^{12}_{\Lambda}B$ hypernuclei are expected to be at the same excitation energy of ^{11}B states because $^{12}_{\Lambda}B$ is considered as weakly coupled ^{11}B core nucleus and Λ hyperon. Core excited states, as obtained from $^{12}_{\Lambda}B$, can be compared to ^{11}B core excited states obtained from proton pick-up $(e, e'p)$ reaction on ^{12}C target resulting in the ^{11}B spectrum through reaction $^{12}C(e, e'p)^{11}B$. Both interactions produce proton-hole states. The results of various proton pick-up reactions producing ^{11}B are summarized in Table 5.2.

Proton pick-up Reaction	J^{π}	E_x [MeV]	S-factor
$^{12}C(p,2p)^{11}B$	$3/2^-$	0.00	2.00
	1/2-	2.12	0.37
	5/2-	4.44	0.15
	3/2-	5.02	1.08
	1/2+	6.79	0.25
$^{12}C(d,^{3}He)^{11}B$	3/2-	0.00	2.98
	1/2-	2.12	0.69
	3/2-	5.02	0.31
$^{12}C(e,e'p)^{11}B$	3/2-	0.00	1.72
	1/2-	2.12	0.26
	3/2-	5.02	0.20

TABLE 5.2: SPECTROSCOPIC FACTORS OF THE ^{11}B FROM PROTON PICK-UP RE-ACTIONS ON ^{12}C.

From the experimental results binding energies and cross sections of the observed peaks in the $^{12}_{\Lambda}B$ spectrum are extracted from fitting the spectrum with combination of function representing quasi-free part and Gaussians for each of the hypernuclear states. Cross sections for ground state and composite p-shell peaks were calculated. Due to smaller S/N ratio and bigger statistical errors in the core excited states the cross section results will not be given. The obtained binding energies and cross sections are represented in table 5.3 and shown in Fig.5.5 and Fig.5.8.

The width of the ground state with resolution of 470 keV (FWHM) represents the best resolution ever achieved in hypernuclear spectroscopy.
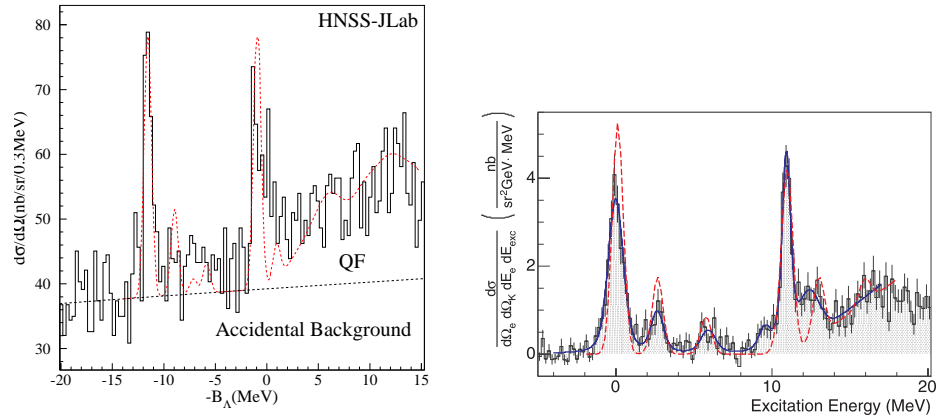
(a) JLab Hall C : E89-009 [56]

(b) JLab Hall A : E94-107 [70] [36]
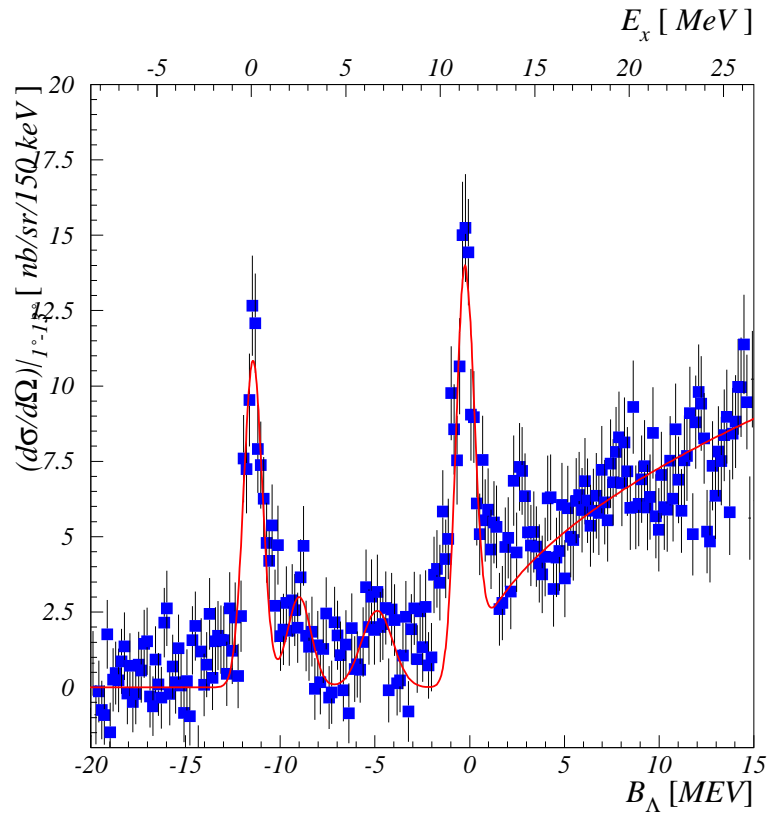
(c) Present study JLab Hall C : E01-011

FIGURE 5.5: SPECTRA OF $^{12}_{\Lambda}$B HYPERNUCLEI AS MEASURED BY THREE JLAB EXPERIMENTS: E89-009 [56], E94-107 [70] AND E01-011 (PRESENT STUDY).

Peak	E_x	B_Λ	Errors	FWHM	Cross sections
No.	[MeV]	[MeV]	[MeV]	[MeV]	[μb/sr]
#1	0	-11.56	$\pm$0.01$\pm$0.15	0.47$\pm$0.07	89$\pm$7$\pm$19
CE#1	2.80	-8.76	$\pm$0.05$\pm$0.15	0.45$\pm$0.07	-
CE#2	6.32	-5.24	$\pm$0.07$\pm$0.15	0.57$\pm$0.07	-
#2	11.20	-0.36	$\pm$0.02$\pm$0.15	0.52$\pm$0.07	98$\pm$7$\pm$22

TABLE 5.3: HYPERNUCLEAR STATES AS OBTAINED BY FITTING THE $^{12}_{\Lambda}$B SPEC-TRUM FROM THE E01-011 EXPERIMENT. B_Λ IS BINDING AND E_x IS EXCITATION ENERGY.

5.2.2 Comparison with previous experimental results

Hypernuclear spectrum of $^{12}_{\Lambda}$B hypernuclei obtained in the E01-011 experiment is compared to results of two previous JLab experiments: Hall C experiment E89-009 (HNSS) [56] [39] [44] [92] (data taking in 2000) and Hall A experiment E94-107 [70] [36]. Comparison of results from mentioned experiments is presented in Tables 5.4 and 5.5.

The binding energy of the $^{12}_{\Lambda}$B doublet obtained in presented study as -11.56 $\pm$0.01 (statistic)$\pm$0.15 (systematic) MeV is consistent with emulsion result -11.37 $\pm$0.06 MeV [82] obtained from decay process $^{12}_{\Lambda}B \rightarrow \pi^- + \alpha + \alpha + \alpha$. The results are also consistent with HNSS result -11.52 $\pm$0.35 [39]. The Λ p-shell doublet binding energy -0.36 $\pm$0.02$\pm$0.15 is consistent with HNSS result -0.5 $\pm$0.2 MeV [110] and JLab Hall A experiment E94-107 result 10.93 $\pm$ 0.03 MeV.

Fig.5.6 shows missing mass spectra as obtained by JLab experiments E01-011 and E94-107 [70]. Fig. 5.5 shows calculated cross section results from all three JLab experiments. As can be seen from the figures JLab Hall A experiment E94-107 produced results for six hypernuclear states in the $^{12}_{\Lambda}$B spectrum. In data comparison the results for s-shell and p-shell doublets and two core-excited states were used.

		Hall C E01-011		Hall C E89-009	
Peak	Structure : J^π	E_x [MeV]	FWHM [MeV]	E_x [MeV]	FWHM [MeV]
#1	$^{11}B(\frac{3}{2};g.s.) \otimes s_{\frac{1}{2}\Lambda} : 1^-$ $^{11}B(\frac{3}{2};g.s.) \otimes s_{\frac{1}{2}\Lambda} : 2^-$	$0\pm0.01\pm0.15$	0.47 ± 0.07	$0.0 \pm 0.1 \pm 0.3$	0.92 fixed
CE#1	$^{11}B(\frac{1}{2};2.12) \otimes s_{\frac{1}{2}\Lambda} : 1^-$	$2.80 \pm0.05\pm0.15$	0.45 ± 0.07	$2.5 \pm 0.2 \pm 0.3$	0.92
CE#2	$^{11}B(\frac{3}{2};5.02) \otimes s_{\frac{1}{2}\Lambda} : 2^-$ $^{11}B(\frac{3}{2};5.02) \otimes s_{\frac{1}{2}\Lambda} : 1^-$	$6.32 \pm0.07\pm0.15$	0.57 ± 0.07	$5.4 \pm 0.3 \pm 0.3$	0.92
#2	$^{11}B(\frac{3}{2};5.02) \otimes p_{\frac{1}{2}\Lambda} : 2^+$ $^{11}B(\frac{3}{2};5.02) \otimes p_{\frac{3}{2}\Lambda} : 3^+$	$11.20 \pm0.02\pm0.15$	0.52 ± 0.07	$11.0\pm 0.1 \pm 0.3$	

TABLE 5.4: COMPARISON OF RESULTS FROM JLAB E01-011 AND E89-009 [39] [56] [92] EXPERIMENTS FOR THE $^{12}_\Lambda$B SPECTRUM.

		Hall C E01-011		Hall A E94-107	
Peak	Structure : J^π	E_x [MeV]	FWHM [MeV]	E_x [MeV]	FWHM [MeV]
#1	$^{11}B(\frac{3}{2};g.s.) \otimes s_{\frac{1}{2}\Lambda} : 1^-$ $^{11}B(\frac{3}{2};g.s.) \otimes s_{\frac{1}{2}\Lambda} : 2^-$	$0\pm0.01\pm0.15$	0.47 ± 0.07	0.0 ± 0.03	1.15 ± 0.18
CE#1	$^{11}B(\frac{1}{2};2.12) \otimes s_{\frac{1}{2}\Lambda} : 1^-$	$2.80 \pm0.05\pm0.15$	0.45 ± 0.07	2.65 ± 0.10	0.95 ± 0.43
CE#2	$^{11}B(\frac{3}{2};5.02) \otimes s_{\frac{1}{2}\Lambda} : 2^-$ $^{11}B(\frac{3}{2};5.02) \otimes s_{\frac{1}{2}\Lambda} : 1^-$	$6.32 \pm0.07\pm0.15$	0.57 ± 0.07	5.92 ± 0.13	1.13 ± 0.29
#2	$^{11}B(\frac{3}{2};5.02) \otimes p_{\frac{1}{2}\Lambda} : 2^+$ $^{11}B(\frac{3}{2};5.02) \otimes p_{\frac{3}{2}\Lambda} : 3^+$	$11.20 \pm0.02\pm0.15$	0.52 ± 0.07	10.93 ± 0.03	0.67 ± 0.15

TABLE 5.5: COMPARISON OF RESULTS FROM JLAB E01-011 AND E92-107 [70] [36] EXPERIMENTS FOR THE $^{12}_\Lambda$B SPECTRUM.
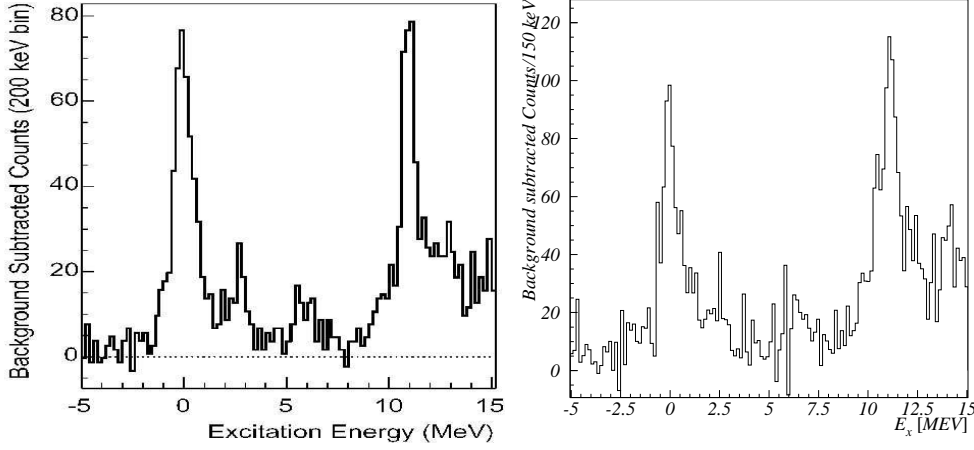
(a) JLab Hall A: E94-107 [70] [36]   (b) Present study, JLab HAll C E01-011

FIGURE 5.6: COMPARISON BETWEEN JLAB HALL A: E94-107 AND HALL C: E01-011 MEASURED $^{12}C(e, e'K^+)_\Lambda^{12}B$ MASS SPECTRA WITH SUBTRACTED BACKGROUND.

5.2.3 Theoretical interpretation

The obtained experimental results in terms of $_\Lambda^{12}B$ cross sections and excitations energies are compared to theoretical calculations based on DWIA with configuration-mixed shell model [83] [84] [94] and with three different isobaric models: Williams-Ji-Cotanch (C4) [67], Saclay-Lyon (SLA) model [57]and Kaon-Maid (KMAID) [55] that describe elementary process ($\gamma p \to \Lambda K^+$) and can be used for electro-production process. Hypernuclear wave functions were obtained by diagonalizing the Hamiltonian:

$$H = H_N^{Cohen-Kurath} + t_\Lambda + \xi(\mathbf{l}_\Lambda \cdot \mathbf{s}_\Lambda) + \sum_N v_{\Lambda N}, \qquad (5.2)$$

where $H_N^{Cohen-Kurath}$ is the Cohen-Kurath shell-model [107] [106] [47] Hamiltonian describing core-nucleus, t_Λ is the kinetic energy of Λ hyperon, $\xi(\mathbf{l}_\Lambda \cdot \mathbf{s}_\Lambda)$ is the spin-orbit potential of Λ and $v_{\Lambda N}$ is the effective ΛN interaction. The effective interaction part, the YNG interaction [111] was deduced on the basis of the G-matric calculation with the Nijmegen soft core model-F (NSCF97f)

[62] interaction.

Fig.5.7 shows the calculated $^{12}_{\Lambda}\text{B}$ spectrum by the (γ, K^+) reaction at $\theta_{K^+}^{Lab} = 3°, E_\gamma = 1.3 GeV$ [94]. The corresponding values are listed in Table 5.6. The spectrum shows the ground state composed of two states, the spin-doublet (non-spin-slip and spin-flip) of s_Λ coupled to the ground state $^{11}B(\frac{3}{2}; g.s.)$ core with configurations $^{11}B(3/2^-)\otimes s_{\Lambda 1/2}$ and $^{11}B(\frac{3}{2}; g.s.)\otimes s_{\frac{1}{2}\Lambda}$ with $J^\pi = 1^-$ and $J^\pi = 2^-$, respectively. Their separation is predicted to be 0.14MeV, due to weak ΛN spin-spin interaction, so they can not be resolved by our experimental resolution. Therefore the ground state doublet peak obtained in the E01-011 experiment was fitted with single Gaussian function. Due to the large spin-flip amplitude in electro and photoproductions, it is believed that the $J^\pi = 2^-$ state dominates in this peak.

The p_Λ peak, as seen from the figure, is composed of high spin stretched states $J^\pi = 2^+$s and $J^\pi = 3^+$, with Λ remaining in the p-shell and coupled to $^{11}B(\frac{3}{2}; g.s.)$ core. The importance of the $(e, e'K^+)$ reaction in the study of hypernuclei manifests here because the $J^\pi = 2^-$ in the ground state and $J^\pi = 3^+$ p-shell substitute state of the $^{12}_{\Lambda}\text{B}$ can only be produced by the electro or photoproduction.

Peak	Experimental results		Theoretical calculation		
	E_x [MeV]	$\overline{(d\sigma/d\Omega)}_{1°-13°}$ [nb/sr]	Structure : J^π	E_x [MeV]	Cross section [nb/sr]
# 1	0.0±0.01±0.15	89 ±7 ± 19	$^{11}B(\frac{3}{2}; g.s.)\otimes s_{\frac{1}{2}\Lambda} : 1^-$	0.0	34.9
			$^{11}B(\frac{3}{2}; g.s.)\otimes s_{\frac{1}{2}\Lambda} : 2^-$	0.14	120.8
# 2	11.20±0.02±0.15	98 ±7 ± 22	$^{11}B(\frac{3}{2}; g.s.)\otimes p_{\frac{3}{2}\Lambda} : 3^+$	10.08	98.3
			$^{11}B(\frac{3}{2}; g.s.)\otimes p_{\frac{1}{2}\Lambda} : 2^+$	10.61	61.5

TABLE 5.6: COMPARISON OF THE E01-011 HYPERNUCLEAR BINDING ENERGIES AND CROSS SECTIONS FROM THE $^{12}_{\Lambda}\text{B}$ SPECTRUM WITH THEORETICAL CALCULATION [94].

The summary of binding energies and cross sections obtained in the E01-011 experiment and theoretical calculations by M.Sotona et al [97] based on three different isobaric models (C4, SLA and KMAID) is in Table 5.7. Theoretical results were done with $E_{Beam} = 1.8 GeV$ with summation over kaon scattering angle in the range $1° < \theta_{K^+}^{Lab} < 13°$. It can be concluded that
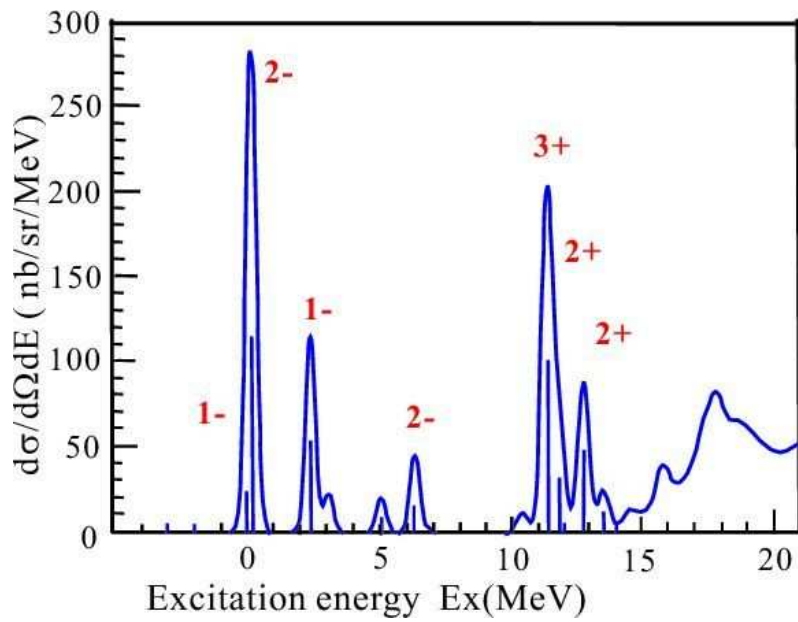
FIGURE 5.7: CALCULATED SPECTRUM FOR THE $^{12}C(e,e'K^+)^{12}_{\Lambda}B$ REACTION AT $E_\gamma = 1.3$ GeV AND $\theta^{LAB}_{K^+} = 3°$ WITH FIXED ENERGY RESOLUTION OF 300keV (FWHM). UPDATE WITH NSC97F FROM [94] [95].

measured excitation energies of the p-shell states is in good agreement with theoretical predictions. Based on measured cross sections the experimental results favor the theoretical calculation with Saclay-Lyon (SLA) isobaric model.

| Peak | Experimental results | | Structure : J$^\pi$ | Theoretical calculation | | | |
| | E_x | $\overline{(d\sigma/d\Omega)}_{1°-13°}$ | | E_x | $\overline{(d\sigma/d\Omega)}_{1°-13°}$ [nb/sr] | | |
	[MeV]	[nb/sr]		[MeV]	C4	SLA	KMAID
# 1	0.0±0.01±0.15	89 ±7 ± 19	$^{11}B(\frac{3}{2}; g.s.) \otimes s_{\frac{1}{2}\Lambda} : 1^-$	0.0	22.8	19.7	20.7
			$^{11}B(\frac{3}{2}; g.s.) \otimes s_{\frac{1}{2}\Lambda} : 2^-$	0.14	82.0	65.7	43.0
# 2	11.20±0.02±0.15	98 ±7 ± 22	$^{11}B(\frac{3}{2}; g.s.) \otimes p_{\frac{3}{2}\Lambda} : 3^+$	10.99	56.9	48.3	38.0
			$^{11}B(\frac{3}{2}; g.s.) \otimes p_{\frac{1}{2}\Lambda} : 2^+$	11.06	107.3	75.3	68.5

TABLE 5.7: COMPARISON OF THE E01-011 HYPERNUCLEAR BINDING ENERGIES AND CROSS SECTIONS FROM THE $^{12}_\Lambda$B SPECTRUM WITH THEORETICAL CALCULATION.

5.2.4   Comparison of the two mirror hypernuclei

The mirror nucleus of $^{12}_\Lambda$B is $^{12}_\Lambda$C hypernucleus and so the observed spectra are compared. The comparison of energy levels of the same spin-parity states will give valuable information about charge symmetry breaking (CSB) effect.

Fig. 5.8 shows two$^{12}_\Lambda$C spectra obtained by KEK-E369 [54] and FINUDA [71] [72] [73] experiments. The $^{12}_\Lambda$B spectrum is also shown for comparison. Since the $^{12}_\Lambda$C hypernuclei are meson induced the spectrum excites only natural parity states and because of that spin assignments are different from the ones in the $^{12}_\Lambda$B spectrum. The KEK-E369 spectra were obtained by the (π^+, K^+) reaction measured by a superconducting kaon spectrometer (INS-SKS) at the K6 beamline of the KEK 12 GeV PS in 2001. The FINUDA spectrum was obtained by the (K^-, π^-) reaction measured by the FINUDA spectrometer for the first time at an e^+e^-collider: DAΦNE, the Frascati Φ-factory in 2004.

Both $^{12}_\Lambda$C spectra have similar structure with two prominent peaks: #1 and #5 in the KEK-E369 spectrum and #1 and #6 in the FINUDA spectrum. Additional structures were observed together with the quasi-free con-

tribution in the unbound region. The FINUDA spectrum was also fitted with six and seven Gaussian functions with later producing a result with better χ^2/d.o.f. The results of the two experiments are summarized in Tables 5.8 and 5.9. The two large peaks are interpreted as neutron-hole Λ-particle configurations: $^{11}C(\frac{3}{2}^-; 0.00) \otimes s_{\frac{1}{2}\Lambda}$ and mixture of $^{11}C(\frac{3}{2}^-; 0.00) \otimes p_{\frac{1}{2}\Lambda}$ and $^{11}C(\frac{3}{2}^-; 0.00) \otimes p_{\frac{3}{2}\Lambda}$, respectively. This configuration is very similar to the proton-hole Λ-particle configurations in the $^{12}_{\Lambda}B$ spectrum, see Fig.5.7 and Fig.5.8.

By comparing the binding (excitation) energies of $^{12}_{\Lambda}B$, listed in Table 5.3, and $^{12}_{\Lambda}C$ the similarity of spectra is obvious.

The spacing between the s-shell and p-shell Λ states from the $^{12}_{\Lambda}B$ spectrum is 11.2±0.1 MeV. The difference in the spacing between s-shell and p-shell Λ states of $^{12}_{\Lambda}B$ and $^{12}_{\Lambda}C$ hypernuclei obtained from experiments and theory is represented in Table 5.10. The difference in s-p shell energy spacing between the $^{12}_{\Lambda}B$ spectrum from present analysis and the $^{12}_{\Lambda}C$ spectrum from KEK-E369 measurement are consistent with theory calculated values. The FINUDA result with seven peaks fit does not (in combination with the results from present study) produce such a consistent result.

Peak No.	E_x [MeV]	$-B_\Lambda$ [MeV]	Errors [MeV]	FWHM [MeV]	Cross sections [μb/sr]
#1	0	10.76	(fixed)	1.44±0.05	8.07± 0.38
#2	2.51	8.25	±0.17	1.44 ± 0.05	1.04±0.14
#3	6.30	4.46	± 0.11	1.44 ± 0.05	1.29 ± 0.21
#4	8.06	2.70	± 0.19	1.44 ± 0.05	0.99 ± 0.17
#5	10.66	0.10	±0.04	1.44 ± 0.05	7.71 ± 0.45
#6	12.37	-1.61	±0.09	1.44 ±0.05	3.01 ± 0.40

TABLE 5.8: HYPERNUCLEAR STATES AS OBTAINED BY FITTING THE $^{12}_{\Lambda}C$ SPECTRUM FROM THE KEK-E369 EXPERIMENT [54]. B_Λ IS BINDING AND E_x IS EXCITATION ENERGY. ERRORS ARE STATISTICAL.
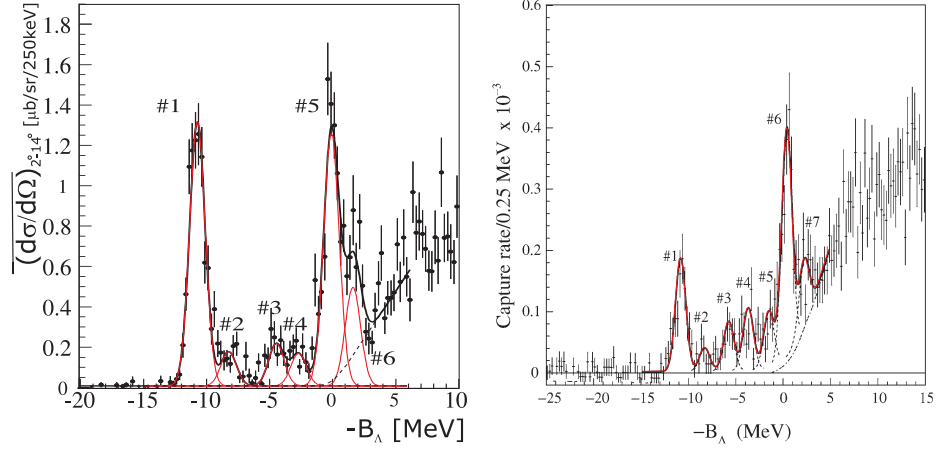
(a) KEK-E369:(π^+, K^+) reaction [54]

(b) INFN-DAΦNE: (K^-, π^-) [71]
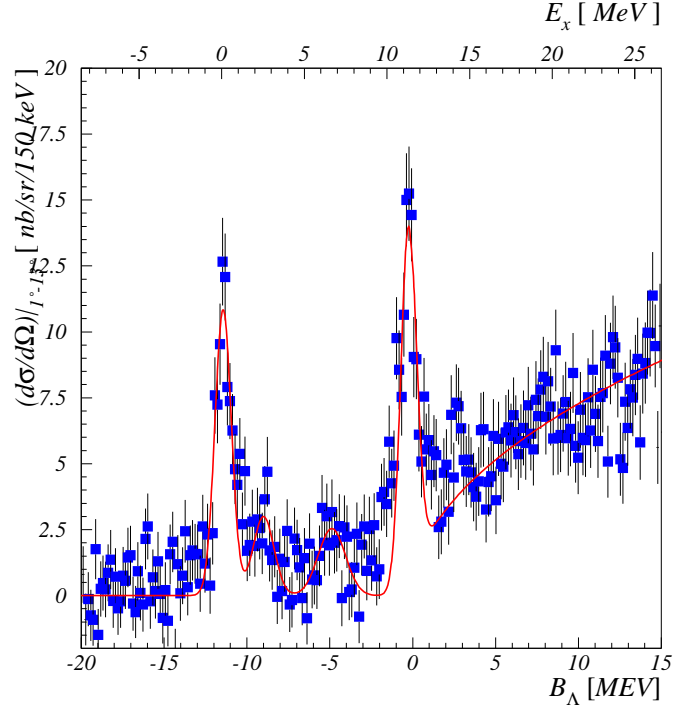
(c) Present study JLab Hall C (E01-011): $(e, e'K^+)$ reaction

FIGURE 5.8: THE HYPERNUCLEAR MASS SPECTRA OF $^{12}_\Lambda$C BY THE (A) EXP. KEK-SKS E369: (π^+, K^+) REACTION (B) EXP. DAΦNE-FINUDA: (K^-, π^-) REACTION AND $^{12}_\Lambda$B BY PRESENT STUDY (C) JLAB HALL C EXP. E01-011: $(e, e'K^+)$ REACTION

Peak number	E_x	$-B_\Lambda$ [MeV]	Capture rate/(stopped K$^-$)[$\cdot 10^{-3}$]
#1	0	10.94±0.06	1.01±0.11$_{stat}$ ± 0.10$_{syst}$
#2	2.56±0.2	8.4±0.2	0.21±0.05
#3	5.04±0.1	5.9±0.1	0.44±0.07
#4	7.14±0.1	3.8±0.1	0.56±0.08
#5	9.34±0.2	1.6±0.2	0.50±0.08
#6	11.21±0.06	-0.27±0.06	2.01±0.17
#7	13.04±0.2	-2.1±0.2	0.58±0.18

TABLE 5.9: HYPERNUCLEAR STATES AS OBTAINED BY FITTING THE $^{12}_\Lambda$C SPECTRUM FROM THE FINUDA EXPERIMENT [71].B_Λ IS BINDING ENERGY.

Reaction	Experiment		Theory	
	Δsp	Δsp($^{12}_\Lambda$B)-Δsp($^{12}_\Lambda$C)	Δsp	Δsp($^{12}_\Lambda$B)-Δsp($^{12}_\Lambda$C)
	[MeV]	[MeV]	[MeV]	[MeV]
$^{12}C(e,e'K^+)^{12}_\Lambda B$	11.20±0.02 ± 0.15	-	11.06 [97]	-
$^{12}C(\pi^+,K^+)^{12}_\Lambda C$	10.66±0.04	0.54±0.16	10.6 [83]	0.46
$^{12}C(K^-,\pi^-)^{12}_\Lambda C$	11.2±0.1	0.0±0.18	10.6	0.46

TABLE 5.10: MEASURED AND THEORY CALCULATED Λ S-P SHELL ENERGY SPACING OF $^{12}_\Lambda$B AND $^{12}_\Lambda$C HYPERNUCLEI [97] [83].

5.3 Spectroscopy of the $^{28}_\Lambda Al$ hypernucleus

5.3.1 Experimental results

The $^{28}_\Lambda Al$ hypernuclear mass spectra represents the first ever hypernuclear spectroscopy by the $(e,e'K^+)$ reaction with Λ populating above the p-shell state. Also it is the first time ever that the $^{28}_\Lambda Al$ hypernuclear mass spectra has been measured.

The measured $^{28}_\Lambda Al$ hypernuclear mass spectra is shown in Fig.5.9 in terms of experimental yields and in Fig.5.10 in terms of cross section with the subtracted background. The obtained spectra show three prominent peaks at $B_\Lambda \approx -18 MeV$ and $B_\Lambda \approx -7 MeV$ in the bound region and an additional peak at $B_\Lambda \approx +2 MeV$ in the unbound region. Peaks are interpreted as being proton-hole with a Λ hyperon configuration $0d_{\frac{5}{2}}^{-1} \otimes s_\Lambda$, $0d_{\frac{5}{2}}^{-1} \otimes p_\Lambda$, and $0d_{\frac{5}{2}}^{-1} \otimes d_\Lambda$, respectively. The spectrum was fitted with three Gaussians and a second-order polynomial representing the continuum part. The fitting results
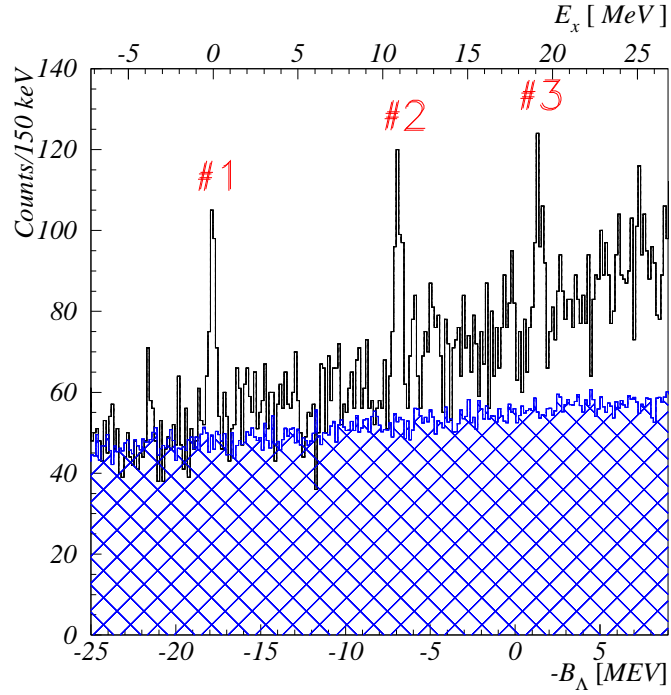
(a) The experimental counts

FIGURE 5.9: THE $^{28}_{\Lambda}Al$ HYPERNUCLEAR MASS SPECTRA OBTAINED FROM THE ^{28}Si TARGET. THE SPECTRUM FROM ACCIDENTAL COINCIDENCE EVENTS IS OVER-LAYED ON BOTH PLOTS. ERRORS ARE STATISTICAL.

of the spectrum are shown in Table 5.11. Additionally, we see significant and un-resolvable strength in between the three prominent peaks.

5.3.2   Theoretical interpretation

The theoretical calculations for the $^{28}Si(e, e'K^+)^{28}_{\Lambda}Al$ reaction and the extraction of hypernuclear properties are based on DWIA formalism with three modern isobar models : Williams-Ji-Cotanch (C4) [67], Saclay-Lyon (SLA) [57] and Kaon-MAID (KMAID) [55]. The differences between the models are mainly due to particular choice of nucleon and hyperon resonances, inclusion of hadronic form factor (or not), SU(3) symmetry constraint required or not [99].
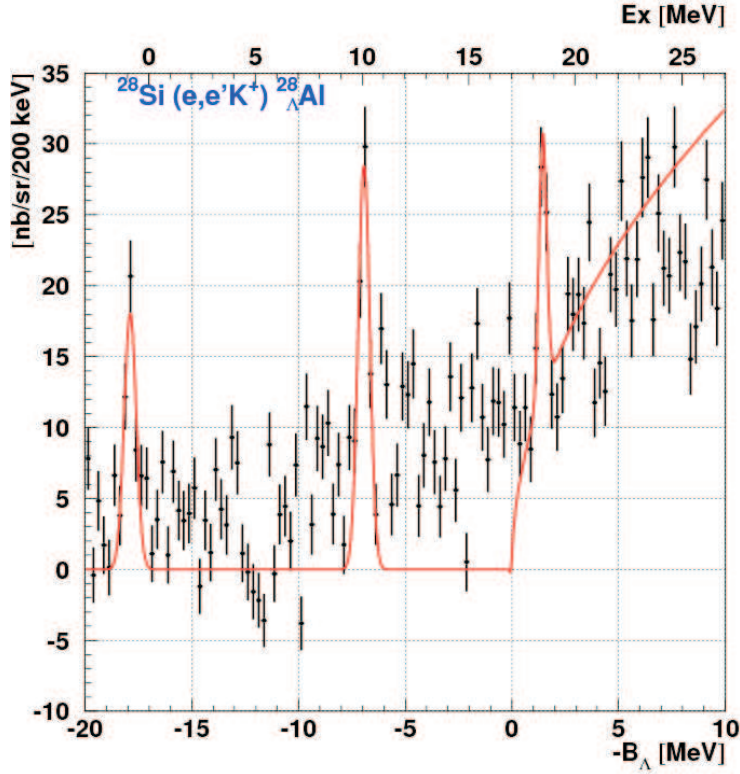
(a) The cross section

FIGURE 5.10: THE $^{28}_{\Lambda}Al$ HYPERNUCLEAR MASS SPECTRA OBTAINED FROM THE ^{28}Si TARGET. THE SPECTRUM FROM ACCIDENTAL COINCIDENCE EVENTS IS OVERLAYED ON BOTH PLOTS. ERRORS ARE STATISTICAL.

Peak No.	E_x [MeV]	B_Λ [MeV]	Errors [MeV]	FWHM [MeV]	Cross sections [μb/sr]
#1	0	-17.82	±0.03±0.18	0.42±0.07	51±10±12
#2	10.91	-6.91	±0.03±0.15	0.48±0.07	78±13±18
#3	19.18	1.36	±0.04±0.15	0.58±0.07	33±7±8

TABLE 5.11: HYPERNUCLEAR STATES AS OBTAINED BY FITTING THE $^{28}_{\Lambda}$AL SPECTRUM FROM THE E01-011 EXPERIMENT. B_Λ IS BINDING AND E_x IS EXCITATION ENERGY.

Fig.5.11 shows calculated spectrum of the $^{28}_{\Lambda}Al$ hypernuclei with SLA isobaric model with fixed kaon scattering angle with aritfical splitting of LS multiplets and $^{28}_{\Lambda}Al$ hypernuclei spectrum as obtained in the E01-011 experiment. The s_{Λ} peak is actually a doublet of natural parity state $0d_{\frac{5}{2}}^{-1} \otimes s_{\frac{1}{2}\Lambda} : J^{\pi} = 2^+$ and unnatural parity state $0d_{\frac{5}{2}}^{-1} \otimes s_{\frac{1}{2}\Lambda} : J^{\pi} = 3^+$. The same structure is also in p-shell ($0d_{\frac{5}{2}}^{-1} \otimes p_{\frac{1}{2}\Lambda} : J^{\pi} = 3^-$, $0d_{\frac{5}{2}}^{-1} \otimes p_{\frac{3}{2}\Lambda} : J^{\pi} = 4^-$) as well as in d-shell. Since the hole-particle interactions for high-spin states are generally very small, the energy difference between the peaks in the doublet is almost equal to the spin-orbit splitting. Relative strengths of the states in the same particle-hole J-multiplet states are shown in Fig. 5.12.

In addition to the major structure with three prominent peaks there are, both in experimental and theoretical MM spectrum, strengths in between. This strengths are consequence of the inclusion of the breakup channels of the $^{28}_{\Lambda}Al$ hypernuclei in the calculation. They were included since heavy hypernuclei or hypernuclei at higher excitations tend to break up into a lighter hypernucleus plus another nucleus. For example: p-shell $^{12}_{\Lambda}C$ hypernucleus tends to break up into $^{11}_{\Lambda}B$+ p or $^{6}_{\Lambda}Li$ hypernucleus which breaks into $^{5}_{\Lambda}He$ + p. This is called hyperfragment process.

In Table 5.12, results obtained from present study and the results of theoretical calculation by Sotona et al [97] for observed peaks are listed. At this stage of optics calibration there seems to be a significant discrepancy both in excitation energy of states and cross section values between present study and theoretical calculations.

5.3.3   Comparison of the two mirror hypernuclei

The comparison of two mirror hypernuclei $^{28}_{\Lambda}Al$ and $^{28}_{\Lambda}Si$ [46] [77] is presented in Fig.5.13 and Table 5.13. The mirror hypernuclei $^{28}_{\Lambda}Si$ spectrum also exhibits three clear peaks (#1, #3, #5) at $B_{\Lambda} \approx -17MeV$ and -8 MeV in the bound region and a broad peak at $B_{\Lambda} \approx 1MeV$ in the unbound region. The mentioned peaks have the same hole-particle configuration as $^{28}_{\Lambda}Al$ states [46] [9].
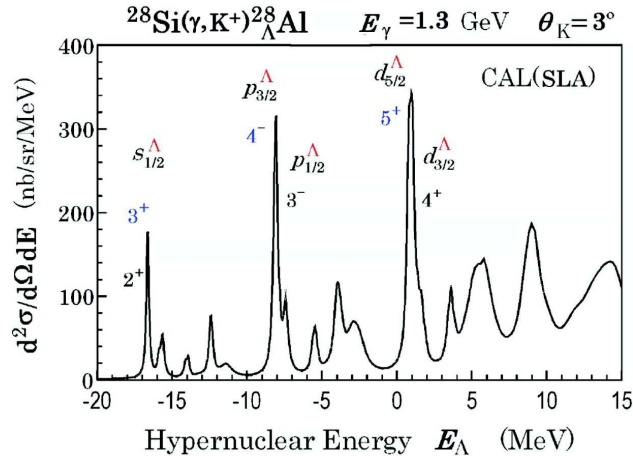
(a) Theoretical calculation
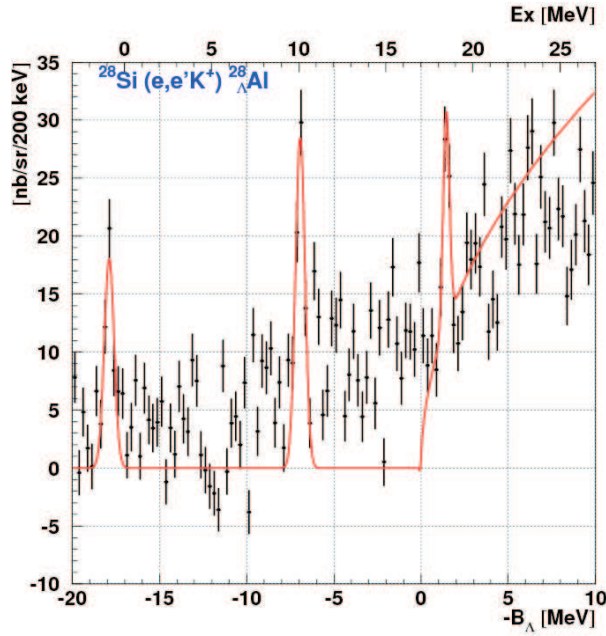
(b) Present study JLab Hall C (E01-011): $(e, e'K^{+})$ reaction

FIGURE 5.11: COMPARISON OF THE $^{28}_{\Lambda}Al$ SPECTRUM OBTAINED IN THE E01-011 EXPERIMENT AND THEORETICAL CALCULATION. (A) CALCULATED SPECTRUM FOR THE $^{28}Si(e, e'K^{+})^{28}_{\Lambda}Al$ REACTION AT $E_{\gamma} = 1.3$ GeV AND $\theta^{LAB}_{K^{+}} = 3°$ WITH SLA MODEL [99] [109]. (B) THE $^{28}_{\Lambda}$AL BY PRESENT STUDY, JLAB HALL C EXP. E01-011: $(e, e'K^{+})$ REACTION
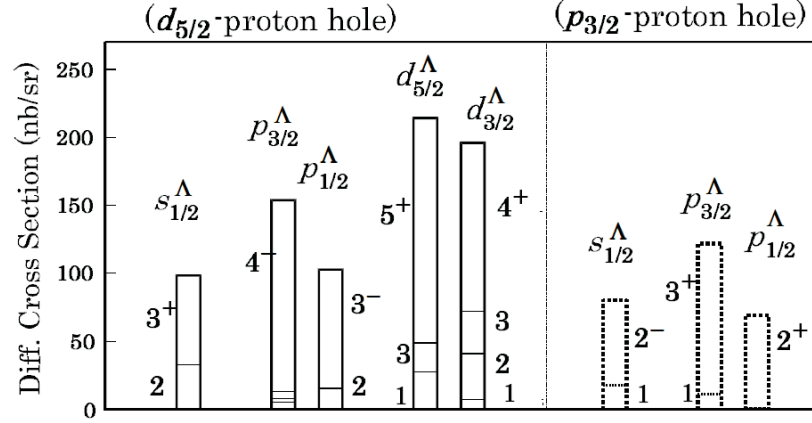
FIGURE 5.12: DIVIDED CONTRIBUTIONS TO THE PARTICLE-HOLE J-MULTIPLET STATE $[j_p^{-1}j^\Lambda]_J$ FOR THE $^{28}Si(e,e'K^+)^{28}_\Lambda Al$ REACTION AT $E_\gamma = 1.3$ GeV AND $\theta_{K^+}^{LAB} = 3°$ WITH SLA MODEL. THE HEIGHT OF EACH PILLAR CORRESPONDS TO THE DIFFERENTIAL CROSS SECTION [99].

| | Experimental results | | | Theoretical calculation | | | |
| | E_x | $\overline{(d\sigma/d\Omega)}_{1°-13°}$ | Structure : J^π | E_x | $\overline{(d\sigma/d\Omega)}_{1°-13°}$ [nb/sr] | | |
Peak	[MeV]	[nb/sr]		[MeV]	C4	SLA	KMAID
# 1	0.0±0.01±0.15	51±10±12	$^{27}Al(\frac{5}{2}) \otimes s_{\frac{1}{2}\Lambda} : 2^+$	0.0	112.7	92.1	71.8
			$^{27}Al(\frac{5}{2}) \otimes s_{\frac{1}{2}\Lambda} : 3^+$				
# 2	10.91±0.03±0.15	78±13±18	$^{27}Al(\frac{5}{2}) \otimes p_{\frac{3}{2}\Lambda} : 4^-$	9.42	167.7	134.9	117.5
			$^{27}Al(\frac{5}{2}) \otimes p_{\frac{1}{2}\Lambda} : 3^-$	9.67	109.1	91.3	58.5
# 3	19.18±0.04±0.15	33±7±8	$^{27}Al(\frac{5}{2}) \otimes d_{\frac{3}{2}\Lambda} : 4^+$	17.6	184.7	148.4	135.1
			$^{27}Al(\frac{5}{2}) \otimes d_{\frac{5}{2}\Lambda} : 5^+$	17.9	167.1	139.1	89.9

TABLE 5.12: COMPARISON OF THE E01-011 HYPERNUCLEAR BINDING ENERGIES AND CROSS SECTIONS FROM THE $^{28}_\Lambda$AL SPECTRUM WITH THEORETICAL CALCULATION.

Table 5.13 shows results of the $^{28}_{\Lambda}Si$ spectrum fit with five Gaussians and a second-order polynomial representing the continuum part. Significant differences between p-shell and d-shell excitation energies of the two mirror nuclei exist.

Peaks	M_{HY}-M_A [MeV]	Errors [MeV]	B_Λ [MeV]	FWHM [MeV]	$\sigma_{2°-14°}$ [νb]
#1	176.6	±0.2	16.6	2.2 (fixed)	0.09±0.01
#2	181.3	±0.4	11.9	4.4±1.0	0.10±0.04
#3	186.2	±0.2	7.0	2.7±0.3	0.27±0.05
#4	189.0	±0.2	4.3	1.4±0.4	0.07±0.04
#5	194.3	±0.8	-1.0	6.5±1.1	0.51±0.16

TABLE 5.13: HYPERNUCLEAR STATES AS OBTAINED BY FITTING THE $^{28}_{\Lambda}$SI SPEC-TRUM [77]. B_Λ IS BINDING AND E_x IS EXCITATION ENERGY.
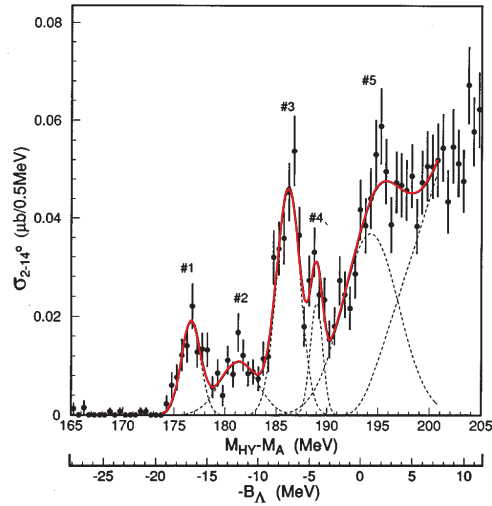
(a) KEK-E369:(π^+, K^+) reaction [77]
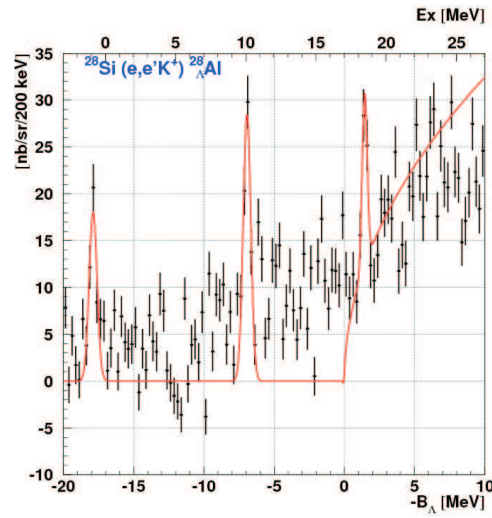
(b) Present study JLab Hall C (E01-011): $(e, e'K^+)$ reaction

FIGURE 5.13: THE HYPERNUCLEAR MASS SPECTRA OF $^{28}_{\Lambda}$SI BY THE (A) EXP. KEK-SKS E369 :(π^+, K^+) REACTION AND (B) $^{28}_{\Lambda}$AL BY PRESENT STUDY, JLAB HALL C EXP. E01-011: $(e, e'K^+)$ REACTION

CONCLUSION

This thesis is based on the experimental activities of the E01-011 HKS collaboration at the Thomas Jefferson National Accelerator Facility, Newport News, Virginia, USA.

In the chapter Physics introduction the topic of Hypernuclear physics is introduced. It has a wide territory of physics problems which are involved in it: hyperon-nucleon interaction, probing of the nuclear interior, examination of medium effects upon hyperon properties... A brief account is given of the past exploration channels of hypernuclei formation being the hadronic one. This thesis, however, deals with the novel channel of electroproduction which features are exposed in the same chapter.

As the important challenge of the collaboration was the achievement of the ultimate energy resolution in the hypernuclear spectra, it was necessary to describe the full complexity of the experiment in the chapter: Experimental apparatus and the data acquisition. The beam energy changes could have negatively influenced the resolution. Therefore, the detection apparatus with the beam monitoring features are described in detail. The essential parts of the HKS system are discussed one by one: hodoscopes, drift chambers for HKS and Enge spectromers, Čerenkov counters of aerogel and water type.

In the Data analysis chapter the procedures of tuning of the components of the system leading to the spectra of optimal resolution are given. Here also each module of the complex system is discussed separately.

The chapter Result and discussion includes a number of spectra demonstrating first the quality of the new apparatus which, due to the Tilt method, has acquired much better statistics and energy resolution of the hypernuc-

lear states. The improvements obtained on the ^{12}C target are also included and compared both to previous experimental efforts and theoretical calculation. Finally, a very new information is displayed using the spectra from the ^{28}Si target. For the targets of ^{12}C and ^{28}Si a detailed discussion of the interpretation of the structures in the spectra is given.

We may conclude that the novel components introduced by the HKS collaboration together with the careful calibration and data analysis explained here, have resulted in both: improved spectrum of ^{12}B hypernucleus and the new spectrum for the ^{28}Al hypernucleus. The latter one is resulting in the observation of the hypernuclear excitation spectrum achieved through electroproduction which goes beyond the known s and p shell excitations.

With the observed hypernuclear spectra, the second generation of the (e,e'K$^+$) hypernuclear spectroscopy experiments has proved that this experimental technique is a practical and powerful tool for the investigation of hypernuclei.

List of Figures

225

List of Tables

Bibliography

[1] D. Halderson A. S. Rosenthal and K. Hodgkinson. *Ann. Phys.*, 184:33, 1988.

[2] C. Armstrong. *Beam Current Measurement in Hall C*. Hall C internal report (unpublished), 1996.

[3] J. Arrington. PhD thesis, Ohio University (unpublished), 1998.

[4] G. Audi, A. H. Wapstra, and C. Thibault. The 2003 atomic mass evaluation: (ii). tables, graphs and references. *Nuclear Physics A*, 729(1):337 – 676, 2003. The 2003 NUBASE and Atomic Mass Evaluations.

[5] H. Band, T. Motoba, and Y. Yamamoto. Narrow widths of λ single particle states in hypernuclei. *Phys. Rev. C*, 31(1):265–267, Jan 1985.

[6] C.B.Dover and D. J. Millener. In B. Frois and I. Sick, editors, *Modern Topics in Electron Scattering*, page 609, Singapore, 1991. World Scientific.

[7] R. E. Chrien and C.B.Dover. *Annu. Rev. Nucl. Part. Sci.*, 39:113, 1989.

[8] R.E Chrien and et. al. States of $^{12}_{\Lambda}c$ formed in the reation $^{12}c(k^-, \pi^-)$. *Physics Letters*, 1979.

[9] Robert E. Chrien. Studies of hypernuclei by associated production. *Nuclear Physics*, 1988.

[10] SAPHIR Collaboration. *Phys. Lett.*, B445:20–26, 1998.

[11] G.A. Krafft C.W. Leemann, D.R. Douglas. *Annual Review fo Particle Science*, page 413. 2001.

[12] C. B. Dover D. J. Millener, A. Gal and R.H. Dalitz. Spin dependence of the λ n effective interaction. *Physical Review C*, 31(2):499, February 1985.

[13] R. H. Dalitz and A. Gal. *Ann. Phys*, 116:167, 1978.

[14] M. Danysz and J. Pniewski. *Philos. Mag.*, 44:348, 1953.

[15] D. H. Davis. *Nucl. Phys.*, A754:3c, 2005.

[16] D. H. Davis and J. Pniewski. *Contemp. Phys.*, 27:91, 1986.

[17] D.F.Geesaman. *Tracking in the SOS spectrometer*. JLab Hall C Internal Report (unpublished), 1993.

[18] C. B. Dover. In B. F. Gibson and W. R. Gibbs, editors, *LAMPF Workshop on (π,K) Physics*, page 3, Los Alamos, NM, 1990. AIP.

[19] C. B. Dover and A. Gal. *Prog. Part. Nucl. Phys.*, 12:171, 1984.

[20] C.B. Dover and D.J. Millener. *Electroproduction of Strangeness*, chapter 3. World Scientific, 1991.

[21] H. Ejiri. *Nucl. Phys.*, A574:311c, 1994.

[22] H. A. Enge. *Nucl. Instr. and Meth.*, 161:161–180, 1979.

[23] A. Bamberger et al. *Phys. Lett.*, 36B:412, 1972.

[24] A. Kerman et al. *Ann. Phys.*, 8:551, 1959.

[25] B. R. Martin et al. *Nucl. Phys.*, B94:413, 1975.

[26] C. Bennhold et al. Hypernuclear physics with photons. In L. Tang and O. Hashimoto, editors, *Proc. of Jlab sponsored Workshop on Hypernuclear Physics with Electromagnetic Probes*, page 1, Hampton, VA, December 1999. Hampton University.

[27] C. Yan et al. *Nucl. Instr. and Meth. in Physics Research*, A365:261, 1995.

[28] C. Yan et al. *Nucl. Instr. and Meth. in Physics Research*, A365:46, 1995.

[29] C.B. Dover et al. *Phys. Rev. C*, 22:2073, 1980.

[30] D.H. Davis et al. *Nucl. Phys.*, A547:269c, 1992.

[31] H. Akikawa et al. *Phys. Rev. Lett.*, 88:082501, 2002.

[32] H. Outa et al. *Prog. Theor. Phys. Suppl.*, 117:177, 1994.

[33] H. Tamura et al. *Phys. ReV. Lett.*, 84:5963, 2000.

[34] H.C.Bhang et al. *Nucl. Phys.*, A639:269c, 1998.

[35] J. Adam et al. *Czech. J. Phys.*, 42:1167, 1992.

[36] J.J.LeRose et al. *Nucl. Phys.*, A804:116–124, 2008.

[37] K. Miwa et al. *Nucl. Phys.*, A754:80c, 2005.

[38] K. Tanida et al. *Nucl. Phys.*, A721:999c, 2003.

[39] L. Yuan et al. *Phys. Rev. C*, 73:044607, 2006.

[40] M. A. Faessler et al. *Phys. Lett.*, 46B:468, 1973.

[41] M. Akei et al. *Nuclear Physics A*, 534:478, 1991.

[42] M. Danysz et al. *Nucl. Phys.*, 49:121, 1963.

[43] M. Ukai et al. *Phys. Rev. Lett.*, 93:232501, 2004.

[44] O. Hashimoto et al. Jlab proposal: Spectroscopic study of λ hypernuclei up to medium-heavy mass region through the (e, e'k+) reaction (unpublished).

[45] O. Hashimoto et al. *Nuclear Phys.*, A 639:93c, 1998.

[46] P. H. Pile et al. *Phys. Rev. Lett.*, 66:2585.

[47] P.G.Roos et al. *Nucl. Phys.*, A255:187, 1975.

[48] R. Bertini et al. *Phys. Lett.*, 83B:306, 1979.

[49] R. Bertini et al. *Phys. Lett.*, 360A:315, 1981.

[50] R. Bertini et al. *Phys. Lett.*, 368A:365, 1981.

[51] S. Aoki et al. *Prog. Theor. Phys.*, 85:1287, 1991.

[52] S. Nozawa et al. *Nucl. Phys.*, A513:511, 1990.

[53] T. Hasegawa et al. *Phys. ReV. Lett.*, 74:224, 1995.

[54] T. Hotchi et al. Spectroscopy of medium-heavy λ hypernuclei via the $(\pi+, k+)$ reaction. *Phys. Rev. C*, 64(4):044302, Sep 2001.

[55] T. Mart et al. *Phys. Rev. C*, 61:012201, 1999.

[56] T. Miyoshi et al. *Phys. Rev. Lett.*, 90:232502–1, 2003.

[57] T. Mizutani et al. *Phys. Rev. C*, 58:72, 1998.

[58] T. Motoba et al. Using kaon electromagnetic production to study hypernuclear t o study hypernuclear systems. In *Sendai 2003, Electrophotoproduction of strangeness on nucleons and nuclei*.

[59] T. Motoba et al. *Prog. Theor. Phys. Suppl.*, 117:123, 1994.

[60] T. Motoba et al. In *Physics with GeV Electrons and Gamma-Rays, Sendai, Japan, 2001*, page 107. Universal Academy press, Inc., 2001.

[61] T. Nagae et al. *Phys. ReV. Lett.*, 80:1605, 1998.

[62] Th. A. Rijken et al. *Nucl. Phys.*, A547:245, 1992.

[63] Th. A. Rijken et al. *Phys. Rev.*, C59:21, 1999.

[64] W. Bruckner et al. *Phys. Lett.*, 55B:107, 1975.

[65] W. Bruckner et al. *Phys. Lett.*, 62B:481, 1976.

[66] W. Bruckner et al. *Phys. Lett.*, 79B:157, 1978.

[67] W.A. Williams et al. *Phys. Rev. C*, 46:1617, 1992.

[68] W.M. Yao et al. *J. Phys. G: Nucl. Part. Phys.*, 33:43, 2006.

[69] Y. Miura et al. *Nucl. Phys.*, A754:75c, 2005.

[70] M.Iodice et al. (JLab Hall A Collaboration). *Phys. Rev. Lett.*, 99:052501, 2007.

[71] M. Agnello et al. (The FINUDA Collaboration). *Phys. Lett.*, B622:35–44, 2005.

[72] M. Agnello et al. (The FINUDA Collaboration). *Nucl.Phys.*, A754:399–409, 2005.

[73] M. Agnello et al. (The FINUDA Collaboration). *Nucl.Phys.*, A752:139–144, 2005.

[74] A. Gal. *Nucl. Phys.*, A754:91c, 2005.

[75] A. Gal, J. M. Soper, and R. H. Dalitz. A shell model analysis of λ binding energies.

[76] B. F. Gibson and E. V. Hungerford. *Physics Reports*, 257:349, 1995.

[77] T. Hasegawa, O. Hashimoto, S. Homma, T. Miyachi, T. Nagae, M. Sekimoto, T. Shibata, H. Sakaguchi, T. Takahashi, K. Aoki, H. Noumi, H. Bhang, M. Youn, Y. Gavrilov, S. Ajimura, T. Kishimoto, A. Ohkusu, K. Maeda, R. Sawafta, and R. P. Redwine. Spectroscopic study of $b\lambda10$, $c\lambda12$, $si\lambda28$, $y\lambda89$, $la\lambda139$, and $pb\lambda208$ by the $(\pi+,k+)$ reaction. *Phys. Rev. C*, 53(3):1210–1220, Mar 1996.

[78] O. Hashimoto and H. Tamura. *Prog. Part. Nucl. Phys.*, 57:564, 2006.

[79] C. Hovater. *Tunning of the CEBAF beam current monitors.* CEBAF internal report, unpublished, 1995.

[80] E.V. Hungerford and et. al. Jefferson lab proposal for e89-09.

[81] H. A. Enge J.E.Spencer. *Nucl. Instr. and Meth.*, 49:181–193, 1967.

[82] M. Jurić and et.al. A new determination of the binding-energy values of the light hypernuclei (a 15). *Nuclear Physics B52*, 1972.

[83] O. Richter K. Itonaga, T. Motoba and M. Sotona. Hypernuclear and λ-spin polarizations produced in the (π^+,k^+) reaction.

[84] T. Motoba K. Itonaga and H. Bando. *Progress of Theoretical Physics Supplement*, (84):291, 1990.

[85] L.Yuan. Spectrometer calibration by expectation maximization method. *arXiv:physics/0512132v1*.

[86] L.Yuan and L.Tang. Optical calibration for jefferson lab hks spectrometer. *arXiv:nucl-ex/0511011v1 [nucl-th]*.

[87] M. May and et al. Observation of levels in c, n, and o hypernuclei. *Physical Review Letters*, 1981.

[88] M. May and et al. Obervation of hypernuclear gamma-ray transition in $^7_\Lambda$li and $^9_\Lambda$be. *Physical Review Letters*, 1983.

[89] D. J. Millener, C.B.Dover, and A. Gal. *Phys. Rev.C*, 38:2700, 1988.

[90] D. J. Millener, A. Gal, and C.B.Dover. *Phys. Rev.*, C31:499, 1985.

[91] C. Milner and et.al. Observation of λ-hypernuclei in the reaction $^{12}c(\pi^+, k^+)^{12}_\Lambda c$ studies of hypernuclei by associated production. *Physical Review Letter*, 54:1237, 1985.

[92] T. Miyoshi. PhD thesis, Tohoku University (unpublished), 2002.

[93] R. M. Mohring. PhD thesis, University of Maryland (unpublished), 1999.

[94] T. Motoba. In *Mesons and Light Nuclei: 8th conference, edited by J. Adam et al.*, page 125, 2001.

[95] Toshio Motoba, Miloslav Sotona, and Kazunori Itonago. Photoproduction of polarized hypernuclei. *Progress of Theoretical Physics Supplement*, 117:123, 1994.

[96] M.Sotona. *Czech. J. Phys.*, 50:Supp. S4, 2000.

[97] M.Sotona. Private communication, 2009.

[98] G. Niculescu. PhD thesis, Hampton University (unpublished), 1998.

[99] T. Motoba K. Itonaga K. Ogawa P. Bydzovsky, M. Sotona and O. Hashimoto. Photo- and electro-production of medium mass lambda-hypernuclei. *arXiv:0706.3836v1 [nucl-th]*, 2007.

[100] P.H. Pile, S. Bart, R.E. Chrien, and et al. Study of hypernuclei by associated production. *Phys. Rev. Lett.*, 1991.

[101] P.Kloeppel. *Beam diagnostics at CEBAF*. CEBAF internal report, 1986.

[102] P.R.Bevington and D.K.Robinson. In *Data reduction and error analysis for the physical sciences*. McGraw-Hill, 2003.

[103] V. Lebedev R. Dickson. In *Fast feedback system for energy and beam stabilization, Proceedings of the 1999 International Conference on Accelerator and Large Experimental Physics Control Systems*.

[104] G. A. Krafft R. Kazimi, C. K. Sinclair. Setting and measuring the longitudinal optics in cebaf injector. In *Proceedings of the XX International Linac Conference*, pages pp. 125–127, August 2000.

[105] M. Rayet. *Nucl. Phys.*, A367:381, 1981.

[106] S.Cohen and D.Kurath. *Nucl. Phys.*, page 1, 1965.

[107] S.Cohen and D.Kurath. *Nucl. Phys.*, A101:1, 1967.

[108] H. Takahashi. Observation of Lambpha and Λ–Λ interaction. In *Bulletin of The American Physical Society, First Joint Meeting of The Nuclear Physics Divisions of APS and JPS*, volume 46, page 56, Hawaii, October 2001. American Institute of Physics.

[109] M.Sotona K.Itonaga K.Ogawa O.Hashimoto T.Motoba, P.Bydzovsky.
      Spectroscopy of medium-mass hypernuclear production.

[110] L. Yuan.   *High precision hypernuclear spectroscopy study by the
      (e,e'K+) reaction.*   PhD thesis, Hampton University (unpublished),
      2002.

[111] Y.Yamamoto and H. Bando. *Progress of Theoretical Physics*, (73):905,
      1985.